TIR-Raman Spectroscopy of Model Supported Lipid Bilayers

CHURCHWELL, JOHN,HAMPILTON

TIR-Raman Spectroscopy of Model Supported Lipid Bilayers.

A thesis submitted in partial fulfilment of the requirements for the degree of Doctor of Philosophy in the University of Durham by,

John H. Churchwell

Department of Chemistry

University of Durham and the College of St. Hild and Bede

February 2014

Abstract

In this thesis the technique of total internal reflection (TIR) Raman spectroscopy was applied to study the properties and interactions of supported lipid bilayers (SLBs) at the silica-water interface, both kinetically and at equilibrium.

First, the formation kinetics of SLB systems from lipid aggregate suspensions was investigated. The lipid systems comprised POPC, POPE, egg-SM and a 1:1:1 mixture of POPE, egg-SM and cholesterol, all in tris buffer with and without added NaCl and $CaCl_2$. Vesicle/aggregate suspensions were prepared by bath sonication and their size distributions were quantified with nanoparticle tracking analysis (NTA). The additional group I and group II salts altered the size distribution of the lipid vesicle/aggregate suspensions produced and played large role in the kinetics observed. For POPC, by changing the buffer conditions the adsorption of extraneous vesicles on the SLB could be tuned. For POPE, a previously unknown formation pathway was observed, whereby larger aggregates spread following adsorption to the interface. For the mixed system, the final ratio of components was found to be the same as that in the initial suspension.

Second, the physical transformations of SLBs composed of DMPC, egg-SM and POPE were examined and the role of NaCl and $CaCl_2$ upon these phase transitions was investigated. Raman spectra were obtained as a function of temperature and quantified using order parameter analysis. The resulting data were interpreted using the Zimm and Bragg model, which yielded the cooperativity of each phase transition. Cooperativity was controlled by the interfacial energy between regions of L_β/P_β and L_α phase. The presence or absence of the above salts altered the number of molecules within the cooperative unit for each of the species listed and controlled the interfacial energy. The most striking result was that of the POPE main phase transition with added $CaCl_2$, for which cooperativity was massively reduced yielding a structural transition over a broad temperature range; AFM images confirmed the nature of this transition, showing domain like structures over a matching broad temperature range.

Third, the interaction of SDS with SLBs composed of POPE, POPC, egg-SM and the 1:1:1 mixture of POPE, egg-SM and cholesterol was explored. Partitioning isotherms were constructed from equilibrium data and interpreted with a non-ideal partitioning model previously applied to vesicular systems. Accounting for the theoretical build-up of surface charge was found to be unnecessary probably owing to counterion binding. Kinetic data of the partitioning process for the different SLBs were obtained and qualitatively interpreted. For POPC at low dSDS concentrations dSDS translocation or flip-flop from the distal to proximal bilayer leaflets did not occur. At higher concentrations a period of rapid uptake lasting for approximately 100 s was followed by a slower increase lasting on the order of 10 minutes thus indicating that translocation was occurring. Upon subsequent rinsing, there was an initial rapid decrease in dSDS followed by a slower protracted decrease indicating that reverse flip-flop was occurring. The most intriguing result was that of the overall lipid signal upon rinsing, often it was observed to recover to levels equal to those prior to dSDS addition. These data suggest the formation of blebs or tubules as a result of dSDS induced spontaneous curvature; kinetic data from the CH region provided further evidence. Comparable data was obtained for POPE and egg-SM which showed very similar dSDS partitioning and rinsing kinetics, although the equilibrium behaviour differed in the strength of the dSDS lipid interaction. Less dSDS partitioned into the 1:1:1 mixture of POPE, egg-SM and cholesterol than any of the other species studied indicating its detergent resistance. Partial removal of this SLB from the interface left the contour of the CH region unchanged.

Acknowledgements

First and foremost I would like to thank Professor Colin Bain, my supervisor, for giving me the opportunity to work in his research group, for his enthusiasm, support, guidance, teaching and patience. I am also indebted to Eric Tyrode for putting me on the right track at the start of my endeavours and for his help and motivation.

Throughout my PhD many others have contributed to my studies. I would like to thank Richard Thompson and Adam Feiler for teaching me about AFM and how to image SLBs in fluid environments. I would also like to thank David Woods for introducing me to LaTeX and target factor analysis and Andy McKeague for coming to the ILL in Grenoble to help me with my neutron reflectometry experiments. I am grateful for the instrument scientists and technicians at the ILL for all their hard work in making my experiments there possible. Many thanks to Daniel Frenkel of Newcastle University for allowing me to conduct an additional experiment on his AFM. I owe much to the machinists and glassblowers in the Department of Chemistry for building and repairing the custom apparatus I used throughout my studies.

Away from the laboratory I would like thank the Bain group – past and present – and the friends I have known in Durham over the years for making my time here so enjoyable. I am grateful for Julie's support and affection. Lastly, I would like to thank my family for their ceaseless support and generosity without which I would not have completed this thesis.

Statement of Copyright

Glossary of Abbreviations

Chemical Species

5-DSA - 5-hydroxy stearic acid
β-DDM - β-D-dodecyl maltoside
APTES - 3-aminopropyltriethoxy-silane
C_{14}BET - *N*-tetradecyl-*N*, *N*-dimethylbetaine
Chol - cholesterol
CAPB - cocamidopropyl betaine
Cer - ceramide
CF - carboxyfluorescein
CHAPS - 3-[(3-Cholamidopropyl)dimethylammonio]-1-propanesulfonate
CTAB - cetyltrimethylammonium bromide
CTB_5 - cholera toxin subunit B_5
D291 - 4-(4-(didecylamino)styryl)-*N*-methylpyridinium iodide
DHPE - 1,2-dihexadecanoyl-*sn*-glycero-3-phosphoethanolamine
DMPC - 1,2-dimyristoyl-*sn*-glycero-3-phosphocholine
DMPG - 1,2-dimyristoyl-*sn*-glycero-3-phosphoglycerol
DMPTE - 1,2-dimyristoyl-*sn*-glycero-3-phosphothioethanol
DNA - deoxyribonucleic acid
DLPC - 1,2-dilauroyl-*sn*-glycero-3-phosphocholine
DOPC - 1,2-dioleoyl-*sn*-glycero-3-phosphocholine
DOTAB - dodecyltrimethylammonium bromide
DOTAP - 1,2-dioleoyl-3-trimethylammonium-propane
DPH - 1,6-diphenylhexatriene
DPPC - 1,2-dipalmitoyl-*sn*-glycero-3-phosphocholine
DPPG - 1,2-dipalmitoyl-*sn*-glycero-3-phosphoglycerol
DSPC - 1,2-distearoyl-*sn*-glycero-3-phosphocholine
DSPE - 1,2-dioctadecanoyl-*sn*-glycero-3-phosphoethanolamine
DTPC - 1,2-ditridecanoyl-*sn*-glycero-3-phosphocholine
EDTA - ethylenediaminetetraacetic acid
egg-SM - egg-sphingomyelin
GalCer - galactosylceramide
GM_1 - monsialganglioside
HEPES - 4-(2-hydroxyethyl)-1-piperazineethanesulfonic acid
NBD-cholesterol - 2,2-(*N*-(7-nitrobenz-2-oxa-1,3-diazol-4-yl)amino)-23,24-bisnor-5-cholen-3β-ol
$NP(EO)_{30}$ - nonylphenol ethoxylate
OG - octyl glucoside
PA - phosphatidic acid
PC - phosphocholine
PE - phosphoethanolamine
PG - phosphoglycerol
PIPES - piperazine-N,N'-bis(2-ethanesulfonic acid)
PL - phosphatidyllinosytol
POPC - 1-palmitoyl-2-oleoyl-*sn*-glycero-3-phosphocholine

POPE - 1-palmitoyl-2-oleoyl-*sn*-glycero-3-phosphoethanolamine
PS - phosphoserine
PTFE - polytetrafluoroethylene
SDS/dSDS - sodium dodecyl sulfate / deuterated sodium dodecyl sulfate
SPM - bovine brain sphingomyelin
TEMPO - (2,2,6,6-tetramethylpiperidin-1-yl)oxidanyl
TNS - 2-(p-toluidinyl)naphthalene-6-sodium sulphonate
TR - Texas Red
tris - tris(hydroxymethyl)aminomethane

Aggregates and Lipid Phases

CAC - critical aggregation concentration
CMC - critical micelle concentration
DRM - detergent resistant membrane
EUV - extruded unilamellar vesicle
GUV - giant unilamellar vesicle
$H_{\|}$ - hexagonal phase
L_{α} - fluid phase
L_{β} - gel phase
L_{o} - liquid ordered phase
LUV - large unilamellar vesicle
P_{β} - ripple phase
SAM - self-assembled monolayer
SLB - supported lipid bilayer
SUV - small unilamellar vesicle
SVL - supported vesicular layer

Techniques and Equipment

AFM - atomic force microscope
CCD - charge coupled device
CMOS - complementary metal-oxide semiconductor
DLS - dynamic light scattering
DSC - differential scanning calorimetry
ESR - electron spin resonance
FCS - fluorescence correlation spectroscopy
FRAP - fluorescence recovery after photo bleaching
FS - fluorescence spectroscopy
FTIR - Fourier transform infrared
ITC - isothermal titration calorimetry
LB - Langmuir-Blodgett
LS - Langmuir-Schaefer

MAC-AFM - magnetic alternating current AFM
MC - Monte Carlo
MD - molecular dynamics
MF - mean field
NMR - nuclear magnetic resonance
NR - neutron reflection
NTA - nanoparticle tracking analysis
PFG-NMR - pulsed field gradient NMR
QCM-D - quartz crystal microbalance with dissipation monitoring
SAXS - small angle X-ray scattering
SFA - surface forces apparatus
SFG - sum frequency generation
SP - streaming potential
SPR - surface plasmon resonance
TIR-Raman - total internal reflection Raman
ZP - zeta potential

Other

IR - infrared
NA - numerical aperture
PCA - principal component analysis
ppb - parts per billion
RG - renormalisation group
SC - stratum corneum
SNR - signal-to-noise ratio
TFA - target factor analysis
TOC - total organic carbon
UV - ultraviolet

Contents

Chapter 1

Introduction

1.1 Background, aims and motivation

Since the first models of the cell membrane were introduced lipid bilayers have been the subject of intense research activity. Their practical relevance extends from their use as boundary lubricants and electrooptical biosensors to the design of drug delivery vehicles and the formulation of personal care products. In the mid 1980's Tamm and McConnell were the first to produce surface supported lipid bilayers (SLBs) as model systems for membrane research;[1] prior to this scientists had utilised black lipid membranes (BLM)s and liposomal suspensions of various kinds. Tamm and McConnell's work has enabled researchers to apply a myriad of surface sensitive techniques to study SLBs and their interactions with peptides, proteins and many other species of practical importance.

Despite intense work and interest, confusion remains in many areas of bilayer research; in this thesis I will explore a number of these areas. The dynamics of SLB formation from lipid aggregate suspensions is still unclear for many lipid species and mixed systems. The interaction of cations with SLBs and their influence on SLB phase transitions also remains unclear. Previous research by Lee and Bain using TIR-Raman showed a broadening of the main phase transition of DMPC distinct from earlier work on SUVs. A survey of the literature hinted that this could be due to the presence of cations in the buffer solution used. Understanding the effects of cations on SLBs is of great importance in more complex biomimetic SLB systems particularly those pertinent to the theory of lipid rafts. Surfactant lipid interactions have been studied in bulk lipid systems but there has been as yet no systematic investigation into their interaction with SLBs; this is of pivotal importance in the design of biosensors and boundary lubricants.

1.2 Overview

My thesis is divided into five chapters and two appendices. In Chapter 1, my introduction, I discuss the physical thermodynamic principles underpinning lipid suspensions and supported lipid bilayers. I describe why bilayers form, and the physics used to model some of their dynamics; lateral and transmembrane diffusion. I also discuss the optics and scattering theory relevant to TIR-Raman spectroscopy. In Chapter 2, materials and methods, I describe my experimental

methodologies and data analysis procedures. Chapters 3–5 correspond to the major aims listed below; they begin with a comprehensive review of the relevant literature. These reviews are followed with my results and related discussion. I will end each of these chapters with summary conclusions and ideas for future work. Appendix A contains subtracted TIR-Raman spectra used in Chapter 4 but too bulky to include in the primary text. Appendix B contains much of the Matlab code used to analyse my data.

1.3 Aims

1. To establish TIR-Raman as a technique for probing the dynamics of SLB formation from lipid aggregates in suspension; focussing on little explored or unstudied lipid systems.
2. To investigate the role of cations in SLB main phase transitions; particularly their effects on transition cooperativity.
3. To investigate the equilibrium and dynamic behaviour associated with SLB surfactant interactions.

1.4 Interfaces and surfaces

By definition, the term interface means a boundary between any two immiscible or partially miscible phases. The term surface is reserved for a specific interface where one of the two phases is a gas. Energy is required to create an interface and the layers of molecules at an interface have higher energy than their counterparts in the bulk. This increase leads naturally to a surface tension at the interface as a force has to be applied to maintain the surface, which is the force acting per unit length of interface.

$$\gamma = \frac{F}{l} \tag{1.1}$$

this tension is equivalent to surface energy or the energy per unit area and has units of $J\ m^{-2}$.

1.5 Surfactants and adsorption

1.5.1 Surfactants

The word surfactant is a contraction of the phrase surface-active-agent. By this we mean a chemical compound that shows an affinity for interfaces and has a great influence on their properties. This affinity exists because of the structure and charge distribution within these molecules. Surfactants have a hydrophobic or lyophilic organic tail and a charged or polar hydrophilic headgroup. Surfactants can generally be grouped into four categories, the anionics with a negatively charged headgroup, the cationics with a positively charged headgroup, the non-ionics with no headgroup charge and the zwitterionics with both anionic and cationic regions. Some example surfactants and their uses are shown in figure 1.1.

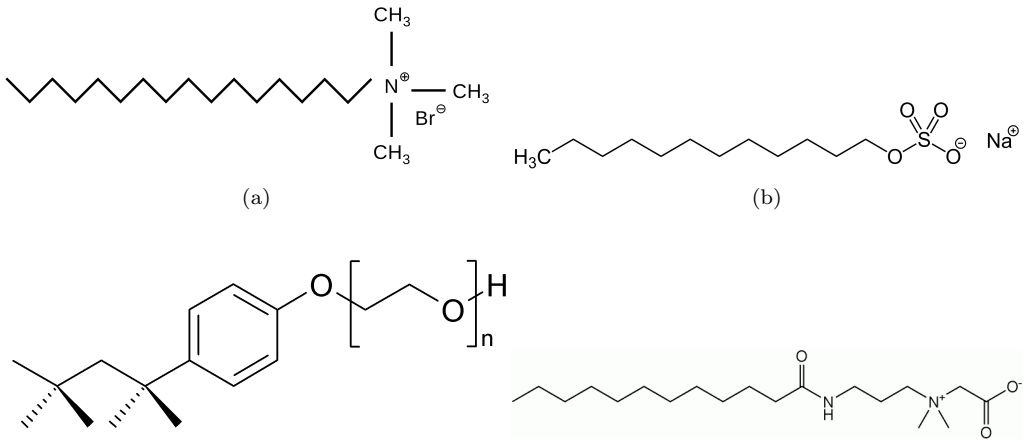

Figure 1.1: Structures of commonly used surfactants: (a) cetyl trimethylammonium bromide (CTAB) - used as (i) an antimicrobial in topical antiseptics, (ii) a surfactant hair conditioning products (iii), in DNA extraction buffers, (iv) synthesis of gold nanoparticles. (b) sodium dodecyl sulphate (SDS) - used in (i) personal care products, (ii) to aid in the lysing of cells, (iii) to aid in the unravelling of proteins for SDS-Page Gels, (iv) for dispersing nanotubes. (c) Triton X-100 - used for (i) the lysing of cells, (ii) the solubilisation of membrane proteins in their native state along with CHAPS, (iii) DNA extraction buffers. (d) cocamidopropyl betaine (CAPB) used as a surfactant in personal care products.

1.5.2 Lipids

Lipids are a special class of surfactants. It is useful to contrast and compare them with "common" surfactants to explain why their behaviour is different. Unlike typical surfactants, such as the fatty acids in soap or sodium dodecyl sulphate, lipids are relatively large and usually have more than one hydrocarbon tail. This structural difference results in a far reduced critical aggregation constant (CAC), on the order of 10^{-10} M, and different aggregate geometries – vesicles rather than micelles. The plasma membranes of cells are primarily comprised of lipids, which not only act as a support for proteins, but as a semi-permeable barrier, allowing the cell to maintain concentration gradients of the ions necessary for life and protecting the internal cell from the outside world. Many types of lipid exist, but those found predominantly in cell membranes are the glycerophospholipids and sphingolipids. Figure 1.2 shows a selection of lipid species, some used in this study and others commonly found in cell membranes.

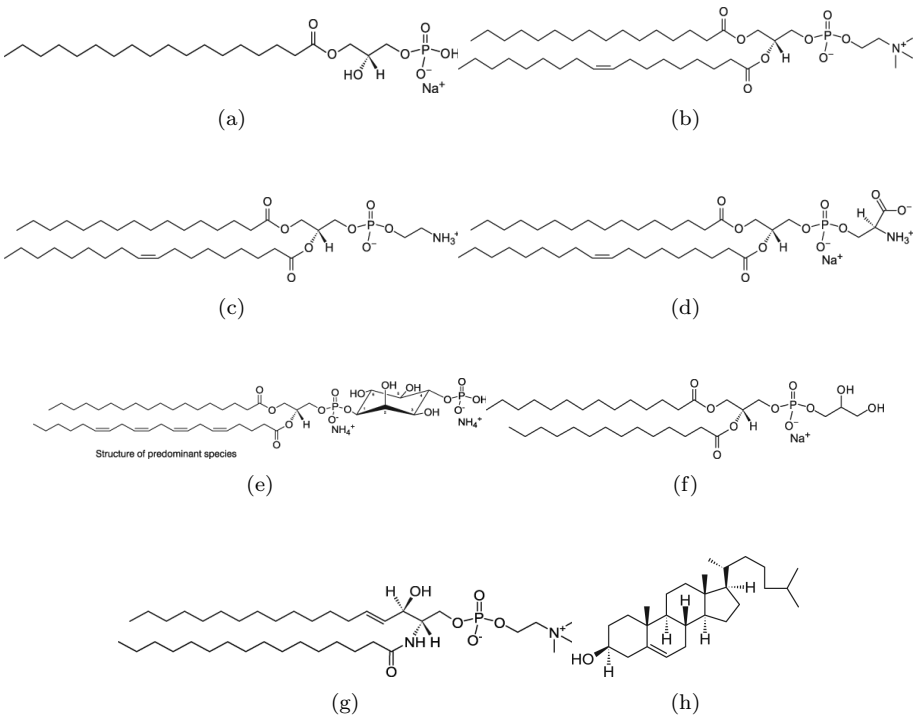

Figure 1.2: (a) phosphatidic acid, (b) POPC, (c) POPE, (d) POPS, (e) phosphatidyllinosytol, (f) DMPG, (g) sphingomyelin, (h) cholesterol.

Glycerophospholipids, as the name suggests, all have phosphate containing headgroups. They are all derived from glycerol-3-phosphate and can be considered modular; one can change the headgroup R-3 and the alkyl chains R-1 and R-2 giving rise to a myriad of compounds that reflects the complexity of natural membranes. The simplest glycerophospholipid, phosphatidic acid (PA), has a single tail and is found only sparingly in natural membranes. Five categories of glycerophospholipds, each with a different addition to the phosphate moiety, constitute the glycerophospholipids found in cell membranes. These are the phosphatidylcholines (PCs), phosphatidylethanolamines (PEs), phosphatidylserines (PSs), phosphatidyllinositols (PLs) and the phosphatidylglycerols (PGs).

The sphingolipids constitute the other major fraction of amphiphilic species found in cell membranes. In contrast to the glycerol backbone of the glycerophospholipids, sphingolipids contain a sphingosine core. Whereas in glycerophospholipids the hydrocarbon chains are attached to the glycerol backbone by ester linkages, the tail in the R-1 position is directly connected to the sphingosine core, and the tail in the R-2 position is connected via an amide bond. Sphingolmyelines all have PC headgroups.

The sphingolipids and glycerophospholipids along with sterols such as cholesterol are the primary building blocks of biological cell membranes.

1.5.3 Adsorption thermodynamics

At the water-air surface charged surfactants will orient their headgroups into the water, whilst their tails protrude into the air. The adsorption of surfactants reduces the surface tension and free energy. Driving adsorption are the hydrophilic and hydrophobic preferences of the headgroup and

tail respectively.

For surfactant adsorption at the solid-liquid interface the principles are similar; adsorption is a result of the more energetically favourable interactions between the surfactant and solid support or the hydrophobic effect. The interactions can either be chemical or physical in origin and the processes by which they occur are called chemisorption and physisorption respectively. The interactions that lead to chemisorption are varied and depend upon the chemical structure of the surfactant and support. In contrast the interactions that lead to physisorption are the van der Waals and hydrophobic forces. Below is a list of possible sources of the reduction in free energy (i.e. adsorption mechanisms):[2]

1. *Ion exchange* - This involves the replacement of pre-existing counterions at the interface from solution by similarly charged surfactant headgroups.

2. *Ion pairing* - This is the adsorption of surfactant ions from solution directly to oppositely charged sites on the solid substrate.

3. *Acid-base interaction* - This occurs when the surfactant adsorbs to the solid substrate by hydrogen bonding or a lewis acid/lewis base reaction.

4. *Adsorption by polarisation of π electrons* - This occurs when the adsorbate contains aromatic centres and the substrate has strongly positive sites.

5. *Adsorption by dispersion forces* - Occurs when van der Waals forces act between the surfactant and the substrate. The strength of these forces increases with increasing surfactant molecular weight; it can operate independently, but also operates along with all the other mechanisms listed.

6. *Hydrophobic adsorption* - This occurs when the combination of mutual attraction between hydrophobic groups of the surfactant molecules and their entropically driven tendency to escape from the aqueous environment becomes strong enough to allow them to adsorb on the substrate by aggregating their alkyl chains. Adsorption of additional surfactant molecules onto or into a preexisting surfactant film may also occur by this mechanism.

Following the arguments of Somasundaran *et al.*[3] we can relate the reduction in free energy associated with the transfer of surfactant to the interface to the concentration of surfactant at the interface by:

$$c_i = c_b \exp \frac{-\Delta G^\circ_{bi}}{RT} \tag{1.2}$$

where c_i and c_b are the concentration of the surfactant at the interface and in the bulk, ΔG°_{bi} is the standard Gibbs free energy of surfactant transfer from the bulk, R is the molar gas constant and T is the temperature. This expression when multiplied through by the average thickness of the adsorbed layer τ gives the surface excess Γ_i:

$$\Gamma_i = \tau \; c_b \exp \frac{-\Delta G^\circ_{bi}}{RT} \tag{1.3}$$

ΔG°_{bi} contains the contributions due to all participating interactions. For example, hydrophobic and van der Waals forces could both be acting on the surfactant species to promote adsorption in which case ΔG°_{bi} is actually a sum of the contributions from the different effects. This principle could also lead to the association of free energy changes with specific structural groupings on the surfactant and support.

Several isotherms have been posited over the last century to model adsorption. For the solid-liquid interface the most notable are those due to Langmuir and Frumkin. The Langmuir is the simpler of the two:[4]

$$\frac{\Gamma_i}{\Gamma_\infty} = \frac{\alpha c}{1 + \alpha c} \tag{1.4}$$

where Γ_i/Γ_∞ is the fractional coverage, c is the concentration of solute and α is the Langmuir constant. The second is a modification due to Frumkin that takes account of interactions between neighbouring adsorption sites on the solid support.[5]

$$\frac{\Gamma_i}{\Gamma_\infty} = \frac{\alpha\ e^{\omega\Gamma_i/\Gamma_\infty} c}{1 + \alpha e^{\omega\Gamma/\Gamma_\infty} c} \tag{1.5}$$

1.6 Surface charge and the electrical double layer

It is clear when we look at the mechanisms of adsorption given above, that surface charge plays a large role within them. It is therefore important to describe how charged surfaces associated with the solution-solid interface behave when immersed and what effect they have on the adjoining solution. Firstly I will describe why ions dissociate in water and less so in air and non polar organic solvents. I will then derive expressions for the electrical double layer.

Coulomb's law describes the attractive force between two point charges of opposite charge.

$$F = -\frac{q_1 q_2}{4\pi\epsilon\epsilon_0 r^2} \tag{1.6}$$

where q_1 and q_2 are the charges in coulombs, ϵ is the dielectric constant of the medium they occupy and is given by the ratio of the static permitivities of the medium and the vacuum ϵ_0 lastly r is this distance between the charges. Integrating this expression with respect to r allows us to calculate the energy or work required to separate two point charges that are a distance r apart in a known medium.

$$W = -\frac{q_1 q_2}{4\pi\epsilon\epsilon_0} \int_r^\infty \frac{1}{r^2} dr \tag{1.7}$$

$$W = \frac{q_1 q_2}{4\pi\epsilon\epsilon_0 r} \tag{1.8}$$

As an example we can calculate the energy required to separate two point charges of positive and negative elementary charge to infinity when they are initially separated by 2 Å. The work required is approximately 1.4×10^{-20} J in water and 1.15×10^{-18} J in air at 20°C comparing half of these values (N.B. the work required per ion) to kT (8.08×10^{-21} J) we see that in air the value is approximately 71 kT and in water is 0.86 kT. Despite the value obtained in water being positive, the gain in entropy associated with dissociation is enough to drive dissociation in this solvent.

Although these values indicate why ions dissociate in high dielectric constant media like water, the real situation is complicated. Near a charged flat interface the electric field is independent of distance from that interface, therefore infinite energy would be required to fully separate the charge ions from the interface. As a result upon dissociation there is a larger quantity of ions in the proximity of the surface and a resulting repulsive contribution to the overall interaction energy; although the attraction to the surface is still stronger. The electric field generated at the surface by the dissociation keeps ions from leaving completely and these ions along with any others in

solution from a bulk electrolyte will form the so called 'diffuse electrical double layer'. To derive equations which describe the concentration or counterions with distance from the interface we must start with the differential form of Gauss's Law, which is one of Maxwell's equations. [6]

$$\nabla \bullet \vec{E}(\vec{r}) = \frac{\rho(\vec{r})}{\epsilon_0 \epsilon} \tag{1.9}$$

where $\vec{E}(\vec{r})$ is the local electric field at position vector r and $\rho(\vec{r})$ is the net local charge density. Equation 1.9 tells us that the flux at a point described by the position vector $\vec{r}$ is directly proportional to the charge density at that point. It is often more useful to use the electrostatic potential $\psi(r)$, which is a scalar and is the free energy gained by moving a charge q from infinity to the position r. The electrostatic potential energy of a charge $Z_i q$ is therefore given by $Z_i q \psi(\vec{r})$ where q is the charge and Z_i is the valency. As $\psi(\vec{r})$ is the electrostatic free energy, the derivative of this function must give us the force acting per unit charge which is the electric field above.

$$\vec{E}(\vec{r}) = -\nabla \psi(\vec{r}) \tag{1.10}$$

For the simple case of a flat surface we can reduce the Maxwell equation to one dimension and replace the vector r with the independent variable x that describes the distance from the interface.

$$\frac{\mathrm{d}^2 \psi(x)}{\mathrm{d}x^2} = -\frac{\rho(x)}{\epsilon_0 \epsilon} \tag{1.11}$$

To solve this equation we find the relationship between $\psi(x)$ and $\rho(x)$. If we consider that the interfacial concentration of a given ion depends on its electrostatic potential energy, and that at this equilibrium the electrochemical potential must be the same for the ion in the bulk as in proximity to the interface we have

$$\mu_i^b = \mu_i^x = \mu_i^0 + kT \ln C_i(b) = \mu_i^0 + Z_i q \psi(x) + kT \ln C_i(x) \tag{1.12}$$

where $C_i(b)$ and $C_i(x)$ are the concentrations of ions in the bulk and at a distance x from the interface respectively. We also assume that this is a dilute solution and therefore the term for the electrochemical potential in the bulk is equal to zero. This expression can be rewritten as the well-known Boltzmann distribution

$$C_i(x) = C_i(b) \exp\left[-\frac{Z_i q \psi(x)}{kT}\right] \tag{1.13}$$

which is useful as it allows one to calculate the concentration of any ion at a distance x from the interface. We can use this result to find the net charge density at a distance x from the interface, as

$$\rho(x) = \sum_i Z_i q C_i(x) \tag{1.14}$$

$$= \sum_i Z_i q C_i(b) \exp\left[-\frac{q\psi(x) Z_i}{kT}\right] \tag{1.15}$$

substituting this expression into (1.11) yields the Poisson Boltzmann equation.

$$\frac{\mathrm{d}^2 \psi(x)}{\mathrm{d}x^2} = -\frac{q}{\epsilon_0 \epsilon} \sum_i Z_i C_i(b) \exp\left[-\frac{q\psi(x) Z_i}{kT}\right] \tag{1.16}$$

This equation is used to solve all electrical double layer problems for flat interfaces. We can now investigate the electrical double layer for specific solutions. For example if we choose the symmetrical electrolyte NaCl we have from equation (1.15)

$$\rho(x) = ZqC(b)\left\{\exp\left[-\frac{Zq\psi(x)}{kt}\right] - \exp\left[\frac{Zq\psi(x)}{kT}\right]\right\} \tag{1.17}$$

$$= -2ZqC(B)\sinh\left[\frac{Zq\psi(x)}{kT}\right] \tag{1.18}$$

combining this with the Poisson Boltzmann equation (1.16) gives

$$\frac{\mathrm{d}^2\psi(x)}{\mathrm{d}x^2} = \frac{2Z^2q^2C(b)}{\epsilon_0\epsilon kT}\sinh\left[\frac{Zq\psi(x)}{kT}\right]. \tag{1.19}$$

This differential equation can be scaled by a parameter

$$\kappa^{-1} = \left[\frac{\epsilon_0\epsilon kT}{q^2\sum_i C_i(b)Z_i^2}\right]^{\frac{1}{2}}, \tag{1.20}$$

such that by dimensional analysis

$$X = \kappa^{-1}x \tag{1.21}$$

where κ^{-1} is known as the *Debye length* and takes into account the dielectric properties of the solution, the concentration of electrolyte ions and their valency. The *Debye length* has units of length and corresponds to the characteristic decay length (meters) of the diffuse double layer at the interface. This scaling procedure allows us to simplify the 2nd order differential equation above to

$$\frac{\mathrm{d}^2\psi(x)}{\mathrm{d}X^2} = \sinh\left[\frac{Zq\psi(X)}{kT}\right]. \tag{1.22}$$

Integration of this expression gives the potential distribution next to a charged interface immersed by a symmetrical electrolyte, [7]

$$\frac{Zq\psi(X)}{kT} = 2\ln\left[\frac{1+\gamma\exp(-X)}{1-\gamma\exp(-X)}\right] \tag{1.23}$$

where

$$\gamma = \left[\frac{\exp\left(Y_0/2\right)-1}{\exp(Y_0/2)+1}\right] \tag{1.24}$$

Y_0 is the scaled electrostatic potential at the surface of the charged plane and is given by

$$Y = Zq\psi(X)/kT \tag{1.25}$$

at X=0.

1.7 Self-assembly and the thermodynamics of aggregation

1.7.1 Aggregates

A property shared by most surfactants is the formation of aggregates above a certain concentration in solution. The most common example is the micelle, but many other structures exist, including rods, disks, vesicles and bilayer sheets. Aggregates form when the chemical potential

of the monomer in solution becomes equal to that of a monomer in an aggregate. When a given mole fraction of surfactant monomer is reached, aggregates begin to form and as one attempts to increase the concentration of monomers in solution one merely increases the number of aggregates. If we plot the chemical potential of a monomer against aggregate size we can find out what size aggregates are the most likely and stable. The driving force behind the self-assembly of aggregates is the *hydrophobic effect* and is outlined below.

1.7.2 The hydrophobic effect

When a surfactant or lipid molecule is placed into water, the strong hydrogen bonds between the water molecules are not destroyed but are forced to order around the surfactant or lipid molecule forming a clathrate type structure. This ordering creates an unfavourable situation where the configurational entropy associated with the water is relatively low. As a result of this, above a certain bulk concentration, aggregates begin to form, as they minimise the quantity of water ordering around monomers. Enthalpic contributions are relatively unimportant because, the ordering effects described do not break hydrogen bonds, they only modify them, dispersion (London) forces between lipid-lipid, water-water and water lipid are all very similar and therefore the van der Waals interaction plays only a very small role in the hydrophobic effect. In essence the hydrophobic effect's origin lies in entropy changes associated with water forming an ordered structure and this leads to aggregation; the structure of the resulting aggregates depends upon the interactions between the constituent molecules.

1.7.3 Fundamental equations of self-assembly

Formally, in a dispersion of lipid monomers and aggregates in water there exists an equilibrium between the monomers, L and the aggregates of size m:[8]

$$mL_1 \rightleftharpoons L_m \tag{1.26}$$

As mentioned earlier the driving force for this process is the hydrophobic effect. However, opposing this driving force is the positive entropy of monomers mixing with water molecules in the bulk solution and any repulsive interactions between the molecules comprising the aggregate; for example hydration repulsion or steric repulsion. In equilibrium thermodynamics the chemical potential of all identical molecules in aggregates of different size must be equal, therefore:

$$\mu_1^0 + kT \log X_1 = \mu_2^0 + \frac{1}{2}kT \log \frac{1}{2}X_2 = \mu_3^0 + \frac{1}{3}kT \log \frac{1}{3}X_3 = ... \tag{1.27}$$

or

$$\mu = \mu_N = \mu_N^0 + \frac{kT}{N} \log \left(\frac{X_n}{N} \right) = \text{constant}, \quad N = 1, 2, 3, ..., \tag{1.28}$$

where, μ_N is the mean chemical potential of a molecule in an aggregate of aggregation number N, μ_N^0 is the standard component of the chemical potential in aggregates of number N, and X_N is the mole fraction of molecules in aggregates of number N, k is Boltzmann's constant and T is the temperature. Equation 1.28 can be re-written as

$$X_N = N \left(X_1 e^{\frac{\mu_1^0 - \mu_N^0}{kT}} \right)^N. \tag{1.29}$$

These equations along with the conservation relation for total solute concentration C completely defines the surfactant or lipid system:

$$C = X_1 + X_2 + X_3 + ... = \sum_{N=1}^{\infty} X_N \tag{1.30}$$

1.7.4 Variation of aggregate energy with aggregation number and geometry

We must now consider how the value of μ_N^0 varies with N to understand why aggregates of size N will form.[8] Aggregates will only form if the free energy associated with their cohesion is different to that of aggregates of other size and monomers of size 1. i.e μ_N^0 must be different for aggregates of different size. If μ_N^0 were constant for all values of N most of the molecules would exist as monomers, this is easily understood if one considers the situation where μ_N^0 is constant, when this happens 1.29 becomes:

$$X_N = N X_1^N \tag{1.31}$$

and if X_1 is less than 1, then for all other values of N, X_N must be much smaller, and increasingly smaller with increasing N. For a proportion of aggregates of size N to form the value of μ_N^0 must be less than that for monomers μ_1^0. To understand why a distribution of aggregates forms from a given solution we must consider how the relationship between the free energy per aggregate changes with N. For three dimentional aggregates such as spherical micelles, the number of monomers per aggregate N is proportional to the volume $4/3\pi R^3$; in fact, generally, the dependence of μ_N^0 is governed by the geometry of the aggregates being formed. It can be shown that for simple aggregate structures, which include vesicles, sheets, rods and spheres, the interaction energy free energy of the molecules is

$$\mu_N^0 = \mu_\infty^0 + \frac{\alpha kT}{N^P} \tag{1.32}$$

where α is a constant characteristic of the intermolecular interactions within the aggregate, and P is a number that depends on the shape or dimensionality of the aggregates. If we substitute 1.32 into the aforementioned fundamental equations we find an important result, that a critical aggregation constant (CAC) exists and is finite and unique for amphiphilic molecules of a given type. For example:

$$X_N = N\left(X_1 e^{\alpha\left(1-\frac{1}{N^P}\right)}\right)^N \approx N\left(X_1 e^{\alpha}\right)^N \tag{1.33}$$

For $X_1 \ll 1$, we have $X_1 > X_2 > X_3 > ...X_N$ for every value of α. However, since X_1 cannot exceed 1 there is a maximum value for $X_1 \approx e^{-\alpha}$ for all values of P. This is the CAC, and adding monomers to solution above this value only results in the creation of more aggregates.

1.7.5 Size distributions of aggregates

Micelles, vesicles and other self-assembled aggregates in solution usually show a size distribution about some mean value, sometimes narrow and sometimes polydisperse. Setting P to 1 in 1.33 we have:

$$X_N = N[X_1 e^{\alpha}]^N e^{-\alpha} \tag{1.34}$$

above the CMC where $X_1 e^{\alpha} \leq 1$, X_N must be proportional to N for small N, so the concentration of the aggregates in solution grows in accordance with their size. Only when N becomes very large

does the $[X_1 e^{\alpha}]^N$ take over, with the result that the fraction of aggregates of size N tends to zero in the limit of infinite aggregation number. Where P is less than one, as occurs for disks or spheres (see above) then a hypothetical infinitely sized aggregate is created above the CMC, in other words the aggregate can be thought of as existing in an entirely separate phase to the monomers still in solution. In this situation the idea of a size distribution no longer applies. Where P is greater than 1 no finite or infinite aggregates form at any concentration so the idea of a size distribution no longer applies here too. The case where $P = 1$ is a special case.

The values of α and P are constant only for simple surfactants and they vary when the surfactant molecule becomes large, flexible or has a complicated charge distribution/polarity. In these situations such surface active species form aggregates of more complex structure, for example lipids forming elastic vesicles (N.B.flexibility). When this occurs μ_N^0 usually reaches a minimum at a certain value of N or reaches a low value that remains almost constant for ever larger N, the first situation results in a Gaussian distribution of aggregate sizes about a mean value, such that:

$$X_N = N \left[\frac{X_M}{M} e^{\left(-M\Lambda(\Delta N)^2/kT\right)} \right]^{N/M} \tag{1.35}$$

in which the variation of μ_N^0 about μ_M^0 can expressed in parabolic form

$$\mu_N^0 - \mu_M^0 = \Lambda(\Delta N)^2 \tag{1.36}$$

1.7.6 Inter-aggregate interactions

At higher concentrations inter aggregate interactions become significant in determining the structure of the aggregate distribution. Where the surfactant concentration becomes significant, the structure of the aggregates may change to minimise their free energy. Also, if the interaggregate forces are net attractive, larger aggregates may separate out from and possibly coexist with the smaller aggregates and monomers in the solution.[8] This kind of transition can occur in solutions of zwitterionic species with limited repulsion or in solutions where there is a high electrolyte concentration or the presence of divalent cations such as Ca^{2+}. If M is the vesicle aggregation number and $\mathbf{M}$ is the superaggregate aggregation number where $\mathbf{M} \gg M$, on the basis of 1.27 we can write:

$$\mu_1^0 + kT \log X_1 = \mu_M^0 + \left(\frac{kT}{M}\right) \log \left(\frac{X_M}{M}\right) = \mu_{\mathbf{M}}^0 + \left(\frac{kT}{\mathbf{M}}\right) \log \left(\frac{X_M}{\mathbf{M}}\right) \tag{1.37}$$

or,

$$\left(\frac{X_{\mathbf{M}}}{\mathbf{M}}\right) = \left(\left(\frac{X_M}{M}\right) e^{M \frac{\left(\mu_M^0 - \mu_{\mathbf{M}}^0\right)}{kT}} \right)^{\frac{\mathbf{M}}{M}} \tag{1.38}$$

we can therefore write in analogy to the CAC arguments above a second critical concentration at which the super aggregates begin to form, where:

$$(X_M)_{crit} \approx M e^{-M \frac{\left(\mu_M^0 - \mu_{\mathbf{M}}^0\right)}{kT}} \tag{1.39}$$

the free energy difference $(\mu_M^0 - \mu_{\mathbf{M}}^0)$ will depend upon the inter-aggregate and intra-aggregate interactions. The critical value for super aggregate formation will depend on M and the free energy difference. It is possible for super-aggregates to form both at the CMC and above it, whilst the basic concentration of first order aggregates, such as vesicles, and of monomers remain unchanged. In

this way we can have multiple CACs of which the traditional CMC or critical micellar concentration is just one example. This process can lead to multiple peaks in the size distribution of aggregates.

1.7.7 Factors affecting aggregate structure

1.7.7.1 Intermolecular forces

As described earlier, the driving force behind aggregation is the hydrophobic effect, this positive attractive interaction can be represented by the typical value of the water/hydrocarbon interfacial energy of $\gamma \approx 50$ mJ m^{-2}.[8] However, various repulsive interactions operating within the polar headgroup region work against this, typically lowering the net surface energy to $\gamma \approx 20$ mJ m^{-2}. The forces contributing to this repulsion are the electrostatic repulsion, steric repulsion and hydration repulsion. Despite the complexity of deriving explicit expressions for the individual repulsive contributions, it is possible to formulate a simple expression for the interfacial free energy per molecule. The first term in the expression should be for the attractive hydrophobic contribution and that the second term for the combined repulsion. We assume that the repulsive contribution should be inversely proportional to the area per headgroup.

$$\mu_N^0 = \gamma a + \frac{K}{a} \tag{1.40}$$

where K is a constant. By finding the minimum of $d\mu_N^0/da = 0$ we can find the optimal surface area per headgroup.

$$\mu_N^0 = 2\gamma a_0 \tag{1.41}$$

where

$$a_0 = \sqrt{K/\gamma} \tag{1.42}$$

we can now write an expression for μ_N^0 in terms of measurable or known values

$$\mu_N^0 = 2\gamma a_0 + \frac{\gamma}{a}(a - a_0)^2 \tag{1.43}$$

which is the minimum interfacial free energy per molecule i.e. for a purely hydrophobic interaction plus the adjusted hydrophobic energy and the associated repulsion energy of the now non-minimal interaction. The combined interaction resulting from the opposing hydrophobic and aforementioned repulsive forces leads to the concept that there is a optimal equilibrium headgroup area per molecule. As a result of this it is possible to consider the structure of aggregates only in terms of their geometry, of which the optimal headgroup as seen above is the basis.

1.7.7.2 Geometry

The geometry of an amphiphile forming part of an aggregate can be defined by three parameters, the optimal headgroup area a_0, the volume of the chains V and their effective chain length l_c. The effective chain length is less than the maximum possible chain length l_{max} assumed by the equivalent crystalline saturated hydrocarbon. They are related by:

$$l_c \leq l_{max} \approx (0.154 + 0.1265n) \text{ nm} \tag{1.44}$$

where n is the number of carbon atoms in the chain. Another semi-empirical relation gives the volume for the same chains:

$$v \approx (27.4 \ + \ 26.9n) \ \times \ 10^{-3} \ \mathrm{nm}^3 \tag{1.45}$$

Once we have all three parameters we can calculate a dimensionless critical packing parameter:

$$Z_p = \frac{v}{a_0 l_c} \tag{1.46}$$

The value of Z_p determines the aggregate structures that can form from the amphiphile in question; for example, amphiphiles that have a packing parameter of 1/3 form spherical micellar structures and those with a value of 1 form bilayer sheets. It must be noted that these are limiting cases, it is possible for the chain length to vary below l_c thereby adjusting the value of the parameter. Ultimately for bilayers to form the constituent amphiphile(s) must have sufficiently small headgroups and adequately bulky hydrocarbon tails to lead to a Z_p of 1.

1.8 Dynamic properties of lipid bilayers

Bilayers are dynamic, their molecules jostle amongst each other, bob up and down, diffuse laterally and flip from one leaflet and flop to the other. Bilayer dynamics are thus important in understanding the physical behaviour of lipid bilayers and their interactions. The most relevant properties for my work are the lateral diffusion and flip-flop behaviours as they are key to understanding the behaviour of SLBs when interacting with soluble surfactants.

1.8.1 Lateral diffusion

1.8.1.1 Diffusion of large components

The lateral diffusion of biological macromolecules such as proteins and complexes in supported lipid bilayers is treated differently to that of individual small molecules such as lipids and surfactant monomers; it is dominated by the frictional force between the macromolecule and the media adjacent to the SLB. As my research has not included integral membrane proteins not much will be described here. The theories generally take a two dimensional continuum approach, where the discrete, molecular nature of the bilayer is not considered; this is deemed acceptable as the cross-sectional area of the integral proteins are significantly larger that that of the individual lipid monomers. The lipid bilayer is treated as a very thin viscous sheet held between two media of different viscocities. In the case of SLBs, the support and solution sub-phase. The diffusing macromolecule is treated as a moving cylinder of height h and radius R, the diffusion relation is then given by the Einstein relation $D = kT/f$ the key point is the determination of f, the frictional coefficient whose form varies depending on the nature of the adjoining media.

Saffman and Delbruck derived an expression of f for the relatively simple case of a cylinder (protein) embedded in a two dimensional sheet adjoined by two identical solution phases comprised of water or dilute electrolyte where $\eta_1 = \eta_2$:[9,10]

$$f = 4\pi\eta h \left(\ln \frac{\eta h}{\eta_1 R} - \gamma \right)^{-1} \tag{1.47}$$

where η is the viscosity of the viscous sheet (bilayer) and Euler's constant $\gamma = 0.5772$. However the key expression for bilayers adjacent to a solid support is found in the work of Evans and Sackman.[11]

$$f = 4\pi\eta h \left(\frac{(\epsilon')^2}{4} + \frac{\epsilon' K_1(\epsilon')}{K_0(\epsilon')} \right)^{-1} \tag{1.48}$$

where K_0 and K_1 are Bessel functions of the second kind. The parameter $\epsilon' = R(b_s/\eta h)^{1/2}$, where b_s is the coefficient of friction between the membrane and support. If a thin layer of buffer or other sub-phase is present between the bilayer and solid support of thickness $\delta << \eta h/\eta_1$ then $b_s = \eta_1/\delta$. When $\delta \approx \eta h/2\eta_1$, then $\epsilon' = (R/h)[(\eta_1 + \eta 2)/\eta]$.

1.8.1.2 Diffusion of small molecular components

In contrast, the diffusion of small molecules, owing to their much smaller size, is governed by the probability of free volume/area being available for the molecule to move in; as well as the activation energy required for overcoming interactions with nearest neighbours. When considering the diffusion of small molecules such as lipids and surfactants in homogeneous fluid like lipid phases, for example the L_α or L_o phases, the diffusion coefficient can be derived from free-volume theory or free-area theory in two dimensional situations. Free volume theory was originally developed by Cohen and Turnbull,[12–15] and developed by Macedo and Litovitz for the two-dimensional case.[16] This was used by Thompson, Hallmann and Sackmann to explain lateral diffusion in lipid bilayer phases.[17–20]

In free volume theory, the diffusion of a particle with a similar size to its neighbours can only take place when a free volume greater than a certain critical size exists next to the particle. Free volumes of smaller size do not contribute to diffusion as they cannot be filled. The two dimensional diffusion coefficient is thus an integral over the distribution of free area above the critical size.

$$D = \int_{a^*}^{\infty} D(a)\rho(a)\ da \tag{1.49}$$

where $D(a)$ is the diffusion coefficient within a free area a, $\rho(a)$ is the probability of finding a free area of a given size and a^* is the critical free area. The probability density $\rho(a)$ is given by:

$$\rho(a) = \frac{\gamma}{a_f} \exp\left[\frac{-\gamma a}{a_f}\right] \tag{1.50}$$

here a_f is the average free area and $a_f = a_t - a^*$ where a_t is the average area per molecule in the system. N.B. because a_t is a function of the system temperature a_f must be also. γ is a geometric correction factor employed to account for the overlap of free volumes, it usually takes on a value between 0.5 and 1.0. As $D(a)$ is a constant we can write,

$$D = D(a^*) \exp\left[\frac{-\gamma a^*}{a_f}\right] \tag{1.51}$$

This limiting expression has been derived taking only geometric considerations into account and more sophisticated treatment expounded in[16] and[20] includes an energy probability density in 1.49. This results in the following expression:

$$D = D' \exp\left[-\frac{\gamma a^*}{a_f} - \frac{E_a}{kT}\right] \tag{1.52}$$

where D' is the unhindered diffusion coefficient and is identical to $D(a^*)$, and E_a is the energy of activation associated with diffusion, i.e. the energy required to overcome the interactions of the diffusing molecule with its neighbours.

Experimentally, techniques including fluorescence correlation spectroscopy (FCS) and pulsed field gradient nuclear magnetic resonance spectroscopy (PFG-NMR) have been used to measure D in different bilayer systems. Diffusion coefficients measured in POPC and DOPC GUV's by FCS were found to be in the range of 5-8 μm^2 s^{-1} at room temperature.[21,22] However, it has also been shown that values obtained for supported lipid systems are considerably lower than their free vesicular counterparts; Przybylo and coworkers having measured a value of 3.1 μm^2 s^{-1} for DOPC bilayers on mica.[23] In addition, cushioning the SLBs with polymer does little to mitigate this effect. At high temperatures the value of D increases substantially despite the bilayer remaining in the fluid phase. For instance Filippov and cowokers have obtained a value of ≈ 26 μm^2 s^{-1} for POPC at 60°C.[24] In general bilayers comprised of sphingomyelins display lower diffusion coefficient values at room temperature, < 0.5 μm^2 s^{-1}, this is expected as bilayers comprised of sphingomyelins are in the more ordered gel (L_β) or ripple (P_β) phase at this temperature. However, at higher temperatures above their T_m values they remain considerably slower than for their glycerophospholipid counterparts.

1.8.2 Transmembrane diffusion (molecular flip-flop)

Whereas lateral diffusion in lipid membranes is fairly well understood and a variety of physical theories exist to explain it, transmembrane diffusion, inversion or flip-flop is notable for the lack of a simple underlying theory. Part of this stems from the fact that several types of flip-flop have been postulated in real membranes, those catalysed by membrane proteins called flipases and flopases respectively and native un-catalysed translocation. Most biological cells show asymmetry in their membrane lipid composition, for instance the human erythrocyte membrane has an exterior leaflet or monolayer primarily composed of PC and sphingomyelin, whereas the inner leaflet is mostly comprised of PS and PE species.[25] Understanding how asymmetries such as this are controlled quantitatively and with physical insight is a key question for modern biophysics.

Molecular flipping in surface multilayers was first considered by Langmuir in barium stearate films.[26] But the first measurements on lipid bilayers were carried out by Kornberg and McConnell in 1971 by electron spin resonance.[27] In this work the authors used a paramagnetic spin-labelled phophatidylcholine to measure the decay of paramagnetic asymmetry in egg-PC vesicles. The asymmetry was created by using sodium ascorbate to remove the paramagnetism of the posterior leaflet prior to acquiring spectra. The authors were able to kinetically model the loss of asymmetry (they are the first to refer to transmembrane diffusion as flip-flop, previously it had been referred to as inversion) as a single-step process. By using measurements at multiple temperatures on the same day they were able to acquire flip-flop activation energies by an Arrhenius analysis. They measured half times ($t_{1/2}$) of between 0.7-3 hours and activation energies in the range of 65-116 kJ mol^{-1}. Since then many measurements have been carried out to measure the rates of flip-flop in multifarious lipid bilayer systems, a large number with fluorescence based techniques. It is not my intention to present a thorough review of these here, but I will describe and discuss some key issues in this area. A major problem is the frequent use of bulky labels to differentiate lipids in the outer and inner monolayers of both vesicles and SLBs; in particular those used in fluorescence based investigations. In these works the native flip-flop rate of the labelled species alone is being monitored and, owing the the relative bulkiness of these modified lipids, the rates obtained are

likely significantly longer than those of the real lipids of interest. Vibrational spectroscopies and or neutron scattering in all likelihood offer the best method of acquiring accurate data as they only require deuteration, a far less intrusive form of labelling. In this vein Conboy and coworkers have recently conducted a number of studies with sum frequency generation (SFG) on SLB systems.[28–32] In these studies it was found that the rate of flip-flop was dramatically increased as the main phase transition was approached, although this increase occurred at temperatures below the main phase transition temperature. Another important observation was noted when the surface pressure of deposition by the LS technique was varied. The translocation rate was significantly reduced at high surface pressures. Conboy and coworkers were able to compare different phosphatidycholines and found that reducing the chain length of the lipids increased the rate of flip-flop – they measured $t_{1/2}$ times as low a minute for DMPC at higher temperatures. They also state that above the main phase transition temperature flip-flop rates were too fast to measure. This observation could imply that native-uncatalysed flip-flop rates are fast in real membranes which exist in the fluid L_α phase. Noteworthy are their measurements on TEMPO-DPPC which showed rates an order of magnitude slower than those of DPPC at similar temperatures – these data clearly highlight the problem of using any technique that relies on a bulky labelling regime, indeed I am extremely wary of any data acquired with techniques that require significant changes to molecular structure – so much so that I have not included any but the pioneering study given above in this short review. More recently Conboy and coworkers have investigated flip-flop rates in a binary mixture of DSPC and DSPE, they state that the native flip-flop rate in the DSPE system was considerably slower than that of the DSPC system prepared under the same conditions and at the same temperature. Also, the lipids displayed a common rate of flip-flop when comprising a binary mixture, this rate varied non-uniformly with fractional composition, but was correlated with changes in molecular packing as a function of DSPE content. The authors go on to justify their observations in terms of headgroup hydrophobicity and headgroup hydration and lipid packing constraints.

1.9 SLB preparation methods

Generally the best supports for SLBs are hydrophilic and include mica, fused silica and TiO_2 amongst others. Several methods exist for the fabrication of supported lipid bilayers on solid substrates: (i) Langmuir-Blodgett/Schaefer deposition, (ii) lipid spin coating (iii) vesicle fusion and (iv) surfactant depletion. Each has its advantages and disadvantages. During my research I used the vesicle fusion method. Below is a description of each of the methods. Specific details for my procedures are found within my methods chapter.

1.9.1 Langmuir-Blodgett/Schaefer deposition

Langmuir-Blodgett or Langmuir-Schaefer (LB/LS) deposition involves the transfer of multiple lipid monolayers onto a solid support of interest using a Langmuir trough. In Langmuir-Blodgett deposition a surface monolayer of lipid is created at the air-water surface by carefully dropping lipid solutions prepared in chloroform or other volatile solvent onto the surface. As the solvent evaporates the monolayer forms with hydrophilic headgroups oriented into the water and the hydrophobic tails projecting up into the air. The lipid monolayer is then compressed with a motorised arm to a constant pressure (the surface pressure required for the SLB being prepared e.g. $\approx$25 mN m^{-1}) generally the pressure must correspond to a condensed phase of the lipid monolayer at the

temperature of the system. The substrate is initially immersed then raised slowly through the surface, as this happens the lipid molecules are transferred onto the support interface with the hydrophilic headgroups oriented toward the interface and the tails pointing outward. Throughout this procedure the trough is operated at as close to constant surface pressure as possible – as the lipid molecules are transferred from the surface the troughs arm continues to compress the surface. When the first layer is complete, a subsequent layer is applied by lowering the substrate through the surface. The result is a interface comprised of two layers with the last or axial monolayer leaflet oriented so the charged headgroups are pointing into the bulk solution. It is worth noting that it is possible for the first layer to be removed during the second immersion. Figure 1.3 shows the two steps of Langmuir-Schaefer deposition. In LS deposition the substrate is initially immersed in the trough prior to the application of the lipid to the air-water surface, the substrate is then pulled through the surface after the formation of the surface monolayer. The substrate is then rotated parallel to the liquid surface and pressed down towards it to transfer to the second lipid layer. Interestingly, the two-step LS procedure allows for the formation of asymmetric lipid layers that closely resemble biological membranes. Unfortunately neither the LB or the LS techniques allow the incorporation of membrane proteins; if that is the subject of study the method of vesicle fusion outlined below is more appropriate. It is also not possible to use LB/LS deposition for layers comprised of unsaturated lipids, as the technique requires the surface monolayer to be compressed to an ordered condensed layer which cannot be done for unsaturated lipids. SLBs prepared by LB or LS deposition can be unstable and the procedure requires a large investment in time and care, for this reason it cannot be scaled easily and would be of limited interest in any commercial setting.

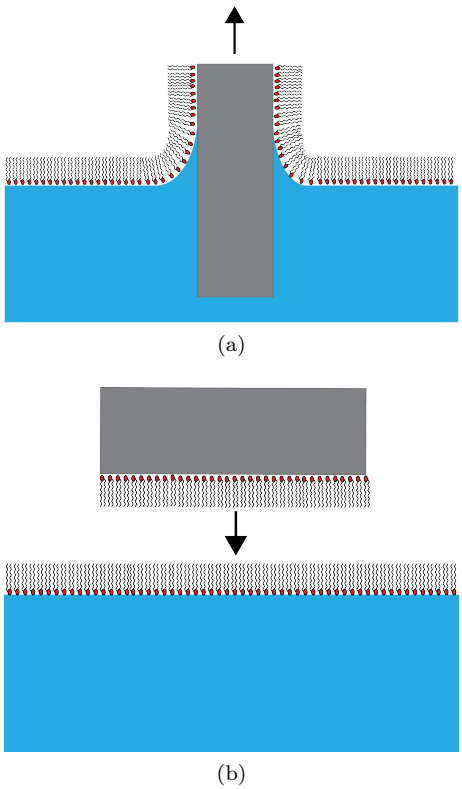

Figure 1.3: A Scheme of the two steps of Langmuir-Schaefer deposition of lipid bilayers on hydrophilic supports. (a) the upstroke and (b) the downstroke.

1.9.2 Lipid spin coating

Spin coating involves the dissolution of the lipid species of interest in a mixture of appropriate solvents (hexane (40%), 2-propanol (20%), acetone (20%) and decane(20%)), and the subsequent dropwise addition of these onto a spinning substrate (300 rpm).[33] Following the dropping procedure the sample substrate is spun at a fast rate, e.g. 3000 rpm for a short time (40 s), the resulting layers are fairly thin 10-20 nm, but nevertheless have an average thickness of greater than one bilayer (4-5 nm). For this reason this technique is not widely used. Its greatest value is the speed of deposition, a complete layer can be prepared in only a few minutes, without the technical difficulties associated with LB-LS deposition, or the lengthy initial preparation times for vesicle fusion (discussed below).

1.9.3 Vesicle fusion

In the technique of vesicle fusion, small unilamellar lipid vesicles are formed by either sonication or extrusion. These vesicles are then brought into contact with the support and, if possible, rupture to form an SLB. The mechanisms by which lipid suspensions form SLBs are not fully understood, nor have they been investigated for all lipid species, particularly the phosphotidylethanolamines and sphingomyelins. The investigation of SLB formation mechanisms forms part of my research (see Chapter 3).

In general vesicles form spontaneously for many lipid species, although for other species this is not the case; the factors which determine aggregate shape and flocculation and thus whether or not vesicle formation is possible were discussed earlier in this introduction. Where there are weak repulsive inter-aggregate interactions, lipid vesicles will flocculate in solution.

The first step in the formation of lipid vesicles by any of the known methods is the preparation of a thin film of the lipid species in some suitable container, generally a round-bottomed flask. The required mass(s) of the lipid species(s) are dissolved in appropriate solvents that are subsequently evaporated whilst rotating the flask. This procedure prepares a thin film of lipid around the flask's interior. The rate of this process is increased by holding the sample under vacuum or by applying a constant stream of dry nitrogen over the solvent surface. The film is then hydrated with the requisite buffer solution or water. In the case of extrusion the newly hydrated lipid suspension is iteratively passed through a polycarbonate membrane carefully sandwiched between two syringes (figures 1.4 and 1.5). During this process the whole system is heated to a temperature above the main phase transition temperature of the lipid/lipid mixture. The greater the number of passes through the filter the more mono-disperse the resulting vesicle suspension. In the case of sonication two procedures are widely used, either bath sonication or probe sonication. For bath sonication a powerful bath sonicator is filled with water warmed to a temperature above the main phase transition of the lipid species or mixture being employed. The hydrated lipid is then clamped into this sonicator and is sonicated constantly for 1.5 hours. In probe sonication an ultra-sonic probe is used after the hydrated sample is transferred to a suitable composite container. Probe sonication results in a more homogenous and smaller size distribution of vesicles, but the increased intensity can lead to intense localised heating within the sample solution; this may result in the break up of lipid molecules thereby reducing the purity of the sample. Also, the titanium probe tips used shed small fragments of titanium metal when in use, it is necessary to remove these by centrifugation after the sonication procedure. Bath sonication results in a more polydisperse size distribution of vesicles but with less chance of degradation. For lipid species that do not form

Figure 1.4: A photo showing the Avanti mini-extruder commonly used for preparing lipid vesicles. Copyright Avanti Polar Lipids Incorporated.

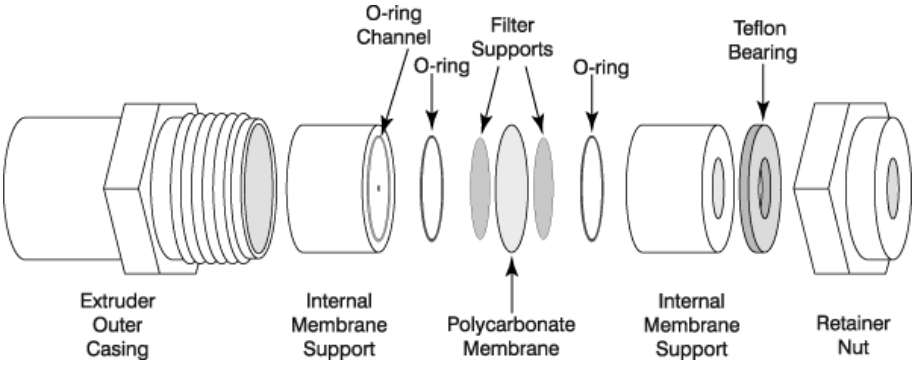

Figure 1.5: A schematic showing the internals of Avanti's Mini extruder. Copyright Avanti Polar Lipids Incorporated.

small unilamellar vesicles the centrifugation step required for removing the titanium particles will also remove the vesicle aggregates.

1.9.4 Surfactant depletion

Surfactant depletion was pioneered by Tiberg and coworkers[34] and investigated further by Lee *et al.*[35] In this relatively new technique, SLBs are constructed by preparing mixed micellar solution solutions of a non-ionic surfactant such as β-D-dodecyl maltoside (β-DDM) with the lipid of interest in a ratio of 9:1. Typically solutions are prepared over a concentration range of two orders of magnitude, at each stage the mixtures are brought into contact with the substrate and then subsequently rinsed with water or buffer solution. As the absolute concentration of the surfactant and lipid are reduced, a greater and greater proportion of the surfactant exists in monomeric form, it is far more soluble than the virtually insoluble lipid component, in fact to begin with more lipid is contained within the micelles than surfactant. At each stage of the process the lipid bilayer becomes more and more complete. As adsorption of non-ionic surfactants on silica is largely reversible, the final SLB is comprised of only the lipid species of interest. As well as phospholipids other system components typically found in membranes can be included, for example, cholesterol. The main advantage of this technique is that of lipid economy, an order of magnitude less lipid is required in comparison to other techniques, which would be extremely advantageous in any

commercial application. The procedure is also conducive to high throughput processing. However, the technique is less useful in fundamental physiochemical studies as the possibility of remnant surfactant or surfactant based impurity could adversely affect results; particularly for my work (Chapter 5) where I examine the interaction of SDS with SLBs.

1.10 Light and optics

1.10.1 Electrodynamic derivation of Snell's Law

Snell's Law was first discovered empirically by Willebrod Van Roijen Snell in 1621. One can derive Snell's Law in a variety of ways, for example from Huygen's principle or Fermat's principle, but the most useful for my purposes is the electromagnetic derivation. Following this approach light is considered as a monochromatic plane wave, a solution of the differential wave equation. From this we are able to derive Fresnel's equations, which are used to calculate the relative amplitudes of the incident, reflective and transmitted rays. These take on added importance when considering the case of total internal reflection and the magnitudes of the three electric field components at the interface. They are pivotal to understanding the relative scattered intensity generated by different polarisation configurations in a TIR-Raman setup. Considering an interface shown in figure 1.6,

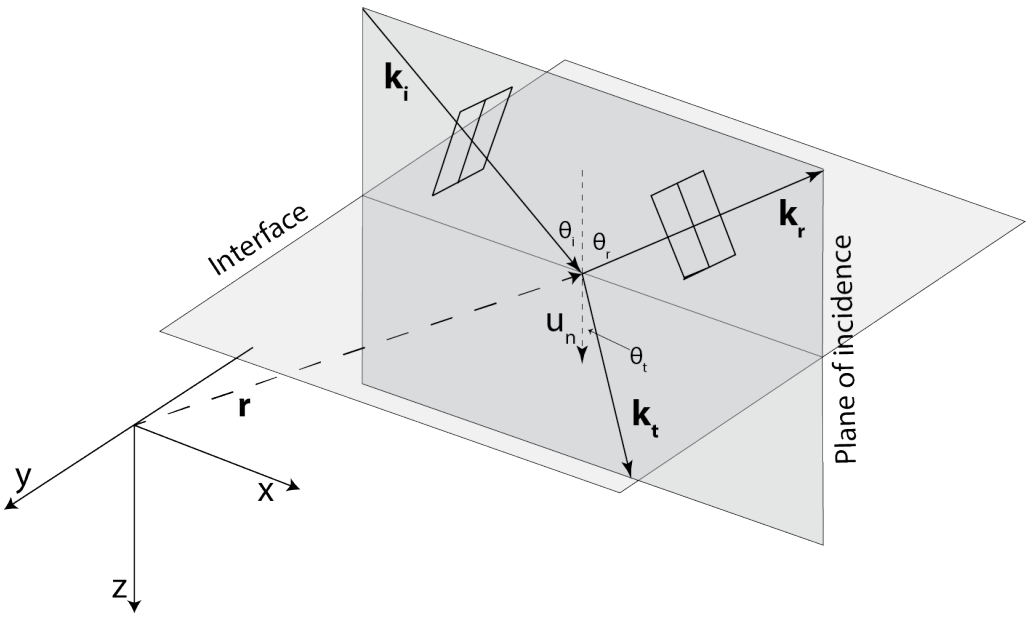

Figure 1.6: A schematic diagram showing a plane wave incident on an interface.

the incident light wave can be described by,[36]

$$\mathbf{E}_i = \mathbf{E}_{0,i} \exp[i(\mathbf{k}_i \cdot \mathbf{r} - \omega_i t + \epsilon_i)] \tag{1.53}$$

where $\mathbf{E}_{0,i}$ is the initial electric field vector which describes the initial field orientation and dictates the amplitude of the wave, $\mathbf{k}_r$ is the wave vector given by $2\pi/\lambda$ which states the direction of the incident light and turns the spatial dependence of the incident wave into a dimensionless parameter, $\mathbf{r}$ is the position vector which describes the location of a point in space, ω_i is the angular frequency

give by $2\pi/\tau$ where τ is the time period given by λ/v, v being the velocity. The reflected and transmitted waves are given by similar expressions with an added *phase*, ϵ, which is present owing to the fact that the position of the origin is not unique.

$$\mathbf{E}_r = \mathbf{E}_{0,r} \exp[i(\mathbf{k}_r \cdot \mathbf{r} - \omega_r t + \epsilon_r)] \tag{1.54}$$

and

$$\mathbf{E}_t = \mathbf{E}_{0,t} \exp[i(\mathbf{k}_t \cdot \mathbf{t} - \omega_t t + \epsilon_t)] \tag{1.55}$$

The laws of electromagnetism dictate several boundary conditions relevant to light at interfaces, the most important of which are the continuities of the tangential components of both the electric and magnetic fields across an interface. We can therefore state that

$$\hat{\mathbf{u}} \times \mathbf{E}_i + \hat{\mathbf{u}} \times \mathbf{E}_r = \hat{\mathbf{u}} \times \mathbf{E}_t \tag{1.56}$$

where $\hat{\mathbf{u}}$ is the unit vector normal to the interface, and therefore

$$\begin{aligned} \hat{\mathbf{u}} \times \mathbf{E}_{0,i} \exp i[\mathbf{k}_i \cdot \mathbf{r} - \omega_i t + \epsilon_i] \\ + \hat{\mathbf{u}} \times \mathbf{E}_{0,r} \exp i[\mathbf{k}_r \cdot \mathbf{r} - \omega_r t + \epsilon_r] \\ = \hat{\mathbf{u}} \times \mathbf{E}_{0,t} \exp i[\mathbf{k}_t \cdot \mathbf{r} + \omega_t t + \epsilon_t] \end{aligned} \tag{1.57}$$

as this relationship has to be true at any instant in time the electric fields $\mathbf{E}_i$, $\mathbf{E}_r$ and $\mathbf{E}_t$ must have the same dependence on t. Thus for the temporal variation to be identical

$$\omega_i = \omega_r = \omega_t \tag{1.58}$$

for the total variation to be constant the spatial variation must also be constant for all points on the interface, so

$$(\mathbf{k}_i \cdot \mathbf{r} + \epsilon_i) = (\mathbf{k}_r \cdot \mathbf{r} + \epsilon_r) = (\mathbf{k}_t \cdot \mathbf{r} + \epsilon_t) \tag{1.59}$$

rearranging and factorising yields two expressions giving the relative phases of the reflected and transmitted waves

$$[(\mathbf{k}_i - \mathbf{k}_r) \cdot \mathbf{r}] = \epsilon_r - \epsilon_i \tag{1.60}$$

and

$$[(\mathbf{k}_i - \mathbf{k}_t) \cdot \mathbf{r}] = \epsilon_t - \epsilon_i \tag{1.61}$$

These two equations define a plane perpendicular to both $\mathbf{k}_i - \mathbf{k}_r$ and $\mathbf{k}_i - \mathbf{k}_t$ which is the interface. Also since, the incident and reflected plane waves are in the same medium we can state that the magnitude of the incident and reflected wave vectors are the same $k_i = k_r$. As $\mathbf{k}_i - \mathbf{k}_r$ has no component tangential to the defined interfacial plane i.e. $\hat{\mathbf{u}} \times (\mathbf{k}_i - \mathbf{k}_r) = 0$ we see that:

$$k_i \sin\theta_i = k_r \sin\theta_r \tag{1.62}$$

and so

$$\theta_i = \theta_r \tag{1.63}$$

which is the law of reflection! The same can be written for $\mathbf{k}_i - \mathbf{k}_t$ which again has no component parallel to the interface and is normal to the interface:

$$k_i \sin\theta_i = k_t \sin\theta_t \tag{1.64}$$

However, the media are now different and $k_i \neq k_t$ and therefore $\theta_i \neq \theta_t$ but since $\omega_i = \omega_t$ we can multiply both sides of equation 1.64 by c/ω_i to obtain Snell's Law.

$$n_i \sin\theta_i = n_t \sin\theta_t \tag{1.65}$$

1.10.2 Derivation of Fresnel's equations

Through the derivation of Snell's Law from electromagnetic theory, I showed the relationship between the phases of the incident, reflected and transmitted waves. I will now derive expressions that relate the relative amplitudes of their respective electric fields with varying refractive index and incident angle. The resulting expressions are due to Augustin-Jean Fresnel (1788-1827). To this end we need to consider the same scheme as in the prior section – the plane wave incident on the interface between two isotropic media – to do this we must separate its **E** and **B** fields into components parallel and perpendicular to the plane of incidence and derive the equations separately for each of the two components. I will start with the components perpendicular to the plane of incidence.

1.10.2.1 Reflection and transmission coefficients when the electric field is perpendicular to the plane of incidence

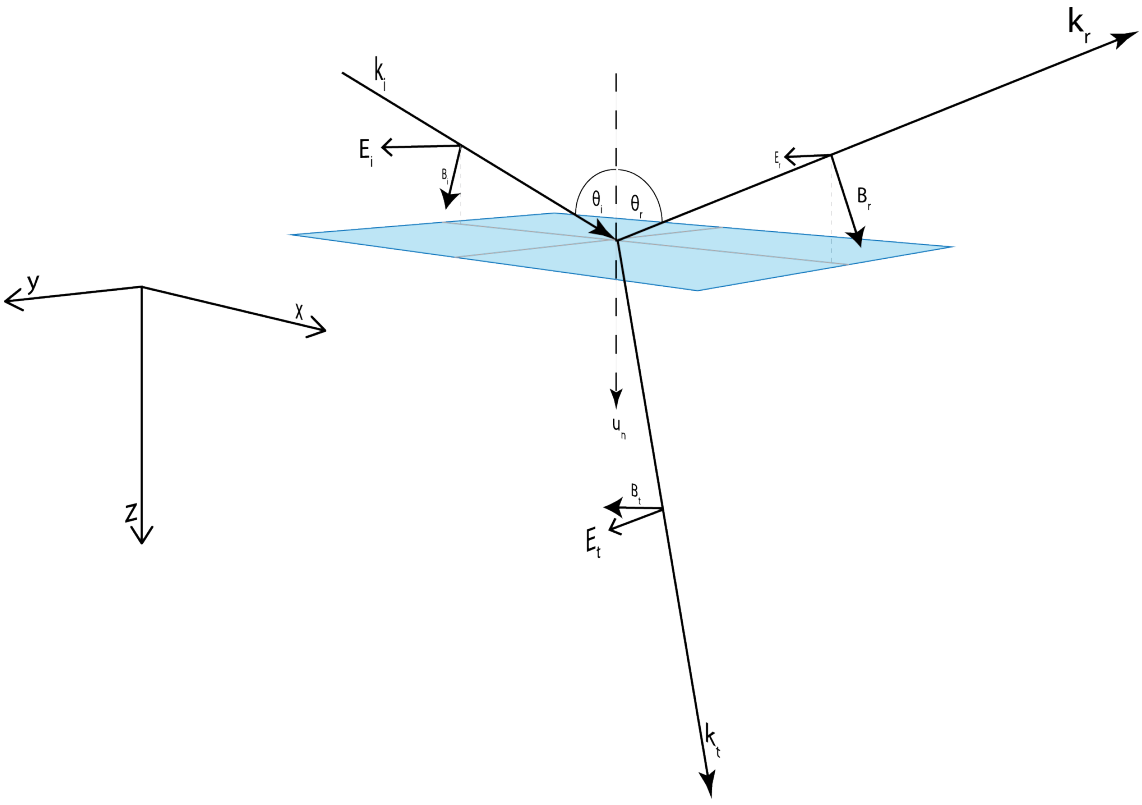

Figure 1.7: A diagram showing the relationship between the electric and magnetic field vectors for a plane wave incident on the interface between two media where the electric field is polarised perpendicular to the plane of incidence.

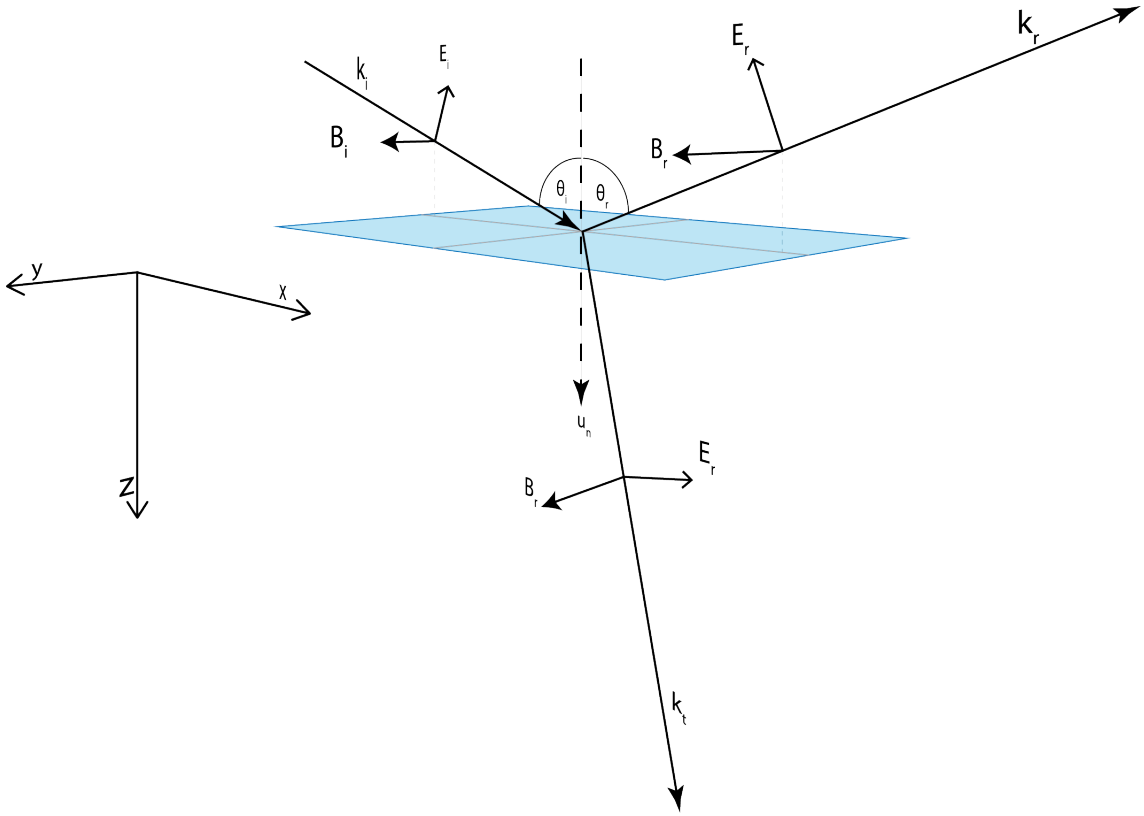

Figure 1.8: A diagram showing the relationship between the electric and magnetic field vectors for a plane wave incident on the interface between two media where the electric field is polarised parallel to the plane of incidence.

We assume that $\mathbf{E}$ is perpendicular to the plane of incidence and $\mathbf{B}$ is parallel to it. As $E = vB$, so

$$\hat{\mathbf{k}} \times \mathbf{E} = v\mathbf{B}, \tag{1.66}$$

where $\hat{\mathbf{k}}$ is the unit wave vector in the direction of propagation. As $\mathbf{k}$ is perpendicular to $\mathbf{E}$

$$\hat{\mathbf{k}} \cdot \mathbf{E} = 0 \tag{1.67}$$

i.e. the three vectors $\mathbf{E}$, $\mathbf{B}$ and $\hat{\mathbf{k}}$ form a right handed system, these are shown in figure 1.7. Recalling the boundary condition of tangential electric field continuity, we have

$$\mathbf{E}_{0,i} + \mathbf{E}_{0,r} = \mathbf{E}_{0,t} \tag{1.68}$$

Although, the tangential component of the electric field must be continuous across the interface between the two media, the normal component does not; the fields associated with the waves polarise the media, which in turn affect the properties of the wave. However, the normal component of $\epsilon\mathbf{E}$ is continuous. Whereas the tangential component of the electric field is continuous, the normal component of the associated magnetic field is continuous, similarly the tangential component of $\mu^{-1}\mathbf{B}$ (or $\mathbf{H}$ the induction) is continuous across the interface, where μ is the magnetic permeability. We can use this last boundary condition to construct an expression analogous to that for the electric

fields in the prior discourse on Snell's Law:

$$-\frac{\mathbf{B}_i}{\mu_i}\cos\theta_i + \frac{\mathbf{B}_r}{\mu_i}\cos\theta_r = -\frac{\mathbf{B}_t}{\mu_t}\cos\theta_t \tag{1.69}$$

n.b. the negative signs come about because of the orientation of the **E** field vectors. If I had chosen to arrange the system such that the electric fields pointed towards the page, the signs would flip as the magnetic field vectors would be aligned in the direction of their mirror images in the zy plane. Since from 1.66 we can write

$$B_i = E_i/v_i \tag{1.70}$$

$$B_r = E_r/v_r \tag{1.71}$$

$$B_t = E_t/v_t \tag{1.72}$$

As the incident and reflected waves are in the same media, $\nu_i = \nu_r$ and $\theta_i = \theta_r$, substituting the above three expressions into equation 1.69 we obtain

$$\frac{1}{\mu_i v_i}(E_i - E_r)\cos\theta_i = \frac{1}{\mu_t v_t}E_t\cos\theta_t \tag{1.73}$$

this can be simplified with our knowledge that for plane waves E_i,E_r and E_t are all constant in time

$$\frac{n_i}{\mu_i}(E_{0,i} - E_{0,r})\cos\theta_i = \frac{n_t}{\mu_t}E_{0,t}\cos\theta_t \tag{1.74}$$

combining this with equation 1.69 yields the Fresnel equations for the reflected and transmitted light respectively, where **E** is perpendicular to the incident plane

$$\left(\frac{E_{0,r}}{E_{0,i}}\right)_\perp = \frac{\frac{n_i}{\mu_i}\cos\theta_i - \frac{n_t}{\mu_t}\cos\theta_t}{\frac{n_i}{\mu_i}\cos\theta_i\frac{n_t}{\mu_t}\cos\theta_t} \tag{1.75}$$

$$\left(\frac{E_{0,t}}{E_{0,i}}\right)_\perp = \frac{2\frac{n_i}{\mu_i}\cos\theta_i}{\frac{n_i}{\mu_i}\cos\theta_i + \frac{n_t}{\mu_t}\cos\theta_i} \tag{1.76}$$

equations 1.75 and 1.76 can be simplified with the knowledge that we are using dielectrics and $\mu_i \approx \mu_r \approx \mu_0$, yielding the commonly seen amplitude reflection and transmission coefficients respectively

$$r_\perp = \left(\frac{E_{0,r}}{E_{0,i}}\right) = \frac{n_i\cos\theta_i - n_t\cos\theta_t}{n_i\cos\theta_i + n_t\cos\theta_t} \tag{1.77}$$

$$t_\perp = \left(\frac{E_{0,t}}{E_{0,i}}\right) = \frac{2n_i\cos\theta_i}{n_i\cos\theta_i + n_t\cos\theta_t} \tag{1.78}$$

1.10.2.2 Reflection and transmission coefficients when the electric field is parallel to the plane of incidence

Very similar equations can be derived for light polarised parallel to the plane of incidence. The boundary condition for the continuity of the electric field parallel to the interface gives

$$E_{0,i}\cos\theta_i - E_{0,r}\cos\theta_r = E_{0,t}\cos\theta_t \tag{1.79}$$

As before we can write an expression from the fact that the tangential component of $\mu^{-1}\mathbf{B}$ must be equal on either side of the interface

$$\frac{1}{\mu_i v_i} E_{0,i} + \frac{1}{\mu_r v_r} E_{0,r} = \frac{1}{\mu_t v_t} E_{0,t} \tag{1.80}$$

As $\mu_i = \mu_r$ and $\theta_i = \theta_r$ we can obtain two more Fresnel equations

$$\left(\frac{E_{0,r}}{E_{0,i}}\right)_{\parallel} = \frac{\frac{n_t}{\mu_t}\cos\theta_i - \frac{n_i}{\mu_i}\cos\theta_t}{\frac{n_i}{\mu_i}\cos\theta_t + \frac{n_t}{\mu_t}\cos\theta_i} \tag{1.81}$$

and

$$\left(\frac{E_{0,t}}{E_{0,i}}\right)_{\parallel} = \frac{2\frac{n_i}{\mu_i}\cos\theta_i}{\frac{n_i}{\mu_i}\cos\theta_t + \frac{n_t}{\mu_t}\cos\theta_i} \tag{1.82}$$

which both can be simplified as before for dielectrics

$$r_{\parallel} = \frac{n_t\cos\theta_i - n_i\cos\theta_t}{n_i\cos\theta_t + n_t\cos\theta_i} \tag{1.83}$$

and

$$t_{\parallel} = \frac{2n_i\cos\theta_i}{n_i\cos\theta_t + n_t\cos\theta_i} \tag{1.84}$$

1.10.3 Total internal reflection

Fresnel's equations tell us for light incident upon an interface where the incident medium has a greater refractive index i.e. $n_i > n_t$ the proportion of light and thus energy in the reflected beam steadily increases, whilst that in the transmitted beam decreases. At the same time, by Snell's Law, the angle of the transmitted beam gets closer and closer to 90° to the surface normal $\hat{\mathbf{u}}$ until a certain *critical angle* defined by

$$\theta_c = \sin^{-1} n_{ti} \tag{1.85}$$

where

$$n_{ti} = \left(\frac{n_t}{n_i}\right) \tag{1.86}$$

above this angle light is totally internally reflected. But despite this seeming restriction, owing the boundary conditions used above, the tangential components of the electric fields must remain equal either side of the interface. As such there is still a transmitted wave, which propagates along the surface in such a way that there is no net transfer of energy to the less optically dense medium.[37] If we treat the surface wave as a plane wave we can write the wave function

$$\mathbf{E}_t = \mathbf{E}_{0,t}\exp i[\mathbf{k}_r\cdot\mathbf{r} - \omega t] \tag{1.87}$$

separating the wave vector into its components (there is no y-component for P-polarised light)

$$\mathbf{k}_t\cdot\mathbf{r} = k_{tx}x + k_{tz}z \tag{1.88}$$

where $k_{tx} = k_t\sin\theta_t$ and $k_{tz} = k_t\cos\theta_t$. From Snell's Law we find that

$$k_t\cos\theta_t = \pm k_t\left(1 - \frac{\sin^2\theta_i}{n_{ti}^2}\right)^{1/2} \tag{1.89}$$

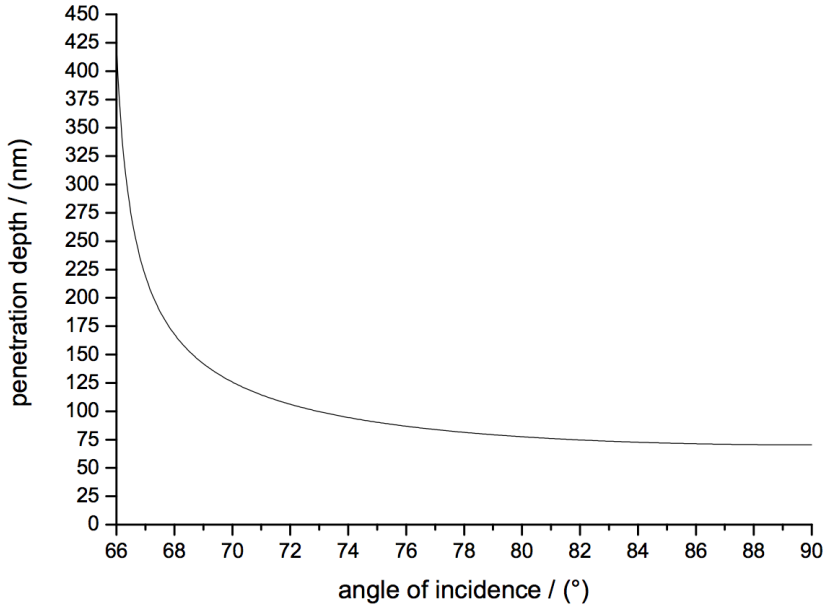

Figure 1.9: A Graph showing the change in characteristic decay length or penetration depth of the evanescent wave at the silica-water interface. $n_{i,silica} = 1.46$ and $n_{t,water} = 1.33$.

as we are concerned with the case when $\sin\theta_i > n_{ti}$ we see that,

$$k_{tz} = \pm ik_t \left(\frac{\sin^2\theta_i}{n_{ti}^2} - 1 \right)^{1/2} \equiv \pm i\beta \tag{1.90}$$

and

$$k_{tx} = \frac{k_t}{n_{ti}} \sin\theta_i \tag{1.91}$$

Hence, we can write the "transmitted" or surface wave as

$$\mathbf{E}_t = \mathbf{E}_{0,t} e^{\pm\beta z} e^{i(k_t x \sin\theta_i / n_{ti} - \omega t)} \tag{1.92}$$

which decays exponentially from the surface. In the first exponential factor only the negative sign is physically permissible as the positive sign would indicate an ever increasing field away from the interface. It is this wave that we use in TIR-Raman spectroscopy to stimulate Raman scattering. This exponentially decaying or evanescent wave has a characteristic decay length of β^{-1} which is the point where the electric field reaches $1/e$ of its initial magnitude. In Raman spectroscopy we are interested in the square of the electric field, so in terms of my experiments we consider the decay length or penetration depth to be $\beta^{-1}/2$; figure 1.9 shows a plot of the changing penetration depth with incident angle and figure 1.10 shows the normalised decaying electric field squared at 73°(the angle of incidence for all my TIR-Raman experiments) for the silica-water interface. It is possible to reformulate the Fresnel equations for the reflection coefficient above the critical angle for both perpendicular and parallel electric fields, given by

$$r_\perp = \frac{\cos\theta_i - (n_{ti}^2 - \sin^2\theta_i)^{1/2}}{\cos\theta_i + (n_{ti}^2 - \sin^2\theta_i)^{1/2}} \tag{1.93}$$

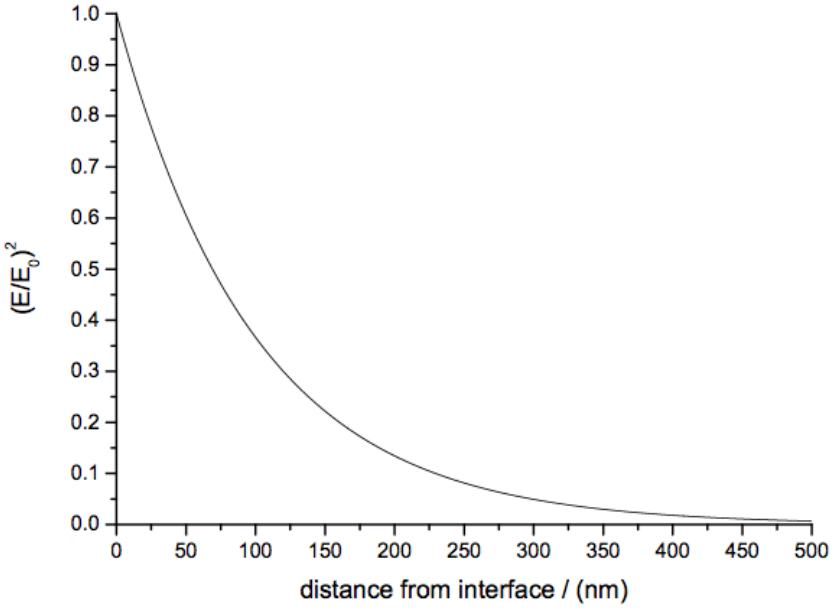

Figure 1.10: A graph showing the decay in z of the normalised evanescent electric field squared, for the silica-water interface. 73° incidence, $n_{i,silica} = 1.46$ and $n_{t,water} = 1.33$.

and

$$r_{\parallel} = \frac{n_{ti}^2 \cos\theta_i - (n_{ti}^2 - \sin^2\theta_i)^{1/2}}{n_{ti}^2 \cos\theta_i + (n_{ti}^2 - \sin^2\theta_i)^{1/2}} \tag{1.94}$$

It is useful for us to express the Fresnel transmission coefficients in a form which relates the three dimensional components of the electric field at the interface to the electric fields of the parallel or perpendicularly polarised incident plane wave, rather than in terms of the two transmission coefficients, parallel and perpendicular hitherto described. The reason for this is that when conducting spectroscopy, we would like to know which planes relative to the interface will generate the greatest signal for each of the two polarisation configurations of incident light and whether or not light of one of the two incident polarisation configurations is likely to stimulate emission from a certain vibrational mode we expect to be oriented in a particular fashion relative to the interface. Above the critical angle these expressions are,[38]

$$t_{\parallel,x} = \frac{2\cos\theta_i(\sin^2\theta_i - n_{ti}^2) + i[2n_{ti}^2\cos^2\theta_i(\sin^2\theta_i - n_{ti}^2)^{1/2}]}{n_{ti}^4\cos^2\theta_i + \sin^2\theta_i - n_{ti}^2} \tag{1.95}$$

$$t_{\perp,y} = \frac{2\cos^2\theta_i - i[2\cos\theta_i(\sin^2\theta_i - n_{ti}^2)^{1/2}]}{1 - n_{ti}^2} \tag{1.96}$$

$$t_{\perp,z} = \frac{2n_{ti}^2\cos^2\theta_i\sin\theta_i - i[2\cos\theta_i\sin\theta_i(\sin^2\theta_i - n_{ti}^2)^{1/2}]}{n_{ti}^4\cos^2\theta_i + \sin^2\theta_i - n_{ti}^2}. \tag{1.97}$$

and their absolute values are plotted in figure 1.11. All of my TIR-Raman measurements were carried out at 73°; this angle of incidence was chosen as a compromise between maximising the interfacial electric field and minimising the penetration depth of the field. It would have been preferable to work nearer the critical angle in order to minimise $t_{\parallel,x}$ as this simplifies spectral analysis. However, for work at the silica-water interface this is not feasible because the penetration

depth becomes infinite and any spectra will be swamped with water signal. In addition, the finite numerical aperture of the pump laser implies that half of the incident light will be transmitted as it will be below the critical angle.

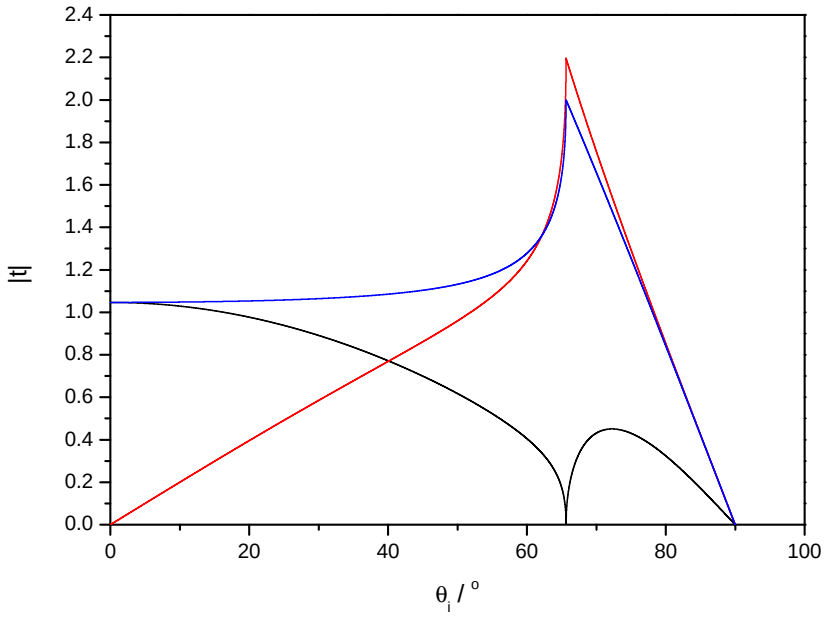

Figure 1.11: A graph showing the variation of the Fresnel transmission coefficients for the silica-water interface (n_{silica}=1.46, n_{water}=1.33) as a function of incident angle. $t_{\parallel,x}$ black line, $t_{\parallel,z}$ red line, $t_{\perp,z}$ blue line.

1.11 The Raman effect

1.11.1 Background

When a monochromatic source of light is incident on a transparent medium most of the light is transmitted but some is scattered.[39] Of this scattered light, the vast majority is of the same wavelength as the incident light source; we say this light has been scattered elastically and the effect is called Rayleigh scattering (Lord Rayleigh, John Strutt, explained this effect with classical wave theory in 1871). Alongside this elastically scattered light is a small component of inelastically scattered light that has a different wavelength to the incident source, sometimes higher sometimes lower, stokes and anti-stokes respectively. This light of shifted wavelength is the result of what is now called Raman scattering after the eponymous Chandrasekhara Venkata Raman who was the first to observe it experimentally in 1928. The Raman effect was first predicted theoretically by Smekal in 1923 and by 1934 Plazek had predicted almost all of the related phenomena now observed. In some German literature it is still known as the Smekal-Raman effect.

The Raman effect can be treated in different ways. It can be given a purely classical description, a mixed classical and quantum description or a purely quantum description. The method appropriate largely depends on the exact nature of the Raman experiments being carried out. For example, when conducting resonance enhanced Raman experiments, the purely quantum or mixed

description is needed as it is not possible to explain the transition from one electronic state to another in classical terms.[40] For this work, although the energy of the incident radiation is much greater than that of the largest vibrational transition, it does not necessitate a quantum mechanical description as only vibrational transitions are involved.

In a Raman setup, the sample is irradiated with an intense monochromatic light source, typically in the visible region of the electromagnetic spectrum. The photons emitted from this light source have inelastic collisions with sample molecules, where the vibrational energy of the molecules is changed by an amount ΔE_m. For energy to be conserved, the energy of the scattered photon, $h\nu_s$, must be different from the energy of the incident photon $h\nu_i$ by the same amount ΔE_m:

$$h\nu_i - h\nu_s = \Delta E_m \tag{1.98}$$

If a sample molecule gains energy, ΔE_m is positive and so ν_s must be smaller than ν_i; it is this increase in energy during the scattering which gives rise to the Stokes lines. If the molecule loses energy as a result of the scattering event, ΔE_m must be negative and so ν_s must be larger than ν_i; the results the anti-Stokes lines in a Raman spectrum. The Stokes/anti-Stokes nomenclature seems to have drifted into the Raman field from the Stoke's Law in fluorescence which states that the emitted light should always be of lower frequency than the exciting radiation.

As shown in figure 1.12, in absorption/emission processes such as those in IR-spectroscopy, the difference ΔE_m between the energies of the two vibrational states has to equal the energy of the incident photon for the transition to take place. For Raman scattering this is not the case; Raman scattering is not a normal absorption/emission process, an incident photon has an energy very much greater than $h\nu_m$, where ν_m is the fundamental vibrational frequency. When the photon interacts with a molecule in the ground vibrational state, the molecule is raised momentarily to some higher level of energy that does not correspond to a normal vibrational level of the molecule, we call this a virtual energy level – it is not an eigenfunction of the Hamiltonian in the absence of the external electromagnetic field. Scattering, unlike absorption/emission, cannot be distinguished into two processes even though it is often drawn like that in Jablonski energy level diagrams.

In Raman spectra, the anti-Stokes lines are much smaller than the Stokes, an experimental fact that can quite easily be explained by the Boltzmann distribution:

$$\frac{n_1}{n_0} = e^{h\nu_m/kT} \tag{1.99}$$

where n_0 and n_1 are the populations of the ground and higher levels respectively, h is Planck's constant, $h\nu_m$ is the energy of n_1, k is Boltzmann's constant and T is the temperature. There are exponentially fewer occupied ν_1 levels compared with ν_0 levels at 298 K.

1.11.2 Classical description

The Raman effect results from a change in a molecule's polarisability with respect to a particular vibrational mode's normal coordinate. This is the fundamental requirement for a vibrational mode to be Raman active.

If a molecule is placed in the electric field of intense electromagnetic radiation then the electrons and protons within the molecule experience a force that acts upon them in different directions. Because of this force the electrons are displaced relative to the protons within the molecule; we

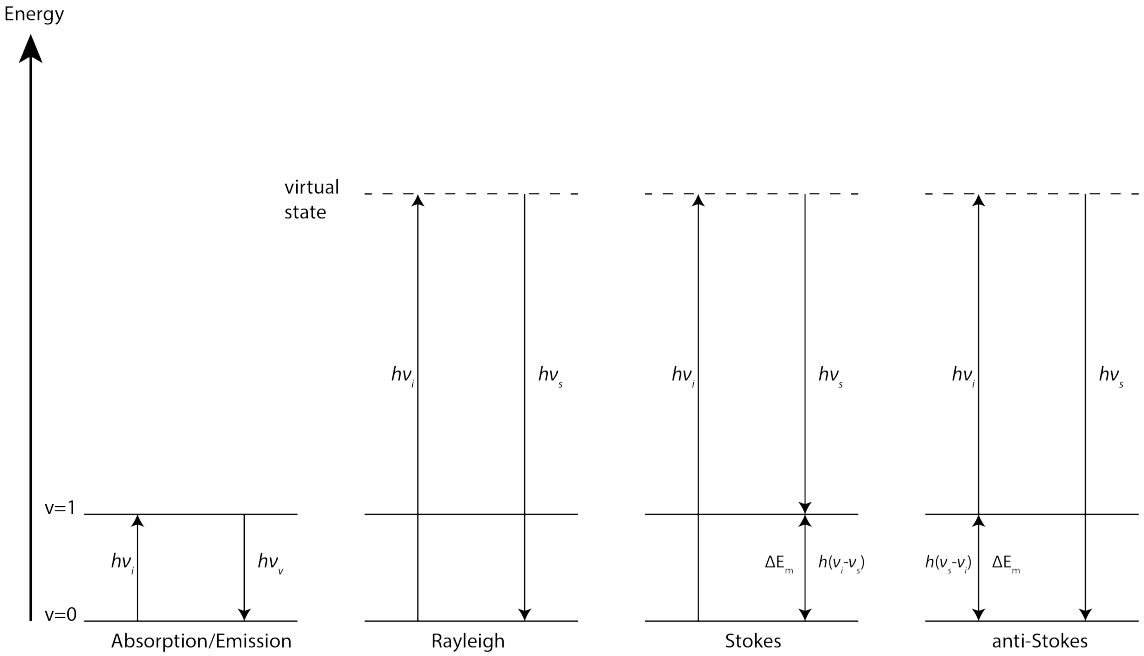

Figure 1.12: A diagram of adsorption/emission, Rayleigh scattering, Stokes-Raman scattering and anti-Stokes Raman scattering.

say that a dipole moment μ has been induced in the now-polarised molecule,

$$\mu = \alpha E. \tag{1.100}$$

Where E is the electric field strength of the radiation inducing the dipole and α is the polarisability of the molecule. The electric field of the incident electromagnetic radiation is given by,

$$E = E_0 \cos 2\pi\nu_i t, \tag{1.101}$$

where E_0 is the maximum electric field strength of the oscillating electric field, ν_i is the frequency of the oscillation and t is the time. The oscillating electric field induces an oscillating dipole within the molecule at the same frequency:

$$\mu = \alpha E_0 \cos 2\pi\nu_i t. \tag{1.102}$$

This oscillating dipole moment emits radiation of the same frequency in all directions, and the intensity of the radiation is proportional to the square of the maximum value for the dipole moment – $\alpha^2 E_0^2$. This mechanism is the source of the Rayleigh scattering which would be the only type of molecular scattering if the molecule did not posses its own internal vibrations.

Generally, in the course of a vibration, a sample molecule changes its size and shape, and subsequently its polarisability. In other words the value of α is not constant with the normal coordinate of a given vibrational mode of a sample molecule. For small displacements the polarisability can be expanded as a Taylor series,

$$\alpha = \alpha_0 + \frac{\partial \alpha}{\partial Q} Q, \tag{1.103}$$

where α_0 is the equilibrium polarisability, Q is the normal coordinate and $\partial\alpha/\partial Q$ is the rate of change of polarisability with respect to Q measured at the equilibrium configuration. Higher-order

terms are neglected in the harmonic approximation. The normal coordinate varies periodically:

$$Q = Q_0 cos 2\pi\nu_v t \tag{1.104}$$

where ν_v is the vibrational frequency. Combining 1.103 and 1.104 yields:

$$\alpha = \alpha_0 + \frac{\partial\alpha}{\partial Q} Q_0 \cos 2\pi\nu_v t \tag{1.105}$$

the substitution of 1.105 into 1.102 gives

$$\mu = \alpha_0 E_0 \cos 2\pi\nu_i t + \frac{\partial\alpha}{\partial Q} E_0 (\cos 2\pi\nu_v t)(\cos 2\pi\nu_i t) \tag{1.106}$$

by making use of the trigonometric identity $\cos\alpha\cos\beta = \frac{1}{2}cos(\alpha-\beta) + \frac{1}{2}\cos(\alpha+\beta)$ we have:

$$\mu = \alpha_0 E_0 \cos 2\pi\nu_i t + \frac{\partial\alpha}{\partial Q}\frac{Q_0 E_0}{2}[\cos 2\pi(\nu_i - \nu_v)t + \cos 2\pi(\nu_i + \nu_v)t] \tag{1.107}$$

Equation 1.107 shows that the induced dipole moment μ varies with three component frequencies; ν_i (Rayleigh frequency), $\nu_i - \nu_v$ (Stokes frequency) and $\nu_i + \nu_v$ (anti-Stokes frequency). The classical description described above corresponds to the quantum mechanical result for Raman transitions when $\Delta\nu = \pm 1$. An important shortcoming of the classical description of Raman scattering is that it incorrectly predicts the relative intensities of the Stokes and anti-Stokes bands.

1.11.3 Polarisability

The *polarisability* α is described by a tensor; for perfectly symmetrical molecule the polarisability is the same in all directions, as a result the induced dipole moment discussed above must be parallel to the vector components of the electric field in each axis:

$$\mu_x = \alpha E_x \ , \ \mu = \alpha E_y \ , \ \mu_z = \alpha E_z \tag{1.108}$$

For all molecules of lower symmetry the polarisability is not identical along each axis (i.e. in all directions) and may be substantially different. Due to this asymmetry the induced dipole moment μ will not be parallel to the incident field components in each axis. We need to write a series of equations that take this into account:

$$\mu_x = \alpha_{xx}E_x + \alpha_{xy}E_y + \alpha_{xz}E_z \tag{1.109}$$

$$\mu_y = \alpha_{yx}E_x + \alpha_{yy}E_y + \alpha_{yz}E_z \tag{1.110}$$

$$\mu_z = \alpha_{zx}E_x + \alpha_{zy}E_y + \alpha_{zz}E_z \tag{1.111}$$

The polarisability which we refer to in the classical description above comprises the whole system of α constants. This system of coefficients which relates the vectors μ and E is called a tensor.

$$\alpha = \begin{bmatrix} \alpha_{xx} & \alpha_{xy} & \alpha_{xz} \\ \alpha_{yx} & \alpha_{yy} & \alpha_{yz} \\ \alpha_{zx} & \alpha_{zy} & \alpha_{zz} \end{bmatrix} \tag{1.112}$$

The polarisability tensor is symmetrical, i.e. $\alpha_{ij} = \alpha ji$. In any coordinate system there are two values that are independent of the coordinate system chosen. These are the mean polarisability:

$$\bar{\alpha} = \frac{1}{3}(\alpha_{xx} + \alpha_{yy} + \alpha_{zz}) \tag{1.113}$$

and the anisotropy γ given by

$$\gamma^2 = \frac{1}{2}[(\alpha_{xx} - \alpha_{yy})^2 + (\alpha_{yy} - \alpha_{zz})^2 + (\alpha_{zz} - \alpha xx)^2 + 6(\alpha_{xy}^2 + \alpha_{xz}^2 + \alpha_{yz}^2)] \tag{1.114}$$

the value of γ tells us how much a molecules polarisability ellipsoid is different from the polarisability of a perfectly symmetric molecule. All these arguments hold for polarisability derivatives $\alpha'_{ij} = \frac{d\alpha_{ij}}{dQ}$ that govern Raman scattering.

Chapter 2

Materials and methods

2.1 Materials

The lipids 1-palmitoyl-2-oleoyl-sn-glycero-3-phosphotidylethanolamine (POPE) (99%), 1-palmitoyl-2-oleoyl-sn-glycero-3-phosphotidylcholine (POPC) (99%), d_{31}-POPE and d_7-cholesterol were purchased from Avanti Polar Lipids Inc. (Alabaster AL). Cholesterol, egg-sphingomyelin (99%) (egg-SM) and tris(hydroxymethyl)aminomethane (Ultra-grade) (tris) were purchased from Sigma-Aldrich. All chemicals were used as received, and phospholipids were used fresh from unopened ampules for each experiment. All water was obtained from a Millipore gradient A-10 water filtration unit (18.2 MΩ cm, TOC >4ppb). Deuterated surfactant dSDS and dCTAB were purchased from CDN isotopes both 98% D with overall purity of 98%.

2.2 Cleaning procedures

For all experiments lab glassware, spatulas, tweezers, PTFE tubing, o-rings and associated valves were cleaned overnight in ≈4% Borer PF15 or Decon-90 solution. The AFM fluid cell was cleaned in the same solution but at a much reduced concentration (1-2%). AFM cantilevers were cleaned in a plasma cleaner (BIO-RAD Plasma Asher E2000), air plasma, for a few minutes prior to use. The optical hemispheres used with the TIR-Raman flow cell were cleaned in chromic acid for at least 4 hours. All of the above were rinsed in 20 eqv vols of MilliQ water before use. Often glassware was examined for cleanliness by visual inspection of wetting by water prior to use.

2.3 Vesicle preparation

Vesicles were prepared solely by the sonication method. For SLB formation kinetics (Chapter 3) all suspensions had a final concentration of 0.5 mg ml^{-1}. Final concentrations varied between 0.3 and 0.5 mg ml^{-1} for other work. The required masses of phospholipid, sphingomyelin and cholesterol were placed in round bottomed-flasks and dissolved in either chloroform for the samples of pure phospholipid or chloroform and methanol (9:1) when sphingomyelin was present. The solvent was evaporated under vacuum and mild heating using a rotary evaporator. Following thin

film formation within each flask, the samples were left under vacuum (< 1 mbar) for one hour to remove any remaining solvent. The films were then hydrated in the required volume of 20 mM tris buffer pH 7.4 with added 2 mM $CaCl_2$ or 100 mM NaCl if required. Finally the suspensions were sonicated for 1.5 hrs in a bath sonicator (Langford sonomatic 475H) at a typical temperature of 40°C ± 2°C to form final lipid suspensions.

2.4 Raman spectroscopy

2.4.1 Overview

The TIR-Raman spectrometer used throughout my studies was based upon a commercial system (Renishaw Ramascope 1000, Wooton-under-edge,UK); originally a confocal system, our group has adapted it for TIR-Raman by the addition of custom delivery optics. The laser used was a frequency-doubled solid-state-laser (Opus 532, Laser Quantum, Manchester, UK), that emits horizontally polarised light of 532 nm wavelength. For most measurements this laser was operated at 800 mW, which corresponded to a power of ≈ 530 mW at the sample. A schematic of the delivery optics is shown in figure 2.1. After leaving the laser head the horizontally polarised incident beam was passed through a polarising beamsplitter to ensure the accuracy of the incident light's polarisation. Subsequently, the beam was directed though a half-wave plate to select the correct polarisation for the measurement being taken, either S or P polarised. After the polariser the beam was passed to a telescope consisting of a -25 and a 125 mm lens, the first to expand the beam and the second to collimate it. The reason for the telescope was to increase the beam's cross-section thereby facilitating a tighter focus on the sample after the final lens. At this stage the beam diameter was approximately 10 mm. Following the telescope the beam was reflected from a mirror at 90 degrees and then directed to a periscope where the beam was delivered vertically to the final mirror. After the final mirror the beam was delivered to a gradient index lens (f=120 mm), to focus the beam down to an ellipse of ≈ 30 μm × 10 μm onto the sample with the minimal optical aberrations.

Generally the sample consisted of an IR or UV grade fused silica hemisphere (Global Optics, Bournemouth, UK) mounted to the top of a closed glass flow cell and temperature control jacket. The translational position of the sample cell could be adjusted by way of micro-motion stages (Newport) to which the cell was attached. Occasionally spectra were acquired from solid samples deposited on silicon wafers by evaporation from solvent solutions. Figure 2.2 shows the collection and spectrometer optics. Light scattered from the interfacial region of the flat bottom of the hemisphere and the solution held within the flow cell was collected by an ultra long working distance 50 X microscope objective NA 0.55 (Olympus) and delivered through a Leica DM-SM microscope to the spectrometer. The microscope was equipped with a white light source and video camera for aligning the sample within the beam. Whether the scattered light was diverted to the spectrometer, or the white light source was shone to the sample and reflected back into the camera depended on the configuration of a half-mirror and a mirror in the filter magazines of the microscope. Within the spectrometer an edge filter removed the 532 nm Rayleigh line and any stray incident reflected light. The Raman light was then passed through a half-wave plate and polariser if polarisation control over the scattered light was considered necessary. N.B. These elements could be removed from the optical path when unnecessary. Subsequently, the beam was focussed through a ≈200 μm slit, collimated, then reflected from a prism onto a motorised diffraction grating finally

being focussed onto the CCD with a lens.

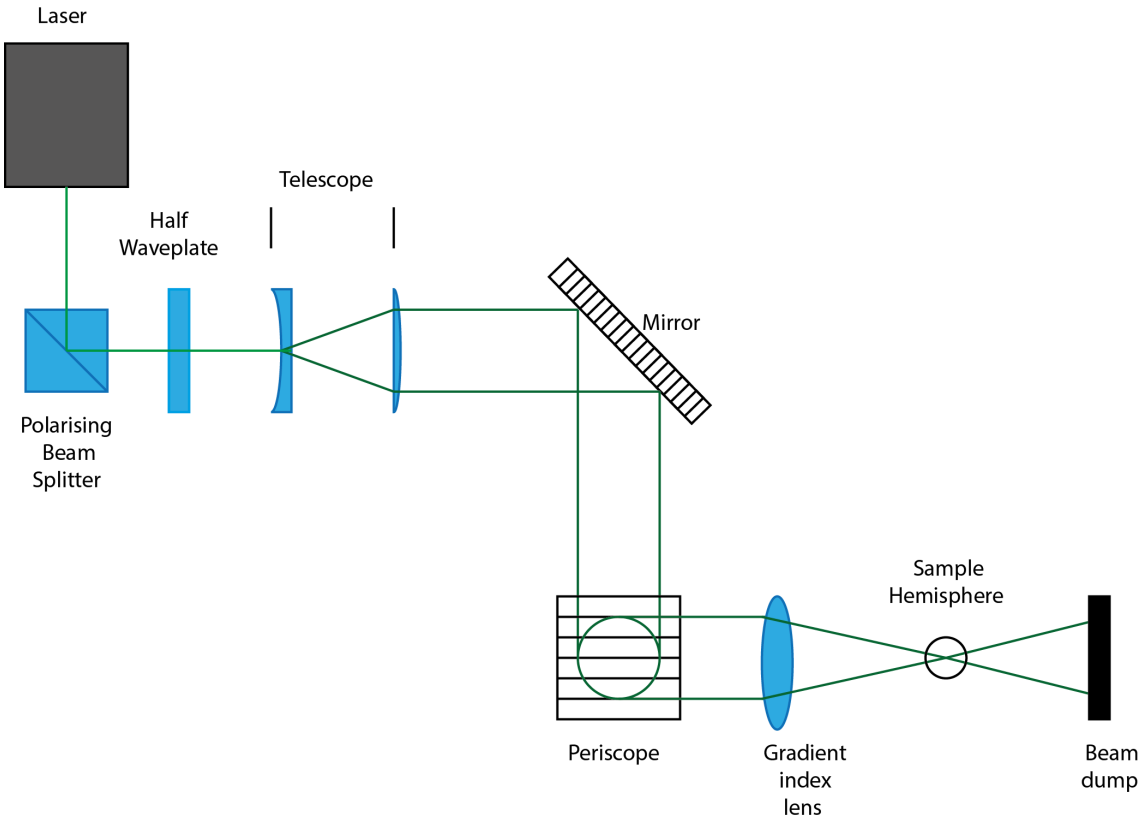

Figure 2.1: A schematic showing the delivery optics for the TIR-Raman spectrometer, shown from above, not to scale.

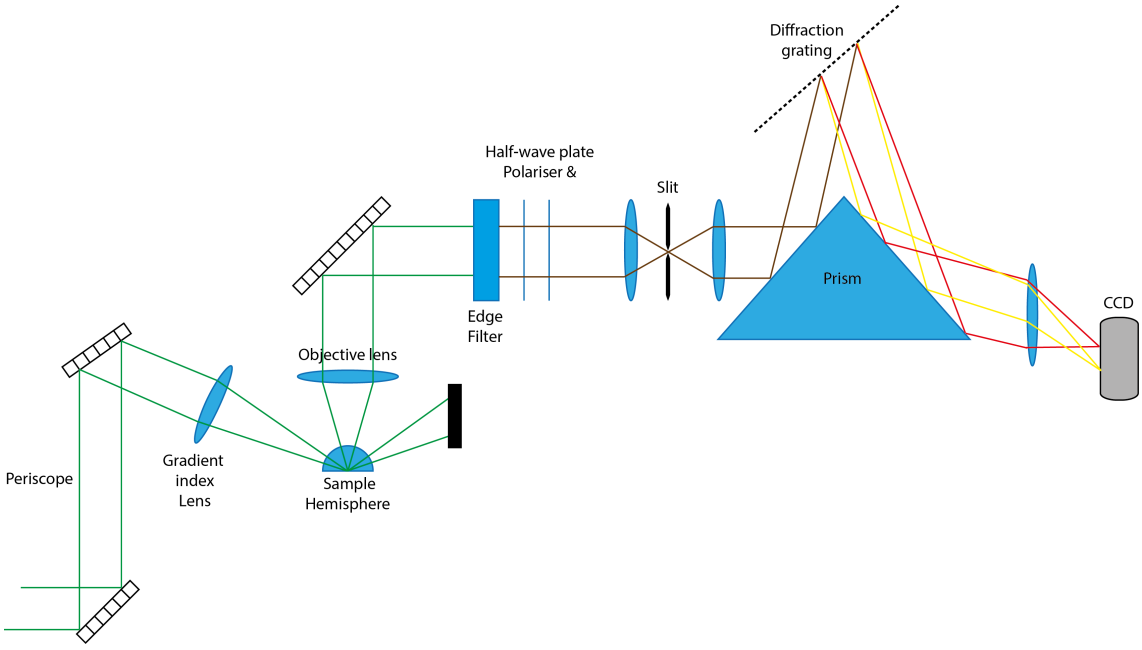

Figure 2.2: A schematic showing the collection optics and the internal optics of the TIR-Raman spectrometer, not to scale.

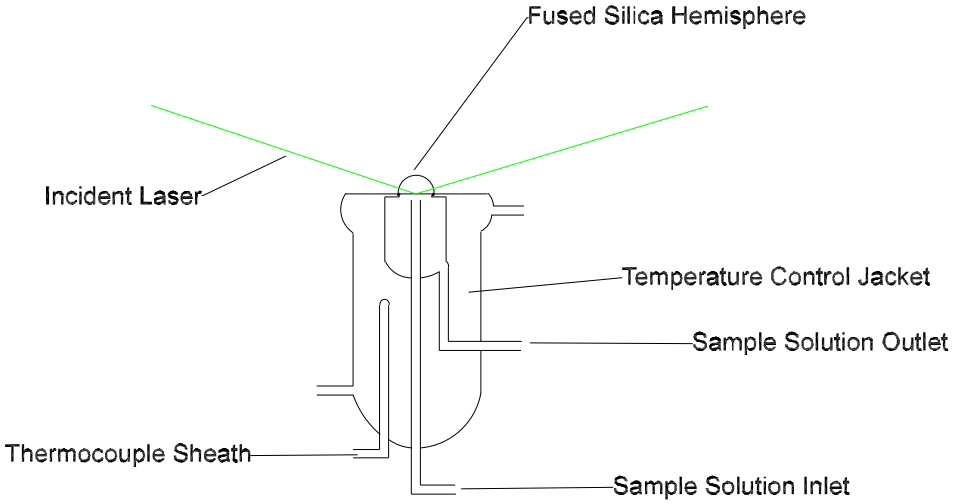

Figure 2.3: A schematic showing a representative section of the flow cell.

2.4.2 Sample environment

The sample environment used for TIR-Raman experiments consisted of a temperature-controlled fluid cell with wall-jet geometry (Figure 2.3). A polished (40:20 scratch-dig ratio) optical UV- or IR-grade, fused-silica hemisphere (Global Optics, Bournemouth, UK) was mounted on the top of the flow cell, into which the external laser beam was delivered at the desired angle of incidence (73°). The hemisphere was used to reduce optical aberrations and increase the collection efficiency; it was sealed to the glass flow cell with a Viton O-ring and a Teflon bracket. The whole assembly was supported in an adjustable mirror holder. Solutions were introduced into the flow cell through PTFE tubing and valves (Omnifit™). The inlet tubing was arranged such that any trapped air bubbles could be removed before entering the flow cell. During kinetic measurements (discussed later) solutions were injected into the flow cell with a motorised syringe pump (Harvard Apparatus) at a constant flow rate of 0.300 ml min^{-1} from a gas tight syringe (Hamilton). For equilibrium measurements the cell was often pre-filled with the required solutions. Temperature was maintained by a circulating temperature control bath connected to the temperature control jacket of the fluid cell. The internal temperature of the flow cell was monitored with a thermocouple and adjusted to the required value by altering the set-point on the control unit of the bath. The central volume

of the flow cell where all experimental solutions passed had a volume of 6 ml and the inlet was positioned 1.8 mm from the flat surface of the optical hemisphere. The inlet tube had an internal diameter of 2 mm. The hydrodynamics of the wall-jet are well defined. This geometry leads to a stagnation point below the centre of the hemisphere where the laser is focussed. This stagnation region makes any mass transport from the bulk to the silica-water interfacial region being studied diffusion limited, if the adsorption kinetics are sufficiently fast.

2.4.3 Alignment

Careful laser alignment was conducted before any series of experiments to ensure that the beam was incident at the correct angle of incidence, 73°, in the correct plane and was of the correct polarisation. Usually the first step in this procedure was to check that the telescope elements were positioned correctly ensuring that back reflections were overlapped on the axis of the original beam and that following the telescope the beam was effectively collimated. Generally alignment before the telescope was unnecessary as these elements were fixed and never adjusted except under unusual circumstances; being within a safety housing surrounding the laser unit itself. The mirror following the telescope was set to deliver the beam to the periscope mirrors at 90°. Between this mirror and the periscope was an iris, used to aid in the alignment procedure of the broad collimated incident beam by reducing the spot size to small point. The centering of this iris about the incident beam was carefully checked. The last mirrors were then adjusted to deliver the beam at the correct angle of incidence. The incident angle was set by checking the height of the beam at two distances measured from the centre of the sample along the beam axis using a section of graph paper fixed to the base support of the microscope marked with these distances. The heights were measured using a brushed metal ruler attached to a brass block acting as a support; at all times during alignment very low laser powers were used by way of neutral density filters positioned at the laser head. The heights required for a 73° angle of incidence are shown in figure 2.4, before the sample was put into position, the heights at -150 mm and +160 mm were used. After the sample was positioned both heights were measured at 150 mm. When the incident angle of the beam was set correctly the gradient index lens could be brought into place, at this stage the back reflection was checked to indicate that the lens was normal to the beam and the centering of the beam within the lens was checked by ensuring that the final height measurement at 160 mm from the sample remained 156 mm. The focal point of the microscope and the beam were then adjusted to coincide in space by subtle adjustments in the position of the final mirrors.

Following the alignment of the delivery optics, the sample flow cell was pre-filled with water and brought into position, attached to the micro-motion stage and the centre of the bottom surface of the hemisphere was located. The focus of the laser spot was optimised and the height and lateral position of the reflected spot were examined on the ruler. If the sample hemisphere was found not to be flat, the reflected spot would not be centred at 251 mm on the ruler but at some other height and possibly displaced laterally from the original beam axis. Thumb screws that were part of the mirror holder were used to correct the positioning of the hemisphere relative to the incident beam, several iterations of this procedure were usually required. At this stage the spectrometers optics were aligned and optimised. A readout of the full CCD area was obtained with the grating centred at 3000 cm^{-1} using the spectrometers software. This wavenumber position corresponds to the the O-H stretching region. This was done firstly to give a strong indication that light was reaching the CCD as the O-H band is generally the largest feature in our spectra and secondly to see what the overall signal levels were like. The translational position of the image on the CCD was then

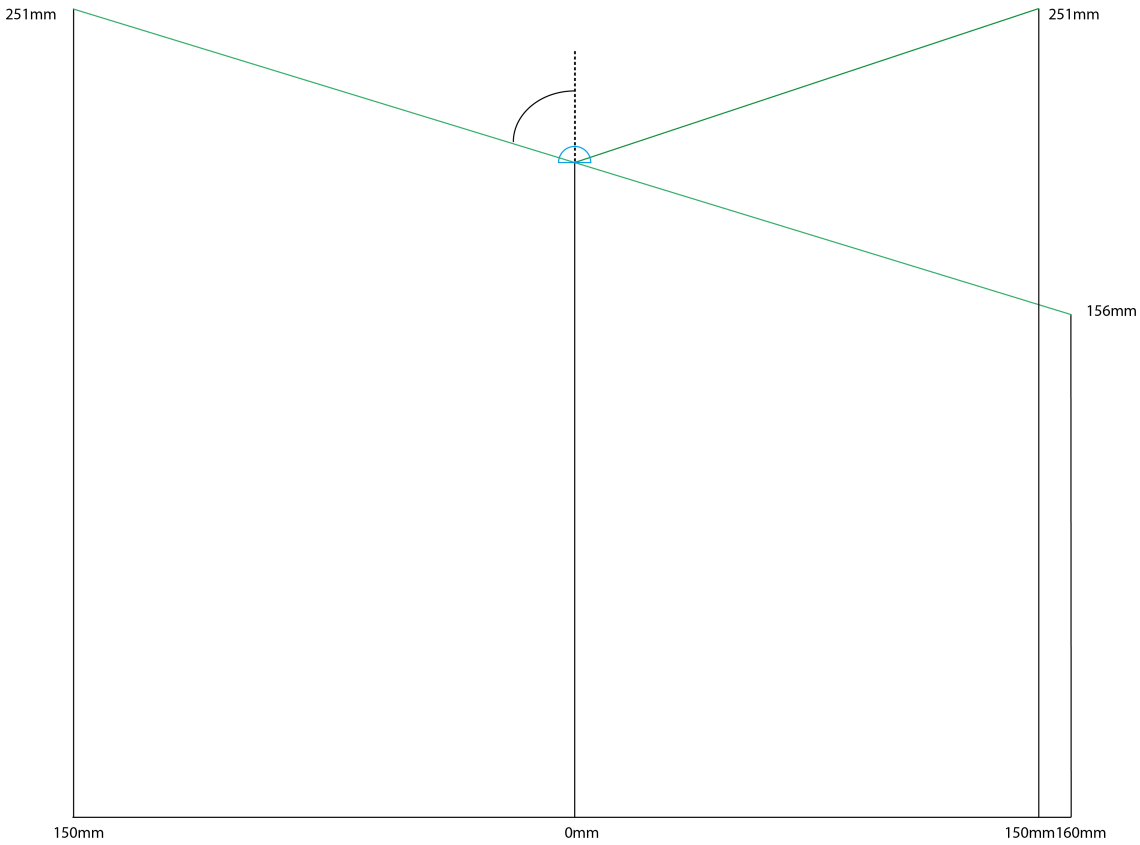

Figure 2.4: A schematic showing the vertical position of the beam at different distances from the sample along the beam axis. Drawn to scale.

optimised by adjusting the translational position of the first focussing lens in the spectrometer (before the slit) and its focus. After this a 1 second acquisition of the water region was acquired in an infinite loop, whilst the same adjustments as before were made to further optimise the overall signal levels. Finally another full scan of the CCD was obtained and the section over which the spectrum was to appear was binned to throw away the noise generated by the unused sections of the CCD. If these actions failed to generate any signal the turret of the microscope needed to be realigned to deliver the scattered light into the the spectrometer correctly; following this the prior procedures for optimising the signal within the spectrometer were carried out again. The final step in the alignment procedure was to calibrate the wavenumber scale of the spectrometer by setting the Si band to 520 cm^{-1}. A good signal level at around 3200 cm^{-1} was ≈2000 counts per second at 73° incidence, S-polarised and unpolarised detection with 800 mW incident laser power.

2.4.4 Measurements

The TIR-Raman spectrometer is controlled by a PC with the WiRE v2 (service pack 9) software from Renishaw. It is in this software that the aforementioned optimisations were carried out. The software allows for customisation of measurements. However, at a basic level two types of measurement can be carried out. The first is a fixed scan, where the diffraction grating is stationary. With the diffraction grating available this corresponded to a total spectral bandwidth of ≈ 660 cm^{-1}. In this mode of operation measurements as short as 0.5 s could be acquired with a CCD readout time of 1 s. In the other fundamental mode of operation the motorised diffraction

grating could be scanned across a wider spectral bandwidth but with a much longer acquisition time, for the spectral region which we were interested in (1200-3200 cm^{-1}) this was 10 s.

2.4.4.1 Extended scans

Extended scans were used to acquire high quality spectra of systems at equilibrium, these were done to gain spectra of pure component systems or to look at the results of interactions after any dynamic processes had taken place. Examples of where I use this type of scan include Chapter 3 where I calculate the composition of a mixed SLB by selective deuteration and also in Chapter 5 where I discuss the interaction of SLBs with surfactants. Typically 10 s spectra were acquired, with 10-20 cumulative acquisitions in order to improve the SNR. These extended scans were mostly acquired between 1200 cm^{-1} and 3200 cm^{-1}. The reasons why we chose the lower and upper bounds for the wavenumber positions was simple; below 1200 cm^{-1} the silica bands from the substrate obfuscate any bands of interest and there were no features of interest above 3200 cm^{-1}. A benefit of extended scans is that the intensity contribution to each data point comes from every pixel and therefore the variations in individual pixel sensitivities that lead to variance in fixed scans are averaged out.

2.4.4.2 Fixed scans

Fixed scans were used where only a small section of the spectrum was required, for example in my phase transition work in Chapter 4; or where the overriding requirement was temporal resolution i.e. where kinetic spectra were required for a specific dynamic process, for example the dynamics of surfactant incorporation into an SLB. As with the extended scans, for systems at equilibrium multiple acquisitions were acquired to improve the SNR. For kinetic measurements the software could be set to take repeat measurements over a fixed period of time. Generally some idea of the length of a process was acquired by conducting a first measurement over an arbitrarily long time period, when it was clear from the raw data that the system was no longer changing, the measurement could be aborted in such a way as to preserve the data acquired. Subsequent measurements of the same process were then acquired for the known fixed time period.

2.4.5 Analysis

TIR-Raman data were analysed in three different ways depending on what kind of experiments were begin carried out and what information was desired. The first which I term "order analysis" involved the direct extraction of information from the spectra using order parameters after the subtraction of a background previously acquired of the silica substrate. The second was target factor analysis (TFA), a form of Eigen analysis, which involves the reconstruction of the spectra acquired for a large set where each individual spectrum contains a relative contribution of certain target pure spectra representative of the components composing the system under study. The last which I call composition analysis was conducted where we wished to learn the composition at the interface but either too few spectra were acquired or there was limited change so TFA was not applicable.

2.4.5.1 Order analysis

When TIR-Raman spectra are acquired from interfacial systems such as SLBs, it is necessary to subtract the combined subphase and substrate background (figure 2.5). Generally a multiplicative factor must be employed as the intensity of the features in the background will be reduced in the spectrum of the system because solvent molecules are displaced from the region closest to the interface. Also, subtle changes between measurements altered the overall signal levels. These changes needed to be accounted for to conduct quantitative analysis. In addition, as features of the background change with temperature, background spectra need to be acquired at or as close as possible to the temperatures used to study the system of interest. For example, the intensity and shape of the O-H stretch change as the temperature is increased. One must also consider the effect of pH changes, as the nature of the functional groups on the silica support will change at different pH. The factor used in subtraction was selected by finding the intensity ratio of the reference background to the background in the spectrum of interest, a suitable data point in the spectrum was chosen for this purpose; commonly this was the peak of the water band.

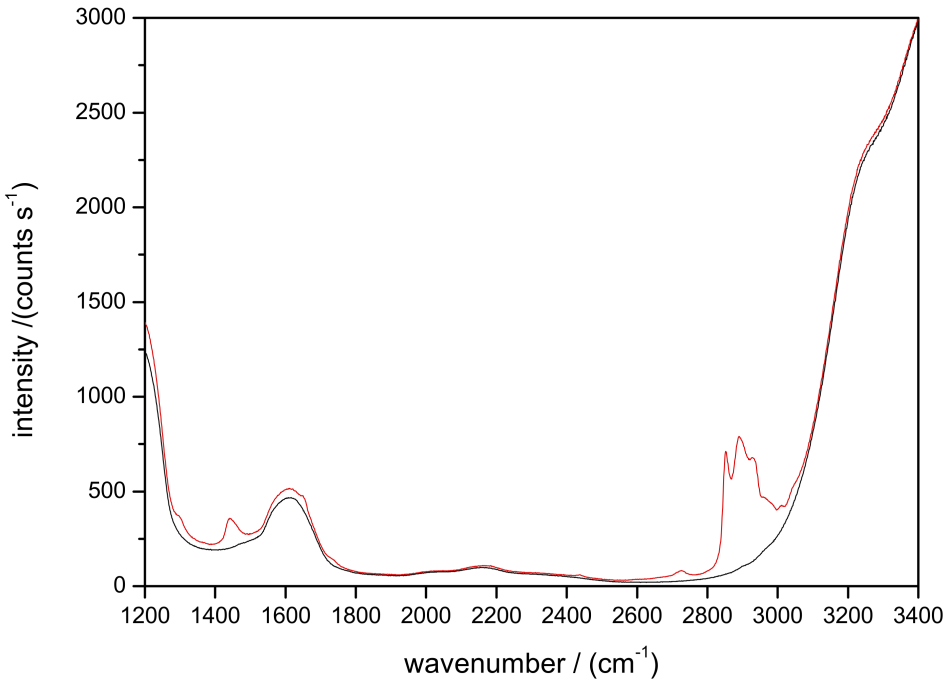

Figure 2.5: TIR-Raman spectra acquired of the silica-buffer interface and an SLB subsequently adsorbed to that interface.

After the appropriate background was subtracted the data were then analysed by using a selection of semi-empirical order parameters developed to understand the structural changes taking place. The primary conformational marker is the ratio of the antisymmetric ($\approx$2890 cm^{-1}) to symmetric ($\approx$2850 cm^{-1}) CH stretch peak intensities, I(d$^-$)/I(d$^+$).[41] This marker is sensitive to rotations, kinks, twists and bends of the alkyl chains present in the sample molecules. A higher ratio indicates relatively ordered chain structure, a lower ratio indicates a more disordered chain

structure; for liquid-like alkanes the parameter ranges from 0.6-0.9, likewise for crystalline alkanes 1.6-2.0. N.B. these ranges will change depending on how an experiment is carried out and the average orientation of the sample molecules within the probed volume; i.e. the polarisation of the incident and scattered light will affect the absolute values of the ratio. For these reasons I calculated the ratio for spectra acquired using S-polarised incident light and unpolarised detection, as the overall signal levels were highest and both stretches had strong signals. In fact, the diffraction grating has different sensitivities to S- and P-polarised light relative to its own surface and this also affects the ratio.

The peak positions of both the anti-symmetric and symmetric CH stretches are also conformational markers; a shift to higher frequency is indicative of increased chain disorder as it corresponds to a reduction of the oscillatory damping between adjacent Raman vibrational centres. i.e. as disorder increases, coupling between adjacent vibrational modes is reduced, the volume available to these modes increases and the effect is an increase in vibrational frequency.

The degree of chain tilting can be calculated by integrating the CH region of the spectrum for both S and P polarised incident light. As the S-polarised incident light primarily samples vibrational models aligned parallel to the the interface and the P-polarised light primarily samples modes perpendicular to it, the ratio of these gives a relative degree of chain tilt. If the chains are mainly all crystalline and upright simple geometric considerations tell us that most of the CH_2 groups will be aligned parallel to the surface and the signal generated in the S-polarised spectrum will be greatest.

For experiments with few spectra the $I(d^-)/I(d^+)$ and peak position order parameters can be calculated most easily using commercially available software. In these instances I used Origin Pro 8.1. However, for experiments with large numbers of spectra, as an example a series of kinetic measurements taken every second for a few hours, this methodology becomes cumbersome. As result I wrote some programs in Matlab to conduct this analysis with the minimum of user intervention. The user can choose to average spectra if required, for example if signal levels are low, and then can select the ranges within the spectra for the above parameters to be calculated and graphed. Peak positions and their intensities are extracted by fitting 4th order polynomials to the peaks of interest and then finding their maxima. These programs are found in Appendix B

2.4.5.2 Target factor analysis

Kinetic TIR-Raman spectra acquired throughout my studies were analysed using the technique of target factor analysis (TFA).[42] TFA is a multivariate statistical technique that reduces a matrix of data to its simplest dimensionality. TFA uses the concept of factor space and transformations of the coordinate axes within that space. The aim is to locate physically recognisable fundamental factors which combine to make up the original data set held within the matrix. TFA and the related principal component analysis (PCA) originate in work carried out by behavioural scientists in the early 20th century. However, it was not until the advent of relatively powerful computers towards the end of the same century that TFA gained the interest of chemists. Today TFA is frequently employed to solve chemical problems, particularly those in spectroscopy.

TFA can be used wherever you have a matrix of experimental data $\mathbf{D}$ with elements d_{ik}, where each measurement can be expressed as a linear sum of product terms.

$$d_{ik} = \sum_{j=1}^{n} r_{ij} c_{jk} \tag{2.1}$$

where r_{ij} is the jth factor associated with row i, and c_{jk} is the jth factor associated with column k. For instance, factor j could be a spectral contribution to a total spectrum comprised of j spectra, where i gives the intensity at the experimentally measured wave numbers k. The number of terms in the summation n is the number of factors necessary to represent the data; at this stage they are purely abstract and are void of physical meaning – but the aim is to transform them into physically realistic factors. The actual number of factors is determined by the smaller of the two dimensions of the n x m matrix $\mathbf{D}$. The first goal of target factor analysis is to decompose $\mathbf{D}$ into two abstract matrices such that

$$\mathbf{D} = \mathbf{RC} \tag{2.2}$$

where $\mathbf{R}$ is an abstract row matrix and $\mathbf{C}$ is an abstract column matrix. There will be n columns in $\mathbf{R}$ and n rows in $\mathbf{C}$. i.e. there will be the same number of columns and rows in each respectively as there are factors (eigenvectors) necessary to adequately model the dataset $\mathbf{D}$. There are several ways in which the decomposition can be done but the most frequently used, and the method chosen here, is singular value decomposition (SVD). In SVD the decomposition into eigenvectors is written as

$$\mathbf{D} = \mathbf{USV'} \tag{2.3}$$

where $\mathbf{US} = \mathbf{R}$ and $\mathbf{V'} = \mathbf{C}$. $\mathbf{S}$ is a diagonal matrix with values equal to the square roots of the eigenvalues of the eigenvectors or abstract factors. Experimentally, there are more factors than are necessary to accurately represent the data set with an abstract model; most of the factors pertain to noise or small spectral changes and are often unnecessary depending on what information one wishes to extract. The next step of PCA/TFA is the selection of the actual number of factors that *are* necessary for the model s; i.e. where we drop the irrelevant factors, leaving only a few factors suggestive of the chemical components of the physical system being studied – thus reducing the dimensionality of the factor space. This action is called *factor compression* and the results are the reduced matrices $\bar{\mathbf{R}}$ and $\bar{\mathbf{C}}$. One can gain an appreciation of the number of factors needed through a consideration of the chemical system under study, e.g. how many chemical components are expected? It is at this point that PCA and TFA differ; in PCA after the number of important factors has been identified, the abstract model is essentially complete. It may be that the user wishes to simplify the abstract solution by finding simpler abstract factors, in this case the coordinate axes can be transformed through orthogonal or oblique rotation. In TFA however, the most rewarding step takes place at this stage; like PCA a coordinate transformation can take place, but the resulting changes to the factors can be tested against user supplied target vectors, $\mathbf{x_{il}}$; in spectroscopy these will often be spectra of the pure component species. Mathematically we have,

$$\hat{\mathbf{X}} = \bar{\mathbf{R}}\mathbf{T} \tag{2.4}$$

likewise

$$\hat{\mathbf{Y}} = \mathbf{T^{-1}}\bar{\mathbf{C}} \tag{2.5}$$

where $\hat{\mathbf{X}}$ and $\hat{\mathbf{Y}}$ are the transformed matrices - the abstract factors now transformed into physically realistic refined spectra representing the target spectra. $\mathbf{T}$ is a transformation matrix of size $n \times n$. The power of this particular method stems from the fact that each target can be looked at individually despite the intrinsic multivariate nature of the overall analysis. Examining 2.4 we can see that the lth row of $\hat{\mathbf{X}}$, $\hat{\mathbf{x}}_l$, is generated by multiplying $\bar{\mathbf{R}}$ by the lth column vector of $\mathbf{T}$.

$$\hat{\mathbf{x}}_l = \bar{\mathbf{R}}\mathbf{t}_l \tag{2.6}$$

When seeking $\mathbf{t}_l$ for $\bar{\mathbf{R}}$ of a given compressed data set a least squares procedure is used. The transformation vector $\mathbf{t_l}$ has vector components $t_{1l}, t_{2l}, ..., t_{nl}$. Considering each row of the matrix $\bar{\mathbf{R}}$ is a row vector with vector components $r_{il}, r_{i2}, ..., r_{in}$. To obtain the projection of the ith row vector of $\bar{\mathbf{R}}$ on the new coordinate axis the dot product of the row vector with the hypothetical transformation vector $\mathbf{t}_l$ is taken

$$\hat{x}_{il} = \mathbf{r_i'} \cdot \mathbf{t_l} = r_{i1}t_{1l} + r_{i2}t_{2l} + ... + r_{in}t_{nl} \tag{2.7}$$

the sum indicated in 2.7 is taken over the s principal factors that were selected. Multiplying each row of $\bar{\mathbf{R}}$ by $\mathbf{t_l}$ gives each element of the newly transformed row vector $\hat{\mathbf{x}}_\mathbf{l}$ i.e. $\hat{x}_{1l}$, $\hat{x}_{2l}$,..., $\hat{x}_{rl}$. In the least squares procedure used here each element of the predicted row vector is compared to that of the test vector; our target. We first calculate the difference between each element of the test vector $\mathbf{x}_l$ and the equivalent element of $\hat{\mathbf{x}}_l$,

$$\Delta x_{il} = \hat{x}_{il} - x_{il} = r_{il}t_{1l} + r_{i2}t_{2l} + ... + r_{in}t_{nl} - x_{il}. \tag{2.8}$$

In our search for the best transformation vector $\mathbf{t}_l$ we sought to minimise each 2.8 by setting the sum of the derivatives of the squares of all of the differences equal to zero. For example the derivative with respect to t_{1l}

$$\frac{d(\Delta x_{il})^2}{dt_{1l}} = 2r_{i1}^2 t_{1l} + 2r_{i1}r_{i2}t_{2l} + ... + 2r_{i1}r_{in}t_{nl} - 2r_{i1}x_{il} \tag{2.9}$$

taking the sum over each row of $\bar{\mathbf{R}}$ we get,

$$\sum_{i=1}^{r} \frac{d(\Delta x_{il})^2}{dt_{1l}} = 0 = t_{tl}\sum_i r_{il}^2 + t_{2l}\sum_i r_{i1}r_{i2} + ... + t_{nl}\sum_i r_{i1}r_{in} - \sum_i r_{i1}x_{il} \tag{2.10}$$

repeating this procedure for each of t_{nl} and rearranging yields a system of r_n simultaneous equations,

$$\sum r_{i1}x_{il} = t_{1l}\sum r_{i1}^2 + t_{2l}\sum r_{i1}r_{i2} + \cdots + t_{nl}\sum r_{i1}r_{in} \tag{2.11}$$

$$\sum r_{i2}x_{il} = t_{1l}\sum r_{i1}r_{i2} + t_{2l}\sum r_{i2}^2 + \cdots + t_{nl}\sum r_{i2}r_{in} \tag{2.12}$$

$$\vdots \tag{2.13}$$

$$\sum r_{in}x_{il} = t_{1l}\sum r_{i1}r_{in} + t_{2l}\sum r_{i2}r_{in} + \cdots + t_{nl}\sum r_{in}^2 \tag{2.14}$$

which we can express in matrix form as,

$$\mathbf{a}_l = \mathbf{B}\mathbf{t}_l \tag{2.15}$$

where

$$\mathbf{a}_l = \begin{bmatrix} \sum r_{i1}x_{il} \\ \sum r_{i2}x_{il} \\ \vdots \\ \sum r_{in}x_{il} \end{bmatrix} \tag{2.16}$$

$$\mathbf{B} = \begin{bmatrix} \sum r_{il}^2 & \sum r_{il}r_{i2} & \cdots & \sum r_{il}r_{in} \\ \sum r_{il}r_{i2} & \sum r_{i2}^2 & \cdots & \sum r_{i2}r_{in} \\ \vdots & \vdots & & \vdots \\ \sum r_{il}r_{in} & \sum r_{i2}r_{in} & \cdots & \sum r_{in}^2 \end{bmatrix} \tag{2.17}$$

$$\mathbf{t}_l = \begin{bmatrix} t_{1l} \\ t_{2l} \\ \vdots \\ t_{nl} \end{bmatrix} \tag{2.18}$$

multiplying both sides of 2.15 by the inverse of $\mathbf{B}$ gives,

$$\mathbf{t}_l = \mathbf{B}^{-1}\mathbf{a}_l \tag{2.19}$$

inspection of $\mathbf{B}$ shows that

$$\mathbf{B} = \bar{\mathbf{R}}'\mathbf{R} \tag{2.20}$$

and similarly for $\mathbf{a}_l$

$$\mathbf{a}_l = \bar{\mathbf{R}}\mathbf{x}_l \tag{2.21}$$

leaving us with the most important equation of target factor analysis,

$$\mathbf{t}_l = (\bar{\mathbf{R}}'\bar{\mathbf{R}})^{-1}\bar{\mathbf{R}}'\mathbf{x}_l \tag{2.22}$$

this expression allows us to calculate the lth column of the transformation matrix for the lth target factor, we then use this to generate the predicted vector in 2.6 and compare this to the original target to see if it is a realistic physically representative factor.

After transformation the end result of TFA is a component weight for each physically meaningful factor or chemical component contributing to the spectra in a series. For pure lipid species in a TIR-Raman experiment these will be for water, the lipid and, depending on the spectral region under study, possibly the substrate. The component weights are purely relative and the absolute values in general have no meaning. If absolute information is required the component weights must be calibrated to gain surface excess values. In general this can be done (granted several assumptions) in TIR-Raman with soluble amphiphiles that form disordered surface layers that become saturated at a bulk concentration.[43] Lipids are in generally virtually insoluble, to form a SLB requires a concentration far greater than the CAC or critical aggregation constant. Given that the calibration curve requires data points of increasing concentration over an order of magnitude above the concentration required for SLB formation, and the fact that this leads to a build-up of extraneous aggregates or vesicles (see Chapter 3), means that the method used for calibration is both prohibitively expensive and technically impossible. In my work I have used the fact that the spectra are very similar for lipid in different buffer solutions to use the same refined spectra for subsequent analyses of formations of the same lipid, this means that component weights acquired in different buffers are comparable.

2.4.5.3 Composition analysis

For composition analysis the component species require either distinct vibrational modes that are un-occluded by other Raman bands or, for overlapping bands, sufficiently distinct contour. Where these criteria are not met, selective isotopic labelling to give a marker for the species of interest is necessary. After obtaining Raman spectra of the pure components of interest, we can relate the size of the isolated band in the mixture to the relative contribution of the species to a region where the system components have bands overlapping. If one normalises the contribution in this region to the number of active modes in the species of interest and then finds the total contribution to that region from the species of interest using the un-occluded band, it is possible to extract the mole fraction of that species. In my studies the shared region is the CH region between 2650-3100 cm^{-1}. TFA can be used to the same ends if spectra of several different compositional ratios are available and the differences between the spectra of the pure components are large enough. For the two component case,

$$I_{CH}^{m} = I_{CH}^{A} + I_{CH}^{B}. \tag{2.23}$$

Where I_{CH}^{m} is the CH region integrated intensity of the mixture, I_{CH}^{A} is the CH region integrated intensity for component A and I_{CH}^{B} is the CH integrated intensity for component B. For each pure component we can integrate an isolated band and the CH region intensities, we then take the ratio of the two,

$$R_{p}^{B} = \frac{I_{CH}^{B,p}}{I_{isol}^{B,p}}. \tag{2.24}$$

Where the subscript and superscript p indicate that these values are for the pure component. Multiplying R_{p}^{B} by I_{isol}^{m}, the intensity of the isolated band in the mixture, yields the contribution of B to the CH stretching region. i.e.

$$I_{isol}^{B,m} R_{p}^{B} = I_{CH}^{B,m} \tag{2.25}$$

the remaining CH signal is due to species A,

$$I_{CH}^{A,m} = I_{CH}^{m} - I_{CH}^{B,m} \tag{2.26}$$

To estimate mole fractions we divide these CH contributions by the number of CH bonds in the respective species, and then divide each by the resulting total normalised CH intensity

$$X_{A} = \frac{I_{CH,n}^{A}}{I_{CH,n}^{A} + I_{CH,n}^{B}} \tag{2.27}$$

and

$$X_{B} = \frac{I_{CH,n}^{B}}{I_{CH,n}^{A} + I_{CH,n}^{B}} \tag{2.28}$$

This ratio method can be applied to mixtures of N species provided there are $N-1$ independent bands available to conduct the analysis. If isotopic labelling is necessary to meet this requirement, the relative Raman cross-section per bond must be found by preparing 50:50 mixtures of the labelled and unlabelled species and calculating the relative intensities in the CH and CD regions of the two. If only partial deuteration is available this must be taken account of at this stage too. This method ignores any changes in the band ratios for the species in the mixture owing to interactions between

the components and associated local environment effects. For instance, it ignores alterations in band ratios resulting from phase transitions associated with mixing and temperature changes – measurements of the calibrating band ratios must be acquired in the same/similar phase to that expected for the mixture under study.

2.5 Atomic force microscopy

AFM measurements were conducted on a Digital Instruments Multimode Nano-scope IV (recently merged with Bruker Corporation) equipped with the J-scanner and temperature control unit. The J-scanner gives a lateral imaging area of 125 μm by 125 μm and was the wider viewing of the two scanners at my disposal – it offers a maximum lateral viewing area larger than the area probed by the TIR-Raman spectrometer (10 x 30 μm) and therefore offered the ability to image interesting phenomena highlighted by TIR-Raman. The AFM was controlled through its proprietary Nanoscope software, which along with Gwyddion was also used for image analysis and correction. As my SLB systems needed to be immersed in buffer solution I used the MTFML fluid cell (figure 2.7) with fluoropolymer sealing O-ring. I chose the Veeco NP-S probe for my studies, using the 0.06 N m^{-1} cantilever. This probe was chosen due to its softness – which is a benefit in fluid tapping mode – and its high reflectivity gold coating, which increased the signal generated at the quad cell in the microscope. Before aligning the AFM, the MTFML cell was positioned with the cantilever onto the substrate (a cleaned silicon wafer or fused silica disk) and the cell was pre filled with buffer solution. Then the optical path within the scanner head was aligned. Within the scanner head, a small diode laser was reflected from a mirror onto the back of the cantilever near the probe. The position of the laser spot was then adjusted using the relevant thumb screws on the scanner head (figure 2.6) and an optical microscope connected to a video camera coupled to a small television screen. After the beam spot position was set, a small tilt mirror on the opposite side of the scanner head was adjusted to reflect the beam onto a small quad photodiode cell; this spot was then centered on the quad cell by adjusting the cells position relative to the spot using further thumbscrews.

In AFM tapping mode one seeks a resonant frequency of the cantilever and a suitable RMS amplitude for the cantilever's oscillation, this is sought manually in fluid experiments but automatically in air. When a suitable resonance is located, the drive frequency is offset very slightly to the side of the resonant peak and the relative phase of the drive and cantilever oscillation is zeroed. The cantilever is then brought down towards to the sample. In fluid work, false surfaces are often detected and you have to ask the software to find the surface multiple times. Once the real surface is found the amplitude of the oscillation is reduced until the cantilever is no longer in contact with the surface, it is then slowly increased until the amplitude of the cantilever's oscillation is just sufficient that the cantilever is touching the sample surface. Following this the microscope was set to scan one line of the sample repeatedly and the integral and proportional gains on the instrument were set to optimise the overlap of the trace and retraces as far as possible. Usually scan rates of 1 Hz were used in fluid as poor image quality is obtained if the instrument is set to run any faster. When the operating parameters had been set satisfactorily, the slow scan axis was enabled and images of the surface were acquired. Each image took 512 s to complete.

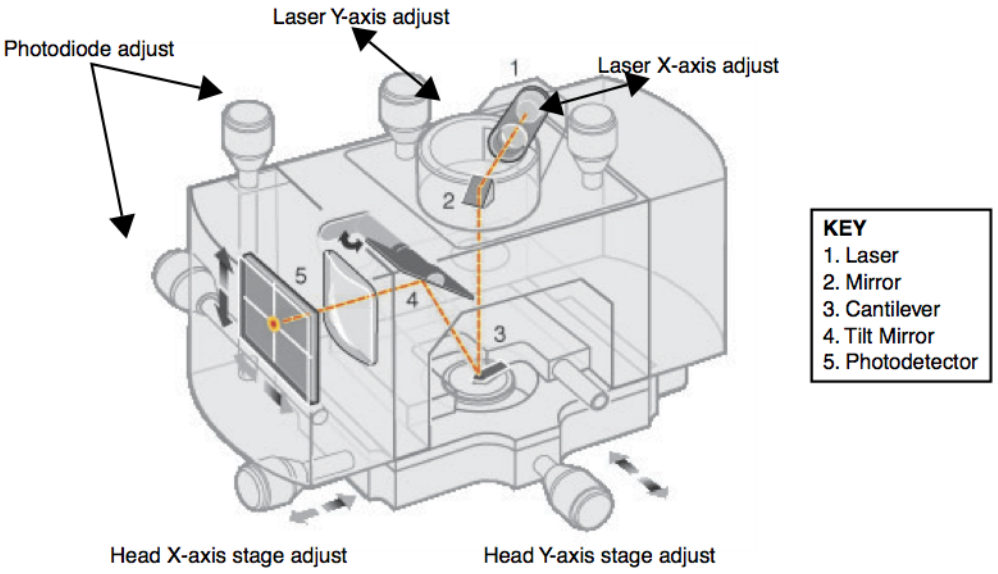

Figure 2.6: A schematic of the AFM scanner head. Courtesy of Bruker Corporation.

Figure 2.7: A Photograph of the MTFML flow cell. Courtesy of Bruker Corporation.

2.5.1 Image analysis

Images acquired by AFM often have artefacts. Some artefacts stem from technical problems associated with a given experiment, for example those associated with damaged probe tips or unwanted vibrations of some kind. Other artefacts are unavoidable and stem from the design of the AFM being used; an example is the bow commonly seen in large area AFM images, which occurs because the piezoelectric scanner moves the probe in a curved motion over the surface – the piezos in the scanner are unable to move the probe with (x, y) components only and so the resulting images appear curved; the larger the image the more the greater the apparent curvature (see figure 2.8). Most manufacturers' software and third party software include options to fit surfaces through an image. This surface is then subtracted from the raw image thereby flattening it. Another frequently occurring artefact is the line defect, this occurs when the tip loses contact/interaction with the surface temporarily and leaves a fixed line or partial line of constant topography. These can be removed by adjacent averaging of corresponding data points from adjacent lines along the slow-scan axis. If an AFM instrument is calibrated with a reference sample of known topography, cross-sections can be drawn across an image giving height information about features of interest.

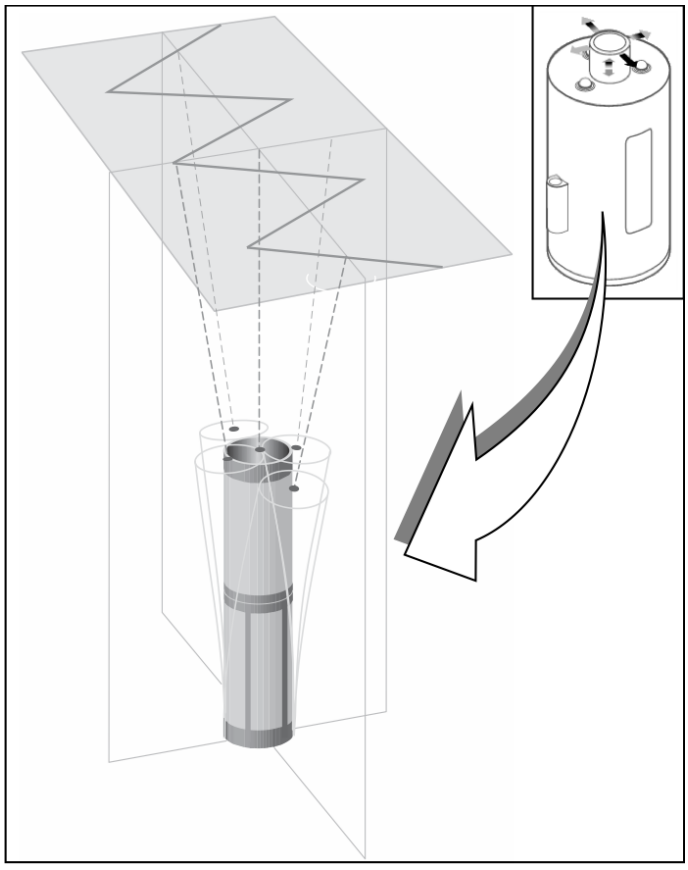

Figure 2.8: A Schematic of the AFM Scanner. Courtesy of Bruker Corporation.

2.6 Nano-particle tracking analysis

2.6.1 Overview

Vesicle size distributions for each lipid suspension for my formation kinetics experiments were measured by nano particle tracking analysis (NTA) utilising a Nanosight LM10-HS (Salisbury, UK). NTA functions by scattering light from nano particles of interest and recording the movement of these particles using a microscope and CMOS camera. At the heart of the system lies a fluid cell comprised of an inlet and outlet with 0.3 ml volume, at the bottom of this cell is a metalled glass prism though which an 488 nm blue solid state laser beam is incident, it is this light that scatters from the particles of interest. The scattering of light from colloidal particles in the 10-1000 nm regime depends on the fourth power of the frequency of the light. For this reason the blue laser was used; the light scattered will be far greater than for a lower frequency laser and thus smaller particles can be tracked (lasers of different wavelength are available for different applications – for instance fluorescence experiments). Owing to the coating on the glass prism, the background is almost completely black. If the frame rate of the camera is known, and the distance moved by the particle owing to Brownian motion can be measured, then the Stokes-Einstein relationship can be invoked to find the hydrodynamic radius of each particle,

$$\frac{\overline{(x,y)^2}}{4} = \frac{2kT}{3\pi d\eta}. \tag{2.29}$$

where $\overline{(x,y)^2}$ is the mean displacement squared, T is the temperature, d is the particle's hydrodynamic diameter, η is the solution viscosity. Following many particles over a period of time builds up a statistically relevant particle size distribution. The longer a particle is tracked the smaller the error associated with the diameter evaluation, thus short tracks are dropped from the determination. The instrument can typically detect particles in the range of 10-2000 nm.

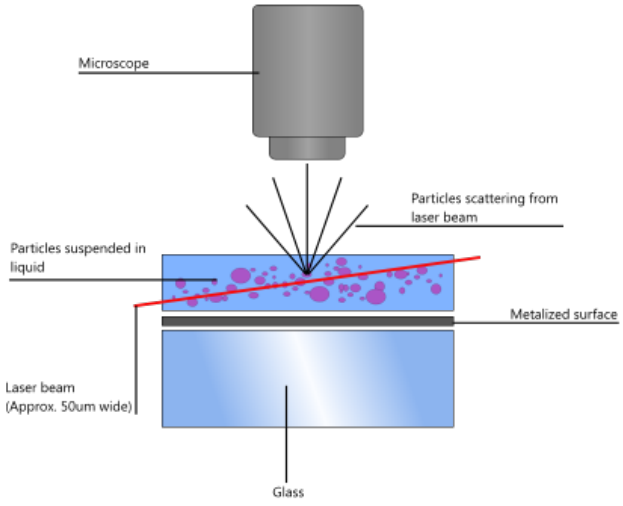

Figure 2.9: A Schematic Representation of the NTA setup. Reprinted with permission of Nanosight Ltd.

2.6.2 Measurements

For each measurement the lipid suspensions were diluted with the relevant buffer solution to a concentration suitable for analysis (10^7 - 10^9 particles per ml). Prior to use the Nanosight chamber was filled with the required buffer solution to check for contaminant particles and to allow the chamber to reach the required temperature; all solutions were measured with the temperature set for the associated TIR-Raman formation kinetics measurements. After the suspensions had been injected into the chamber, the microscope was focused and the video was recorded for 215 s (the longest user selectable value in the software). The video was analysed with Nanosight's proprietary NTA software.

2.7 Neutron reflection

Neutron reflectometry was carried out at at the Institut Laue-Langevin (ILL) in France using the D17 and FIGARO (Fluid Interfaces Grazing Angles Reflectometer) instruments. D17 is a vertically oriented time of flight neutron reflectometer and FIGARO is a newer horizontally oriented instrument with wider q range.

By studying the specular reflection of neutrons as a function of the incident angle and neutron wavelength, the scattering length density profile normal to the interface can be obtained. From a set of density profiles obtained from chemically identical SLBs but with selective isotopic labelling, this affords us the ability to directly measure the distribution of chemical components relative to the interface in an unambiguous way. As the angle of incidence for moderated neutrons required for total external reflection are very small, the incident neutron beams are generally oriented at grazing angles of less than 2°, as a result the beams have to be highly collimated.

Chapter 3

The formation of supported lipid bilayers (SLBs) from lipid suspensions

3.1 Review

Supported lipid bilayers were first studied by Tamm and McConnell in 1985.[1] Their interest stemmed from a desire to study and understand biological membrane-membrane interactions, and they saw supported lipid bilayers as a way to incorporate membrane proteins into a model system. Until the time of their work researchers had used systems composed of a lipid monolayer supported by a previously alkylated substrate. The totally lipid-based system provided the authors with a more accurate mimetic system. Tamm and McConnell used an epifluorescence microscope to investigate many of the physical properties of lipid bilayers – such as phase transitions and diffusion rates. Fluorescence recovery after photo bleaching (FRAP) was used to measure the diffusion rates of DOPC and DPPC. The authors discovered several intriguing behaviours, most notably the formation of microtubules in the DPPC systems when the system was heated into the liquid crystalline phase and the formation of voids when the DOPC system was cooled into the gel phase. They also noted subtle interactions between the silicon oxide substrate and the supported bilayer, particularly within the transition temperature region. Although McConnell *et al.* chiefly used the Langmuir-Blodgett/Schaefer technique for preparing their SLBs they also used the method of vesicle fusion.

As far as I am aware the first direct investigation into the dynamics of SLB formation from lipid suspensions was that of Nollert *et al.*[44] who used fluorescence measurements to understand the adsorption behaviour of vesicles composed of POPC and lipids extracted from *E. coli*. Their motivation stemmed from previous work aimed at developing a biosensor,[45] where they found that a permeation barrier sometimes existed of thickness greater than the expected 0.2 nm thick water layer between support and SLB; these results indicated the presence of un-ruptured vesicles on the support. The authors observed that in sodium phosphate buffer (40 mM pH 7.4) POPC formed SLBs, whereas the *E. coli* lipid system did not, instead forming supported vesicular layers (SVLs). They also found that the total quantity of POPC adsorbed was independent of salt concentration

whereas for the *E. coli* system the amount adsorbed increased with increasing salt concentration and that the *E. coli* lipid vesicles fused somewhat when the concentration of Na^+ in solution was increased from 40 mM to 100 mM (29% of vesicles fusing) and even more so when 20 mM Ca^{2+} was added after initial incubation in HEPES buffer (100% of vesicles fusing). These results showed that the additional salts had not only a screening effect, but also an ion specific interaction that facilitated vesicle rupture. This last fact is particularly relevant to my work on POPE systems as *E. coli* membranes contain 65% PE.

Nollert *et al.* used impedance spectroscopy to scrutinise a selection of SLB preparation techniques.[44] As part of this work they looked at 1,2-dimyristoyl-*sn*-glycero-3-phosphatidylcholine (DMPC)/ 1,2-dimyristoyl-*sn*-glycero-3-phosphothioethanol (DMPTE) vesicle fusion on gold ([1 mg/ml]), they found that SLB formation took 6 hours in 10 mM Bis-Tris buffer at pH 5.5 at 50°C and that the layer was stable for 2-4 days.

Keller and Kasemo were the first to apply quartz crystal microbalance microscopy with dissipation monitoring (QCM-D) to the study of SLB formation kinetics in 1998.[46] QCM-D utilises a coated quartz crystal oscillating at a specific resonant frequency. When lipid vesicles adsorb onto the crystal the resonant frequency changes. The dissipation factor D is defined as the loss of energy per oscillation period divided by the total energy in the system; it is primarily a measure of the viscous properties of the system. These two parameters can be used to investigate the adsorption kinetics of lipid vesicles in considerable detail offering mechanistic insight. The frequency shift tells one about the total mass of material at the interface including trapped water and the dissipation factor tells one about changes in the viscoelastic properties of the layer; in this context the rupture of the vesicles. The authors examined the formation kinetics for small unilamellar vesicles ($\approx$ 25 nm diameter) of egg-PC in 10 mM tris buffer pH 8 + 100 mM Na^+ onto alkanethiol SAM-coated crystals, SiO_2 crystals and gold coated crystals (figure 3.1). They prepared their vesicles by probe sonication and centrifugation, a small quantity of Texas Red dye was included to measure the concentration of the resulting vesicles suspensions. The authors found a marked difference of the behaviour on the SAM, gold and silica: on the SAM the vesicles adsorbed and ruptured concomitantly, on the gold they adsorbed and did not rupture, and on silicon oxide they adsorbed and stayed intact until a certain coverage had been reached and then began to rupture, eventually forming a complete SLB.

Cremer and Boxer, using fluorescence microscopy, investigated the role of ionic strength and pH in determining the ability of SUV suspensions to adsorb and rupture on glass surfaces (coverslips).[47] SUVs of different net charge were prepared by the probe sonication method in sodium phosphate buffer between 0 and 80 mM and pH 2.5 and 12.3. To obtain the net charge on the lipids the bulk lipid was egg-PC but small fractions of appropriately charged fluorescently modified lipids were used (anionic N-(Texas Red sulfonyl)-1,2-dihexadeconoyl-*sn*-glycero-3-phosphoethanolamine, triethylammonium salt [Texas Red DHPE], neutral 2,2-(*N*-(7-nitrobenz-2-oxa-1,3-diazol-4-yl)amino)-23,24-bisnor-5-cholen-3β-ol [NBD cholesterol] and cationic 4-(4-(didecylamino)styryl)-*N*-methylpyridinium iodide [D291]. They found that for anionic lipid vesicles, fusion was favourable at high ionic strength and low pH. In addition they ascertained that zwitterionic and cationic lipids would fuse under any of the conditions explored. The authors state that this is likely as van der Waals and electrostatic interactions determine the outcome of the interaction with the support. The authors specifically avoided the use of tris buffers explaining that they did so to avoid the influence of trace Mg^{2+} and Ca^{2+} impurities. They stated that 1 ppm of Ca^{2+} severely shifted the fusion regime of anionic vesicles, moving it to higher pH and lower ionic strength. For this reason in my work, ultra-pure tris was used.

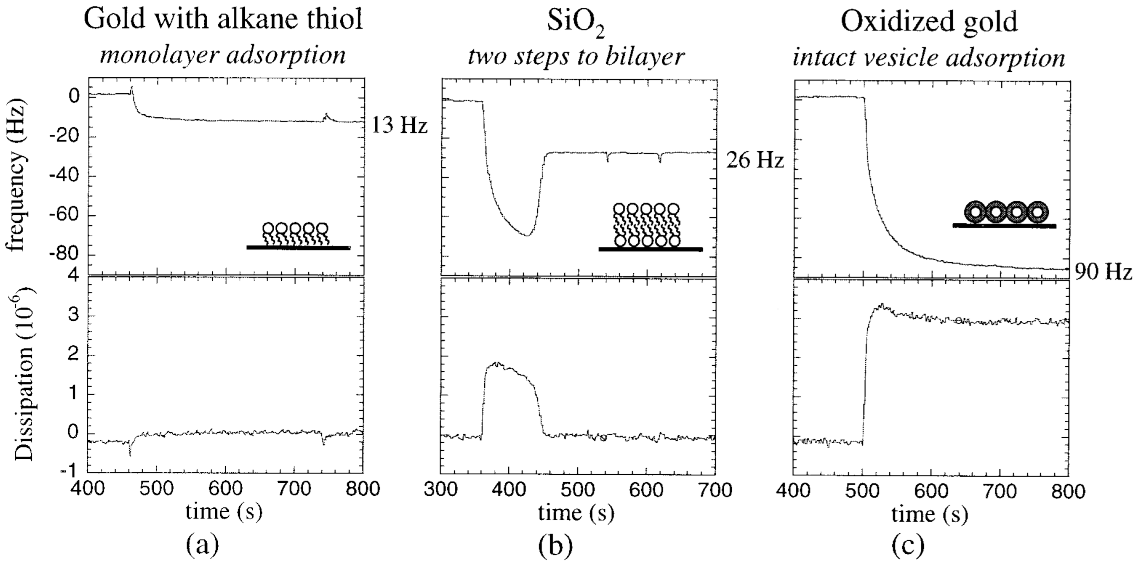

Figure 3.1: QCM-D frequency and dissipation shifts for POPC vesicle adsorption onto (a) gold with alkane thiol SAM, (b) SiO_2 (c) oxidised gold. 10 mM tris + 100 mM NaCl, 21.8°C. Reprinted from Keller *et al.*[46] with permission from Elsevier.

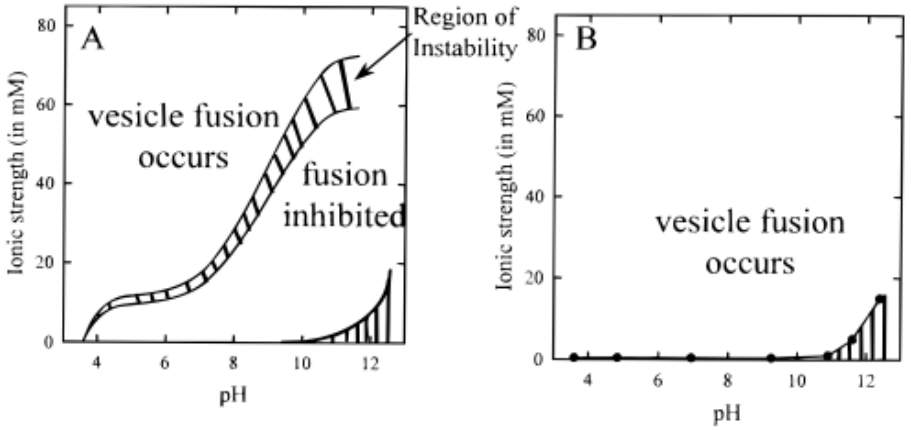

Figure 3.2: Phase diagrams for SLB formation from Egg-PC vesicles in sodium phosphate buffer of varying ionic strength and pH. (A) 1 mol % of anionic Texas Red DHPE. (B) 1% of the cationic D291. Shaded areas represent regions of phase instability. Vertical shaded regions indicate regions where buffer preparation is impossible. Reprinted with permission from Cremer *et al.*[47] Copyright 1999 American Chemical Society.

Egawa and Furusawa investigated the formation of lipid bilayers from bovine-PE and egg-PC on mica supports using atomic force microscopy.[48] Part of their work focussed on measuring the ζ-potentials of the vesicles prepared in various group I and II salt solutions; this area of their work will be discussed later in a review section on cation binding to lipid aggregates. For now I will stick to a description of their methodology, AFM data and conclusions. All lipid suspensions were prepared in purified distilled/deionized water containing the salts of interest. The authors prepared their PC vesicles by extrusion through 200 nm polycarbonate membranes. PE vesicles were prepared by sonication, but they found that the resulting suspensions were non-uniform and decided to use filtration to remove the larger aggregates and dialysis to remove the smallest. Using DLS they found their PC vesicles to have an average size of 200 nm with a monodispersity of 1.05

(their definition of this parameter is unclear from the text as they do not define variables, giving $[D_w/D_n]$). They found their PE vesicles to have a size of 100 nm with a monodispersity index of 1.30 (N.B. the authors are unclear as to whether this is a diameter or radius, although one assumes it is a diameter owing to the 200-nm pore size of their filter). For egg-PC vesicles in 20 mM Mg^{2+} on mica, after a 60 minute incubation period, even at low lipid concentrations (0.0003 mg/ml) the vesicles ruptured spontaneously to form bilayer patches. AFM images acquired over 240 minutes showed the full SLB formation process. In the first 30 minutes, vesicles and intermediate structures were present on the surface and during the remaining time a complete SLB was formed. The authors found that increasing the Mg^{2+} concentration or the concentration of POPC vesicles led to an increase in the rate of formation and a higher SLB coverage. These resulting from the reduced electrostatic repulsion between the net anionic PC vesicles and the negatively charged mica surface and also the increased collision rate of vesicles resulting from the increased bulk concentration. The authors found that PE vesicles aggregated readily, and suggest that this stems from the reduced hydration repulsion between PE aggregates in comparison to that between PC vesicles. When PE vesicles adsorbed on mica, the authors found that the PE vesicles formed hierarchical structures; some PE vesicles adhered to a preexisting patches of SLB whereas others were trapped within SLB patches. Secondary rupture events of the SLB supported vesicles appears to have taken some time, suggesting a reduced interaction between the PE SLB and the second layer vesicles than between the initial PE vesicles and the mica surface. The authors examined the formation of SLBs with PE+PC mixtures and found that the greater the proportion of PE the more negative the ζ-potential. They observed that increasing the PE content led to a greater degree of double bilayer formation, i.e. as more PE was added the coverage of a second bilayer upon the surface increased.

Reviakine and Brisson have also used AFM to study the formation of lipid bilayers on mica and SiO_2 substrates.[49] They looked at how solution conditions affected the formation of bilayers and specifically at the effect of the Ca^{2+} cation. They also critically examined the effect of vesicle preparation procedure, either probe sonication or extrusion. Utilising cholera toxin sub unit CTB_5 as a contrast enhancer and system perturbing probe, they were able to distinguish adsorbed vesicles of different sizes from bilayer disks formed from the rupture of vesicles on the surface; CTB_5 adsorbs to bare mica but not into lipid bilayers unless they contain GM_1, it also displaces adsorbed vesicles but not bilayer patches. Owing to the vast number of systems studied I have summarised their results in table 3.1. The buffer solutions used for the formation and rinsing are given below. (1) 2 mM EDTA, 10 mM HEPES, pH 7.4; (2) 40 mM NaCL, 2 mM EDTA, 10 mM HEPES, pH 7.4; (3) 20 mM NaCL; (4) 2 mM $CaCl_2$, 150 mM NaCl, 10 mM HEPES, 3 mM NaN_2, pH 7.4; (5) 2 mM EDTA, 150 mM NaCl, 10 mM HEPES, 3 mM NaN_2, pH 7.4; (6) 2 mM $CaCl_2$, 40 mM NaCl, 10 mM HEPES, pH 7.4.

substrate	vesicles	lipid species	sol_n	rinse	structure
mica	SUVs	Egg-PC or DOPC	1,2 or 3	1, 2, 3	no fusion, SVL
		Egg-PC or DOPC	1, 2, 4	4 or 6	fusion, SLB
		Egg-PC or DOPC	4	all	fusion, SLB
		1 mg/ml Egg-PC	5	5	defective SLB
		DOPC + GM_1	4	all	fusion, SLB
		DOPC + DOPS	4	all	fusion, SLB
	EUVs (30/50 nm)	< 3 mg/ml Egg-PC	4	4	vesicles, no SLB
		0.001-0.1 mg/ml Egg-PC	4	4	vesicles, disks, defective SLB
	EUVs (100 nm)	0.006 mg/ml Egg-PC	4	4	disks, vesicles
		0.06 mg/ml Egg-PC	5	5	vesicles, disks
	EUVs (200 nm)	1.5 mg/ml Egg-PC	4	4	SLB
SiO_2	SUVs	Egg-PC	1	1	fusion, SLB

Table 3.1: A table showing a summary of the experimental results of Reviakine and Brisson.[49] Lipid suspensions prepared at 0.5 mg/ml unless otherwise stated. EUVs are extruded unilamellar vesicles.

The authors explained their results in terms of theory developed by Seifert and Lipowsky.[50,51] Seifert and Lipowsky have stated that the adsorption of a vesicle to an attractive flat substrate is determined by the balance between the interaction potential with the wall and the bending energy gained by the vesicle owing to its deformation after it has adsorbed. The former can be expressed as

$$F_a = -WA^* \tag{3.1}$$

where F_a is the binding energy, A^* is the contact area and W is the contact potential. The bending energy is given by

$$F_b = \frac{1}{2}k_c \int (c_1 + c_2)^2 \, \mathrm{d}A \tag{3.2}$$

where k_c is the bending rigidity of the bilayer, where c_1 and c_2 are the principal curvatures and A is the surface area of the vesicle. F_b depends on k_c but not vesicle size, F_a depends on vesicle size. This implies that there is a critical vesicle size R_a where $F_a \geq F_b$, given by

$$R_a = \left(\frac{2k_c}{W}\right)^{1/2} \tag{3.3}$$

above which vesicle adsorption will occur. An adsorbed vesicle may rupture if the free energy of the vesicle is greater than that of the associated bilayer disk after rupture. We can express the free energy of the adsorbed and flattened vesicle as

$$F_{bv} = -2\pi W R^2 + 2\pi g(2k_c W)^{1/2} R \tag{3.4}$$

where g is a numerical constant and R is the radius of the vesicle. The free energy of the associated ruptured disk is given by

$$F_{bd} = -4\pi W R^2 + 4\pi \Sigma R \tag{3.5}$$

where Σ is the line tension of the bilayer disk. As $F_{bd} \leq F_{bv}$ for a vesicle to rupture we can define a critical radius for vesicle rupture as

$$R_{rup} = \frac{2\Sigma - g(2k_c W)^{1/2}}{W} \tag{3.6}$$

Evidently for vesicles of size greater than R_a but smaller than R_{rup} will remain stable unless there is some mechanism by which they can fuse on the surface to form a vesicle of size greater than R_{rup}. Seifert and Lipowsky gave the following expression for the change in free energy associated with the fusion of two vesicles on the surface

$$\Delta F_{bv} = constant \times (k_c W)^{1/2} R + 4\pi \bar{k}_c \tag{3.7}$$

where $\bar{k}_c$ is the bending energy associated with the Gaussian curvature of the bilayer.

In their work Reviakine and Brisson found that vesicles of all sizes adsorb onto the mica substrates contrary to the theory of Seifert and Lipowsky which states that only vesicles above a critical size adsorb. They also observed that vesicles ruptured above R_{rup} in accordance with the theory. They found that extruded vesicles (EUVs 30-50nm diameter) remained intact upon the mica surface and did not fuse unless Ca^{2+} was present; they found that sonicated vesicles always adsorbed and ruptured to form SLBs regardless of the presence of Ca^{2+}, but that a higher concentration of lipid vesicles was required in the absence of Ca^{2+}; they assert that their observations compare favourably with those of Keller and Kasemo.[46] However, the authors attribute the differences in EUV and SUV behaviour to differing bending modulii of vesicles prepared by the two procedures. The preparation method should not affect the fundamental bending modulus of unilamellar vesicles of a given size – bending modulus is independent of vesicle size. It is more likely that there was a difference in size or lamellarity of the vesicles prepared in the two methods which was not accurately measured by the authors; their paper does not contain extensive control data on the size distributions of the vesicles used. Understanding the composition of lipid suspensions is critical to a detailed understanding of SLB formation kinetics by vesicle fusion. Generic terms like SUV and EUV are simply too vague and uninformative; in fact few authors in any of the studies on SLB formation from vesicles include detailed vesicle size distributions – not even in their supplementary data. Lastly the authors state that the variance in behaviour after the addition of Ca^{2+} is due to its effect on fundamental bilayer properties.

Leonenko *et al.* used magnetic alternating current mode atomic force microscopy (MAC-AFM) to study the formation of DOPC SLBs on mica and on mica modified with 3-aminopropyl-triethoxy-silane (APTES).[52] They prepared their vesicles in 100 mM acetate buffer at pH 6.5 and at a lipid concentration of 2.0 mg/ml by bath sonication diluting them prior to measurement (0.1 or 02. mg/ml). They provided DLS and AFM data for the size distributions of the vesicles obtained: the pure DOPC vesicles were found to have a mean diameter of 22 nm by AFM and 30 nm by DLS. The authors observed three stages of bilayer development: in the first, the images showed disc-like features which they associated with semi-fused vesicle patches; second, they observed a partially covered surface and third a complete SLB. They found that for the relatively short time periods left for adsorption to take place (no more than 5 minutes) the pure DOPC systems on the unmodified mica rarely showed signs of fusing. They saw fusion on the modified surface most of the time. These last two observations could be a result of the slightly negative ζ-potential of zwitterionic lipids in solutions containing no added salt or the short exposure times. I will discuss the effects of salt binding on vesicles in the following section. The authors estimated that only a small fraction of the vesicles reaching the surface were adhering. They also note differences in their observations in comparison to those in the aforementioned work by Reviakine and Brisson. Those authors noted the presence of vesicles as well as discs in the fusion process, whereas the current authors did not; they assert that the difference is due to Reviakine and Brisson using buffer to rinse the system in order to arrest it mid formation and their use of pure water for the same purpose.

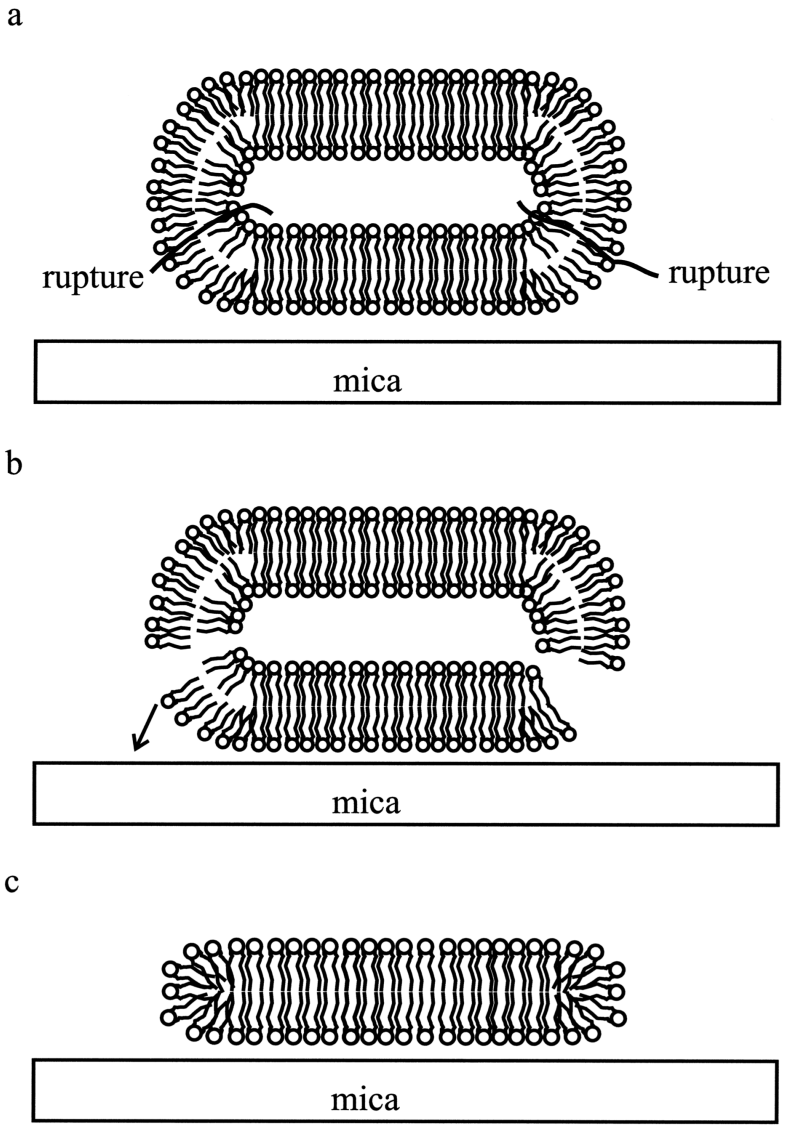

Figure 3.3: A schematic showing the steps in vesicle rupture leading to intermediary disk formation as suggested by Leonenoko *et al.*[52] with permission from Elsevier.

It is worth digressing from my discourse on the formation studies to examine the work done on cations and specifically Ca^{2+} interacting with lipid bilayers. Most of the older work (30 years plus) investigating the interaction of cations with SLBs concerned anionic lipids such as the phosphotidylserines, partly due to their biological significance in cell signalling and membrane protein activation but primarily due to the fact that the interactions of cations with lipid bilayers comprised of zwitterionic lipids are comparatively weak and thus harder to measure. In the older work on anionic lipids it was found that the binding constants for alkali cations followed the Hofmeister series originally proposed in 1888 and thus binding depended on the size of the cations studied. More recently, enhanced computational power and also more modern experimental methodologies have enabled workers to investigate the weaker interactions with zwitterionic lipids in detail. As most SLBs prepared for biomimetic studies contain primarily zwitterionic lipid, these studies are particularly relevant – the substrates used for SLB formation are mostly anionic and therefore preclude pure anionic lipid as a primary model constituent. My main interest in lipid-cation inter-

actions stems from the fact that monovalent cations have been shown to affect the bending rigidity of lipid bilayers,[53] which is a pivotal parameter in the theory developed by Seifert and Lipowsky hitherto described. A brief review of the relevant literature ensues.

Cunningham *et al.* investigated the influence of monovalent cationic species on PC bilayer structure and packing using X-ray diffraction and differential scanning calorimetry (DSC).[54] They found that the X-ray data did not provide any evidence that monovalent cations affected the packing of the lipid bilayers investigated. However, their DSC data highlighted the fact that cations in general and Li^+ in particular bind to DPPC lipid bilayers.

As I discussed earlier, Egawa and Furusawa investigated PE and PC SLB formation on mica with AFM.[48] As part of their study they conducted ζ-potential measurements on the egg-PC and bovine-PE containing vesicles they prepared in various salt solutions. They found that both the PC and PE vesicles prepared had negative zeta potentials in pure water, and that upon the addition of salt the potential became less negative or slightly positive in Mg^{2+} and Na^+ and took on a significant positive charge in La^{3+}.

Böckmann *et al.* investigated the influence of NaCl on POPC bilayers by fluorescence correlation spectroscopy (FCS) and molecular dynamics (MD) simulations using the Gromacs forcefield.[55] Atomic-scale MD simulations of ion bilayer interactions have been challenging owing to the long time-scales involved with the binding process, therefore only recently have such simulations been carried out. The authors found that increasing the concentration of NaCl reduced the diffusion coefficient of POPC lipids within the lipid bilayer. The diffusion coefficient the authors calculated in their simulations over 100 ns agree with those measured experimentally on a 1 ms timesecale indicating that the length scales of their simulations where adequate to model the behaviour of the POPC bilayer system. Their simulations showed that the Na^+ ions bound tightly to the lipid carbonyl oxygens. They also found that the bilayer thickness increased by $\approx$2 Å upon binding and that the order parameter of the lipid acyl chains increased too.

Garcia-Manyes *et al.* studied the interaction of NaCl with a variety of SLBs comprised of different lipids (DMPC, DLPC, DPPC, POPE and *E coli* lipid extract) with AFM and associated force "spectroscopy".[56] They authors found that increasing the concentration of NaCl for the systems studied increased the yield threshold force for punching the probe tip through the SLB. They found that the elastic deformation region of their force plots was extended with increasing NaCl concentration and speculated that this may be the result of the increased packing density of the phospholipid network. They examined the kinetics of ion binding and unbinding by replacing the solution in contact with the layer with the opposite respectively whilst constantly acquiring force plots. They found that the time taken for the force plot to become constant in each case was $\approx$10 min.

Cordomí *et al* conducted a molecular dynamics study of the interaction of several cation chlorides, including Ca^{2+}, with simulated DPPC bilayers.[57] They found that the cations preferentially bind to the phosphate and carbonyl headgroup oxygens whereas the Cl^- anions are located further out in the aqueous phase. They also found that ion binding affected the lipid order, the area per molecule, the exact orientation of the headgroup dipole and the overall charge distribution of the system and thus the electrostatic potential across the headgroup region. The changes in the structure of the simulated bilayer are at odds with the earlier work by Cunningham *et al.* The effects observed were specific to the cation chosen and thus must depend on the radius and charge of each cation as well as their coordination properties. Interestingly, they found that K^+ did not bind to the DPPC layers simulated; this, if real, would offer a way to increase the ionic strength of a solution surrounding an SLB whilst having a minimal effect on its physical properties. The calculated ion distributions show that the maxima of the chloride and cation distributions are

separated by between 0.7 and 1.2 nm for the disparate cation systems, this distribution effectively generates a dipole moment that opposes that intrinsic to the DPPC headgroup. The authors end with a proviso about the effects of using different force fields and how these can affect the results of their simulations (they used the Gromacs force-field). They stated that experimental work needs to be carried out in order to critically evaluate the exact choice of force field for simulations of this type.

In earlier MD simulations, Gurtovenko and Vattulainen examined the interaction of the monovalent salts NaCl and KCl with both POPE and POPC membranes with multiple force-fields.[58] In accordance with the later work of Cordomí *et al.*[57] the authors found that the cations primarily occupy the region close to the carbonyl oxygens and that the interaction of the monovalent cations with PC was far greater than with PE; this they explained by the fact that PE unlike PC can form inter- and intramolecular hydrogen bonds and thus it nominally forms a closer packed lipid bilayer. They found that Na^+ showed a greater affinity to the bilayers than K^+, which they rationalised on the basis of the size of the cations. Interestingly, they examined the effects of different force fields on the simulation results to extract information on the force-field sensitivity. They critically examined the results for both the Gromacs and Charmm force-fields. They found that using Gromacs K^+ did not bind to the lipids at all and suggested that this is due to the overestimated size of K^+ when using the Gromacs force field (diameter 0.64541 nm as opposed to 0.31426 nm in Charmm). They discussed how their results would be applicable *in vivo* by postulating that POPE bilayers are analogous to inner membrane leaflets and POPC to outer leaflets.

To the best of my knowledge the first experimental study comparing the binding strengths of alkali metal chlorides (LiCl, NaCl, KCl RbCl, CsCl) to POPC membranes was by Klasczyk *et al.*[59] They used highly sensitive isothermal titration calorimetry (ITC) along with zeta potential (ZP), differential scanning calorimetry (DSC) and dynamic light scattering (DLS) to investigate the binding properties. ITC provided the authors with thermodynamic information on the strength and stoicheometry of the ion binding, the zeta potential measurements provided information about the ion concentration close to the membranes. They prepared their vesicles by extrusion in 15 mM HEPES at pH 7.0, adjusting the pH of their buffer with KOH. They state that the final concentration of K^+ from this source was $\approx$ 2 mM in the final vesicle suspensions. They give the average radius of their vesicles as 56.1 nm $\pm$ 2.4 nm. They varied the salt concentration from 10 mM to 500 mM but in its absence they found that the POPC vesicles had a slightly negative zeta potential, even though the PC headgroup is zwitterionic at neutral pH. This negative zeta-potential has been interpreted by several other groups in terms of hydration ordering, the orientation of the headgroups in the hydrated bilayers, water polarisation effects and impurities in the lipid sample. As the electrolyte concentration was increased for all the cation systems, the net charge on the vesicles increased, becoming more positive. The vesicles became saturated between 50 and 150 mM salt concentration with the saturation concentration depending on the ion used – lithium bound to the bilayers with the greatest affinity. The degree of binding affinity followed the Hofmeister series, $\zeta(\mathrm{Li}) > \zeta(\mathrm{Na}) > \zeta(\mathrm{K}) \approx \zeta(\mathrm{Rb}) \approx \zeta(\mathrm{Cs})$. The thermodynamic data acquired by ITC are summarised in table 3.2; they show that the binding process is endothermic and hence is driven entropically. The authors assumed that the increase in entropy was a result of the expulsion of water molecules from the headgroup region during ion binding. Using this assumption and the equipartition theorem they were able to estimate the number of water molecules being removed to be between 2 and 4 molecules with the specific number increasing with cation size and thus with the Hofmeister series.

cation	apparent binding constant, K l/mol	molar enthalpy, ΔH kcal/mol	Gibbs free energy ΔG kcal/mol	entropic contribution, $T\Delta S$ kcal/mol
Li^+	1.37±0.06	2.39±0.09	-2.58±0.03	4.97±0.09
Na^+	1.25±0.05	2.33±0.09	-2.53±0.02	4.86±0.09
K^+	1.17±0.13	2.13±0.23	-2.49±0.07	4.62±0.24
Rb^+	1.14±0.28	1.75±0.40	-2.47±0.15	4.22±0.43
Cs^+	1.10±0.14	1.67±0.19	-2.45±0.08	4.12±0.20

Table 3.2: A table summarising the thermodynamic data acquired in Klasczyk *et al.*[59]

I shall now return to my discussion of the work on SLB formation by vesicle fusion. Zhadanov *et al.* simulated SLB formation by vesicle fusion in an attempt to explain their QCM-D and SPR observations.[60] They modelled the kinetic process using a hybrid monte-carlo (MC) method where the diffusion of vesicles to the surface in their flow cell was treated by mean field theory (MF), but the actual surface bound kinetics were given an explicit MC analysis. Their simulations take into account the interactions between neighbouring vesicles and bilayer patches as well as allowing patches to coalesce and vesicles to diffuse on the surface. They attained qualitative agreement with their experimental data if their simulation included the possibility of vesicle rupture being induced by existing bilayer patches and incoming additional vesicles. They found experimentally that the rate of vesicle rupture and bilayer formation increased with time until SLB completion. If the interplay between existing vesicles, new vesicles and existing patches was not included in the model, this feature of the experimental data sets could not be realised in their simulations.

In a letter Zhadanov and Kasemo described a theory developed to predict the rate constant of vesicle decomposition from fracture theory as applied to vesicle rupture mechanics.[61] They state that although the thermodynamic criteria (see the work of Seifert and Lipowsky above) for vesicle rupture may be met, it may not actually occur owing to kinetic constraints. They go on to describe that on an abstract level the kinetic problem is related to that of materials under external tensile stress and that, although rupture may be thermodynamically favourable, it will only take place if the stress on the vesicle is large as the Griffith condition for "crack" growth. In the vein of Griffith, the authors argued that the formation of a small rupture void in the vesicle goes alongside a decrease in energy due to the relaxation of the external stress and also a concomitant increase in the energy due to the increase in SLB footprint on the support.

Reimhult *et al.* have investigated egg-PC and POPC adsorption onto a variety of substrates using QCM-D in an effort to understand the mechanism of SLB formation from vesicles in solution.[62] They examined effects of substrate, temperature, vesicle size and osmotic stress. The smallest vesicles were prepared by probe sonication and ultra-centrifugation with only the smallest fraction of vesicles reserved. Larger vesicles were prepared by extrusion using membranes of the required sizes. For all measurements except those investigating the effects of osmotic stress, 10 mM tris buffer pH 7.4 with 100 mM NaCL was used. On silica (SiO_2) and silicon nitride (SiN_3) vesicles adsorbed intact until a certain critical coverage, whereupon they began to rupture, eventually leading to complete SLBs. However, on oxidised platinum and titania (TiO_2) surfaces, the vesicles adsorbed intact, never rupturing. Increasing the temperature reduced the apparent critical coverage of vesicles required for bilayer formation. They also observed that SLB formation from adsorbed vesicles can be arrested by reducing the temperature. Increasing the osmotic stress on

the vesicles facilitated faster formation kinetics on the silicon nitride and silica, but did not change the fact of intact vesicle adsorption on the platinum and titania surfaces. The overall features of bilayer formation appear to be unrelated to vesicle size. Complete bilayer formation was never observed; there were always some residual trapped vesicles in the range of 1-2% of surface coverage.

Most studies hitherto carried out on SLB formation by vesicle fusion have been average in nature; the data acquired are of an ensemble. In an effort to gain specific local mechanistic information about the kinetic processes taking place Chu, Boxer and coworkers have used wide-field fluorescence microscopy with total internal reflection excitation.[63] In their study, the vesicle bilayers were labelled with a small quantity of Texas Red dye, and internally contained carboxyfluorescein dye. A small number of these labelled vesicles were then allowed to settle onto a quartz substrate. Subsequently unlabelled vesicles were flowed into the system. Their idea was to use the change in the Texas Red signal to ascertain when the vesicles had either fused with other vesicles on the surface or with an existing SLB patch, and to use the CF signal to discover when the vesicles actually ruptured not simply fused with their nearest neighbours. The authors found that they could distinguish all of the features of the adsorption, rupture and fusion processes. They did ample control experiments to ensure at the concentrations used the dyes were not altering the essential behaviour of the system. For example, in one such control they increased the concentration of texas red from 0.5% to 6% and found that at the higher concentration the vesicles spontaneously ruptured on the surface whereas at the lower concentration a great number were stable to spontaneous rupture until either they encountered a number of other nearby vesicles and fused or encountered a bilayer patch. All their studies were carried out with egg-PC as the primary lipid constituent. They prepared their vesicles in 10 mM tris buffer pH 8.0 with 100 mM NaCl by extrusion, using polycarbonate membranes of 30, 50 and 100 nm diameter. The proportion of labelled vesicles undergoing the different kinds of processes was distinguished from their fluorescence traces. A summary of their data is shown in table 3.3. Notable, and not included in the table, were the 50 % of vesicles that leaked CF dye prior to observation. From complementary AFM they deduced that this was largely a result of partial pre-rupture (pore formation), rather than isolated pre-rupture, although some isolated rupture does occur as evidenced by data acquired during observation. Finally they were able to estimate gross formation rates for complete SLB formation and found that the rate of formation was proportional to vesicle concentration.

	30-nm vesicles	50 nm vesicles	100 nm vesicles
No of vesicles in sample	17	37	40
Primary fusion	41%	32%	37.5%
Simultaneous fusion and rupture	53%	49%	55%
Isolated rupture	6 %	19 %	7.5%

Table 3.3: Percentages of the different SLB formation processes taking place at the interface in the work of Johnson *et al.*[63] Data do not include vesicles that ruptured prior to the initiation of observation.

Brisson and coworkers have conducted further experiments on SLB formation kinetics with AFM and QCM-D.[64] They aimed to combine the specific local information provided by AFM with the averaged high temporal-resolution-information offered by QCM-D. They looked at the effects of lipid composition, overall charge and Ca^{2+} on the formation behaviour. The lipids chosen were DOPC, DOPS and DOTAB. They found that the charge and composition of the vesicles had a significant effect on the formation behaviour, for example mixed lipid vesicles containing a 1:1 ratio

of DOPC and DOPS formed an SVL in buffer without Ca^{2+} but formed an SLB when 2 mM Ca^{2+} was included in the buffer. Their results somewhat support the theory and prior experimental work carried out. They observed the same general behaviour as Kasemo and coworkers with regard to the critical coverage of vesicles and the initial build-up of vesicles followed by rupture for systems comprised predominantly of PC. However, they also found that DOTAB vesicles ruptured spontaneously on the SiO_2 substrates used and neighbouring vesicles were not required to induce rupture – thereby finding another pathway for SLB formation on SiO_2 substrates. They observed small trapped particles within DOTAB SLBs at the end of the formation and found them to be of the same dimensions of vesicles. They claim that these are contaminant particles as they were unable to use the AFM tip to induce rupture. However, this conclusion could be incorrect: in their simulations, Zhadanov *et al.* found that there were always some trapped vesicles at the end of the formation as a result of steric barriers to rupture, "where would the lipid material go?". I think that the "contaminants" observed by Brisson and coworkers were in fact vesicles and they underestimated the barrier to rupture by mistakenly believing that their tip could rupture any trapped vesicle regardless of steric considerations. In fact they often used their tip to induce the rupture of vesicles on the surface in order to probe the system and explore its resulting behaviour. They state that accidental rupture by the tip is a rare phenomenon but they provide no evidence for this claim. During the course of their studies on the DOPC and the primarily DOPC systems, they found no evidence of vesicle/vesicle fusion on the surface, as predicted by Seifert and Lipowsky, for vesicles below a certain size. Despite discussing the effects of surface charge, they never reference the fact that the zwitterionic lipids have a slightly negative zeta potential even at neutral pH in the absence of electrolyte, only briefly mentioning that the ions probably bridge the oxygens between neighbouring lipids (see for example the MD simulation work described earlier). Figure 3.4 shows the different pathways observed by the authors.

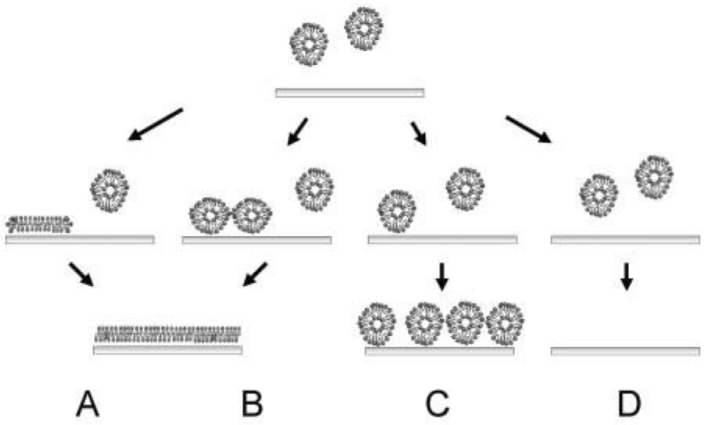

Figure 3.4: A figure showing the possible paths of SLB formation suggested by Brisson and coworkers. Reprinted from Richter *et al.*[64] with permission from Elsevier.

Lastly the authors found that for the systems containing 50% or more POPS the layer restructured in the presence of calcium after the formation of the SLB; this process was evidenced by the slow decrease in frequency and concomitant increase in dissipation. The latter observation suggests that the lipid present at the interface was becoming more flexible during the change in structure. Interestingly the same phenomenon was observed even if the excess lipid was washed away with copious buffer after the initial completion of the SLB.

Reimhult *et al.* have used SPR and QCM-D simultaneously to measure bilayer formation kinetics.[65] In this study they used POPC in 10 mM tris with 100 mM NaCl at pH 8.0. Vesicles were prepared by extrusion through polycarbonate membranes and had a mean diameter of 60 nm. Their experimental system was based around a home-built combined flow cell, with the QCM-D crystal on one side and the SPR surface on the other. They were able to accurately deduce the ratio of SLB to residual vesicles during the formation process by coupling the two datasets in their analysis. There results also highlighted the different water structures associated with the vesicles. It was reasonably expected that water contained within the vesicles contributed to the total adsorbed mass in QCM-D datasets. However, they also found out that water from the hydration shells surrounding the adsorbed vesicles/SLB contributed, as well as that trapped in-between the adsorbed vesicles.

Richter and Brisson have conducted further work on the DOPC, DOTAP and DOPC systems studied earlier.[64] They investigated the adsorption behaviour of the vesicles on mica in contrast to the silica studied earlier.[66] They observed some marked differences in comparison to the earlier work. Firstly for the DOPC:DOPS (4:1) system they found that the vesicles continued to rupture and form bilayer patches regardless of the stage of adsorption evidenced in the QCM-D data. i.e. SLB forms regardless of any critical vesicular coverage. Secondly, they found that the resulting patches of bilayer could move freely on the mica surface and adopted circular shapes to minimise the energetic cost of their edges. On silica, irregular shapes were seen to be stable. However, the authors also observed at a late stage, when rinsing, the bilayer patches took on an irregular shape, and did not form the spherical patches as described above. They also saw QCM-D evidence of structural changes taking place within the layer after the removal of vesicles from the bulk by rinsing: there was a slow increase in the frequency and a decrease in the dissipation. Whilst investigating the effects of charge on the formation behaviour they found that a significantly lower mole fraction of DOPS in a DOPC:DOPS mixture prevented vesicle adsorption to the mica surface, 20% instead of 50% on silica. They also found that in the absence of Ca^{2+}, DOPC adsorbed as vesicles but these did not rupture to form an SLB. These observations suggest that the repulsive electrostatic interaction with the surface is somewhat stronger with mica than silica – mica has a higher surface charge. In addition, in the absence of Ca^{2+}, vesicles containing DOPS never ruptured on the surface; in contrast, SLB formation on silica for adsorbed vesicles containing DOPS was only inhibited above 33%. For the cationic DOTAP, the dissipation values from the QCM-D work were always lower on mica than on silica suggesting more rapid vesicle rupture. Interestingly, they found that after forming a DOPC SVL and rinsing the system with buffer, adding buffer with Ca^{2+} led to the formation of an SLB. The measured dissipation values of DOPC on silica were far lower than on mica suggesting that the vesicles become less flattened on mica. When Ca^{2+} was added SLBs were formed over the entire range of lipid mixtures studies albeit slowly for the most anionic. They discuss the possibility of multiple pathways on the surface as an explanation of the earlier rupture events seen on the underpopulated mica surface for the DOPC:DOPS (4:1) system; some vesicles are strained enough and large enough to rupture spontaneously, whilst others required the build-up of neighbouring vesicles or a bilayer edge to lead to stress capable of inducing rupture. In comparing the adsorption on the two substrates (mica and silica), they argue that the electrostatic forces must dominate despite the difference in non-retarded Hamaker constants for the substrate-vesicle van der Waals interactions ($H = 2 \times 10^{-20}$ J and 0.8×10^{-20} respectively), and that this explains the salient features of Ca^{2+} for SLB formation even for vesicles with a high anionic lipid component. N.B. by this point the authors had come across the paper on the small negative ζ-potential of zwitterionic lipids, *vide* Egawa and Furusawa, although they do not recognise its effect of increasing the bending modulus of the lipid bilayers. Instead they spend time

suggesting how negative charge may lead to mica-PS complexes or alter the expected asymmetric distribution of lipids within the adsorbed mixed lipid vesicles in a time-dependent fashion (slow flip flop kinetics) and thus could potentially lead to slow rupture. They briefly mention the possibility of "other" forces moderating the behaviour in a reference to the poorly understood "hydration forces".

Tawa and Morigaki have employed SPR and surface plasmon fluorescence microscopy to study SLB formation on both gold-SAM substrates and silica substrates.[67] They used egg-PC and prepared their vesicles by extrusion through 50 nm pore size membranes. Vesicles were prepared in 10 mM phosphate buffer at pH 6.6 with 150 mM NaCl added. SPR was used to calculate the thickness of the SLBs and the fluorescence intensity to distinguish between adsorbed vesicles and SLB, (the vesicles show a much greater fluorescence intensity). Their values compared well with bilayer thicknesses measured by AFM and NR in other studies for the vesicles prepared on silica, ($\approx$ 4 nm). They used their apparatus to conduct FRAP measurements to find the lateral diffusion coefficient of lipid molecules in the systems studied. They compared their technique extremely favourably with others such as AFM and QCM-D to justify its use.

Seantier and coworkers have investigated the formation kinetics of DMPC and DPPC vesicles and mixtures thereof on silica as a function of pH, temperature, lipid composition, lipid concentration and buffer composition.[68] They found that the choice of buffer, either 20mM HEPES or 10 mM tris, seemed to alter the quantative kinetics of the SLB formation process although not changing the overall qualitative nature of the adsorption. The authors observed that pH had a marked influence on SLB formation kinetics: increasing the pH to 12 precluded SLB formation, while lowering the pH < 6 changed the kinetics to a path of spontaneous rupture rather than one where a critical coverage of vesicles was necessary. In all systems studied, increasing the concentration of vesicles increased the rate of SLB formation and increasing the temperature increased the rate of bilayer formation. This was the first study of high transition temperature lipids (T_m above room temperature) in the literature in terms of SLB formation kinetics, reducing the temperature had a slowing effect on the rate of SLB formation.

Musser and coworkers have investigated the effect of the average phospholipid geometry within vesicles on the formation of SLBs on glass. In this study they prepared vesicles of $\approx$90-180 nm diameter by extrusion through polycarbonate membranes. The vesicles were comprised of various ratios of DOPC, DOPE, DOPE-Me, DOPE-Me_2 and DOPE-TR and were suspended in 50 mM HEPES, 200 mM KCl at pH 8.0. DOPE-TR was added as a fluorescent dye allowing them to image the vesicles on the substrate. The idea was to change to composition of the vesicles with the above lipids in order to set values of the average intrinsic curvature and then to observe the effect on their SLB formation behaviour. As the number of methyl groups on the PE headgroup was reduced from PC to PE, the average intrinsic negative curvature of the lipid mixtures decreased. As the value decreased from DOPC to DOPE, less and less SLB was formed – leaving in the case of pure DOPE an SVL. The authors assert that the only deciding parameter in forming an SLB or SVL is the average intrinsic curvature of the lipid molecules making up the vesicle. This clearly ignores all of the kinetic effects required for vesicle rupture, although it does provide a good indicator of the likelihood of SLB formation.

Israelachvili and coworkers have investigated the formation of DMPC SLBs on silica substrates by vesicle fusion.[69] They used a wide variety of techniques namely surface forces apparatus (SFA), QCM-D, fluorescence recovery after photobleaching (FRAP), fluorescence spectroscopy (FS) and streaming potential measurements (SP). Unlike most of the previous work, which is largely experimental, relying on fact gathering and subsequent discussion in an effort to understand SLB formation by vesicle fusion (with the exception of Seifert and Lipowsky and Zhadanov), Israelachvili

takes a more rigorous approach combining theoretical models of the interactions at the interface with measured quantities, such as the forces between silica and the DMPC bilayer on mica in the SFA. At the same time the authors utilise the QCM-D measurements and fluorescence microscopy images to get a conceptual idea of the processes taking place during the formation process. In his theoretical introduction Israelchvili describes the forces acting at the silica-neutral SLB interface at constant potential, these are the van der Waals interaction and the electrical double layer interaction. For these lipid bilayer systems the van der Waals interaction is approximated by,

$$F_{VDW}(d) = -\frac{H_{123}}{6\pi}\left(\frac{1}{d^3} - \frac{2}{(d+a)^3} + \frac{1}{(d+2a)^3}\right) \tag{3.8}$$

where the Hamaker constant H_{123} is typically (3–4) $\times$ 10^{21} J in concentrated salt solutions, for symmetrical systems this force is always attractive but between different interfaces it can be repulsive too. At small separations where d<<a, it becomes,

$$F_{VDW}(d) = -\frac{H_{123}}{6\pi d^3} \quad \text{N m}^{-2}, \tag{3.9}$$

and the associated energy per unit area is given by,

$$W_{VDW}(d) = -\frac{H_{123}}{12\pi d^2} \quad \text{N m}^{-1}. \tag{3.10}$$

The double-layer interaction is given by the Hogg-Healy-Fuerstenau (HHF) equation,

$$W_{DL}(d) = \frac{\epsilon_0\epsilon\kappa\left[2\psi_1\psi_2 - (\psi_1^2+\psi_2^2)e^{-\kappa d}\right]}{(e^{\kappa d} - e^{-\kappa d})} \quad \text{J m}^{-2}. \tag{3.11}$$

In the the case of a neutral bilayer interacting with a charged substrate where ψ_2 (the bilayer potential)=0 and ψ_1 becomes ψ_0 this simplifies to,

$$W(d) = \frac{-\epsilon_0\epsilon\kappa\psi_0^2 e^{-\kappa d}}{(e^{\kappa d} - e^{-\kappa d})}. \tag{3.12}$$

Therefore the interaction is attractive for all separations where $\psi_2 = 0$; for $\psi \neq 0$ the interaction can be attractive or repulsive at larger distances. He contrasts the double layer interaction at constant potential with that at constant charge where,

$$P(d) = \rho_\infty kT\left[2\left\{1 + \left(\frac{zq(\psi_1+\psi_2)/kT}{e^{\kappa d/2} - e^{-\kappa d/2}}\right)^2\right\}^{\frac{1}{2}} - \frac{\{zq(\psi_1-\psi_2)/kT\}^2 e^{-\kappa d}}{1 + \left(\frac{zq(\psi_1+\psi_2)/kT}{e^{\kappa d/2} - e^{-\kappa d/2}}\right)^2} - 2\right] \quad \text{N m}^{-2}, \tag{3.13}$$

and states that for different interfaces the constant charge interaction is always repulsive.

In his theoretical estimations Israelachvili finds that the contribution due to the double layer interaction at constant potential will far outweigh any of the contributions from the other interactions at the interface and so there is a strong electrostatic interaction between the anionic silica interface and the (assumed) neutral SLB.

Moving on the practical results in the paper, we start start with the SP measurements, these showed a net increase in the negative (silica) potential as the SLB formed at the interface, interestingly, they showed a marked jump after a significant quantity of lipid had been injected into the instrument, suggesting that a critical coverage of vesicles was required for formation. Intriguingly the final surface did not have zero potential as expected for a complete SLB composed of neutral

lipid. I think this is either due to an incomplete layer forming, or that the DMPC lipids have a small negative ζ-potential as measured for other zwitterionic species in earlier work. Surface force measurements, showed that the SLBs prepared by Langmuir Blodgett deposition present different interactions than those prepared by vesicle fusion. This is attributed to the possibility that LB-deposited SLBs are under tension post formation, and that this suppresses undulation forces that would reduce the effective attractive component of the silica-bilayer interaction potential. From the QCM-D measurements the authors observed that increasing the bulk concentration of DMPC vesicles increased the rate of bilayer formation, and that reducing the ionic strength i.e. using distilled water instead of buffer prevents SLB formation; n.b. see earlier comments about the electrostatic interaction and constant potential vs constant charge. According to the authors the reason why the system should interact at constant potential at high ionic strength and constant charge in low (or no) salt are non-trivial. They refer to the cause of constant potential as "charge-regulation" which involves the exchange of surface ions with the bulk ionic reservoir as the silica and DMPC surfaces approach one another; this situation is prevented when there are no or a limited supply of ions available in solution. Unfortunately the theory given by Israelachvili applies only to symmetrical electrolytes such as NaCl, not asymmetrical ones such as the $CaCl_2$ utilised by many groups to enhance the SLB formation of zwitterionic lipids.

Fygenson and coworkers have investigated the effect of bilayer edges on SLB formation kinetics with video fluorescence microscopy.[69] They prepared DMPC vesicles in 10 mM phosphate buffer at pH 7.5 with 140 mM NaCl. Figure 3.5 is a reprint from their paper which shows several stages of the SLB formation process over time. The vesicles are more fluorescent than the SLB patches, they see a marked increase in fluorescence that accelerates as time goes on reaching a peak value, it then decreases and settles at a constant value indicating the formation of the SLB. The last stage is a FRAP measurement to certify that the layer adsorbed is an SLB. The final plateau value of fluorescence was slightly lower after photobleaching owing to trapped vesicles. The authors claim that the increase in fluorescent build-up nearing the peak shown in the figure, comes about as result of an enhanced vesicle affinity for the surface which is a result of favourable vesicle SLB edge interactions after the SLB starts to form. In explanation, there has to be some surface at the interface that is more attractive to vesicles than glass or the majority SLB surface, otherwise they would observe a slowing in the rate of fluorescence increase owing to saturation kinetics. Although the idea that SLB edges catalysing vesicle rupture is not new, previous studies have stated it has a strong impact on the rate of vesicle rupture by increasing strain in vesicular bilayers, it is interesting to see how it can impact the rate of vesicle uptake. The authors state that they observe an excess of vesicles at the interface prior to SLB completion, and that these excess vesicles leave the interface *en masse* as the SLB reaches completion. Controversially the authors re-examine the QCM-D data acquired on silica and on other anionic surfaces previously by other workers. In these data, there is a peak in the frequency shift and dissipation which had been attributed to a critical vesicular coverage necessary for bilayer formation, although this did not appear to be the case on mica. The authors of this paper assert that these changes are actually the build-up and subsequent departure of the excess vesicles.

Ahmed *et al.* have investigated the effect of hydration repulsion on the formation of SLBs by vesicle fusion.[71] Their fundamental premise stems from the idea of ordered water surrounding lipid headgroups in vesicles and substrate surfaces. In order for the bilayer to form, energy must be supplied to remove this ordered water and this leads to a repulsive force that affects the rate of SLB formation. The authors prepared DMPC SUV's by extrusion in 100 mM phosphate buffer at pH with 150 mM NaCl. SLBs were prepared by allowing these SUVs to fuse onto silica nano particles that had been pre-treated (heating and piranha treatment) to control their surface chemistry (the

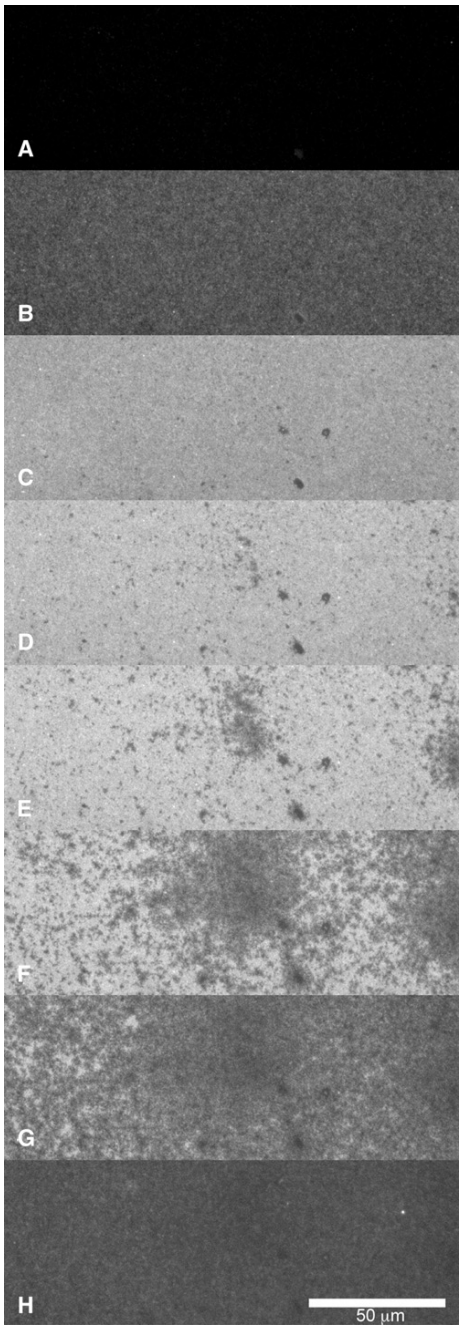

Figure 3.5: Fluorescence images of different stages during DMPC SLB formation on borosilicate glass coverslips. Experiment conducted in 10 mM phosphate buffer at pH 7.5 with 140 mM NaCl. Fluorescent probe molecule was 1,2-dimyristoyl-*sn*-glycero-3-phosphoethanolamine-*N*-(7-*nitro*-21,3-benzoxadiazol-4-yl) (DMPE-NBD). At first the surface is dark indicating the absence of any lipid. As vesicles adsorb the surface brightens. As SLB begins to form dark patches appear, which continue to grow with time until the surface is completely covered with SLB. Reprinted from Weirich *et al.*[70] with permission from Elsevier.

number of surface silanol groups). Thermogravimetric analysis, FTIR spectroscopy, DLS and ζ-potential measurements were all used to characterise the effects of treatment on the silica particles and DLS and ζ-potential measurements were used to characterise the size and surface potential of the extruded SUV's. The actual fusion process was monitored by examining the intensities of the gel-to-liquid-crystal phase transition temperatures on the cooling cycle for SUVs and SLBs by nano-differential scanning calorimetry. These temperatures differed by 2°C and so their relative intensities would show the extent of binding to the nanoparticles. The authors found that reducing the surface silanol density increased the rate of SLB formation, thereby indicating that the surface hydration is an important factor in determining the rate of SLB formation. They made sure to examine the effect of treatment on the silica nano particles ζ-potentials to prove the validity of their results.

Zhu *et al.* have investigated the effect of Ca^{2+} on the formation of DPPC SLBs by vesicle fusion above and below the main phase transition of the lipids. They prepared their vesicles by extrusion in 100 mM tris pH 7.3 with and without added 2 mM Ca^{2+}. They prepared two sizes of vesicles, 105 nm ± 5 nm and 180 nm ± 20 nm. They studied the adsorption behaviour using QCM-D and fluorescence microscopy using 1 mol % of Texas red DHPE as a dye. The authors found that above the main phase transition temperature the qualitative behaviour was similar to that observed earlier on silica – a minimum in the frequency and a maximum in the frequency and dissipation were observed. They interpreted these observations, as in the older studies, in terms of a critical vesicular coverage despite the more recent report by Fygenson and coworkers; in fact they seem to ignore some of the important recent work. Below the main phase transition the authors noted that a complete SLB was never formed although the amount of SLB was enhanced by Ca^{2+}.

Unwin and coworkers have developed evanescent wave cavity ring down spectroscopy as a platform for studying the kinetics of SLB formation.[72] They examined the formation of DOTAP SLB on a quartz surface and found that the optical loss of their cavity changed with time, as vesicles adsorbed and ruptured on the surface forming an SLB. From the combined extinction coefficient they were able to measure the quantity of lipid at the interface giving an area/molecule in agreement with previous work on DOTAP by QCM-D.

Hernandez *et al.* have recently used attenuated total reflection Fourier transform infrared spectroscopy (ATR-FTIR) to probe the formation kinetics of DPPC SLBs on a variety of substrates (Au, Ge and a 1-octadecanethiol SAM).[73] The gold layers were prepared via an oxidation-reduction reaction between the Ge crystal and 1 mM $HAuCl_4$ in a flow cell environment. The gold layers generated were 30 nm thick and had a roughness of 20%. The authors found that their IR spectra were different for the layers formed on the different substrates depending on the amount of lipid at the interface. For instance they could observe the difference between the lipid monolayer that formed on the SAM and the SLB formed on the gold substrate. They were able to follow the SLB formation process by plotting the integrated intensity in the CH region vs time. The different behaviours in these plots for vesicle interaction with the different substrates was clear. In the case of germanium where an SVL formed, there was a monotonic increase in the amount of material at the interface that reached a plateau. However, for the gold and SAM substrates, vesicle fusion was evidenced by a subsequent dip in the integrated intensity following mass vesicle rupture. They also tracked the physical transformation in these systems by utilising order parameters, such as the full width at half maximum and the peak positions of the symmetric and any symmetric stretches. They found that these were essentially constant for Germanium where intact vesicles formed but decreased in the SAM and gold cases where the vesicles ruptured to form a monolayer on the SAM or a bilayer on the gold substrate.

In summary, it is clear that several parameters affect the formation of SLBs on solid supports.

For instance, substrates such as gold lead to the formation of supported vesicle layers, whereas SLBs form on anionic glasses such as silica, mica, borosilicate glass and quartz. Zhadanov and Lipowsky's theoretical work shows that this is due to the degree of stress on the vesicle brought about by its interaction with the substrate, which is moderated in some fashion by the ionic conditions of the buffer the vesicle is suspended in. It is known that cations in solution bind to vesicle bilayers thereby altering their structure but principally their bending modulii. A change in the bending modulus changes the critical radius necessary for rupture on support surfaces and may alter the path of vesicle rupture. For instance, a change in the minimum rupture radius may mean more vesicle fusion events are necessary so that the resulting large vesicle (but not too large) can rupture on the surface. Interactions with neighbouring vesicles and bilayer edges seem to increase the rate of SLB formation from the rupture of adsorbed vesicles, but these are not necessary in all cases; more isolated rupture is observed on mica than silica. The actual adsorption of the vesicles seems to depend on the balance of forces at the interface in the solution conditions chosen. But primarily depends on whether the vesicle and substrate surfaces are interacting at constant potential or constant charge. Hydration repulsion has an effect on the overall rate of formation but is not controlling as the nature of the electrical double layer interaction. Fygenson[70] has questioned the interpretation of previous QCM-D data with regards to the concept of a critical vesicular coverage, at least on borosilicate glass. Also a large majority of lipid species such as the phosphoethanolamines, spingomyelins, and mixtures relevant to the study of functional domains in real membranes (lipid rafts) have been given scant attention in these studies. The first and the last are the most concerning: bacterial membranes are primarily comprised of PE and lipid rafts are the subject of much research. It is important to elucidate the formation of SLBs from suspensions of these lipids and to find out under what conditions formation is well defined and reproducible. The lack of work on the PE family of lipids is probably due to their general preference for hexagonal phases rather than vesicular ones. TIR-Raman would be an excellent technique to study the mechanism of SLB formation on optical glass. It offers several advantages over ATR-IR for the study of thin films, including a reduced penetration depth and much weaker water background. Order parameters, in theory, provide a way to distinguish different states of lipid aggregation at the interface that does not rely on mechanical perturbation i.e. AFM.

3.2 Results

3.2.1 A framework for interpretation

In this section I will describe how I have interpreted my TIR-Raman spectra of SLB formation and associated NTA data. Kinetic TIR-Raman data were analysed using the chemometric technique of target factor analysis (TFA), (see section 2.4.5.2). TFA has allowed me to quantify the amount of material at the interface in terms of uncalibrated but normalised component weights. Although component weights alone do not afford the surface excess, as long as the same refined spectrum is used for comparable systems, the relative surface coverage can be obtained. In order to gain a greater understanding of the processes taking place during vesicle adsorption and rupture, I also endeavoured to extract information from the subtracted TIR-Raman spectra by order analysis (see section 2.4.5.1). The order parameters provide evidence for any structural changes taking place during the adsorption process and therefore allow me to infer whether or not vesicle rupture was taking place and in what way. With this in mind, I wrote a function in Matlab to locally fit 4th order polynomials to the symmetric and antisymmetric CH stretches; from these fits information about the peak intensity ratio of the anti-symmetric to symmetric CH stretches was obtained and their respective positions were extracted. These values were then plotted against time and inferences made. Often adjacent spectra within the time series were averaged in order to reduce the noise in the parameters; unfortunately, this was done at the loss of data points pertaining to transient events such as rapid initial adsorption. Information regarding the number of spectra in each average and the associated time period over which they were calculated is included in the captions of the relevant figures. In summary, the component weights quantified how much lipid was that the surface and the order parameters provided information about the structure of this material and its environment.

Despite the large amount of detailed information which I have been able to extract from TIR-Raman data, several artefacts were encountered during my measurements that could not be avoided. The artefacts do not bring into doubt my interpretations so long as they are recognised. The primary cause of the artefacts was the defocussing of the microscope from the interfacial region. This occurred because of slow but steady drift in the micro-motion stages used to control the flow cells position. In general for equilibrium spectra defocussing is not an issue. However, for the long duration measurements made of SLB formation sometimes defocussing did occur and this could alter the spectra obtained in two key ways. When focus of the interface is lost, it may coincide with the displacement of the laser spot, which moves the image of the laser spot on the detector, this can lead to an offset in the peak positions i.e. there is effectively a loss of calibration until refocussing. This artefact brings into question the interpretation of changes in the peak positions with time wherever it occurs, and I have only included this order parameter for two of the three systems investigated for illustrative purposes. If there is a large drop in signal the $I(d^-)/I(d^+)$ will also be affected. In the CH region there is also some residual background that does not pertain to water. If the signal becomes sufficiently low the non-water background contribution to the peak intensities of the symmetric and anti-symmetric stretches will become large enough to lower the ratio. However, this effect is much smaller than that leading to variation in the peak positions.

Important to any investigation of SLB formation by in-situ vesicle fusion is an accurate understanding of the lipid suspensions prepared. In my work I have used bath sonication to prepare lipid vesicles. Probe sonication requires centrifugation to remove contaminant metal particles from the probe tip which break off during each cycle, and may cause damage to the lipids in the sample,

resulting in lower purity. However, the vesicles prepared by bath sonication are expected to be larger and of significantly wider size distribution than those prepared by probe sonication. By measuring the sizes of the vesicles/aggregates I have yet more information to help me understand my TIR-Raman data as I have information about what aggregates could present themselves at the interface.

In the coming sections on different lipid systems, we shall see that SLB formation takes place in several distinct stages. In stage I there was a dead time which depended on the length of inlet tubing and was equal to the time required for the vesicle suspension to reach the silica substrate. In stage II there was a period of rapid increase in component weight that corresponded to the adsorption of lipid; the exact nature of the rapid adsorption depended on the lipid system under study and the bulk buffer conditions employed. In stage III, the component weights gradually increased or maintained a stable value. In stage IV, whilst the flow cell was rinsed using pure buffer, either the material adsorbed through stage III was removed or the constant component weight was maintained. I have been able to associate stage II, the period of rapid uptake, as the primary SLB formation stage. I have shown stage III build-up to be the weak adsorption of extra lipid material. Stage IV was the removal of this material if it had adsorbed.

3.2.1.1 Assignments

Figure 3.6 (a) shows a TIR-Raman spectrum of the CH region for a POPC SLB at the silica–water interface. Figure 3.6 (b) shows TIR-Raman spectra of the fingerprint region of POPE and egg-SM SLBs at the silica water interface. The relevant spectral assignments are shown. The main features are the anti-symmetric methylene stretch (d^-) at ≈2890 cm^{-1} and the symmetric methylene stretch (d^+) at ≈2852 cm^{-1}; using these I monitor changes in the primary order parameter ($I(d^-)/I(d^+)$) and peak positions to understand the state of the lipid alkyl chains at the interface. Unfortunately we are unable to resolve the symmetric terminal methyl stretch (r^+) at ≈2870 cm^{-1} as is it occluded by the (d^-) mode. I have been able to resolve the other CH bands: the CH_2 scissoring mode at ≈1470 cm^{-1}, the CH_2 twisting/wagging mode at ≈1300 cm^{-1}, the overtone of the CH_2 scissoring mode with its Fermi resonance at ≈2927 cm^{-1}, the antisymmetric terminal methyl stretch (r^-) at ≈2960 cm^{-1}, the symmetric headgroup methyl stretch (r^+_{HG}) at ≈2985 cm^-1, the vinylic CH stretch at 3010 cm^{-1} from the cis-double bond of the oleoyl chain in POPC, and the anti-symmetric headgroup methyl stretch at ≈3041 cm^{-1}. The small band at ≈2725 cm^{-1} is tentatively assigned to an overtone of the CH_2 bending modes. The ester carbonyl stretch is found at ≈1740 cm^{-1}.

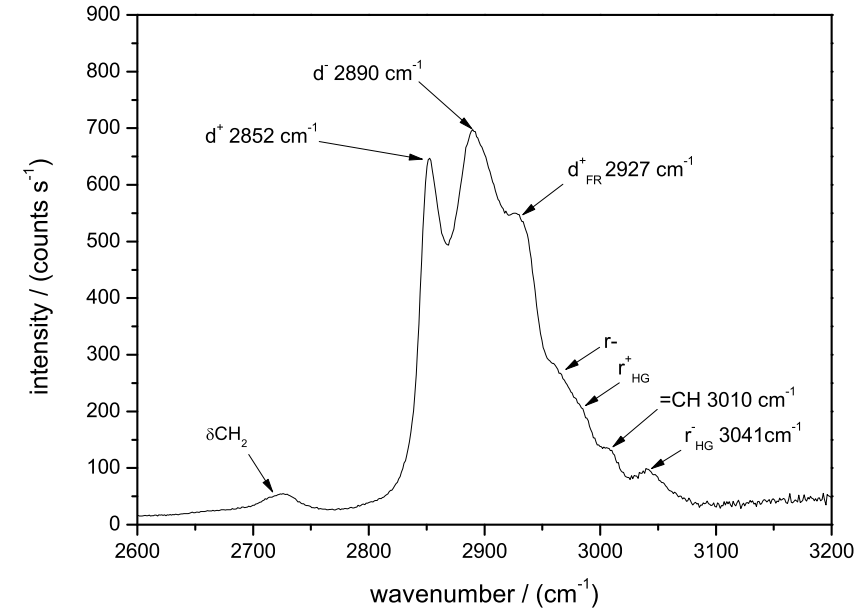

(a)

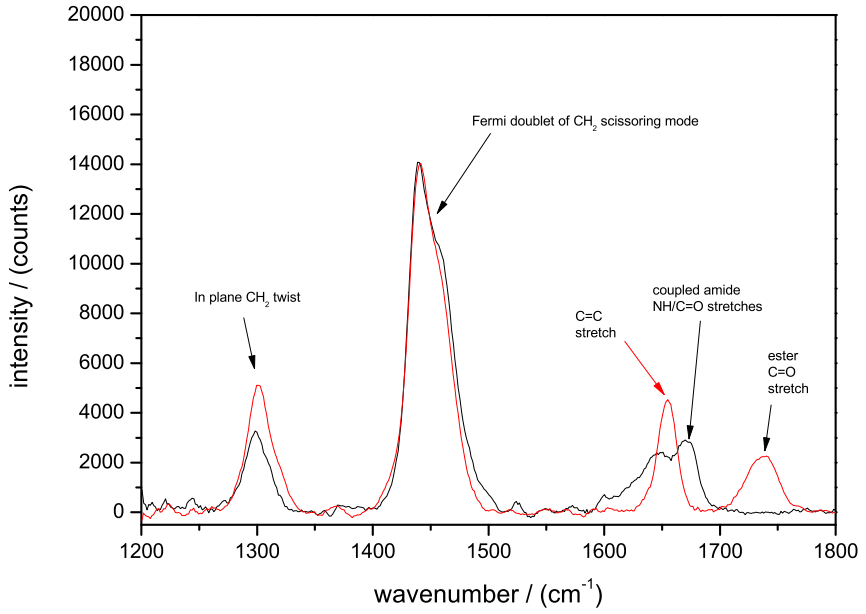

(b)

Figure 3.6: (a) An S-polarised TIR-Raman spectrum (unpolarised detection), SiO_2/H_2O background subtracted, showing the CH region of a complete L_α phase POPC SLB with spectral assignments highlighted: (d^+) - symmetric CH stretch, (d^-) - anti-symmetric CH stretch, (d^+_{FR}) - overtone of the CH scissoring mode with its Fermi resonance, (r^-) - antisymmetric terminal methyl stretch, (r^+_{HG}) - symmetric headgroup methyl stretch, (r^-) - antisymmetric stretch choline headgroups, (=CH) - vinylic CH vibrations, (δCH_2) - overtone of the CH_2 bending mode. (b) S-polarised TIR-Raman spectra (unpolarised detection), SiO_2/H_2O background subtracted, showing the finger print region of complete POPE (red) and egg-SM (black) SLBs in the L_α phase, relevant spectral assignments shown. Notice the un-occluded ester carbonyl stretch of POPE, which I have used to calculate the composition of the mixed SLB.

3.2.2 POPC

I decided to study the formation kinetics of POPC SLB on silica by TIR-Raman spectroscopy in an effort to validate TIR-Raman as a technique for studying SLB formation by vesicle fusion; POPC has been used for work on SLB formation kinetics frequently by others and so comparisons can be made.

3.2.2.1 Vesicle size distributions

I acquired size distributions for POPC vesicles in (i) 20 mM tris pH 7.4, (ii) 20 mM tris + 100 mM NaCl and (iii) 20 mM tris pH 7.4 + 2 mM $CaCl_2$. The size distributions were acquired at 32°C, the same temperature as used in the formation kinetics shown later. These vesicle size distributions are shown in figure 3.7. Interestingly, Na^+ and Ca^{2+} resulted in larger vesicles, probably a result of the higher bending modulus of vesicles with bound cations. A higher bending modulus would imply a greater energy required to break a vesicle up in the ultra-sonic field. Consequently, a smaller proportion of vesicles would undergo rupture in the ultra-sonic field at any one time. After a finite sonication time the number of smaller vesicles would therefore be lower in the salt solutions where lipid bilayers have higher bending modulus. The mean diameters of the vesicles were i) 110 nm, ii) 166 nm and iii) 149 nm, roughly in order of ionic strengths, I, where i) $I \approx 0$ (ii) I =100 mol dm^{-3} and (iii) $I = 6$ mol dm^{-3}. The fact that the vesicles are larger when prepared in Ca^{2+} than when those prepared in the Na^+ containing buffer is indirect evidence of a stronger interaction between the POPC headgroups and Ca^{2+} than with Na^+. The small artefacts at the bottom of the size distributions are most likely due to noise on the CMOS detector of the NTA apparatus operating at high gain. The lower detection limit for the vesicles I prepared was in the range of 30-50 nm.

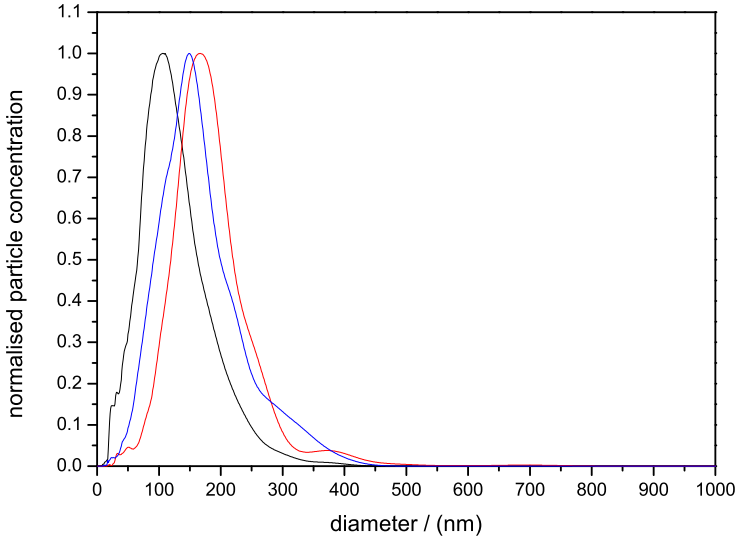

Figure 3.7: Vesicle size distributions obtained for POPC in (i) 20 mM tris pH 7.4 (black) (ii) 20 mM tris pH 7.4 + 100 mM NaCl (red), (iii) 20 mM tris pH 7.4 + 2 mM $CaCl_2$ (blue). All at 32°C.

3.2.2.2 POPC adsorption

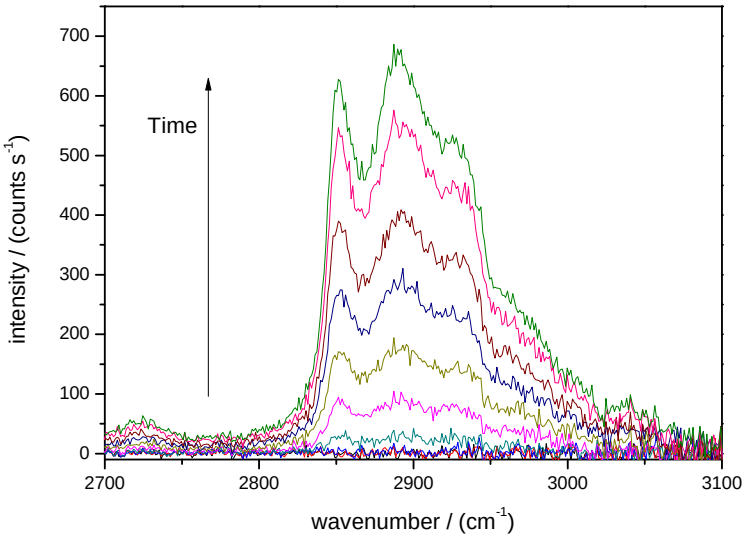

Figure 3.8: Subtracted TIR-Raman spectra showing stage II, the period of rapid uptake for POPC SLB formation in (ii) 20 mM tris pH 7.4 + 100 mM NaCl at 32°C. S-polarised (un-polarised detection), 73° incidence, 800 mW, 5 s acquisition per spectrum, 63 s total.

Figure 3.8 shows example background subtracted TIR-Raman spectra of POPC vesicle adsorption at the silica-water interface in buffer (ii) containing 100 mM NaCl. The spectra shown are from stage II, the period of rapid uptake described in my framework above. It is from spectra like these that the rest of my analyses are carried out. Figure 3.9 (a) shows the component weights of POPC, normalised by the component weight of water, with time for the adsorption of POPC vesicles to the silica substrate. In all traces there was a short initial dead time which depended upon the length on inlet tubing and the flow rate used. During the dead time the lipid suspension was still passing through the tubing. After the dead time there was a rapid increase in component weight for all three buffers. A close-up of this region is shown in 3.9 (b). Examination of this time period showed an acceleration of uptake on the surface with time lasting for (i) 31 s, (ii) 54 s and (iii) 51 s. Following this rapid uptake, in all conditions there was a slow increase of component weight with time. This build-up was lowest in buffer (i), and increased to a far higher level in buffers (ii) and (iii) where Na^+ and Ca^{2+} were present. The final levels of the build-up as measured in (ii) and (iii) were approximately the same. However, during this stage the degree of build-up appeared more rapid and higher in (iii) than in (ii); it also appeared to be more irregular. After approximately 6000 s the syringe was replaced with one containing pure buffer. The laser was shuttered for safety during the exchange of syringes so there is a break in the data. Following the syringe exchange, the laser was refocussed on the hemisphere surface to correct for any defocussing. After the flow and data collection were recommenced there was a short period during which the last remaining vesicle-containing buffer flows into the cell of the same approximate duration of the initial dead time. When the pure buffer reached the surface, the component weights decreased rapidly until they reached a stable value which did not change over the remaining experimental duration. We associated this plateau with a complete SLB. The total quantity of material at the interface after rinsing with buffer varied by approximately 13% when compared to final component

weight level obtained for buffer solution (ii). In repeat measurements the final component weights were similar indicating consistent final surface coverages.

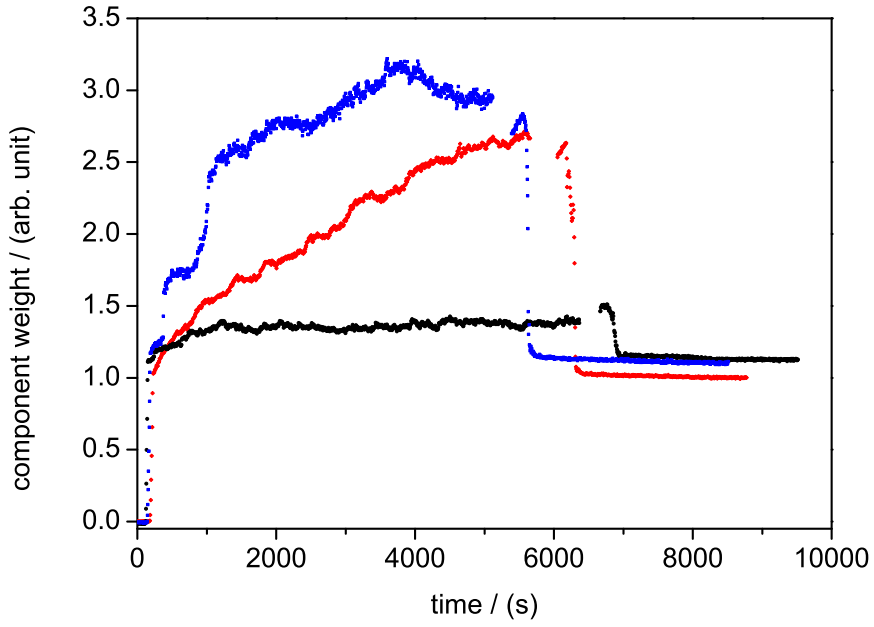

(a)

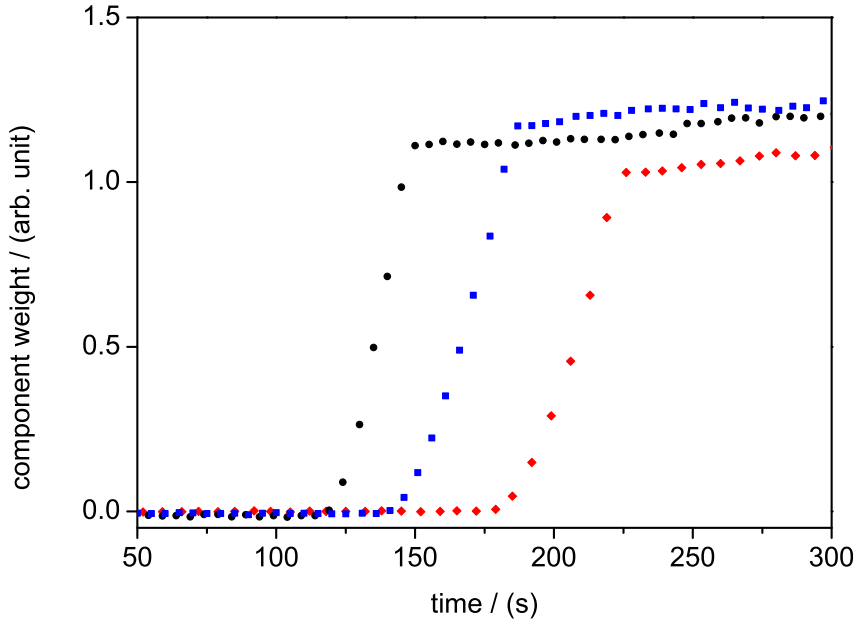

(b)

Figure 3.9: Two graphs showing the normalised component weights of POPC at the silica-buffer interface with time in solutions (i) 20 mM tris pH 7.4 (black circles), (ii) 20 mM tris pH 7.4 + 100 mM NaCl (red diamonds) and (iii) 20 mM tris pH 7.4 + 2 mM $CaCl_2$ (blue squares) (a) full duration (b) blow up of initial rapid increase. Acquisition times per spectrum, (i) 3.5 s, (ii) 5 s, (iii) 3.5 s. All at 32°C.

3.2.2.3 Rupture and build-up

Figure 3.10 (a) shows no significant change in peak positions in the absence of added ions. Figure 3.10 (b) shows the peak positions with time in tris buffer with 100 mM Na^+. We observe little change in the antisymmetric stretch but a pronounced decrease and subsequent increase in the wavenumber of the symmetric stretch, corresponding to the build-up of component weight and loss thereof upon rinsing with pure buffer. Figure 3.10 (c) shows the peak positions vs time in tris buffer with added 2 mM Ca^{2+}. As in the Na^+ experiment, there is little variation in the antisymmetric stretch with time, however, there is a significant decrease in the peak position of the symmetric stretch corresponding to the build-up period in the component weight data. Upon rinsing the symmetric stretch shifts to higher frequency.

The corresponding plots of the peak intensity ratio, $I(d^-)/I(d^+)$ are shown in figure 3.11 (a) through (c). Figure 3.11 (a) shows the intensity ratio data for buffer solution (i) 20 mM tris pH 7.4. Here we see very little change in the parameter as time passes; there is a slight decrease during component weight build-up followed by a similarly small increase upon rinsing. However, figure 3.11 (b) and (c) are more interesting, they show changes that closely follow the behaviour shown in 3.9 for the same buffer solutions (ii) and (iii). In (b) there is a slow decrease corresponding to the increase shown in the component weight data. During rinsing $I(d^-)/I(d^+)$ recovers, ultimately leading to values identical for those acquired in figure 3.11 (a). These data suggest that lipid in a form other than an SLB is adhering to the surface after the initial rapid adsorption. It is highly likely that the additional signal corresponds to vesicle build-up; we know that vesicles are present in solution and the intensity ratio values are distinct from SLB, the additional signal is also removed readily upon rinsing. As the final values of the order parameter are slightly higher than those at the early peak, which corresponds to the period of rapid accelerating uptake in figure 3.9, I believe that the bilayer was incomplete at the early stage, only reaching completion at some point during the build-up phase. Figure 3.11 (c), shows the intensity ratio data for the Ca^{2+} containing solution. The behaviour is similar to (b) however, the initial data points correspond more closely to the final ones implying that the POPC at the interface at this stage is in the same state as that after rinsing. SLB formation takes place more rapidly in the calcium-containing buffer than the sodium-containing buffer – vesicle rupture required to create an SLB has taken place before the onset of build-up. In general for molecules aligned in the same direction relative to the interface $I(d^-)/I(d^+)$ is a quantitative measure of lipid order. However, in this case where one contributing component is SLB and the other is spherical vesicles, it is not possible to compare the quantitative values directly, but it is possible to say there are clearly different contributions to the spectra, one corresponding to vesicles and the other to SLB. At each time step the actual spectrum is a weighted average of the two contributions. These differences are however, very small, in this sense they do not affect the TFA analysis, and thus the TFA analysis did not require an additional factor corresponding to the second state as they are so similar. The overall differences in the intensity ratio are also quite small (0.06), compared to the change of 0.3 in the $I(d^-)/I(d^+)$ ratio at the main ($L_\alpha \rightarrow L_\beta$) phase transition (see Chapter 4). The final average $I(d^-)/I(d^+)$ values after rinsing for the three buffer solutions were: (i) 1.065±0.006, (ii) 1.069±0.007 and (iii) 1.057±0.011.

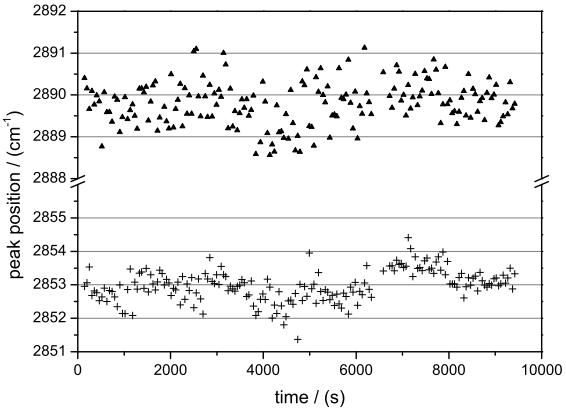

(a)

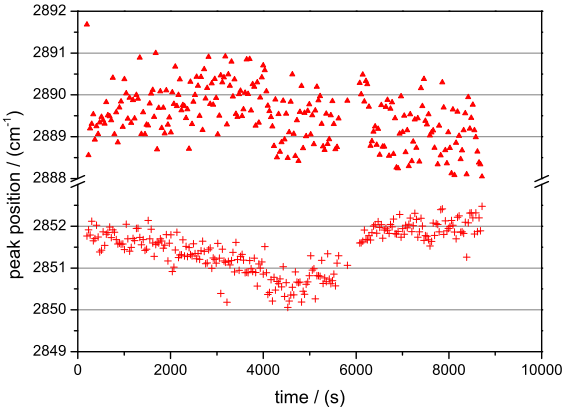

(b)

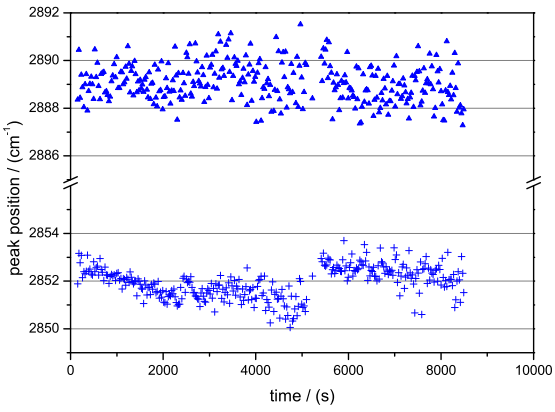

(c)

Figure 3.10: Graphs (a), (b) and (c) showing the change in the symmetric and anti-symmetric CH stretch positions during POPC SLB formation with time for (i) 20 mM tris pH 7.4 (black triangles and crosses), (ii) 20 mM tris pH 7.4 + 100 mM NaCl (red triangles and crosses) and (iii) 20 mM tris pH 7.4 + 2 mM $CaCl_2$ (blue triangles and crosses) respectively. All at 32°C. Data were compiled from averaged background subtracted TIR-Raman spectra: (i) 10 spectra over 53 s, (ii) 4 spectra over 33 s and (iii) 5 spectra over 25 s.

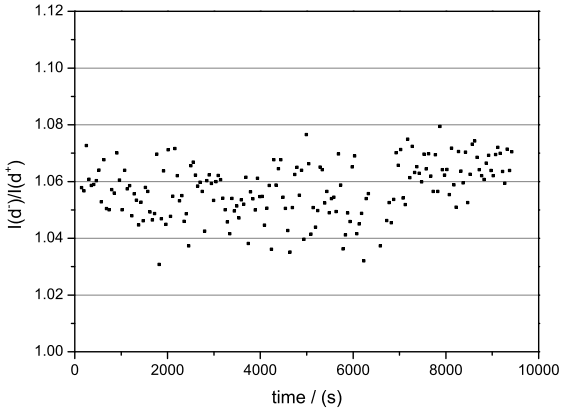

(a)

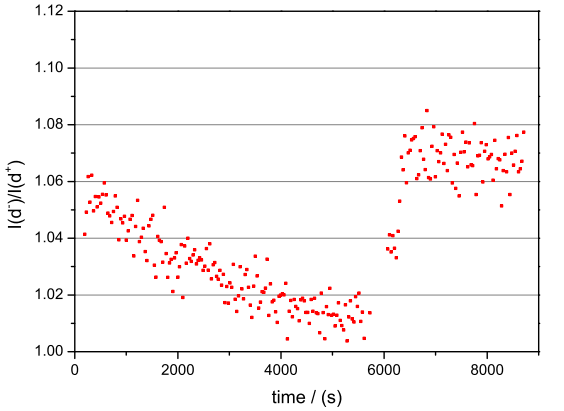

(b)

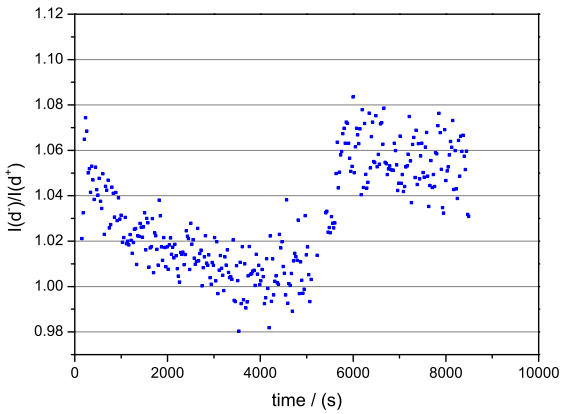

(c)

Figure 3.11: Graphs (a), (b) and (c) showing the change in the peak intensity ratio $[I(d^-)/I(d^+)]$ for POPC SLB formation with time for (i) 20 mM tris pH 7.4 (black triangles and crosses), (ii) 20 mM tris pH 7.4 + 100 mM NaCl (red triangles and crosses) and (iii) 20 mM tris pH 7.4 + 2 mM $CaCl_2$ (blue triangles and crosses) respectively. All at 32°C. Data were compiled from averaged background subtracted TIR-Raman spectra: (i) 10 spectra over 53 s, (ii) 4 spectra over 33 s and (iii) 5 spectra over 25 s.

3.2.2.4 Critical vesicular coverage

The minima in figure 3.11 (b) and (c) give an idea of the value of the order parameter for pure vesicles, it must be lower than the minimum values measured as SLB is contributing to the spectra at these points. We can ascertain that even in the initial data points shown, bilayer formation is almost complete for all three systems. Lower vesicle concentrations would be needed to find out categorically whether or not a critical vesicular coverage was required for SLB formation for POPC in the buffers used here. It is unclear why a POPC SLB would form faster from a tris only solution than one containing 100 mM Na^+. Previously authors have shown that vesicles composed of zwitterionic lipids have a slightly negative zeta potential; the sodium cations could be screening the expected repulsive electrostatic interaction between the silica support and incoming vesicles. In addition, larger vesicles are likely to diffuse more slowly than smaller ones; my data show that vesicles prepared in the tris only buffer are the smallest. Also why do we observe a build-up at all? Other workers have recently stated that vesicles show a poor affinity for the SLB buffer interface and have observed the active loss of remnant vesicles upon bilayer completion.[70] I have observed vesicle build-up after the formation of the lipid bilayer. The duration of my experiments was longer than those observed by other workers and the concentration of vesicles was greater. If vesicles were to desorb upon SLB completion, we would expect to observe desorbtion sooner than Fygenson and coworkers,[70] as the SLB forms faster with higher vesicle concentrations. The acceleration observed during the phase of rapid vesicle adsorption is in agreement with other work; this shows that the surface has a stronger interaction with bulk phase vesicles as the lipid coverage increases.

3.2.3 Egg-SM

Sphingolipids make up ≈33% of lipid raft fractions,[74] and form a total of 10-20% of the lipid found in human plasma membranes.[25] They are important in a wide variety of cellular processes such signal transduction and extracellular recognition. To my knowledge there has been no systematic investigation into the formation of SLBs comprising lipids from this group. The sphingolipids are similar to the phosphatidylcholines in that they have a choline headgroup, but the backbone of the lipid is sphingosine not glycerol. The acyl chains are attached by amide bonds not ester linkages. The position of the amide and hydroxyl groups on these lipids allows for intra-bilayer hydrogen bonding leading to the formation of more ordered bilayer structures. It is for this reason that they also possess higher main phase transition temperatures than many glycerophospholipids with hydrocarbon chains of similar length.[75]

3.2.3.1 Vesicle size distributions

Vesicle size distributions were acquired in the same three buffer conditions as before (i) 20 mM tris pH 7.4, (ii) 20 mM tris pH 7.4 + 100 mM NaCl and (iii) 20 mM tris pH 7.4 + 2 mM $CaCl_2$. These are shown in figure 3.12. Figure 3.13 shows a screenshot of the raw NTA output of egg-SM vesicles for illustrative purposes. The mean vesicle diameters were (i) 110 nm, (ii) 177 nm and (iii) 131 nm respectively. These diameters were for the most part very similar to those acquired for POPC however, the measurements for solution (iii) containing the 2 mM Ca^{2+} were significantly smaller. Interestingly for the two suspensions with added electrolyte, the distribution extends out as a tail to much higher sizes showing the screening of the electrostatic double layer repulsion between neighbouring vesicles resulting in some degree of flocculation.

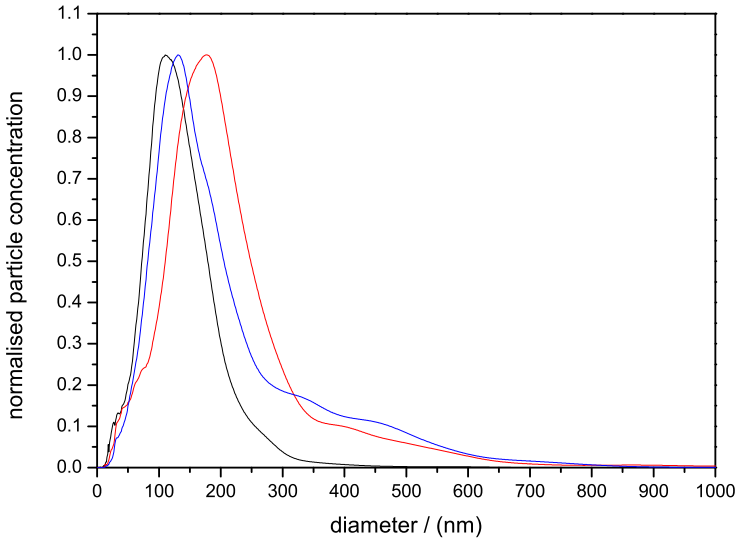

Figure 3.12: Vesicle size distributions acquired for egg-SM in (i) 20 mM tris pH 7.4 (black), (ii) 20 mM tris pH 7.4 + 100 mM NaCl (red) and (iii) 20 mM tris pH 7.4 + 2 mM $CaCl_2$ (blue). All at 44°C.

Figure 3.13: A screenshot from the NTA raw video output of egg-SM vesicles. Image approximately 120 μm x 90 μm.

3.2.3.2 Egg-SM adsorption

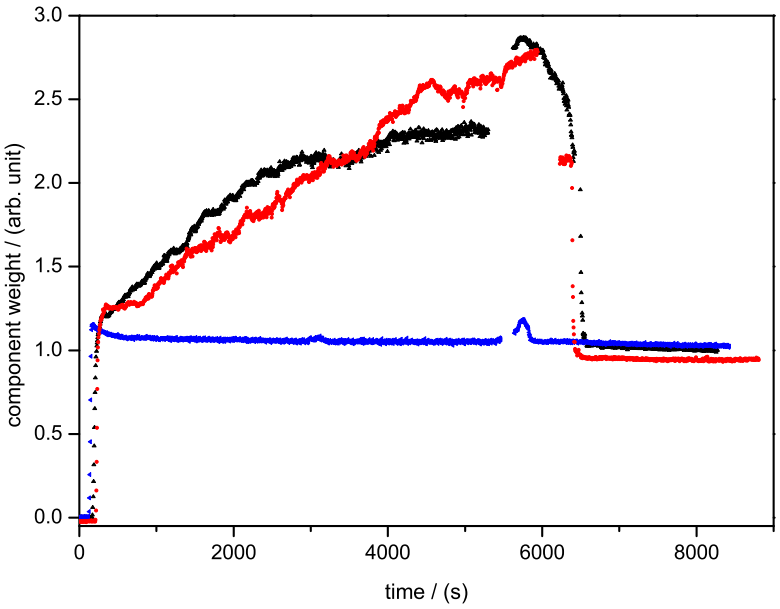

(a)

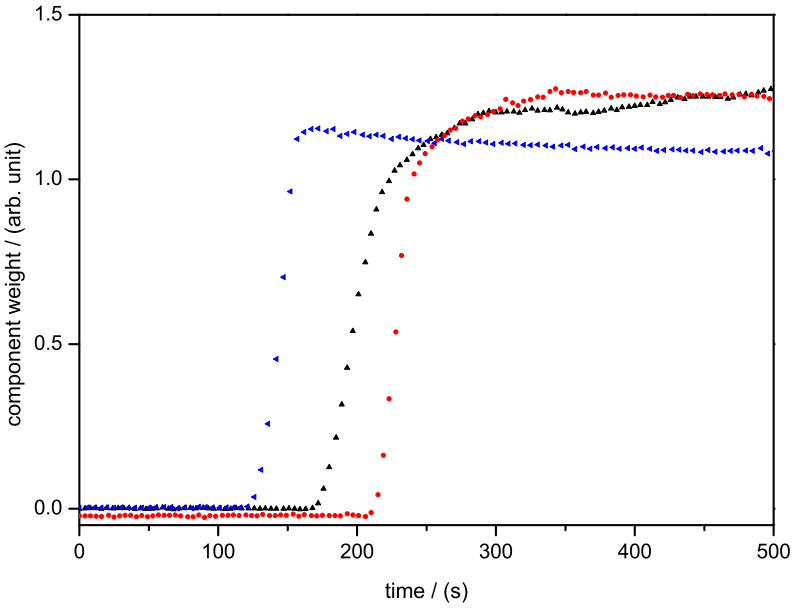

(b)

Figure 3.14: Graphs showing the normalised component weights of egg-SM at the silica-buffer interface with time in solutions (i) 20 mM tris pH 7.4 (black triangles), (ii) 20 mM tris pH 7.4 + 100 mM NaCl (red circles) and (iii) 20 mM tris pH 7.4 + 2 mM $CaCl_2$ (blue left point triangles), 44°C, 800 mW, 73° incidence, S-polarised, unpolarised detection: (a) full duration, (b) closeup of initial rapid increase. Acquisition times: (i) 2.5 s, (ii) 2.5 s, (iii) 3.5 s.

The egg-SM used in this section of my work is in fact a natural mixture of lipids, the predominant species is shown in my introduction and makes up 86% of the total content. Nevertheless I was able to represent the mixture by a single component or representative spectrum in the TFA analysis; the individual spectra will all be very similar and using independent factors for each of them is not necessary to measure the amount of lipid at the interface. The component weights are shown plotted against time in figure 3.14 (a) and (b). As before there was an initial dead time followed by a rapid increase in the component weight for all of the solution conditions investigated. However, for egg-SM, although the data for all buffer conditions show a rapid increase with an accelerating increase in signal, the sodium and pure tris data slow as they approach the end of this stage. The total times for this period of initial uptake were (i) 127 s, (ii) 97 s and (iii) 46 s. Interestingly for buffer (iii) with Ca^{2+} there was a slight over-shoot; the signal level dropped by a small amount to reach the plateau value, which remained virtually constant until rinsing at ≈5500 s (the small bump at ≈3200 s most likely corresponds to a larger aggregate that passed through the evanescent field. For buffer solutions (i) and (ii) the stage of rapid increase is followed by a subsequent build-up similar to what was observed for the POPC systems with buffers (ii) and (iii). As rinsing began, the signal levels dropped with buffers (i) and (ii) reaching a stable plateau value. However, there was a discrepancy in the time taken to remove the extra material from the interface; in the sodium containing buffer it takes approximately 121 s to remove, but in the tris only system it takes 815 s. For buffer (iii) no extraneous material had adsorbed to the surface and so with rinsing the component weight remained constant. Between all buffer conditions the final SLB coverage varied by approximately 6%.

3.2.3.3 Rupture and build-up

Figure 3.15 shows the peak positions with time for the respective SLB formation processes shown in figure 3.14. When comparing figures 3.15 (a) and (b) with the data for buffers (i) and (ii) in figure 3.14 there are changes in the CH stretch positions that correspond to the build-up of vesicles. However, when comparing figure 3.15 (c) with the data in figure 3.14 for buffer (iii) we notice that there is a decrease in the peak position but no corresponding build-up of material in the component weight data. Either some restructuring process is taking place within the layer that belies the constant normalised component weights, or the change is an artefact of defocussing. However, questions about the state of lipid material at the interface can still be answered by looking at figure 3.16 (a) to (c) showing the change in the primary order parameter with time. As we shall see in the next paragraph, the data presented follow the changes in the component weights well, thus implying that the peak shifts for buffer (iii) are artefacts and that the peak positions are the least reliable of the two order parameters used.

For figure 3.16 (a) showing the change in the intensity ratio for the tris-only system we observe similar behaviour to POPC SLB formation. However, there are more data points for the initial rapid stage of vesicle adsorption; and these provide an indication of un-ruptured vesicles at the silica-buffer interface. The data points that correspond to the peak of the initial rapid increase in the component weight data are lower than the final values after rinsing, suggesting that for the pure tris system, as for POPC, formation is not complete until some time after the onset of the additional build-up. Again, this build-up is only removed upon rinsing.

Figure 3.16 (b) shows the $I(d^-)/I(d^+)$ data with time for the sodium containing buffer. The initial change, between 0 and 1000 seconds, in the $I(d^-)/I(d^+)$ values is very clear as we have more data points for this system than any other examined so far. The very first intensity ratio

values correspond well with those obtained at maximum vesicle build-up at ≈6000 s; indicating that at the earliest times the surface was mostly occupied with vesicles and not SLB. As the total amount of material as shown by figures 3.14 (a) and (b) increased in the rapid uptake stage, so did the $I(d^-)/I(d^+)$ values, therefore a constant transformation into SLB took place; there was no CVC in this case – I observed spontaneous rupture. In the other systems described above, the final values of $I(d^-)/I(d^+)$ after rinsing were higher than those after the initial rapid uptake before build-up therefore the SLB was not complete until after the build-up period had commenced. The $I(d^-)/I(d^+)$ data for buffer (iii) show absolutely no change; the SLB formed very quickly at the start of the procedure. Similar to POPC, different buffer conditions promote the adsorption of extraneous vesicles. For POPC not adding electrolyte limited the degree of vesicle build-up, but for egg-SM the inclusion of 2 mM Ca^{2+} in tris buffer prevented it completely. The origin of this effect is not bulk electrostatic screening as the inclusion of 100 mM Na^+ also led to vesicle build-up for egg-SM. The effect must be related to specific cation chosen, specific binding and thus its specific physical properties. For this system the mean order parameter values after rinsing in the three buffers were: (i) 1.08±0.01, (ii) 1.10±0.01 and (iii) 1.11±0.01. These values show virtually no difference in the order of the egg-SM SLB in the presence of the cations in comparison to the tris-only buffer.

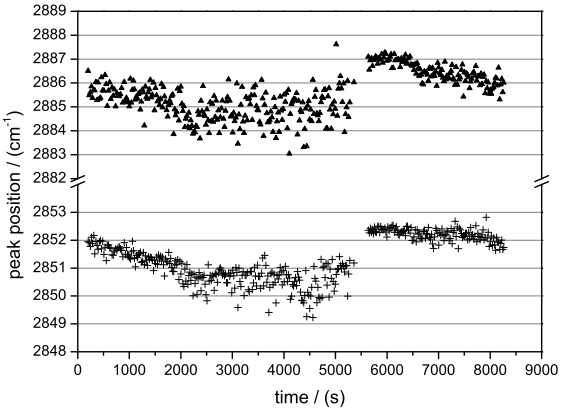

(a)

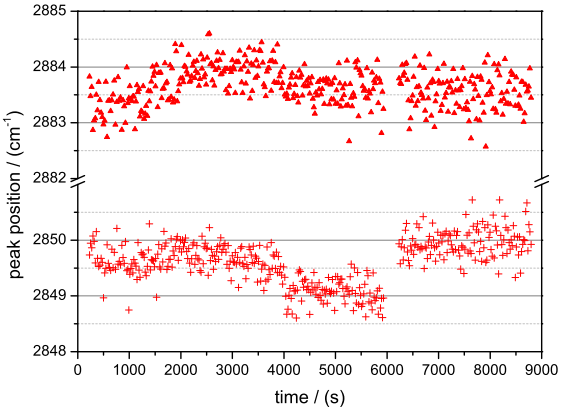

(b)

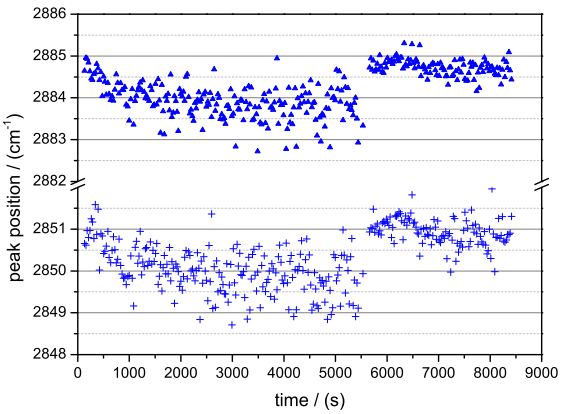

(c)

Figure 3.15: Graphs (a), (b) and (c) showing the change in the peak positions of the symmetric and anti-symmetric CH stretches during egg-SM SLB formation with time for (i) 20 mM tris pH 7.4, (ii) 20 mM tris pH 7.4 + 100 mM NaCl and (iii) 20 mM tris pH 7.4 + 2 mM $CaCl_2$ respectively. All at 44°C. Data were compiled from averaged background subtracted TIR-Raman spectra: (i) and (ii) 5 spectra over 20 s, (iii) 5 spectra over 25 s.

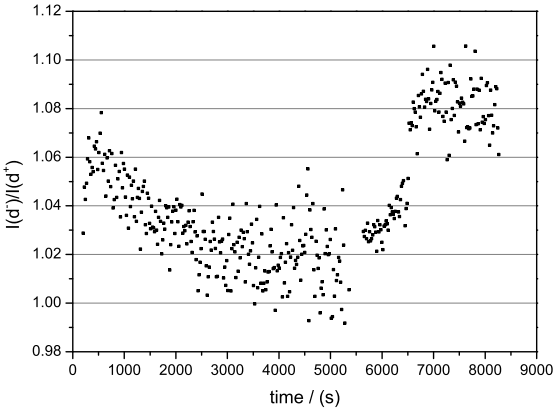

(a)

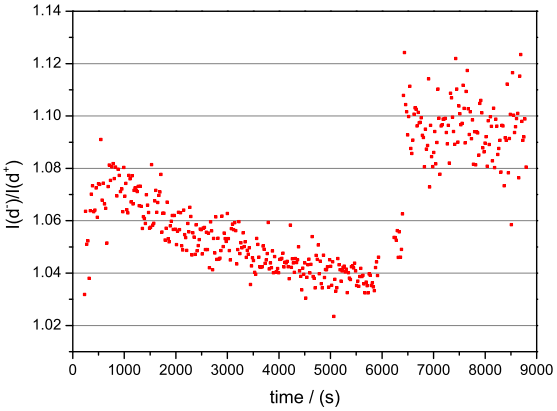

(b)

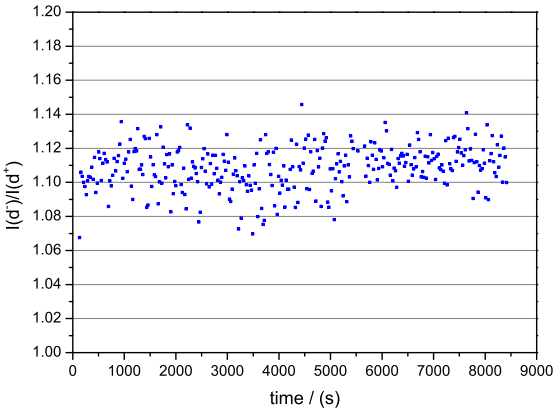

(c)

Figure 3.16: Graphs (a), (b) and (c) showing the change in the peak intensity ratio [$I(d^-)/I(d^+)$] during egg-SM SLB formation with time for (i) 20 mM tris pH 7.4, (ii) 20 mM tris pH 7.4 + 100 mM NaCl and (iii) 20 mM tris pH 7.4 + 2 mM $CaCl_2$ respectively. All at 44°C.

3.2.4 POPE

The phosphatidylethanolamines make up approximately 25% of all phospholipids and are the primary class of lipids in bacteria; for instance *Escherichia coli* cytoplasmic membranes are composed of 70-80% PE.[76] In addition, it replaces PC as the primary phospholipid component in mammalian inner membranes. Despite its relevance in biological processes and its ubiquity in bacterial membranes, little work has been done on the preparation of SLBs from this class of lipids. Several authors have, however, used it as a model system.[77] It is well known that PE prefers to form hexagonal phases and, where vesicles do form, it tends to flocculate in solution owing to its dehydrated headgroups. Owing to the obvious practical difficulties that arise from these properties, no work that I am aware of has been carried out to study the kinetics of POPE SLB formation by 'vesicle fusion'. However, other authors have stated that they have prepared POPE SLBs by vesicle fusion when conducting experiments on SLBs.[78]

3.2.4.1 Aggregate size distributions

It has been reported that PE does not form vesicle suspensions at physiological pH.[79] To understand the structure of the POPE aggregates formed in: (i) 20 mM tris pH 7.4, (ii) 20 mM tris pH 7.4 + 100 mM NaCl and (iii) 20 mM tris pH 7.4 + 2 mM $CaCl_2$ I have conducted NTA measurements. The resulting size distributions are shown in figure 3.17. POPE does not form a suspension with a single peak and narrow size distribution in any of the conditions studied. These results are to be expected as all measurements were conducted at pH 7.4. What we observe is a distribution of sizes with irregular structure, with particles in the range of 30 to <1000 nm. Adding sodium and calcium reduces the number of large particles and decreases the mean size. Video sequences from the NTA apparatus, show a few small particles, but also a greater number of much larger aggregates, that appear to comprise a number of smaller particles (not shown). The NTA recognises particles as small spherical light sources. Larger aggregates are often interpreted as a number of coalesced particles, which leads to errors in the size distributions. It's measurement of the moderately sized aggregates is probably correct. Clearly in the buffer conditions used POPE does not form vesicle suspensions like the other lipids used in this study, it forms a more diverse suspension of aggregates.

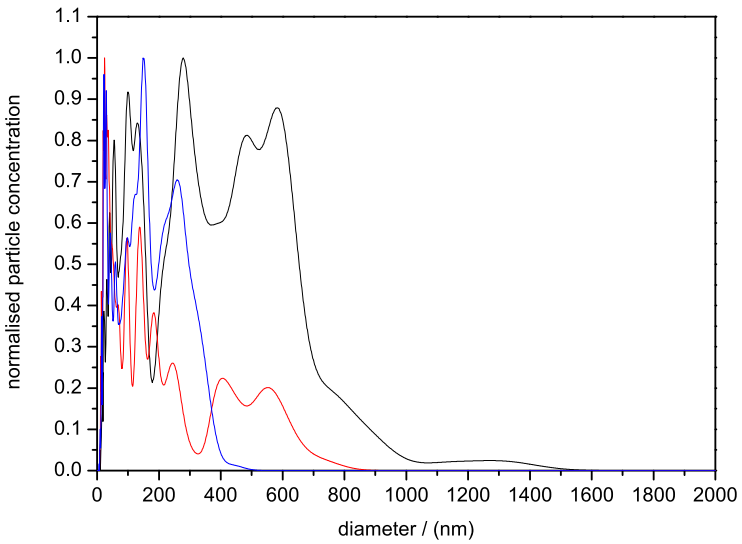

Figure 3.17: Aggregate size distributions acquired for POPE in (i) 20 mM tris pH 7.4 (black), (ii) 20 mM tris pH 7.4 + 100 mM NaCl (red) and (iii) 20 mM tris pH 7.4 + 2 mM $CaCl_2$ (blue). All at 32°C.

3.2.4.2 POPE adsorption

Figure 3.18 (a) and (b) show the component weights with time for the formation of POPE SLBs on silica in: (i) 20 mM tris pH 7.4 + 100 mM NaCl and (ii) 20 mM tris pH 7.4 + 2 mM $CaCl_2$. POPE did not adsorb on silica in pure 20 mM tris at pH 7.4. However, it always adsorbed when Ca^{2+} was included in the buffer and inconsistently when Na^+ was present. For the buffer containing Na^+ (i), between 400 and 700 seconds, we observe a stepwise increase in the component weight. At 700 seconds, this stepwise behaviour ceases and a plateau is reached which is unchanged when we rinse the system (marked by the arrows). The break in the data data at approximately 6000 seconds was due to the refocusing of the microscope. With Ca^{2+} (ii), we observe a similar stepwise increase but it is much faster. During the plateau phase we observed the adsorption of additional material to the SLB, this material is removed from the interface after a very large aggregate rolled across the surface (see the two data points at very high component weight). There was very little change in the component weight upon rinsing – the plateau continued. The overall signal levels acquired for POPE compare well with those of POPC. I acquired neutron reflectivity data, which, confirm the presence of an SLB (20 mM tris pH 7.4, 32°C, ILL, FIGARO). These data are shown in figure 3.19 and the corresponding parameters used to model the lipid layer are shown in table 3.4. The model parameters indicate that I have successfully created a complete SLB in the presence of Ca^{2+}. For measurements in Na^+ (i) we found that bilayer formation was irreproducible – many SLB formations failed. But, POPE SLBs could always be prepared in Ca^{2+} (ii). The stepwise increase in Raman signal could arise from the adsorption and spreading of larger flocs in the suspensions, such as those visible in the NTA measurements.

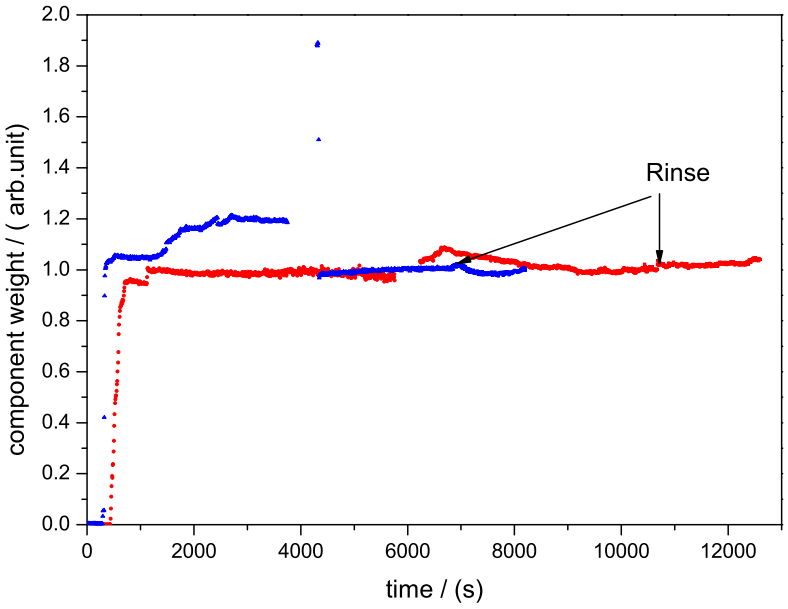

(a)

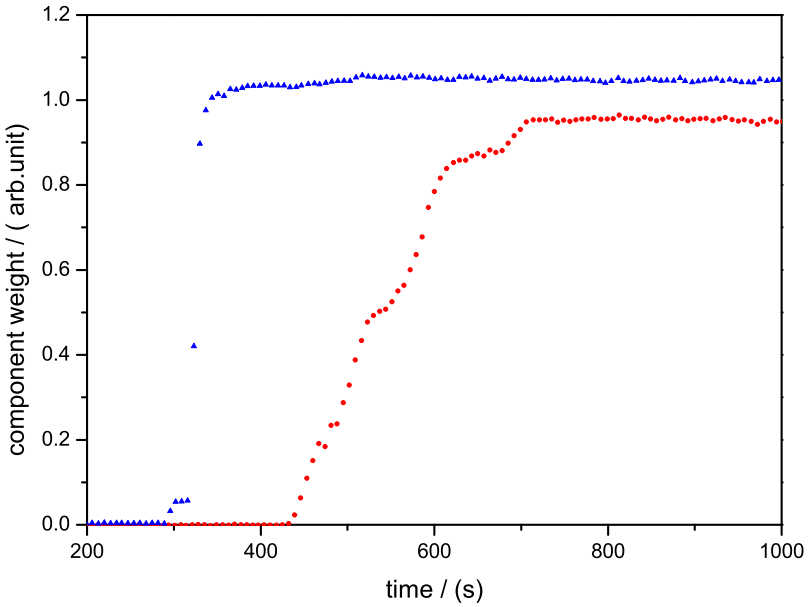

(b)

Figure 3.18: Graphs showing the normalised component weights of POPE at the silica-buffer interface with time in solutions, (i) 20 mM tris pH 7.4 + 100 mM NaCl (red) and (ii) 20 mM tris pH 7.4 + 2 mM $CaCl_2$ (blue), 32°C, 800 mW, 73° incidence. (a) full duration, (b) closeup of the initial step-wise adsorption. Acquisition times 5 s.

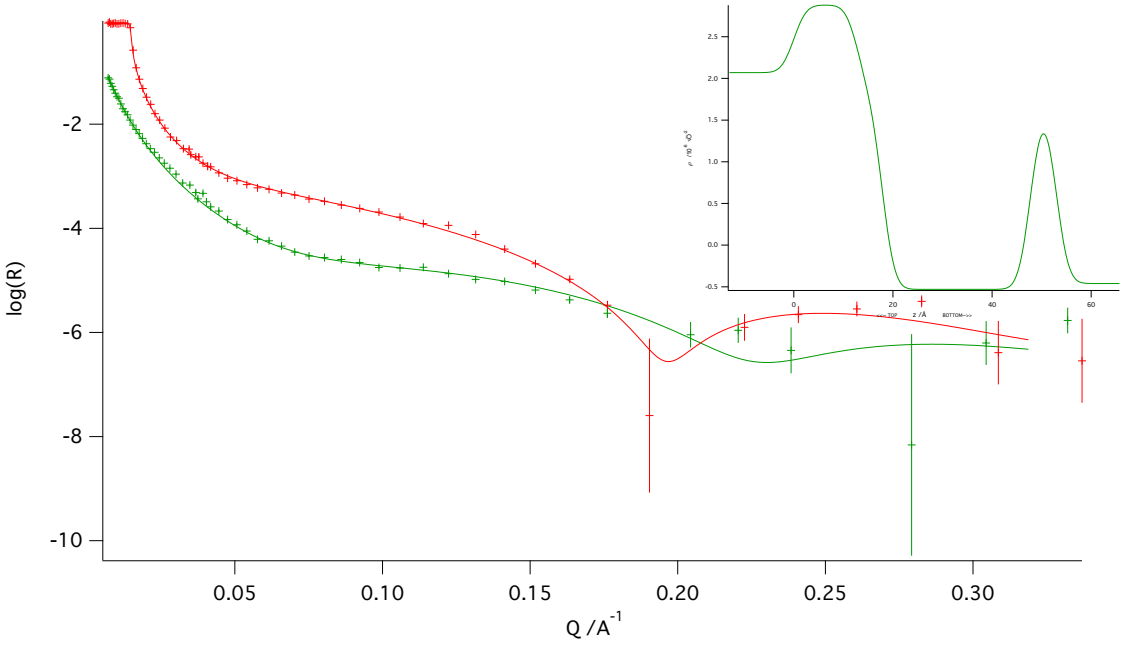

Figure 3.19: Neutron reflectivity as a function of momentum transfer for POPE adsorbed on an SiO_2 layer on a single crystal silicon block in 20 mM tris buffer at pH 7.4, 32°C; acquired at the ILL on FIGARO. Points are the reduced raw data. Lines are the model fits; the parameters used for modelling are shown in table 3.4. Green line and points H_2O contrast, red line and points D_2O contrast. The inset shows the scattering length density profile normal to the interface as a function of distance as determined from the model.

Region	Thickness / Å	SLD / x 10^{-6} Å^{-2}	Solvent / %	Roughness
SiO_2	12.85	3.47	19	2
POPE HG	5	3.7221 (2.51)	15.43	2
POPE Chains	15	-0.53	0	2
POPE Chains	15	-0.53	0	2
POPE HG	5	3.7221 (2.51)	15.43	2

Table 3.4: Model parameters used to fit the data shown in figure 3.19. The numbers in brackets correspond to the scattering length density of the headgroups in H_2O. As the protons on the ammonium headgroup are labile, they are exchanged when the bulk sub-phase reservoir is changed from D_2O or H_2O and vice versa. When fitting the data for the different contrasts, the different SLDs for the headgroup region must be used to account for this exchange.

3.2.4.3 Order parameters

Since I have shown that interpretation of the peak positions is compromised when focus is degraded, I have omitted these data here. The $I(d^-)/I(d^+)$ data are shown as a function of time in figure 3.20 (a) and (b). Subfigure (a) shows data for the Na^+ containing system. Between 0 and 6000 seconds, there was a steady decrease in $I(d^-)/I(d^+)$ with time and a concomitant increase in scatter. Upon refocussing, at 6000 seconds, the decrease was lost and the parameter recovered to its initial values. After rinsing at ≈11000 seconds, the $I(d^-)/I(d^+)$ values increased slightly. These data are difficult to interpret as a result of the very high degree of defocussing for this run. In my introductory framework of this chapter I described how an artificial reduction in $I(d^-)/I(d^+)$ can occur when signal levels drop by a large factor. Figure 3.18 (a) shows a clear increase of variance in component weight with time; in fact the total signal dropped to 10% of its original value. I think that the decrease in the $I(d^-)/I(d^+)$ data between 0 and 6000 seconds was a result of the high signal loss for this experiment and was not indicative of any structural change. However, I have included these data here as they are the only kinetic data I have of formation for this system despite having successfully prepared POPE SLBs in this buffer several times.

The data for POPE in Ca^{2+} are shown in figure 3.20 (b). These data show an increase in $I(d^-)/I(d^+)$ between 1000 and 4000 seconds. This increase coincides with an increase in component weight above the initial stepwise increase shown in figure 3.18 (a). These two data-sets show that extraneous POPE adsorbed to the surface during this period. For POPC and egg-SM the build-up of loosely bound vesicles to the SLB was characterised by a decrease in $I(d^-)/I(d^+)$. For POPE in Ca^{2+} as the value of $I(d^-)/I(d^+)$ increased, the aggregates comprising the build-up cannot be vesicles. It is not possible to interpret the actual $I(d^-)/I(d^+)$ values in this case as we have no knowledge of the aggregates internal structure. In general, given similar molecular orientation to the evanescent electric field, the greater the $I(d^-)/I(d^+)$ value the more ordered the alkyl chains of the probed structure. The final order parameter values after rinsing were again very similar being 1.102±0.005 for the Na^+ containing buffer and 1.097±0.006 for the Ca^{2+} containing buffer.

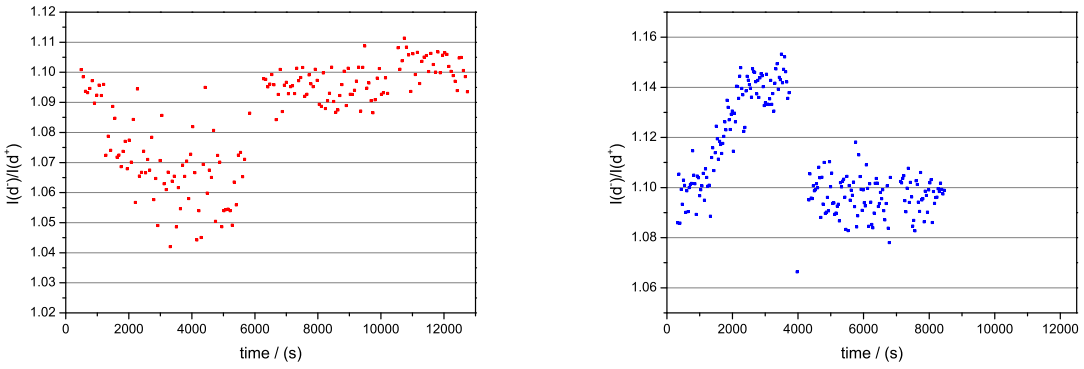

(a) (b)

Figure 3.20: Graphs (a) and (b) showing the change in the peak intensity ratio $[I(d^-)/I(d^+)]$ with time for (i) 20 mM tris pH 7.4 + 100 mM NaCl and (ii) 20 mM tris pH 7.4 + 2 mM $CaCl_2$ respectively. 32°C, 800 mW, 73° incidence. Data were compiled from averaged background subtracted TIR-Raman spectra: (i) 10 spectra over 70 s and (ii) 5 spectra over 35 s.

3.2.5 POPE:egg-SM:Cholesterol

SLBs composed of lipid mixtures have become relevant in recent years due to the growing interest in lipid rafts. Rafts are regions within real cell membranes enriched in cholesterol and sphingomyelin relative to the surrounding membrane, which act as domains for specific membrane proteins.[80,81] To model the cellular processes associated with lipid rafts, SLBs are required that approximate their behaviour. Accurate biomimetic models will therefore contain multiple lipid species. Owing to the increase in SM and cholesterol these regions are more ordered than the surrounding bilayer and form a distinct phase the L_o or liquid ordered phase. One current problem is that these "rafts" would need to exist on both sides of the cell membrane but the distribution of lipids on either side of real membranes are quite different; they would have to be coupled in some way.[74] For example, for human erythrocyte membranes, PC and sphingomyelin dominate the phospholipid component on the external side, whilst PE and PS dominate the inner leaflet.[25] Interestingly these ordered regions have been found to be resistant to solubilisation by surfactants and have hence been called detergent resistant membranes (DRMs).[82]

An advantage of TIR-Raman spectroscopy is that if offers chemical information which few other techniques commonly used for studying the formation of SLBs can offer. Chemical information can be extracted from neutron reflectometry data, but this technique is signal limited and is used infrequently to study kinetic processes at the time scale necessary for SLB formation. ATR-FTIR spectroscopy, which has been used recently to study SLB formation, has several disadvantages in comparison to TIR-Raman when studying very thin films at interfaces; it also has practical difficulties which are unimportant in TIR-Raman.[83] For example a very large water background that overwhelms the CH absorptions and a much greater penetration depth. In this section I describe the use of TIR-Raman to study the formation of SLBs from a 1:1:1 molar mixture of POPE, egg-SM and cholesterol and show how TIR-Raman can be used to find the composition of the final SLB.

3.2.5.1 Vesicle size distributions

Figure 3.21 shows the vesicle/aggregate size distributions for the lipid mixture in (i) 20 mM tris pH 7.4, (ii) 20 mM tris pH 7.4 + 100 mM NaCl and (iii) 20 mM tris pH 7.4 + 2 mM $CaCl_2$. In the pure tris buffer (i), the lipid mixture has a broad size distribution similar to POPE. When sodium and calcium are added there is a well defined narrow peak with a smaller number of large aggregates; inspection of the video sequences used to generate these size distributions show similar images to those obtained for POPC and egg-SM. I have therefore interpreted these primary peaks as vesicles. The peak in the vesicle distribution is 161 nm with Na^+ and 158 nm with Ca^{2+}.

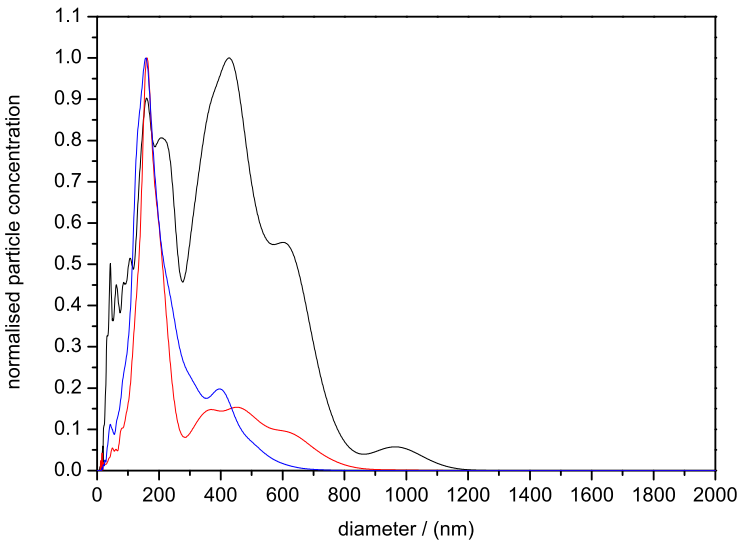

Figure 3.21: Vesicle size distributions acquired for 1:1:1 POPE:egg-SM:Cholesterol aggregates/vesicles in: (i) 20 mM tris pH 7.4 (black), (ii) 20 mM tris pH 7.4 + 100 mM NaCl (red) and (iii) 20 mM tris pH 7.4 + 2 mM $CaCl_2$ (blue). All at 32°C.

3.2.5.2 POPE:egg-SM:Chol adsorption

As the CH-region was virtually identical for all measurements of the mixture, a single representative spectrum could be used as the target for TFA analysis. In addition, by using the same refined spectrum for all systems the component weight data were directly comparable. Using targets for the three individual components was not possible as the differences between them in the CH-region were too small for TFA to recognise them as different factors in the abstract reproduction. In theory it is possible to determine the composition of this mixture by making use of the finger print region, but the signal levels attainable at the laser powers suitable for studying SLBs are too low to allow kinetic measurements. Selective deuteration of one species in the mixture could be used, but this would only allow one of the three components to be measured independently. It was unfortunate that the composition of the mixed SLB could not be observed during my kinetic measurements as studying the change in composition of the SLB as it formed would have been interesting. These considerations do not preclude one from calculating the composition from extended equilibrium scans following the formation of the mixed lipid SLB.

In 20 mM tris at pH 7.4 I did not observe SLB formation. However, I was able to form SLBs in tris with added sodium and calcium. Figure 3.22 (a) and (b) show the component weights with time for (i) 20 mM tris pH 7.4 + 100 mM NaCl and (ii) 20 mM tris pH 7.4 + 2 mM $CaCl_2$. Both show a rapid increase in the mixture component weight after the initial dead time. The uptake of mixture was quicker for the calcium containing buffer (ii) than the sodium containing buffer (i) taking 36 s and 69 s respectively. In figure 3.22 (b) a closeup of the region of rapid increase, we see that for both the sodium and calcium containing systems, the rate of adsorption accelerates with time. After this period of rapid increase, I observed a small degree of build-up for buffer (i) and a larger build-up for buffer (ii). Note the passing of a larger aggregate across the interface in the buffer (ii) data at approximately 2000 s. Rinsing was commenced at approximately 6000 seconds

and the build-up was removed for both systems.

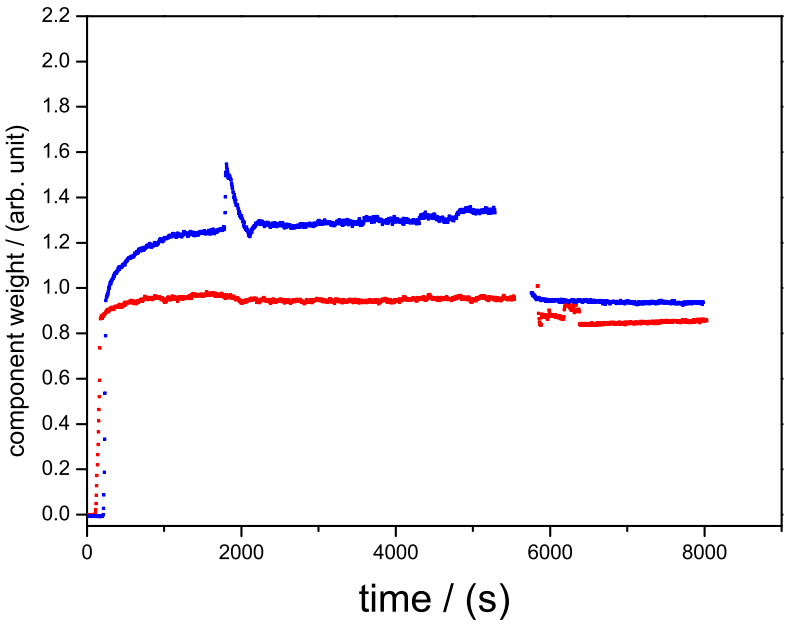

(a)

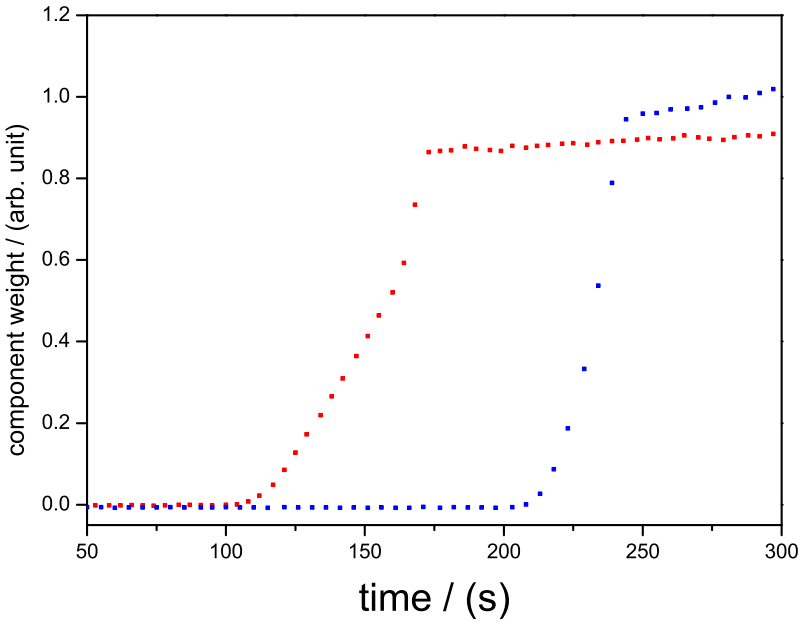

(b)

Figure 3.22: Graphs showing the normalised component weights of the POPE:egg-SM:cholesterol mixture at the silica-buffer interface with time in solutions (i) 20 mM tris pH 7.4 + 100 mM NaCl (red) and (ii) 20 mM tris pH 7.4 + 2 mM $CaCl_2$ (blue), 32°C, 800 mW, 73° incidence. (a) full duration, (b) closeup of rapid adsorption stage. Acquisition times: (i) 3 s, (ii) 3.5 s.

3.2.5.3 Order parameters

The $I(d^-)/I(d^+)$ data as function of time are shown in figure 3.23 (a) and (b) for sodium and calcium containing tris buffers respectively. For the Na^+ containing buffer the first few data data points show a significantly lower order parameter compared to the final SLB. These values indicate the presence of vesicles at the interface; the fact that only two of these points exist suggests that SLB formation took place in under 1 minute. Also, as these values increase with component weight they lead to the conclusion that there was no, or an extremely low, critical vesicular coverage for this system. As the vesicle build-up was low, the decrease in the $I(d^-)/I(d^+)$ ratio between 500 and 5500 seconds is lower than the equivalent period for egg-SM and POPC. Upon rinsing intensity ratio recovers to values very similar to those acquired just prior to the onset of build-up. In buffer containing 2 mM Ca^{2+}, the intensity ratio follows a similar trend to the Na^+ containing system, but as the formation of the SLB occurred too quickly we were unable to observe intermediate data points corresponding to the early stages of bilayer formation. Between 500 and 5500 seconds we observe a decrease in the $I(d^-)/I(d^+)$ ratio corresponding to the build-up observed in the component weight data. Interestingly, the final order parameter values measured for this system are higher than those measured for any of the other pure lipid systems in the L_α phase; being 1.167±0.007 for the Na^+ containing system and 1.163±0.008 for the Ca^{2+} containing system. These values indicating that the finished fluid phase SLB after rinsing is more ordered than the SLBs composed purely of POPC, egg-SM and POPE.

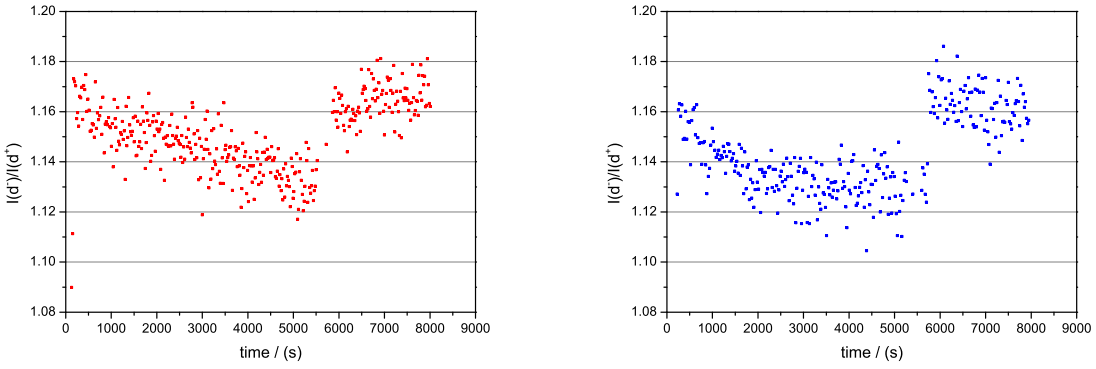

(a) (b)

Figure 3.23: Graphs (a) and (b) showing the change in the peak intensity ratio $[I(d^-)/I(d^+)]$ with time for the 1:1:1 POPE:egg-SM:cholesterol mixture in: (i) 20 mM tris pH 7.4 + 100 mM NaCl and (ii) 20 mM tris pH 7.4 + 2 mM $CaCl_2$ respectively. Both at 32°C. Data were compiled from averaged background subtracted TIR-Raman spectra: (i) 4 spectra over 20 s and (ii) 4 spectra over 25 s.

3.2.5.4 Compositional analysis

For the 1:1:1 POPE:egg-sm:cholesterol mixed system it was important to confirm that the finished SLB contained the expected mole fractions of the intended components. This is especially true considering a recent article that found compositional differences between mixed component vesicles suspensions and SLBs formed from them.[84] By preparing a series of mixed SLBs by vesicle fusion, where one component of the mixture was deuterated, I found the mole fraction of the deuterated species by quantitative analysis (see section 2.4.5.3). By collating the results of two

formations, the composition of the mixed SLB at equilibrium was deduced – this was done twice for certainty. In addition, a similar procedure was carried out with deuterated cholesterol only, where the ester C=O stretch of POPE, an isolated band, was used as a quantitative marker for that species. By only deuterating cholesterol the mole fractions of all three species could be found in a single preparation. The former method relied on the assumption that the ratio of components was the same for the two vesicle suspensions used for any pair of experiments. However, the C=O ester stretch is very weak, thus slight changes in the background can lead to large errors in the composition. For this reason I used both methods. From these experiments I found that within a few percent the composition was 1:1:1 in general agreement with the relative quantities used in the preparation of the mixed vesicles.

3.3 Conclusions

In this chapter I have examined the formation of SLBs of POPC, egg-SM, POPE and a 1:1:1 mixture of POPE, egg-SM and cholesterol in: (i) 20 mM tris pH 7.4, (ii) 20 mM tris pH 7.4 + 100 mM NaCl and (iii) 20 mM tris pH 7.4 + 2 mM $CaCl_2$. I found that POPC formed SLBs in all buffer conditions used, but that the degree of extraneous vesicle adsorption varied depending on the solution conditions. For egg-SM, SLBs could be prepared in all buffer conditions, but the degree of build-up was the same for tris only and sodium containing buffers and build-up did not occur for the calcium containing buffer. For POPE it was not possible to prepare an SLB in pure tris buffer at pH 7.4, however it was possible to prepare SLBs in the calcium and sodium containing buffers although less reproducibly in the latter. It was not possible to prepare an SLB composed of the mixed system in pure tris. However, it was possible in the sodium and calcium containing buffers. I have been able to compare my observations with those made before. In most of my data, formation occurred quickly and so I was unable to gain a detailed view on the formation of SLBs at that early stage. However, in some of the systems studied I was able to glimpse this stage and in those systems I saw no evidence for the CVC espoused by Kasemo and coworkers; this is in line with Fygenson's recent work on DMPC. I did however observe the acceleration of the formation process with time in most systems, although it was moderated in some, slowing near to completion; this particular feature has not been observed in the literature before. These data suggest a highly cooperative formation mechanism where the more vesicles and SLB existing at the interface the faster additional vesicles adsorb and rupture to form SLB. But this synergy is hindered in the latter stages of formation of egg-SM SLBs in tris only and sodium containing buffers. Interestingly, the build-up of additional aggregates at the SLB interface that are only removed with pure buffer rinsing directly contrasts with the observations of Fygenson and coworkers who suggest that lipid leaves *en masse* upon SLB completion. In my work on the POPE system, I observed a stepwise SLB formation pathway not previously known; it appears that the larger aggregates attach to the surface and subsequently spread to form SLB. In further work I would study the formation behaviour for lipid systems with much reduced vesicle concentrations, this would reduce the rate of formation drastically and give much more insight into the early stages of formation, which occurred too quickly to be observed in any detail in this work. Further work searching for ways to estimate mixed species SLB composition kinetically could also be very rewarding.

Chapter 4

Phase transitions in supported lipid bilayers

4.1 Introduction

In this chapter I will investigate the phase transitions of a selection of SLB systems hydrated in tris buffer on SiO_2 with additional NaCl or $CaCl_2$. The physical state of lipid bilayers plays an important role in many biological processes. The desire to understand the phase behaviour of lipid bilayers thus stems from a desire to understand the properties of real cell membranes. Without a thorough understanding of how single component lipid bilayers and mixed lipid systems behave with regard to their environment and temperature we cannot understand real membrane behaviour. This prime concern is important because the state of lipid molecules within bilayers has influence on the interaction of the lamellar part of the bilayer with its embedded proteins and hence protein function.[85] In addition one cannot ignore the roles of other species prevalent in biological systems when studying model membranes. For instance, as I previously discussed in the review of the last chapter, cations have been shown to bind and alter the structure of supported lipid bilayers. Studying the effect of cation binding on the phase behaviour of lipid bilayers will provide greater insight into real membranes. A practical reason to study these systems is that lipid biophysics has great relevance in nanotechnology and pharmaceutical design. Specifically if vesicles/liposomes are to reach target cells, specific requirements have to be met so they survive the journey – generally having the liposome bilayer in the gel phase under physiological conditions is preferred.[86]

4.2 Background Theory

Phase transitions occur as temperature, pressure and composition change because the chemical potential of the components in one phase is lower than any other. At the temperature, pressure and composition where multiple phases exist and the chemical potential of each component is equal to all others, the system is said to be in equilibrium.

4.2.1 Phase transitions in lipid bilayers

Lipid bilayers as found in biological membranes and related model systems are two dimensional lyotropic liquid crystals and can exist in a number of phases. For illustration, DPPC, like most other hydrated medium chain phosphatidylcholines and phosphatidylglycerols, displays four lamellar phases. In order of increasing temperature these are: (1) the crystal phase (L_c), (2) the gel phase (L_β), (3) the ripple phase P_β and (4) the fluid or "liquid crystalline" L_α phase.[87] The most well known phase transition and that with the highest transition enthalpy commonly referred to as the "main phase transition" lies between the ripple (P_β) and fluid (L_α) phases in many phosphatidylcholines. Using DPPC as an example, the main transition enthalpy change is ΔH = -33 kJ mol^{-1}. The transition from the L_β to P_β phase is commonly referred to as the pretransition, and during cooling a long incubation is often required to enter the L_c phase owing to the metastability of the L_β phase – the pretransition often displays a marked hysteresis. It is worth noting that in PCs the hydrocarbon chains are tilted with respect to the bilayer normal. Many classes of glycerophospholipids, such as the phosphatidylethanolamines, do not display a P_β phase and show a non-tilted L_β phase. Also, short chain PEs show a metastable L_β phase undergoing a phase transition to the L_α phase at a temperature (T_t) above T_m. Some lipids, of which POPE is member, display non-bilayer phases. For instance at a relatively high temperature (74.8°C), POPE displays a lamellar to inverse hexagonal phase ($L_\alpha \rightarrow H_{||}$) transition.[88] Referring to my introductory chapter about preferred geometry and the critical packing parameter, it is easy to see why this might be the case; POPE's headgroup occupies a far smaller cross-sectional area than its hydrocarbon tails – its Z_p value is greater than one above this transition temperature. What defines the different lamellar phases are the intramolecular order of their constituent molecules, their chain packing geometry, internal fluidity in terms of lateral and vertical translocation, the degree of thermal protrusion and lastly the number of thermal fluctuation modes. Several good sources of thermodynamic data on different lipid bilayers and their phase transitions are available.[75,89,90]

4.2.2 Gibbs phase rule

Josiah Willard Gibbs developed his "phase rule" after coming to a mathematical realisation about the number of intensive system variables that can be changed whilst still retaining the same number of phases. His expression is given by,

$$F = C - P + 2 \tag{4.1}$$

where F is the variance or the number of degrees of freedom, C is the number of chemically independent components and P is the number of phases. The total number of intensive variables is given by,

$$X = P(C-1) + 2. \tag{4.2}$$

Here '2' corresponds to the temperature and pressure, $(C-1)$ corresponds to the compositional knowledge required to define the composition of any one phase. Lastly the multiplication by factor P scales the number of intensive variables according to the total number of distinct phases.
We can write equalities between the chemical potentials of a given component in the different phases as functions of the intensive variables to define equilibrium.

$$\mu(\alpha, p, T) = \mu(\beta, p, T) = \cdots \tag{4.3}$$

where α and β label the different phases. This forms a system of linear simultaneous equations. To solve this system we need to satisfy $P-1$ equations for each chemical component. As there are C components the number of equations required is, $C(P-1)$. Each of the equations in the system reduces our freedom to vary one of the intensive variables concomitantly with the others, this implies that,

$$F = P(C-1) + 2 - C(P-1) = C - P + 2, \tag{4.4}$$

which is the Gibbs phase rule. This expression essentially defines the internal geometry of phase diagrams. For instance, for a one component system such as water, if we imagine a situation where solid, liquid and gas exist as three phases in equilibrium we find that we have no degrees of freedom, or $F = 0$. In other words this equilibrium can only exist as a point on the phase diagram and this point is commonly known as the triple point. This also tells us that the maximum number of phases that can exist in equilibrium for a single component system is three, imagining any higher number would lead to a variance of less than 0 which is meaningless. This simple rule elegantly defines what is possible in terms of the physical state of matter for any system under consideration.

4.2.3 Ehrenfest classification

Many types of phase transition exist in many different contexts; from the commonplace – such as the vaporisation of water – to the exotic – smectic to nematic transitions in liquid crystals, but how do we classify them logically? Ehrenfest suggested a rigorous method devised in terms of the derivatives of the free energy for a given system. Many phase transitions are accompanied by enthalpy and volume changes, so for a transition from a phase α to a phase β one finds,

$$\left(\frac{\partial\mu(\beta)}{\partial p}\right)_T - \left(\frac{\partial\mu(\alpha)}{\partial p}\right)_T = V_m(\beta) - V_m(\alpha) = \Delta_{trs}V \tag{4.5}$$

or

$$\left(\frac{\partial\mu(\beta)}{\partial T}\right)_p - \left(\frac{\partial\mu(\alpha)}{\partial T}\right)_p = -S_m(\beta) + S_m(\alpha) = -\Delta_{trs}S = -\frac{\Delta_{trs}H}{T_{trs}} \tag{4.6}$$

these changes in system properties at the transition temperature are discontinuous. Ehrenfest defined first order transitions as those with discontinuities in the first derivative of the chemical potential with respect to temperature or pressure. A common property of systems which have a discontinuous change in enthalpy at the phase transition temperature is that their constant pressure heat capacities become infinite during the transition. Second order transitions are those where the changes in the first derivatives are continuous but those in the second derivative are discontinuous, examples include the conducting-superconducting transition in metals at low temperatures.

4.2.4 Basic thermodynamics of lipid bilayer main phase transitions

For first order phase transitions, the Gibbs free energy is continuous but there are discontinuous changes in the enthalpy and entropy of transition.[91] We can therefore write,

$$\Delta G_t = \Delta H_t - T\Delta S_t = 0 \tag{4.7}$$

where the subscript 't' indicates at the transition temperature T_t. The transition temperature is thus defined by,

$$T_t = \frac{\Delta H_t}{\Delta S_t}. \tag{4.8}$$

Hydrocarbon chain melting is the primary contributor to the main phase transition enthalpy. When considering lipids with constant chain asymmetry or no asymmetry, the transition enthalpy and entropy depend linearly on chain length, n,

$$\Delta H_t(n) = \Delta H_{inc}(n - n_H) \tag{4.9}$$

and

$$\Delta S_t(n) = \Delta S_{inc}(n - n_s), \tag{4.10}$$

where ΔH_{inc} and ΔS_{inc} are the incremental transition enthalpy and transition entropy per CH_2 group. n_H and n_S are the chain lengths for which the transition enthalpy and entropy extrapolate to zero – these are included to account for "end" effects which include contributions to the transition enthalpy and entropy from a number of sources. These sources include contributions from lipid headgroups, the hydrocarbon chain linkages, chain terminal methyl groups, chain asymmetry effects and are given by,

$$\Delta H_{end} = n_H \Delta H_{inc} \tag{4.11}$$

$$\Delta S_{end} = n_s \Delta S_{inc} \tag{4.12}$$

The temperature of transition can be defined by,

$$T_t(n) = T_t^{\infty}\left(1 - \frac{n_H - n_s}{n - n_s}\right) \tag{4.13}$$

where T_t^{∞} is the transition temperature extrapolated to infinite chain length ($T_t^{\infty} = \frac{\Delta H_{inc}}{\Delta S_{inc}}$). The chain melting transition temperatures of diacyl phospholipids with symmetrical cis-monoenoic chains, or with a saturated *sn*-1 chain and a cis-monoenoic *sn*-2 chain, show a biphasic dependence on the position of the double bond within the chain, n_u. At some position within the chain, the transition temperature shows a minimum about which the melting transition temperature increases linearly. The minimum is usually close to the center of the chain but not exactly at it and we can define it position as n_c. The variation of the transition enthalpy and entropy as a function of the double bond position are given by,

$$\Delta H_m(n, n_u) = \Delta H_m^c(n) + \Delta h_c|n_u - n_c(n)| \tag{4.14}$$

$$\Delta S_m(n, n_u) = \Delta S_m^c(n) + \Delta s_c|n_u - n_c(n)|, \tag{4.15}$$

where $\Delta H_m^c(n)$ and $\Delta S_m^c(n)$ are the extreme values of $\Delta H_m(n, n_u)$ and $\Delta S_m(n, n_u)$ which are the values obtained when the double bond is at the critical position on the chain.

4.2.5 Cooperativity and the statistical mechanics of bilayer thermotropic phase transitions

A little discussed topic of relevance for the phase transitions of lipid bilayers is the degree of cooperativity of the phase transition. Main phase transitions are dependent on the size of the

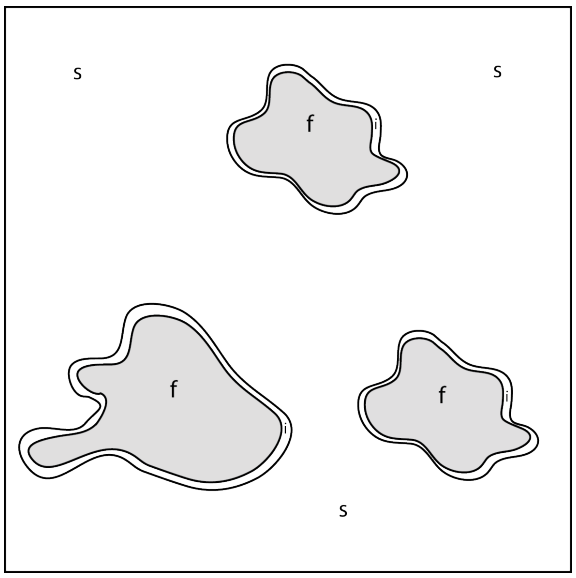

Figure 4.1: A diagram showing the three states assumed by the Zimm and Bragg model; s, f and i show the gel, fluid and interfacial regions respectively.

cooperative unit of the phase transition, or the size of the lateral domain in which lipid molecules undergo the phase transition as a collective group. This cooperativity determines the 'sharpness' of the transition or the temperature range over which phase separation of the gel/ripple and fluid phases exists.

The Zimm and Bragg model,[92] originally conceived as a statistical mechanical model for the transition of random coils to alpha helices in peptide chains, can be applied to describe phase transitions in lipid bilayers.[93] In this model it is assumed that there are three lipid states during the transition: the gel state, s, the fluid state, f, and an intermediate state that corresponds to the interface between domains of gel and fluid phase, a diagram is shown in figure 4.1. The free energies of the lipid molecules that comprise the three hypothetical states are principally determined by the internal energy associated with the structure of their hydrocarbon tails as well as from the intermolecular interactions between the lipid molecules themselves, such as the van der Waals interaction, the electrostatic interactions between the charged lipid headgroups and the hydration interaction between adjacent lipid headgroups. Taking the free energy of an L_β phase all trans configured lipid molecule to be $G_s = 0$ and the free energy of a fluid state lipid fully embedded within a fluid domain to be G_f. We can define the free energy of a lipid molecule at the interface of the two phases to be $G_i + G_f$ where G_i is the additional free energy associated with the structural mismatch between the two phases. N.B this additional free energy is assigned to a fluid molecule out of convention, it corresponds to the molecules on either side of the interface but can only be counted once. G_i is unfavourable because disruption to the interactions between the molecules on each side of the phase boundary are greater than the gain in configurational entropy. Entropy provides a smaller contribution in this situation owing to the rapid fall of the van der Waals interaction with distance between the adjacent lipid chains and the other interactions in the headgroup region. The cooperativity that exists between lipid molecules stems from the fact that it is energetically favourable for a molecule to be embedded amongst other lipid molecules in the same physical state as itself. This cooperativity can be represented by a statistical weight matrix, the elements of which, $u_{\zeta\eta}$, are the statistical weights of molecules in a state ζ with surrounding

molecules in state η

$$U = [u_{\zeta\eta}] = \begin{array}{c} \\ s \\ f \end{array} \begin{array}{c} \begin{array}{cc} s & f \end{array} \\ \begin{pmatrix} 1 & \sigma s \\ 1 & s \end{pmatrix} \end{array}. \tag{4.16}$$

Where s is the statistical weight of a fluid state molecule, and is given by,

$$s = \exp(-G_f/RT), \tag{4.17}$$

where the fluid state free energy is,

$$G_f = \Delta H_t - T\Delta S_t \tag{4.18}$$

here ΔH_t and ΔS_t are the transition enthalpy and entropy respectively. The second parameter, σ is the cooperativity parameter, which is related to the size of the domains that change phase as units,

$$\sigma = \exp(-G_i/RT). \tag{4.19}$$

The molecular partition function is then,

$$Q = \sum_{n_s, n_f, n_i} z_s^{n_s} z_f^{n_f} z_i^{n_i}. \tag{4.20}$$

In this expression n_s and n_f are the number of lipid molecules in the gel and fluid liquid crystalline phases respectively; n_i is the number of fluid phase molecules at the interface between the two phases. Incidentally, the total number of molecules is given by $n = n_s + n_f$. z_s and z_f are the molecular partition functions of molecules in the ordered gel and fluid liquid crystalline phases. z_i is the partition function pertaining to the excess energy of molecules at the interface. Substituting for the partition functions in equation 4.20,

$$Q = \sum_{n_f=0}^{n} s^{n_f} \sigma^{n_i} \tag{4.21}$$

This partition function can be evaluated by sequential multiplication of the statistical weight matrix taking into account the lipid molecules present at the interfacial region. This multiplication is aided by diagonalising the statistical weight matrix. The roots of equation 4.16 are,

$$\lambda_{1,2} = 1/2[(1+s) \pm \sqrt{(1-s)^2 + 4s\sigma}]. \tag{4.22}$$

Since the number of molecules in the ensemble is large, an approximation for the partition function can be employed,

$$Q = \lambda_1^n \tag{4.23}$$

where λ_1 is the larger of the two roots gained from equation 4.22. From equations 4.20 and 4.21, we can deduce the mean fraction of lipid molecules in the fluid or liquid crystalline state or the degree of transition, θ,

$$\theta = \frac{\langle n_f \rangle}{n} = \frac{1}{n} \frac{\partial \ln Q}{\partial \ln s} = \frac{\partial \ln \lambda_1}{\partial \ln s}. \tag{4.24}$$

Substitution of equation 4.22 into this expression yields theta as a function of σ and s,

$$\theta = \frac{1}{2}\left[1 + \frac{s-1}{\sqrt{(s-1)^2 + 4\sigma s}}\right]. \tag{4.25}$$

A similar procedure can be carried out to determine the average number of molecules in the interfacial region during the transition,

$$\eta = \frac{\langle n_i \rangle}{n} = \frac{1}{n}\frac{\partial \ln Q}{\partial \ln \sigma} = \frac{\partial \ln \lambda_1}{\partial \ln \sigma}, \tag{4.26}$$

Again we can follow this with substitution of equation 4.22 to yield η as a function of s and σ,

$$\eta = \frac{2\sigma s}{(1+s)\sqrt{(1-s)^2 + 4\sigma s + (1-s)^2 + 4\sigma s}}. \tag{4.27}$$

Knowledge of the mean size of gel and fluid regions during a phase transition are of interest as they aid in understanding the structure of an SLB during a transition. These mean sizes can be expressed as the number of gel or fluid molecules per interfacial molecule for each value of θ. For the fluid phase,

$$\langle \nu_{L_\alpha} \rangle = \frac{\theta}{\eta} = \frac{1 + s + \sqrt{(1+2)^2 + 4s\sigma}}{1 - s + \sqrt{(1-s)^2 + 4s\sigma}}, \tag{4.28}$$

and for the solid phase,

$$\langle \nu_{L_\beta} \rangle = \frac{(1-\theta)}{\eta} = \frac{1 + s + \sqrt{(1-2)^2 + 4s\sigma}}{-1 + s + \sqrt{(1-s)^2 + 4s\sigma}}. \tag{4.29}$$

At the center of the transition where s, by definition, must equal 1, the mean sizes given by the expressions above must be equal, and we can therefore say,

$$\langle \nu_{L_\beta} \rangle_{T_m} = \langle \nu_{L_\alpha} \rangle_{T_m} = \frac{1}{\sqrt{\sigma}} + 1. \tag{4.30}$$

To compare the model with calorimetric experiments, equation 4.17 can be made linear by a Taylor expansion about the transition temperature,

$$s \simeq 1 + \frac{\Delta H_t}{R T_t^2}(T - T_t), \tag{4.31}$$

By differentiating equation 4.25 after substituting for s by equation 4.31 we obtain,

$$\left.\frac{d\theta}{dT}\right|_{T_t} = \frac{1}{4\sqrt{\sigma}} . \frac{\Delta H_t}{R T_t^2}. \tag{4.32}$$

By considering a broadened or cooperative phase transition as a pseudo unimolecular reaction with an equilibrium established between the gel and fluid phases, $L_\beta \rightleftharpoons L_\alpha$, with an equilibrium constant given as a function of θ, $K_t = \theta/(1-\theta)$, equation 4.32 can be expressed in the van't Hoff form where $\Delta H_{vH} = (1/\sqrt{\sigma})\Delta H_t$:

$$\left.\frac{d\theta}{dT}\right|_{T_t} = \frac{\Delta H_{vH}}{4 R T_t^2} \tag{4.33}$$

These expressions show that in the vicinity of $T = T_m$, θ has a linear dependence on $1/T$. Equation 4.33 implies the plot will have a gradient of $-\Delta H_{vH}/4R$. Experimentally, if some parameter is available that is sensitive to the fractional coverage of the L_α phase during a phase transition, the

van't Hoff transition enthalpy can be found. Comparison of equations 4.32 and 4.33 shows that,

$$\Delta H_{vH} = \frac{1}{\sqrt{\sigma}} \Delta H_t, \tag{4.34}$$

which implies,

$$\frac{1}{\sqrt{\sigma}} = \frac{\Delta H_{vH}}{\Delta H_t}. \tag{4.35}$$

The reciprocal square root of the cooperativity parameter yields the number of molecules within each cooperative unit, the individual contributors to the 'reaction' van't Hoff enthalpy. With knowledge of σ at T_t it is possible to quantitatively fit experimental θ values with equation 4.25 by varying s using a least squares procedure. Some example plots of predictions made by the Zimm and Bragg model are shown in figure 4.2: subfigure (a) shows how s has been scaled with T for the plots in subfigures (b) and (c), in general s will not be linear in T (see equation 4.17). Subfigure (b) shows the variation in θ for two values of the cooperativity parameter, σ, the smaller σ, the sharper the transition or the narrower the temperature range over which it occurs. Subfigure (c) shows the variation of the free energy of a fluid state molecule embedded within a fluid phase domain as a function of temperature, notice how $G_f = 0$ at $\theta = 0.5$. As G_s is defined as zero at the phase transition temperature, the phase transition is still first order even though the structural transition occurs over a range of temperatures.

4.2.6 The effect of electrolyte on the main phase transition and ion binding

No significant changes in the calorimetric transition enthalpy of phosphatidylcholines have been observed until very high salt concentrations.[90] In general smaller electrolytes increase the temperature of the main phase transition of lipid bilayers. For charged lipids the initial increase in transition temperature is a result of the screening of their headgroup charge as this otherwise acts to reduce to the transition temperature.[94] However, for zwitterionic lipids and effectively screened charged species, higher concentrations of electrolyte reduce the hydration of the lipid headgroups by specific binding. By dehydrating the headgroup region bilayers become more like their anhydrous analogues which have higher transition temperatures. To date there has been little or no discussion of the role of salts on the cooperativity of bilayer main phase transitions. Some work has been carried out on the modulation of the support-SLB interaction potential; this will be discussed in the following review sections.

4.3 Review

A large quantity of experimental and computational work has been carried out with the aim to understand various lipid phase transitions for pure species and mixtures in the bulk as well as at the interface. Owing to the large quantity of literature in this field, I will mostly stick to articles which provide the specific context for my experimental work. Many techniques have been used to study bilayer phase transitions each with their benefits and limitations. I will structure this review according to whether a study was conducted on a bulk lipid phase or on an interfacial system. I will also have a smaller section for computational studies.

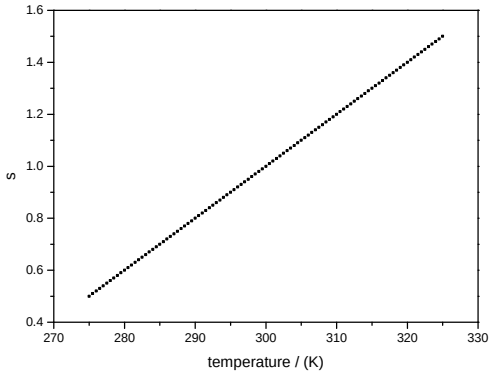

(a)

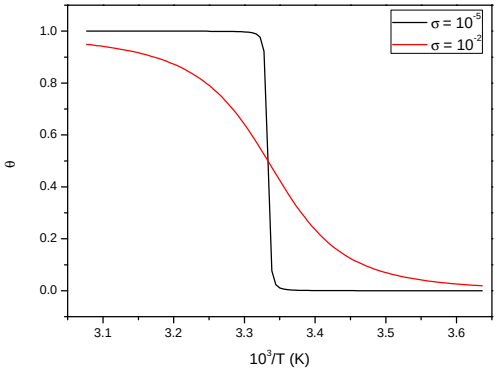

(b)

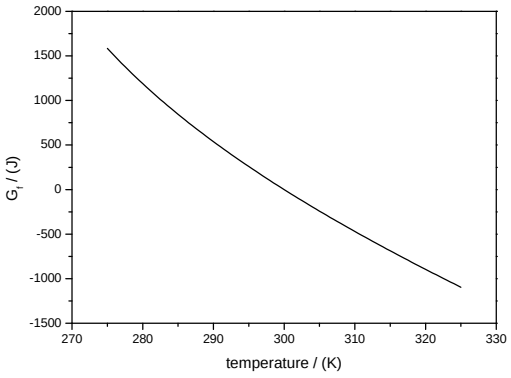

(c)

Figure 4.2: Some theoretical predictions of the Zimm and Bragg model. Subfigure (a) shows how s has been scaled with T. Subfigure (b) shows the variation in θ calculated from equation 4.25, for the values of s shown in (a) and fixed values of σ. Subfigure (c) shows the variation in the free energy of a fully embedded fluid phase lipid molecule relative to an embedded solid state molecule at the transition temperature.

4.3.1 Studies on bulk lipid phases

^{31}P and ^{13}C NMR have been used by Martin and coworkers to study phase transitions in unsonicated hydrated suspensions of bovine brain sphingomyelin (SPM).[95] ^{31}P NMR is particularly useful in finding evidence of non-bilayer phases – such as the hexagonal phase – as a result of the motional averaging commonly found in these phases. They found evidence of four phases: L_β, L_α a lamellar phase and a non-bilayer phase. However, they found that the heating measurements did not produce the same spectra as the cooling scans – indicating some metastability of the non-bilayer phase at high temperature. It is worth noting that this study is quite old (1976) and the authors themselves indicate a lack of reducibility between SPM consignments. Regardless the authors found that the presence or absence of 100 mM NaCl had no measurable effect on the transition. The authors found evidence for phase transitions at 28°C and between 37-48°C although these values should be considered approximate owing to the reproducibility issues stated before.

Differential scanning calorimetry (DSC) has been used to quantify the phase transitions of a variety of lipids and lipid mixtures under a variety of conditions over the years. This ensemble includes one study where POPE SUV's were investigated with and without the presence of 10 mM Ca^{2+} in solution.[96] However, the solution to which the Ca^{2+} was added was already fairly complex comprising; 20 mM Pipes, 150 mM NaCl, 0.02 mM ml^{-1} NaN_3 pH 7.40 with 1 mM EDTA in the absence of Ca^{2+}. In this work it was shown that the T_m of the POPE bilayer was approximately 25°C in accordance with the generally accepted figure and that 10 mM Ca^{2+} had a negligible effect on the main phase transition enthalpy but did result in a slightly lower transition temperature (they do not provide a tabulated value). Unfortunately DSC cannot give morphological or conformational information about the state of the lipid bilayer but only average thermodynamic data. For this reason the authors of the previous paper used ^{31}P NMR to study these aspects, but sadly they only did so for the hexagonal to lamellar phase transition. This is unfortunate as previously mentioned in the review of the last chapter, Ca^{2+} is expected to bind to the phosphate diester oxygens in POPE which could result in morphological changes.

Ogino *et al.* using ATR-IR (zinc selenide cell) and DSC have investigated the effect of group II cations (Ba^{2+}, Ca^{2+} and Mg^{2+}) on the thermotropic phase transitions of bulk vesicles composed of DPPC and DPPG.[97] The behaviour in H_2O and D_2O was compared. The authors note that DPPG is more ordered in the presence of Ca^{2+} and that an isothermal crystallisation can take place at a high Ca^{2+} concentration; however, the same effect was not observed for Ba^{2+} and Mg^{2+}. Crystallisation was not observed for the DPPC system. Examination of the carbonyl stretches allowed the authors to determine the state of headgroup hydration in D_2O and H_2O respectively as well as in the presence of the different cations; the presence of salt affects the hydrogen bonding network between the lipids and thus changed the overall order within the lipid bilayers – it is thus likely to have an influence over the phase transitions of the lipid bilayers.

When looking specifically at the interaction of Ca^{2+} with lipid bilayers one encounters a number of studies. Experimental studies investigating the interaction of Ca^{2+} with anionic lipids are understandably fairly profuse, this resulting from the fact that cationic binding to anionic lipids induces so many biological phenomena – for instance protein kinase C activation by Ca^{2+} binding to adjacent PS lipids.[96] In contrast to this, the number of studies with zwitterionic lipids are very limited, and, when one tries to include studies relating to the thermotropic behaviour the list becomes short. I will give a brief overview of studies with zwitterionic and anionic lipids as they are not necessarily mutually exclusive. An interesting study relating to phosphatidylserine bilayers investigates the effect of unsaturation on the interaction of the lipid species with Ca^{2+}

and other cations.[98] The authors used a variety of techniques including surface monolayer compression, DSC, ^{31}P NMR and spin labelled ESR. They discovered that Na^+ and NH_4^+ interacted only weakly with PS bilayers, that there were no significant changes in conformation within the bilayer and that structural and dynamic properties were little affected. Unsaturation appeared to affect the Li^+ interaction and this was likely due to the changing headgroup areas for the PS species with differing degrees of unsaturation. Lastly Ca^{2+} was shown to have a strong interaction with all PS species investigated and for this class of lipids, unsaturation and headgroup area only had a very small effect on this interaction. Earlier works by the same authors show that Ca^{2+} forms dehydrated crystalline PS complexes, these having a greater degree of order than their lipid only counterparts.[99–102] Fairly recently, aqueous dispersions of DMPG vesicles were investigated, again with ATR-IR spectroscopy; the authors reported observing an induced crystalline-like gel phase in the presence of 1 M solutions of cations including Ca^{2+}, with both the acyl chains being in the all-trans configuration.[103] What was interesting about this study was that the ordering was observed after incubation at low temperature for a 24 hour period – the crystalline gel phase was metastable. When these complexed lipids were heated, different transition temperatures were observed compared with each other and with the nominal T_m of DMPG. When subsequently cooled the disordered fluid phase was also metastable and thus resistant to reversion to a gel L_β phase – the binding was increasing the kinetic energy barrier of the phase transition.

Harris and coworkers have used confocal Raman spectroscopy combined with optical trapping (using the incident pump confocal beam) to monitor the phase transitions in DPPC vesicles.[104] The Raman spectra acquired were analysed using self-modelling curve resolution (SMCR) a form of factor analysis. This form of factor analysis does not use spectral targets – such as those used in the previous chapter – but instead rotates the abstract solutions to match "pure spectra" in the original data. As with most forms of factor analysis this method has trouble dealing with more than two or three factors. For this reason the authors were forced to break their data up into several temperature ranges in order to get the analysis to work. As DPPC has four phases, three temperature ranges had to be used where the internal spectra (representing the gel phase (L_β) and the ripple phase (P_β)) had to be averaged; this implies the internal factors were not exactly the same and could imply a problem with the analysis although the authors point out that subtraction prior to averaging results in an almost flat "baseline". The authors found that the data they acquired compared favourably with calorimetric data acquired by DSC and they found evidence for all four phases from their factor analysis strategy. They also applied the suite of "order" parameters available with Raman spectroscopy to glean evidence of chain disordering, chain decoupling, rotational disorder and gauche defects.

Nagarajan *et al.* have explored the dynamics of the L_β to L_α phase transition in unilamellar DPPC vesicles. They used time-resolved infrared spectroscopy with laser induced temperature jump initiation. They found that the spectral changes which characterised the phase transition were complex and occurred over several timescales. At first there was a rapid partial melting of the hydrocarbon chains (sub-microsecond) initiated at preexisting defects. Soon after, the concomitant lateral expansion increased the pressure within the bilayer essentially raising the transition temperature. Subsequent melting follows stretched exponential kinetics, which resulted from the relaxation of the induced lateral pressure on different timescales by an increase in certain bilayer fluctuation amplitudes. The slowest kinetic step was the transfer of water through the vesicle bilayer to allow it to expand to accommodate the larger equilibrium molecular area.

Recently Law and coworkers have investigated the pressure and temperature phase behaviour of natural sphingomyelin extracts, these included bovine brain sphingomyelin, egg yolk sphingomyelin and milk sphingomyelin.[105] These natural sources have different compositions, which are

shown in figure 4.3. The authors used small and wide angle X-ray scattering along with solid state NMR to follow the phase behaviour of these samples, the samples were not sonicated or extruded prior to use. The authors found the main phase transition temperature of egg-SM to lie between 37 and 40°C. They also found compelling evidence of a low temperature ripple phase and that the gel phase does form unless the system is under high pressure. They note significant differences in the phase diagrams of the three sources, but I have limited my discussion to the data pertaining to egg-SM as it is most relevant for my studies. Figure 4.4 shows the temperature pressure phase diagram of egg-SM taken from reference.[105]

4.3.2 Studies on SLBs and interfacial systems

Tamm and McConnell carried out the earliest work on phase transitions in SLBs using fluorescence recovery after photobleaching (FRAP) to measure lateral diffusion coefficients.[1] The SLBs studied comprised of DPPC, DOPC and DMPC and were prepared by Langmuir-Schaefer deposition. The authors found that for DPPC in the L_β phase the diffusion coefficient increased linearly with temperature. This period of linear increase ended at 32°C and was followed by a plateau from 32 to 39°C. The authors believed that this plateau corresponded to the ripple phase (P_β). Between 39°C until 42°C there was a rapid increase in the diffusion coefficient which then levelled off between 42 and 48°C; this region corresponded to the L_α phase. An interesting feature of the DPPC system was the formation of tubules when the SLBs were heated through their main phase transition temperature; this indicated a lateral expansion and thus an increase in area per lipid upon heating into the L_α phase – a fact that has relevance to my later work on dSDS lipid interactions in Chapter 5. Conversely DOPC showed the formation of hole defects upon cooling. Both DMPC and DOPC showed large increases in their diffusion coefficients when heated above T_m.

Bayerl and coworkers have used DSC, ^{31}P NMR, ^{2}H NMR and FTIR to study a hybrid SLB system composed of DPPC bilayers supported on silica beads.[106] They found that the T_m of this system was 2°C lower than for a DPPC MLV suspension and that the transition enthalpy was 25% less than for DPPC multilayers. Their spectroscopic measurements show no loss of coupling between the bilayer leaflets. As shall been seen later, other workers have found that the support can have a strong influence of the phase transition, especially in the proximal bilayer leaflet. The authors also observe a suppression of the ripple phase in this supported system in comparison to multilayers where it is observed. They relate this last observation to the higher "stress" in the SLB system. Lastly, the authors used DSC to follow the kinetics of lipid transfer between the two bilayer leaflets comprised of DMPC and chain perdeuterated DMPC. They find that the translocation process is symmetric and takes on the order of 3-4 times longer than for small sonicated vesicles of the same constitution.

Lee and Bain used TIR-Raman spectroscopy to observe phase behaviour in SLBs on silica that were composed of DMPC or DPPC. POPC was also investigated but owing to the low T_m no phase transition behaviour was observed.[107] TIR-Raman provided insight into the conformational order, fluidity and tilt of the phospholipid molecules within the bilayer, and, because changes of these parameters occur at the main phase transition temperature (T_m), they allowed the authors to determine this transition. A curious feature of this data was the broadening of the DMPC phase transition in comparison to data acquired by DSC (≈10°C). In my experiments, I have considered the effects of different salts as a possible cause for this broadening. Nevertheless, the data obtained match the calorimetric phase transition temperature in terms of the temperature of onset. The

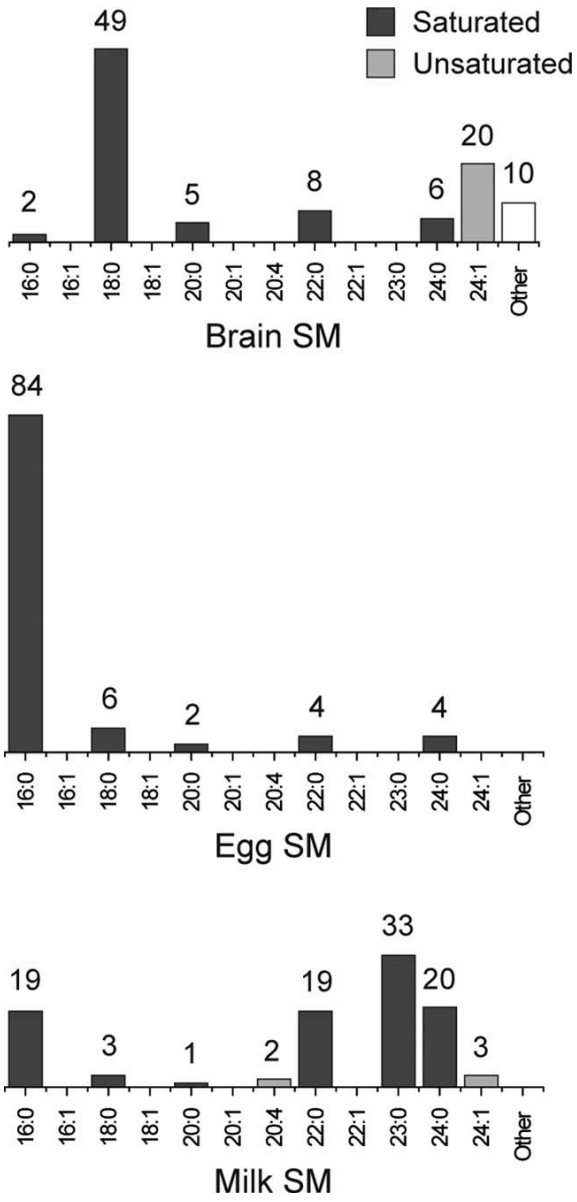

Figure 4.3: Compositions of the different natural sphingomyelin sources available from Avanti Polar Lipids Inc. Notice egg-SM has the "purest" composition in the sense of having the greatest contribution from a single component. Reproduced from Law and coworkers,[105] with permission of The Royal Society of Chemistry.

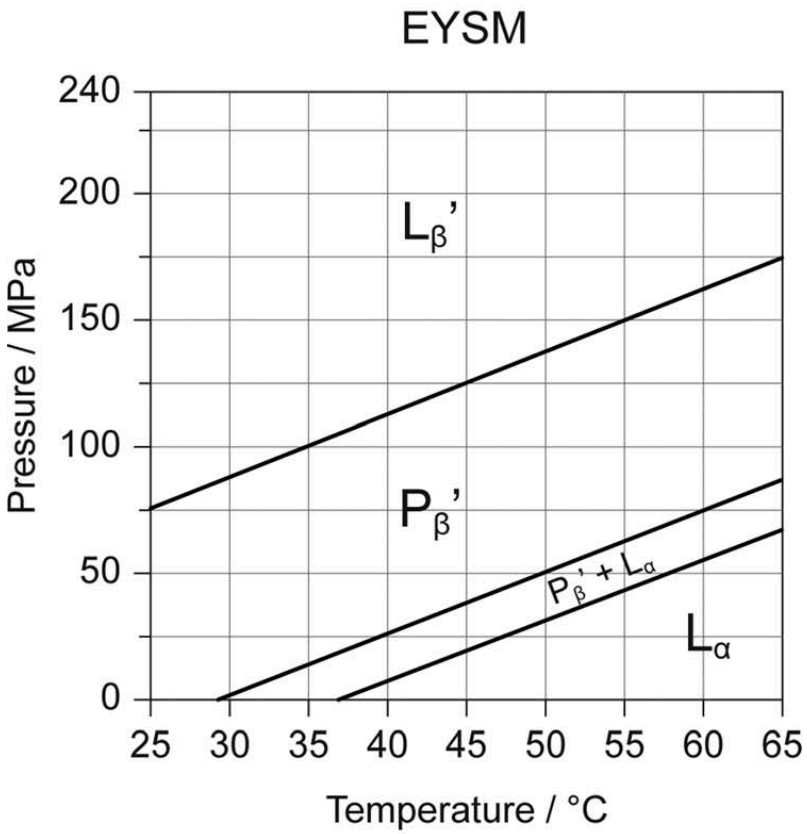

Figure 4.4: A figure showing a temperature/pressure phase diagram of egg-SM from Avanti Polar Lipids Inc. Reproduced from Law and coworkers,[105] with permission of The Royal Society of Chemistry.

phase transition of the DMPC SLB was compared to that of DMPC vesicles in bulk suspension and found to be almost identical. Little evidence was found for a ripple phase in DPPC despite is detection in earlier work on SLBs, see for instance the plateau in Tamm and McConnell's data, however a small plateau in the frequencies of the symmetric and antisymmetric stretches was observed which could be interpreted as an indication of a separate phase and, as mentioned above, Bayerl and coworkers have observed its suppression. Clearly the suppression of the P_β phase is ambiguous and may depend on the specific system being studied or the experimental procedure employed.

Bonn and coworkers have used vibrational sum-frequency generation in conjunction with surface pressure measurements and fluorescence measurements to observe the effects of Na^+ and Ca^{2+} on DPPC and DMPS monolayers at different surface pressures.[108] At low surface pressures (5 mN m^{-1}) the Ca^{2+} cation induces the formation of ordered domains within the lipid monolayers at the air-water interface. However, as the surface pressure was increased to moderate surface pressures (5-25 mN m^{-1}) Ca^{2+} increases disorder. At high pressures (>25 mN m^{-1}) they show how Ca^{2+} expands the monolayers investigated. They observe identical behaviour for both zwitterionic and anionic lipids, highlighting that the ions are most likely binding to the phosphodiester oxygens and lastly they show how the stoichiometry of the cation lipid complex changes from 2:1 to 1:1 at high surface pressures.

Enders and coworkers have investigated the phase behaviour of DMPC SLBs on ruby muscovite mica with AFM.[109] Specifically they observed the ripple phase in order to resolve the structure of this phase in detail. Enders used "structural calorimetry" to estimate the transition enthalpy. This was done by capturing AFM images at a number of stages during the phase transition and then calculating the fraction of surface that was covered with the phase of interest. Their experiments were complicated by the fact that their vesicles were prepared in one buffer (5 mM K-HEPES pH 7.3, adsorbed and ruptured in another (1 mM EDTA, 5 mM K-Tris, pH 9) and finally imaged in yet another (50 mM KCl, 5mM $MgCl_2$, 5mM K-HEPES, pH 7.3) which were exchanged in order by dilution. This use of different buffers in this way could lead to residual constituents in the final imaging buffer which might lead to structural features that would not be present in the pure imaging buffer.

Seeger *et al.* have used AFM to study the main phase transition of POPE and POPE:POPG (3:1) SLBs.[78] Generally, their SLBs were formed by vesicle fusion on muscovite mica in 450 mM KCl, 25 mM HEPES buffer pH 7 at 23°C, but this solution was exchanged after formation for others during imaging. The imaging buffer was either pure water, 10 mM KCl or 150 mM KCl all at pH 5.6. Sometimes higher formation temperatures were used. The study was primarily conducted from the point of view of elucidating the role of the support on the main phase transitions. The authors found that for both the mixture and pure POPE the main phase transition on mica was decoupled – the two leaflets changed phase at different temperatures. Variation of the imaging buffer ionic strength and formation temperature allowed them to moderate this behaviour. For instance, for the mixed system they state that the proximal bilayer leaflet converts from the fluid phase to the gel phase followed by the distal leaflet as the temperature is reduced – they observe the formation of domains and subsequent homogenising of the topography twice during the temperature decrease. Increasing the KCl concentration from 10 mM to 150 mM had the effect of narrowing the difference in temperature between the respective transitions of the two leaflets in this mixed system. However, for the pure POPE system changing the ionic strength from pure water to 150 mM KCl had no effect on the decoupling of the phase transitions in the two leaflets. The authors found that by forming the mixed SLB at a higher temperature (27°C) they observed a coupled phase transition. However, with formation at 35°C for both the mixed and pure system

this was not the case. They reasoned that by changing the ionic strength they were able to weaken the electrostatic interaction between support and SLB. By changing the formation temperature, they argued that a different lateral profile and a moderated interaction between the tails in the two opposite leaflets would result. They claim their results have implications for real biological membranes as physically the cytoskeleton is analogous to the mica support.

In a more recent work, Seeger *et al.* have investigated the role of support structure on the main phase transition of POPE:POPG (3:1) SLBs.[110] They examined how the thermotropic phase transition changed when mica was replaced with silica (SiO_2) as the support. Measurements showed that the mica support used had an rms roughness of 0.05 nm whereas after cleaning procedures the silica had an rms roughness of 0.20 nm. In the previous study the authors had found a decoupled phase transition for POPE regardless of ionic strength or formation temperature and a decoupled transition for the mixture depending on the formation and solution conditions. However, on silica the authors found a completely coupled transition for the mixture regardless of the formation temperature or solution conditions. They attributed this difference in behaviour to the enhanced roughness of the silica support and stated that this could only be the result of a moderated interaction owing to the pockets of water between the substrate and the SLB. It is worth noting that they stated the differences in surface charge between the mica and SiO_2 were negligible under the conditions used and so could not be used as an explanation for different behaviour on the two supports. However, in general whilst the buffer they used for the formation of their SLBs was the same as in their prior work, the imaging buffer was different; in this study 150 mM KCl, 10 mM potassium dihydrogen citrate was used – the pH was either 7, 5.6 or 3. They suggested that silica is a more appropriate substrate for biophysical studies on membrane-bound proteins owing to this weaker support-bilayer interaction. They also observed how pH affects the main phase transition. They found that by reducing the pH from 7 to 3 they were able to shift the phase transition temperature of the mixture from 22°C to 27°C owing to the modification in surface charge.

Yarrow and Kuipers have used temperature-controlled contact mode AFM to study the thermotropic phase behaviour of DPPC SLBs.[111] The authors found that melting from the L_β to the L_α phase starts from pre-existing line defects (grain boundaries). They also observed that the cantilever force exerted on the SLB can affect the phase transition observed. They noted that whatever force was used the phase transition was higher than that observed in vesicles owing to support-SLB interactions. When undergoing the inverse cooling transition, the SLB showed the formation of line defects at the edges of gel phase regions and that these defects originated from distinct nucleation points. The number of these defects depended on the rate of cooling. Both heating and cooling transitions took place over approximately 5°C. All of their measurements were carried out on muscovite mica in 20 mM NaCl. The authors do not describe any decoupling of the phase transition in the two bilayer leaflets. A series of their heating images is shown in figure 4.5.

Szmodis *et al.* have investigated the phase transition dynamics in binary supported phospholipid bilayers using imaging ellipsometry.[112] The authors prepared SLBs comprised of DLPC (1,2-dilauroyl-*sn*-glycero-3-phosphocholine) and GalCer (Galactosylceramide) on SiO_2/Si. These lipids where chosen for two reasons: first the wide difference in main phase transition temperature (DLPC, -2°C and GalCer, 50-70°) allowed for access to both the homogeneous phase and the miscibility gap, and second the gel phase forming GalCer preferentially forms part of the outer bilayer leaflet and so minimises the direct interaction with the support. The authors found the modulation of two topographic features during the phase transition. First, the formation of defect chains due to a reduction in molecular area during cooling and, second, the formation of fractal-like domains suggestive of low line tension owing to their irregular shape. By following a time-lapse

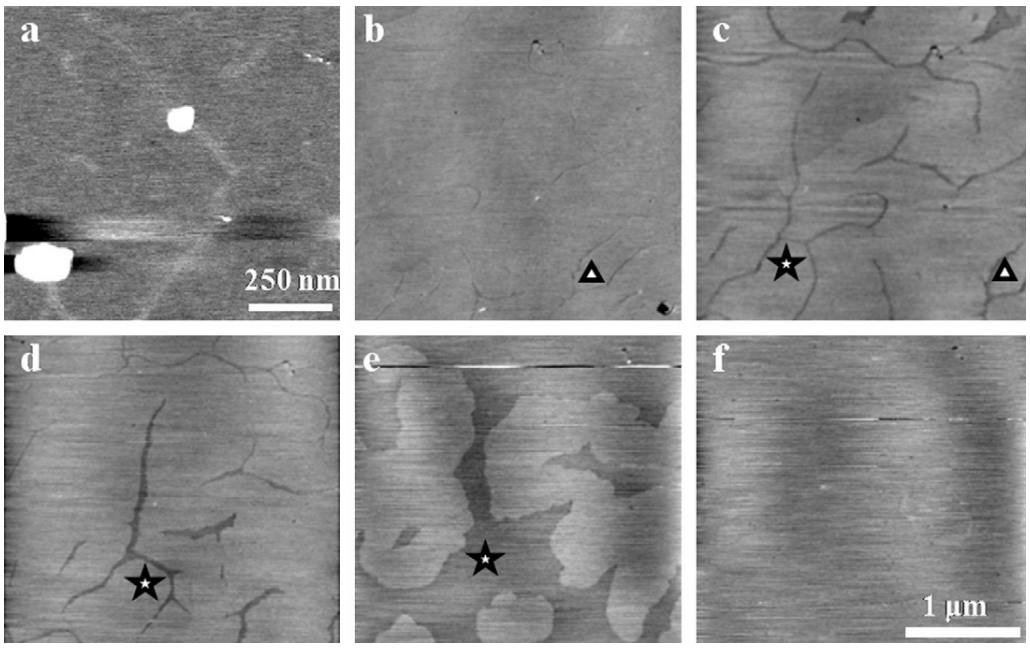

Figure 4.5: A series of heating contact mode AFM images of A DPPC SLB, (a) 25°C, (b) 39.4°C, (c) 40.9°C, (d) 41.9°C, (e) 43.9°C and (f) 44.3°C. Reprinted from Yarrow *et al.*[111] with permission from Elsevier.

of images they were able to infer the formation of domains containing 4-20 molecules during the phase transition, indicating weak transition cooperativity for this bilayer. The authors note that they were only able to observe the outer leaflet, but owing to the depth of the gaps during the defect formation period they were able to infer a dynamically coupled phase transition between the proximal and distal bilayer leaflets despite the intrinsic asymmetry.

Kasemo and coworkers have used QCM-D to monitor structural changes taking place in 1,2-ditridecanoyl-*sn*-glycero-3-phosphocholine (DTPC) vesicles adsorbed onto TiO_2 surfaces during the main phase transition.[113] The authors fitted their frequency and energy dissipation data with a Voigt model. The temperature induced changes changes in the vesicle viscosity and thickness were used to define the temperature of the phase transition. They found that modifying the pH and temperature to increase the interaction with the substrate resulted in a phase transition at higher temperature – this result compares favourably with the work of Seeger *et al.* described above,[110] but this increase in T_m could have been the result of headgroup dehydration alone.

4.3.3 Computational work

There is a notable molecular dynamics study (MD) by Pedersen *et al.*, in which the association of Ca^{2+} with various anionic lipid species was investigated.[114] They found that, even in bilayers of lipids with anionic headgroups, the calcium ions were located preferentially within a 0.1 nm band around the phosphate moieties within the layer but were also associated with the ester carbonyls. By comparison, Na^+ had a much lower specific site preference associating with other groups and had a wider distribution within the bilayer. The equilibration time for the association of Na^+ with DMPS was found to be 25 ns. In comparison the equilibration time for various cations with zwitterionic lipids was found to be 100-200 ns.[115] One can rationalise this last point on the basis of the Gouy-Chapman theory; it has been shown that the rate of association is proportional

to the surface electrostatic potential and not the strength of ion binding for Ca^{2+} and retinal lipid membranes.[116] This last fact has also been observed in a much older experimental study where the degree of Ca^{2+} binding was quantified by taking radioactivity measurements using the $^{45}Ca^{2+}$ isotope.[117] A recent MD study by Perez *et al.* has shown the lipid-cation interaction of a wider range of ions (K^+, Li^+, Na^+, Ca^{2+}, Mg^{2+}, Sr^{2+}, Ba^{2+}, and Ac^{3+}) than Pedersen *et al.* but only with DPPC.[57] Perez's simulations showed that K^+ did not bind to lipid headgroups but that the other ions did. The authors give a very similar ion distribution profile in comparison to the earlier work on anionic lipids. Perhaps the most general conclusion was that the degree of binding was related to the ionic radius and formal charge of the cation in question.

4.4 Results

4.4.1 Overview

In this section, I will describe and discuss my results from investigations into the thermotropic main phase transitions of SLBs on SiO_2 comprising 1) DMPC, 2) POPE and 3) egg-SM. The SLBs were hydrated in 20 mM tris buffer at pH 7.4. The primary aim of this chapter is to explore the role of NaCl and $CaCl_2$ on these transitions, thus these salts were included in the buffer when necessary. In general the raw subtracted spectra are discussed followed by the extracted order parameters. Subsequently the Zimm and Bragg model was applied, thermodynamic parameters were calculated and then discussed. In the interests of saving space, I have collated the extracted order parameters for the different buffer solutions into the same figures; I have also included the subtracted TIR-Raman spectra from the most interesting of the three buffer conditions for each system – the other spectra are available in Appendix A. I end with my concluding remarks.

4.4.2 DMPC

Previously, Lee and Bain followed the main phase transition of DMPC in 10 mM tris buffer with 100 mM NaCl at pH 8.0.[118] They found that the main phase transition was broadened in contrast to that measured by DSC; it is worth pointing out that a broader transition was also observed in SUV's studied by Raman spectroscopy so the substrate was not solely responsible for the difference. One question I have been interested in was whether or not the presence of the additional sodium chloride could have led to the broadening. I decided a topic worth pursuing was the influence of group I and II chlorides on the main phase transition of SLB systems. To this end I have observed the phase transition of DMPC in pure tris buffer pH 7.4 with additional 100 mM sodium chloride or 2 mM calcium chloride. I chose these concentrations or two reasons, first I used the same concentration of NaCl as Lee and Bain so direct comparisons to the earlier work could be made. Second the low concentration of calcium chloride was chosen as similar low concentrations had been used by other workers for various reasons and I wanted to enable comparison with their work – generally Ca^{2+} has been shown to have much stronger interactions with SLBs than Na^+.

Figure 4.6 (a) shows S-polarised TIR-Raman spectra of a DMPC SLB as a function of temperature with added $CaCl_2$ and (b) shows a close-up of the same data. As the temperature was raised the intensity of the CH region decreased. Figure 4.7 (a) and (b) show the equivalent P-polarised data, in which we see very few changes in intensity. In this group's previous study,

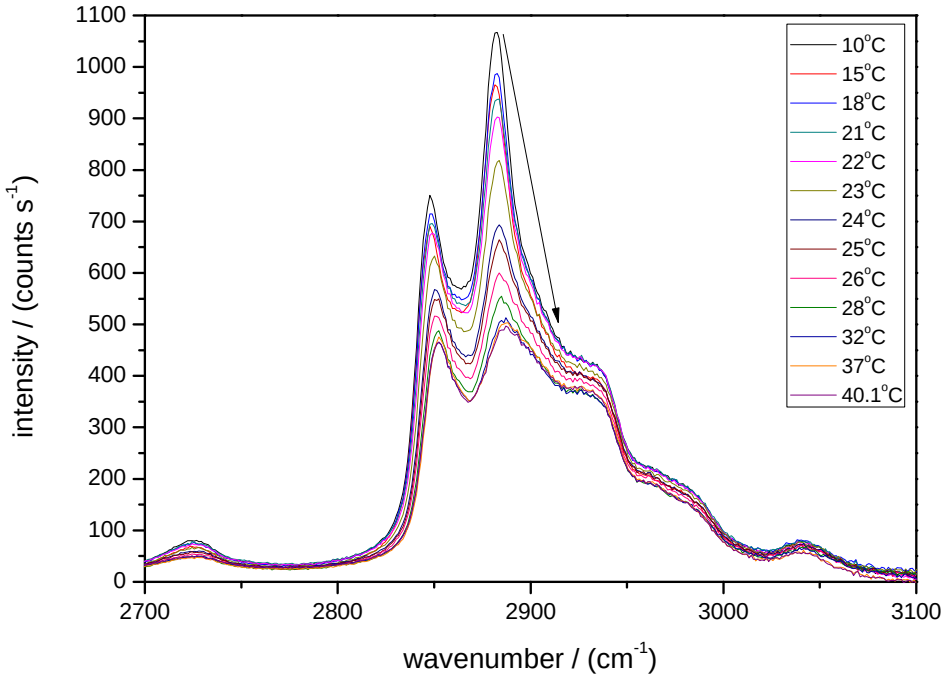

(a)

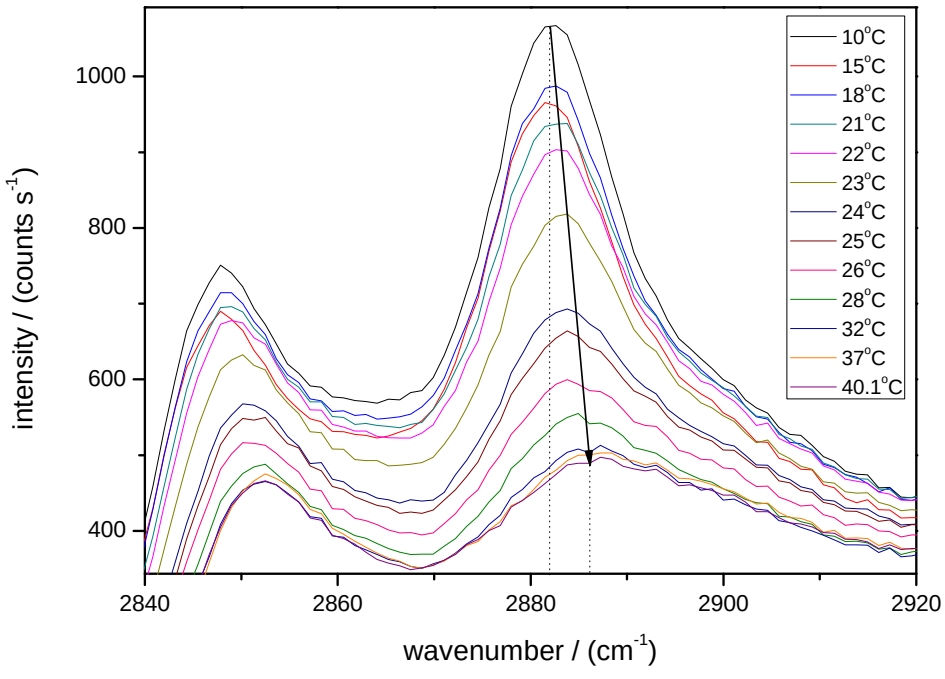

(b)

Figure 4.6: S-polarised TIR-Raman spectra of DMPC as a function of temperature in 20 mM tris pH 7.4 with 2 mM $CaCl_2$, 800 mW laser output power, 73° incidence, unpolarised detection. Arrows indicate the direction of increasing temperature.

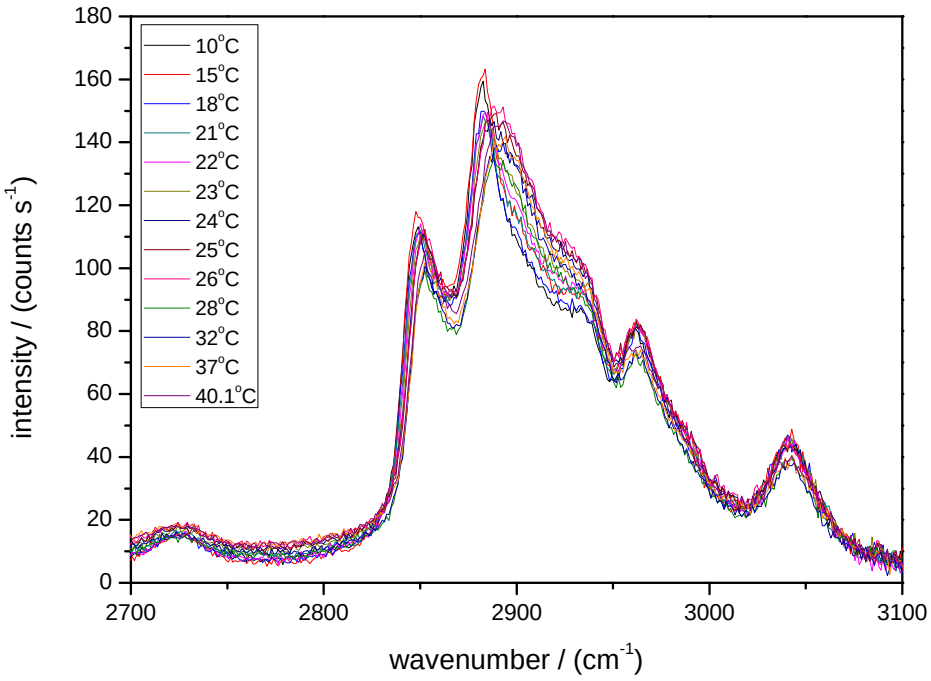

(a)

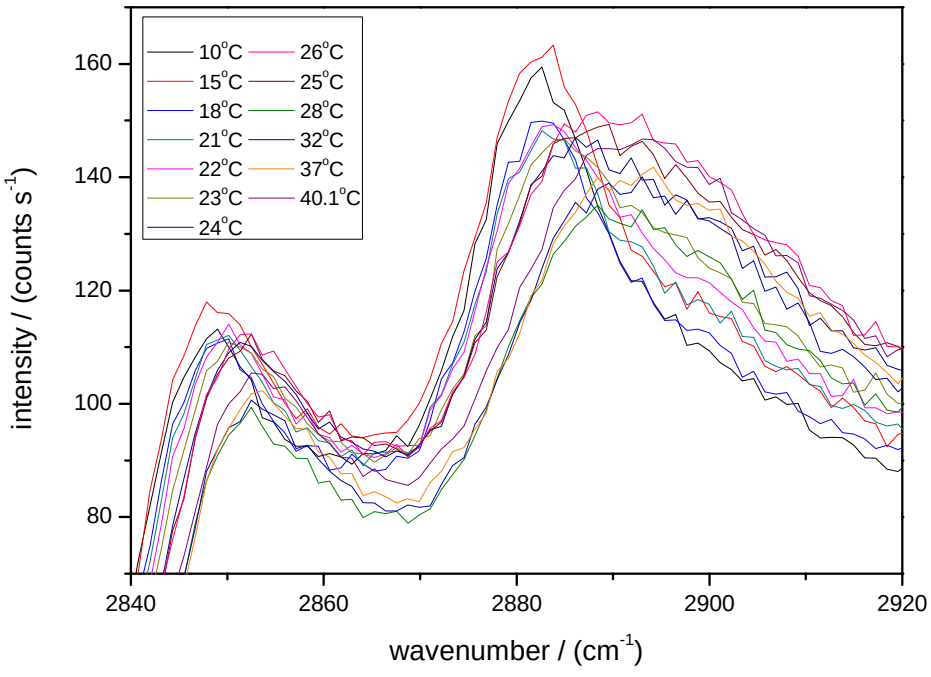

(b)

Figure 4.7: P-polarised TIR-Raman spectra of DMPC as a function of temperature in 20 mM tris pH 7.4 with 2 mM $CaCl_2$, 800 mW laser output power, 73° incidence, unpolarised detection.

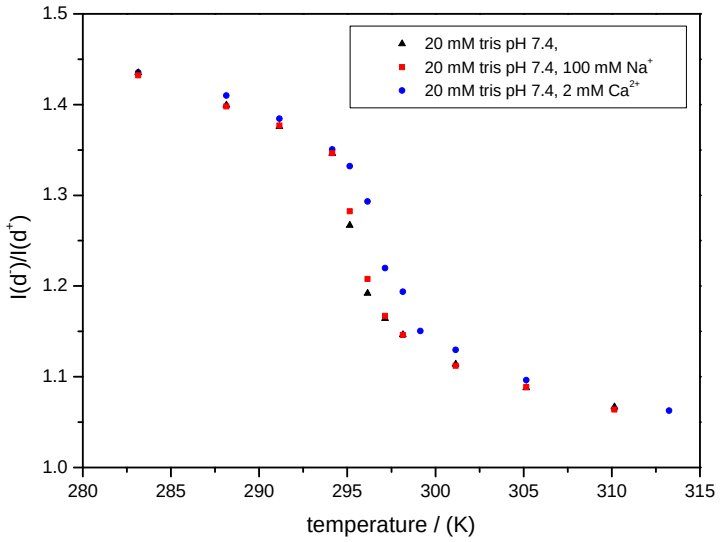

Figure 4.8: A graph showing the change in the peak $I(d^+)/I(d^-)$ ratio as a function of temperature for three DMPC SLBs prepared in different buffers. 20 mM tris pH 7.4 (black triangles), 20 mM tris pH 7.4 + 100 mM NaCl (red squares) and 20 mM tris pH 7.4 + 2 mM CaCl (blue circles). The intensities were extracted from S-polarised spectra by polynomial fitting.

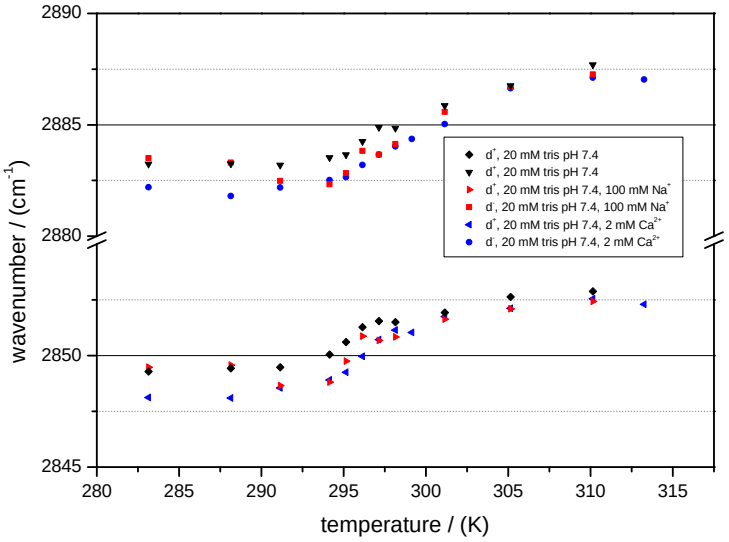

Figure 4.9: A figure showing the variation in the peak positions of the symmetric and antisymmetric CH stretches as a function of temperature. 20 mM tris pH 7.4 (Black triangles and diamonds), 20 mM tris pH 7.4 + 100 mM NaCl (red triangles and squares), 20 mM tris pH + 2 mM CaCl (blue triangles and circles). The positions were extracted from maxima in the polynomial fits.

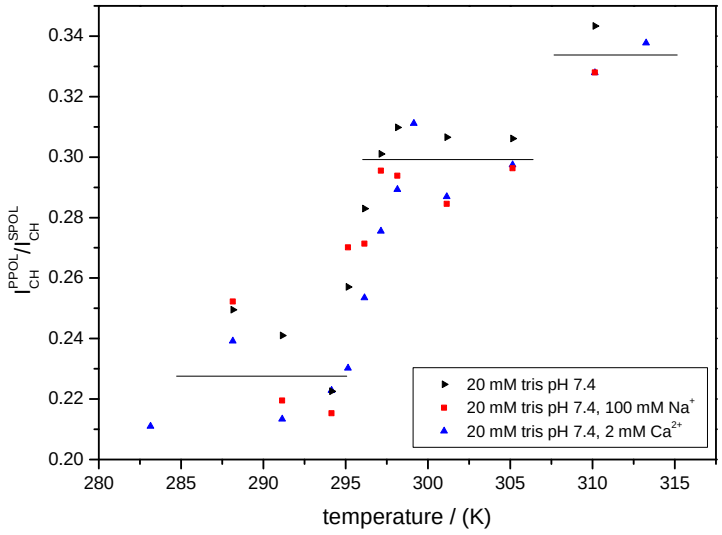

Figure 4.10: A graph showing the variation of the integrated intensity ratio of the P-polarised and S-polarised CH stretching regions, which is correlated with chain tilt. 20 mM tris pH 7.4, 20 mM tris pH 7.4 + 100 mM NaCl and 20 mM tris pH 7.4 + 2 mM $CaCl_2$.

a significant change in intensity was observed for the P-polarised temperature dependent-spectra, however, in that study the angle of incidence was quite close to the critical angle 68.6° whereas in my work the angle of incidence was 73°. This difference in incident angle explains the difference in behaviour; at the lower angle of incidence there is a greater sensitivity to Raman modes oscillating close to the surface normal. In any case, if the P-polarised intensities do not decrease in proportion to a change in the equivalent S-polarised spectra then a change in molecular tilt is occurring. In both S- and P-polarised data sets we notice an upward shift in the peak positions of the symmetric and antisymmetric CH stretches as the temperature increases. There is also a concomitant decrease in the ratio of the antisymmetric to symmetric CH stretch peak intensities. These changes are indicative of a decrease in chain order in terms of packing and the number of gauche defects.

Quantitative analyses of these spectral changes are shown in figures 4.8 and 4.9. These data were extracted by fitting 4th-order polynomials locally to the symmetric and antisymmetric stretches and taking the respective maxima and associated peak positions from these. Inspecting figure 4.8 we note the similarity in the shape of the transition for all three buffer conditions and the equality of the values at high and low temperatures in all solutions; the added salt does not appear to affect the phase transition in terms of internal molecular order. However, note the increase in the phase transition temperature of the $CaCl_2$ containing system: the low concentration of Ca^{2+} increases the temperature of the main phase transition by approximately 1.5 K. The peak positions shown in figure 4.9 are more complicated to interpret. Although at high temperature the peak positions all appear to converge, during the main phase transition and leading up to it there are small but noticeable differences; these could be indicative of real differences between the systems, or a product error, as such a description will be given but the conclusions should be taken cautiously. For the tris-only system, there appears to be a step during the transition *possibly* indicating the presence of some intermediate chain packing state. For the sodium containing solution, there is a downward shift in the peak positions just prior to the phase transition, again *possibly* indicating the presence of some intermediate packing state. Of all the buffers used, that

containing Ca^{2+} shows the "smoothest" transition with no evidence of intermediate structures; this is interesting considering the increase in phase transition temperature as evidenced by the primary order parameter data ($I(d^-)/I(d^+)$).

Figure 4.10 shows the variation in the ratio of the integrated intensities in the CH region for the temperature dependent P-polarised and S-polarised TIR-Raman spectra. This parameter is strongly correlated with average lipid chain tilt relative to the surface normal: an increase implies an increase in tilt from the surface normal. The data shown can be divided in to several characteristic regions: there is relatively constant plateau at low temperatures, followed by a period of rapid increase, after this there is another plateau, and then another at the highest recorded temperatures. On average the lipid molecules are becoming more tilted as the transition proceeds.

None of the order parameter data examined indicate a decoupled phase transition as observed by Seeger *et al.* If this were the case one would expect to see double sigmoidal behaviour in the plots of the order parameters, especially that of the primary order parameter. An important question can be raised about where the phase transition starts and ends, and how we decide on a rigorous procedure to specify the transition temperature of the main phase transition. The different order parameters often show differences that could lead to different interpretations of the transition, particularly at low and high temperatures. For instance, the primary order parameter shows gradual changes at the extremities with a sharp change at middle temperatures in the transition 'region', whereas other order parameters, such as the peak positions, show more irregular changes. As the primary order parameter is generally considered to be the most sensitive, I will use it as the parameter to define the transition temperature. Where small changes are occurring, or perhaps only a few domains have changed phase, the other order parameters are less likely to show a measurable change.

The degree of the phase transition (θ) can be extracted from the primary order parameter data by rescaling the measured values on a scale of 0 to 1. By plotting these data against $1/T$, σ and the van't Hoff enthalpy can be extracted and the Zimm and Bragg model can be applied. This procedure has been carried out for the three DMPC systems and is shown in figure 4.11, the resulting plots have been fitted with the bi-dose-response sigmoidal model in Origin Pro. The fitting function was chosen only to facilitate a good fit, no physical basis has been considered in its application. From the gradient at θ=0.5, obtained numerically in Origin Pro, equation 4.33 can be used to estimate the van't Hoff enthalpy of the phase transition. The van't Hoff enthalpy is related to the calorimetric enthalpy by a factor which corresponds to the cooperative unit or domain size of the transition (the number of molecules that change phase as a unit). Using literature values for the transition enthalpy collected under similar conditions, an estimate for the cooperative unit can be obtained. However, it must be pointed out that although several good sources of calorimetric data on lipid phase transitions are available,[75,89,90] there is scant data specific to SLB systems. It was also not possible to find calorimetric data corresponding to the precise solution conditions used here, and the ΔH_t values chosen were the closest matches available. The alternative to this strategy is to find the cooperative unit size by direct experimental means such as by AFM or imaging ellipsometry, as was done by Enders *et al.*, but the analysis of AFM images is unlikely to provide as accurate calorimetric data as that obtained by direct calorimetric means. Perhaps a solution is to prepare bulk supported systems, where SLBs are fused on large silica beads with small radii of curvature – as in the work of Bayerl and coworkers. Regardless, rescaling the order parameter data also provides a way to define the phase transition temperature from the spectroscopic data. It is clear from all the order parameters, that the changes in structure take place over a broad temperature range. By fitting the rescaled order parameter data I have been able to determine at what temperature the structural changes are half completed and have

defined this as the transition temperature. This more rigorous method removes the ambiguity of giving a rough estimate based on the raw spectra and extracted order parameter values. The thermodynamic data acquired by applying the Zimm and Bragg model are shown in table 4.1. The values of the fluid phase statistical weight s required to fit the experimental degree of transition, θ, are shown in figure 4.12 as a function of temperature. The associated fluid molecule free energy change as a function of temperature is shown in figure 4.13. In both these plots we observe slight variations in the quantitative values, but the qualitative features are all similar. Returning to table 4.1 we notice slight differences in the transition temperatures, but larger changes in the transition van't Hoff enthalpy. The literature values for the calorimetric transition enthalpy only differ slightly with added salt, thus these data imply that the primary effect of the added NaCl or $CaCl_2$ and associated binding of Na^+ and Ca^{2+} is to alter the cooperativity parameter σ; this in turn implies a change in the interfacial free energy (G_i) between regions of L_α and L_β/P_β phase. Indeed for DMPC this additional energy is significantly lower for the $CaCl_2$ containing system especially. Having a lower interfacial free energy means there is a lower cost associated with additional interface and so the cooperative unit is smaller – hence the broadening of the transition. It is unclear what structural change in the interfacial region leads to the reduction in the interfacial free energy, one possibility is that bound Ca^{2+} ions bridging adjacent phosphate groups are not broken between lipids on either side of the interface, this would reduce the overall significance of the loss in van der Waals contribution between chains across the interface after it has formed. Previously researchers from my group had suggested that the broadening of the main phase transition of DMPC was a result of the decoupling of the calorimetric phase transition from structural changes. My data show that although the presence of NaCl and $CaCl_2$ can influence the transition temperature itself (added salt increases T_m) and the van't Hoff enthalpy, they only appear to have a limited effect on the general qualitative nature of the transition—it remains broad regardless of the presence of these additional salts. Indeed it appears that cooperativity during the main phase transition is intrinsically suppressed for SLB systems. The influence of the additional salts appears to be specific to the SLB itself, rather than between the support and substrate in terms of electrostatic screening of SLB and SiO_2 substrate as the same broad transition is observed in SUV's.[93,107] The shifting of the main phase transition temperature in the presence of salts has previously been attributed to the dehydration of the lipid headgroups, although I have no data that explicitly confirms that the headgroup region is being dehydrated (for instance I am unable to observe the phosphate P-O bands owing to overlap with SiO_2 modes), I still observe the expected increase in phase transition temperature. The absolute values of the van't Hoff enthalpy that I have obtained are significantly lower than the values obtained by Enders *et al.* on mica by AFM; this could be a result of the different method for calculating the enthalpy, the different buffer conditions, the different substrate, or just a problem with one of the techniques.

4.4.3 POPE

Figure 4.14 shows S-polarised TIR-Raman spectra of a POPE SLB in 20 mM tris pH 7.4 with 2 mM Ca^{2+} added. The spectra have a similar appearance to those of DMPC, however we notice the loss of the choline band at 3040 cm^{-1} and the addition of the vinylic CH stretch at 3020 cm^{-1}. The raw spectra for all the POPE data show the same overall trends as those for DMPC, a decrease in intensity in the S-polarised data with increasing temperature, little change in the P-polarised data, upward shifts in the peak positions and a decrease in the $I(d^-)/I(d^+)$ ratio. Interestingly, when considering the Ca^{2+} system, there is additional increase in the vinylic CH stretch and a

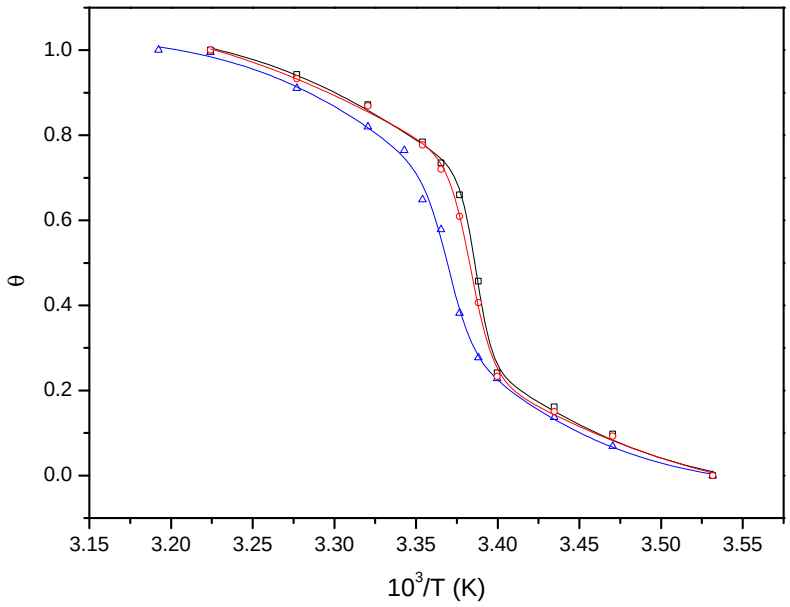

Figure 4.11: A figure showing the degree of transition θ as a function of $1/T$ for DMPC SLBs in: 20 mM tris buffer pH 7.4 (black squares and line), 20 mM tris pH 7.4 + 100 mM NaCl (red circles and line), 20 mM tris pH 7.4 + 2 mM $CaCl_2$ 20 mM tris pH (blue triangles and line). The gradient of these plots at $\theta = 0.5$ yields the van't Hoff enthalpy and comparison of this value with the appropriate calorimetric enthalpies affords the cooperativity parameter σ.

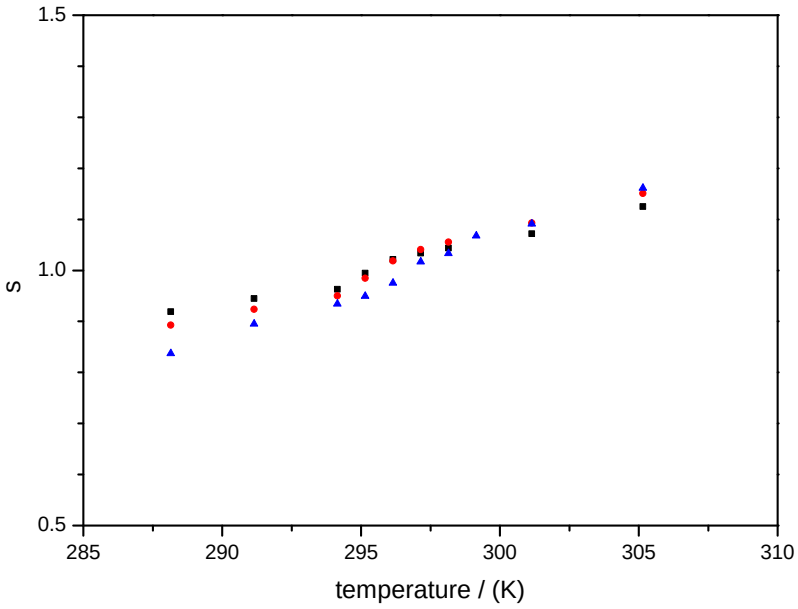

Figure 4.12: A graph showing the scaling of s the statistical weight of a fluid state molecules as a function of temperature for DMPC SLBs in: 20 mM tris pH 7.4 (black squares), 20 mM tris pH 7.4 + 100 mM NaCl (red circles), 20 mM tris pH 7.4 + 2 mM $CaCl_2$. The values were obtained numerically by a least squares procedure following the determination of σ at $\theta = 0.5$.

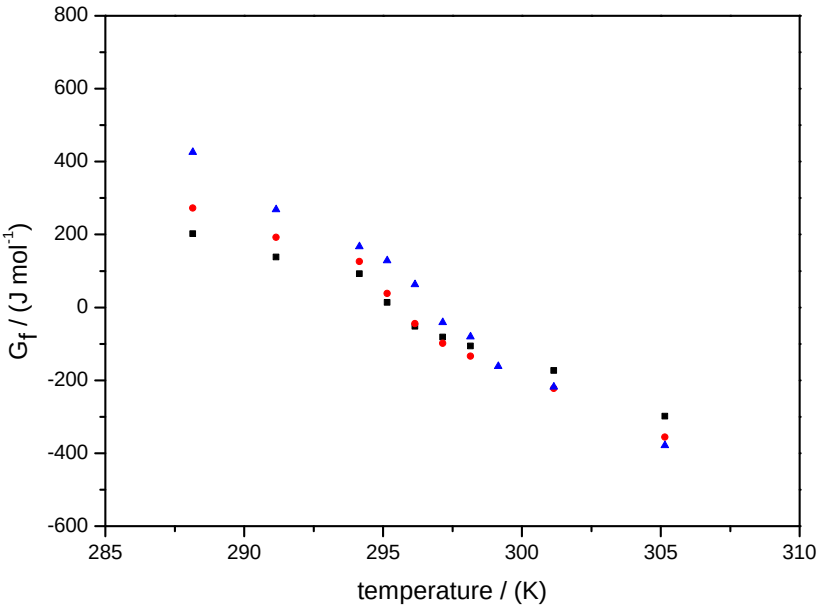

Figure 4.13: A figure showing the variation of G_f the free energy of a non-interfacial fluid phase lipid molecule, relative to the free energy of a solid state molecule, as a function of temperature for a DMPC SLBs on silica in: 20 mM tris buffer pH7.4 (black squares), 20 mM tris buffer pH 7.4 + 100 mM NaCl (red circles), 20 mM tris buffer pH 7.4 + 2 mM $CaCl_2$ (blue triangles).

Solution	T_m/ (°C)	ΔH_{vH}/ (kJ mol^{-1})	$[\Delta H_t]$/ (kJ mol^{-1})	$1/\sqrt{\sigma}$	G_i/ (kJ mol^{-1})
20 mM tris pH 7.4 + 2 mM $CaCl_2$	23.7	-504	-26.4	19 (2.74x10^{-3})	14.6
20 mM tris pH 7.4 + 100 mM NaCl	22.5	-651	-26.4	25 (1.65x10^{-3})	15.8
20 mM tris pH 7.4	22.2	-801	-24.8±2.2	32 (9.6x10^{-4})	17.1

Table 4.1: A table showing the transition temperatures, van't Hoff enthalpies, cooperative unit sizes, and interfacial free energies calculated for DMPC SLBs in tris buffer with added $CaCl_2$ or NaCl - pH 7.4. The cooperative unit sizes are given as the nearest whole integer values and the extracted σ values used in their calculation are given below in brackets. The literature calorimetric transition enthalpies are given for reference; the value for the pure tris buffer was an average of the values in reference [75] for pure water – pp 308-310. Whereas the value used for the salt containing buffers pertained to a single value in 0.1 mM NaCl, 10 mM tris-HCL, 1 mM EDTA, 1 mM NaN_3 pH 7.4. Where multiple calorimetric enthalpies are available in the literature the standard deviations is fairly high - suggesting very weak effect of the added salt (see above).

concomitant decrease of the same band the in P-polarised spectra. These changes do not occur in the sodium containing system or the tris only system. This variation suggests a further structural modification of the chains below 15°C for the Ca^{2+} containing system. An increase in this band at low temperature in the S-polarised spectra along with the P-polarisation decrease indicates a tilting of the lipid chains so the vinylic CH bonds are oriented closer to the interfacial plane.

Figure 4.16 shows the variation in the primary order parameter as function of temperature for POPE SLBs in the three buffer solutions. Similar to DMPC I observe a step in the order parameter for the pure tris and NaCl containing systems as they pass from the L_β to the L_α phase. However, the $CaCl_2$ containing system shows a much broader transition with no rapid drop; we also note several outliers; given the reproducibility of my other phase transition data, and taking account of the repeat data points added for the pure tris and NaCl containing systems, it is unclear if these outliers are the result of experimental error, or some manifestation of the transition itself – repeat data for the Ca^{2+} system are available, but the experiment was conducted at another angle of incidence and so the absolute order parameter values are different, but outliers were not observed. It is clear that the pure tris system displays greater ordering of the hydrocarbon chains at the lowest temperatures; all systems display similar ordering in the fluid phase. Perhaps the binding of Na^+ and Ca^{2+} leads to a disordering of the chains in the L_β phase as the binding of these cations deforms their preferred structure. In general these data show a much more 'irregular' transition in comparison to that acquired for DMPC.

The wave numbers of the anti-symmetric and symmetric CH stretches are shown as functions of temperature in figure 4.17. At all temperatures the $CaCl_2$ containing system shows the greatest degree of chain packing disorder, and, as with the primary order parameter, the peak positions for both stretches increase gradually with temperature; this compares well with the primary order parameter data. Nevertheless, the pure tris and NaCl containing systems show very similar behaviour in terms of peak position changes; both of these systems have very similar absolute values, but they also show abrupt stepwise increases in the peak positions at the transition temperature. At higher temperatures both of these systems display further increases in their peak positions suggesting a subsequent decrease in interchain packing density and an increase in disorder.

Figure 4.18 shows the change in the ratio of the integrated intensities in the CH region for the temperature dependent P-polarised and S-polarised TIR-Raman spectra of POPE. I have linked the data points with connecting lines to make following the overall trends easier. Interestingly, in terms of average lipid chain tilt, the tris only system displays the most gradual behaviour whereas the sodium and calcium containing systems show changes over a narrower temperature range in terms of average chain tilt. These trends are in stark contrast to the other order parameters where the $CaCl_2$ containing system displayed more gradual behaviour. Although for the tris only system the average chain tilt appears to increase at high temperature (see the last two data points), for the NaCl and $CaCl_2$ containing systems it reaches a plateau after the SLB enters the L_α phase. It is unclear if this is the result of error/variability or is a real consequence of the absence of bound cations.

Figure 4.19 shows the rescaled primary order parameter data for POPE in the three buffer solutions. As mentioned above, unlike the DMPC systems which all displayed broadly similar behaviour with changes in their interfacial free energies, the data for POPE show markedly different behaviour; the $CaCl_2$ system shows a very broad transition, with no observable step, whereas both the pure tris and NaCl containing systems show distinct sharp steps, n.b. I have removed the outliers from the Ca^{2+} dataset for the analysis. Fitting these data with the bi-dose-response model in Origin Pro was less successful in this instance owing to the irregular shape of the experimental datasets. This is particularly noticeable at low temperature where the model fits the tris

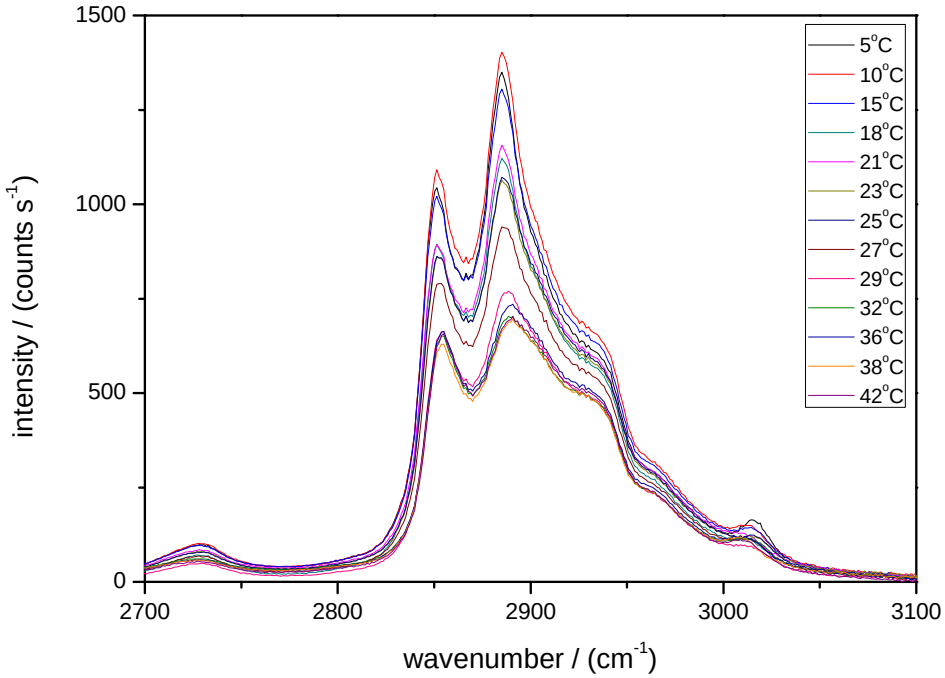

(a)

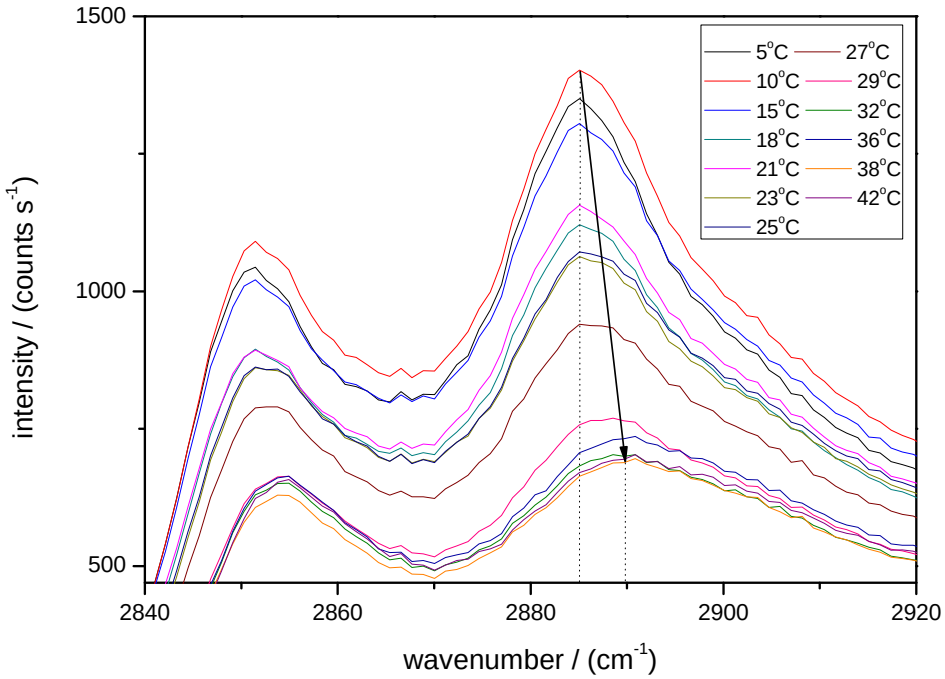

(b)

Figure 4.14: Temperature dependent S-polarised TIR-Raman spectra of a POPE SLB on SiO_2 in 20 mM tris pH 7.4 + 2 mM $CaCl_2$. 800 mW laser output power, 73° incidence, unpolarised detection. Arrow indicates the direction of increasing temperature.

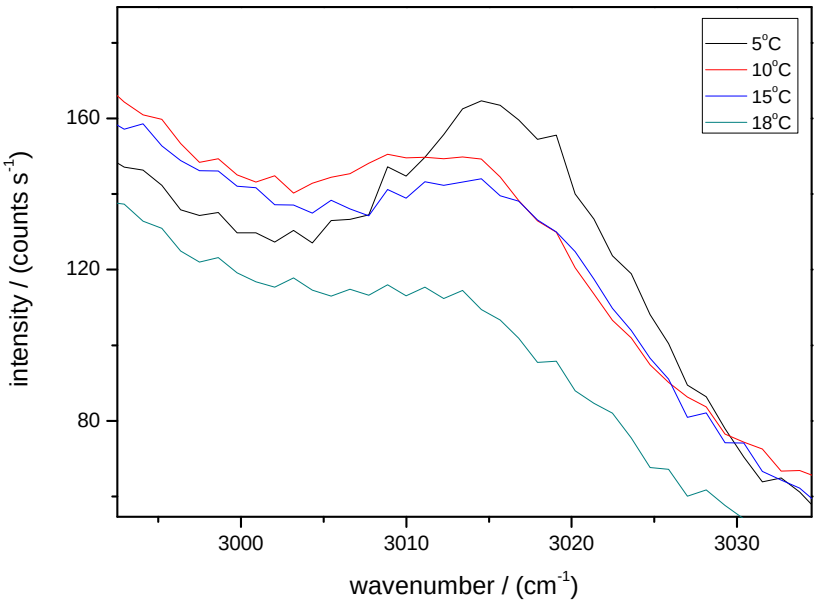

Figure 4.15: Close-up view of the vinylic CH stretching band from 4.14 (a). High temperature spectra removed for clarity.

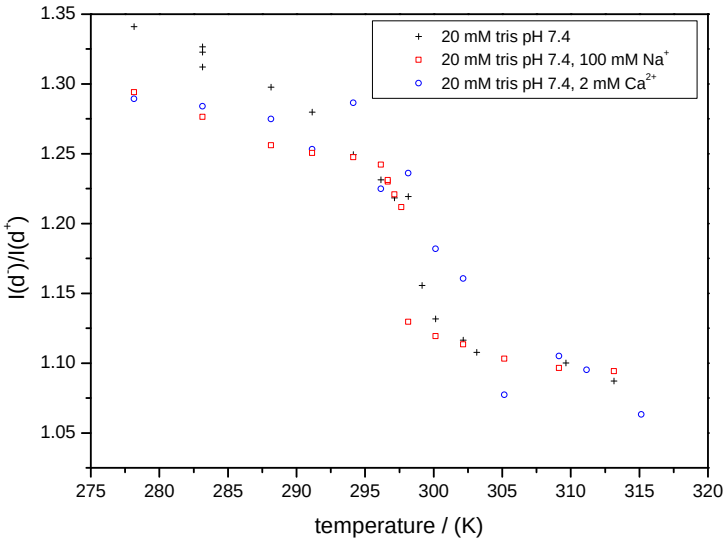

Figure 4.16: Graph showing the variation in the peak $I(d^-)/I(d^+)$ ratio as a function of temperature for three POPE SLBs in three different buffers: 20 mM tris pH 7.4 (black crosses), 20 mM tris pH 7.4 + 100 mM NaCl (red squares), 20 mM tris pH 7.4 + 2 mM $CaCl_2$ (blue circles).

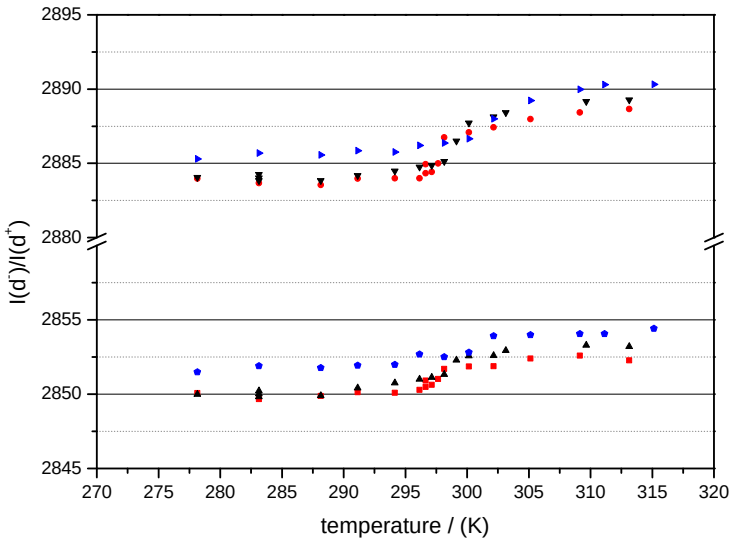

Figure 4.17: Graph showing the variation in the peak positions of the symmetric and antisymmtric CH stretches as a function of temperature for POPE SLBs in three different buffers: 20 mM tris pH 7.4 (black up pointing and down pointing triangles), 20 mM tris pH 7.4 + 100 mM NaCl (red circles and squares) and 20 mM tris pH 7.4 + 2 mM $CaCl_2$ (blue pentagons and side pointing triangles).

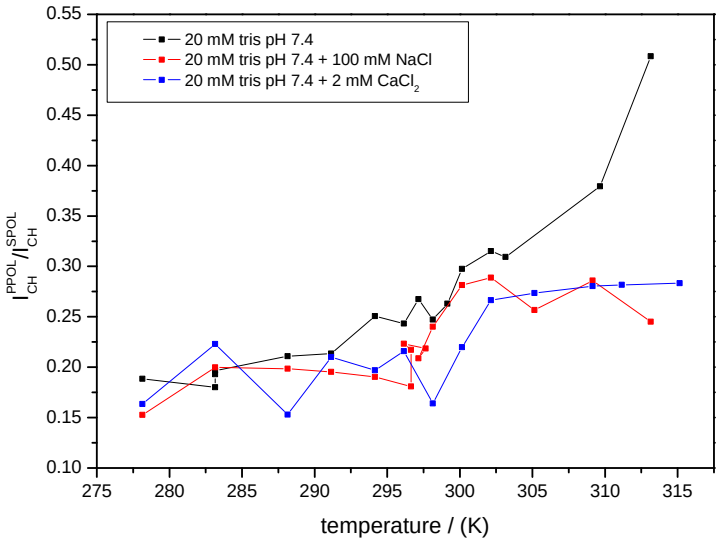

Figure 4.18: Graph showing the variation in the ratio of P-polarised to S-polarised CH region integrated intensity as a function of temperature for three POPE SLBs: 20 mM tris pH 7.4, 20 mM tris pH 7.4 + 100 mM NaCl, 20 mM tris pH 7.4 + 2 mM $CaCl_2$.

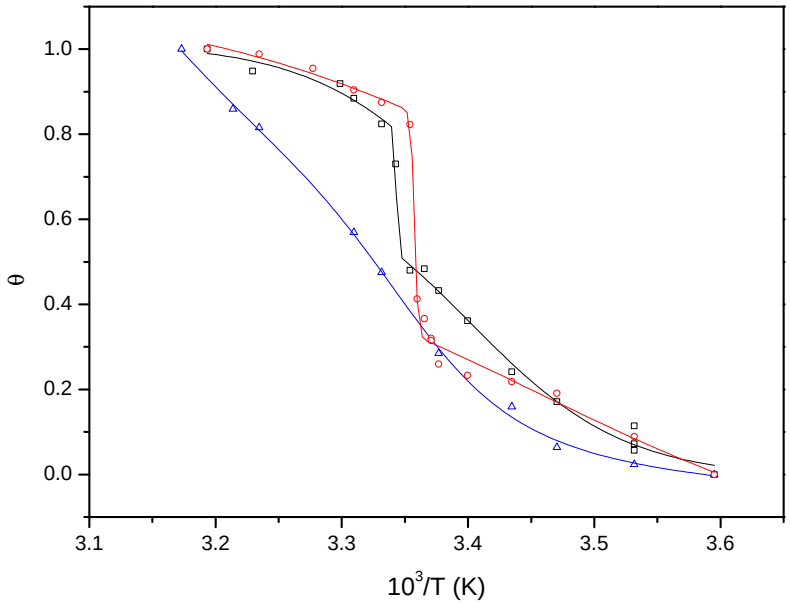

Figure 4.19: A graph showing θ, the rescaled primary order parameter plotted against $1/T$ for POPE SLBs in: 20 mM tris buffer pH 7.4 (black squares and line), 20 mM tris pH 7.4 + 100 mM NaCl (red circles and line), 20 mM tris pH 7.4 + 2 mM $CaCl_2$ (blue triangles and line). N.B extreme outliers were removed from the $CaCl_2$ data to facilitate fitting.

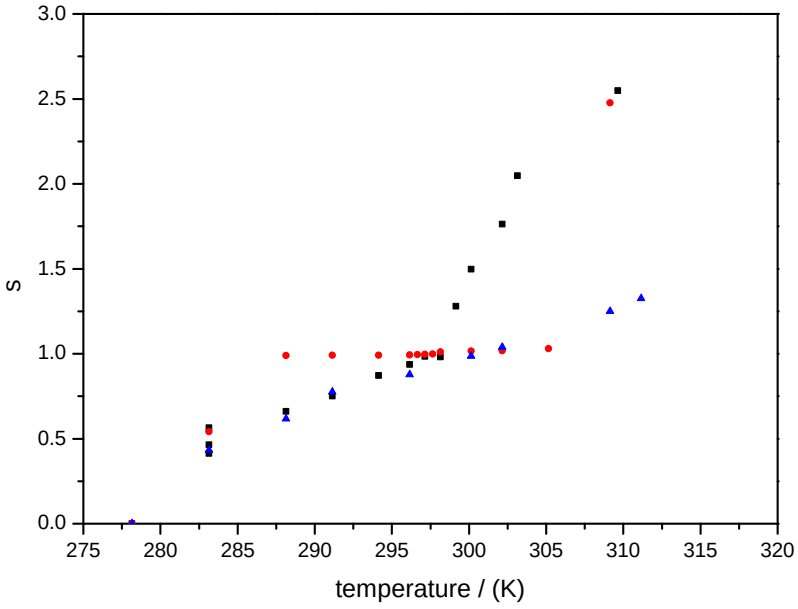

Figure 4.20: A graph showing the scaling of s the statistical weight of a fluid state molecules as a function of temperature for POPE SLBs in: 20 mM tris pH 7.4 (black squares), 20 mM tris pH 7.4 + 100 mM NaCl (red circles), 20 mM tris pH 7.4 + 2 mM $CaCl_2$. The values were obtained numerically by a least squares procedure following the determination of σ at $\theta = 0.5$.

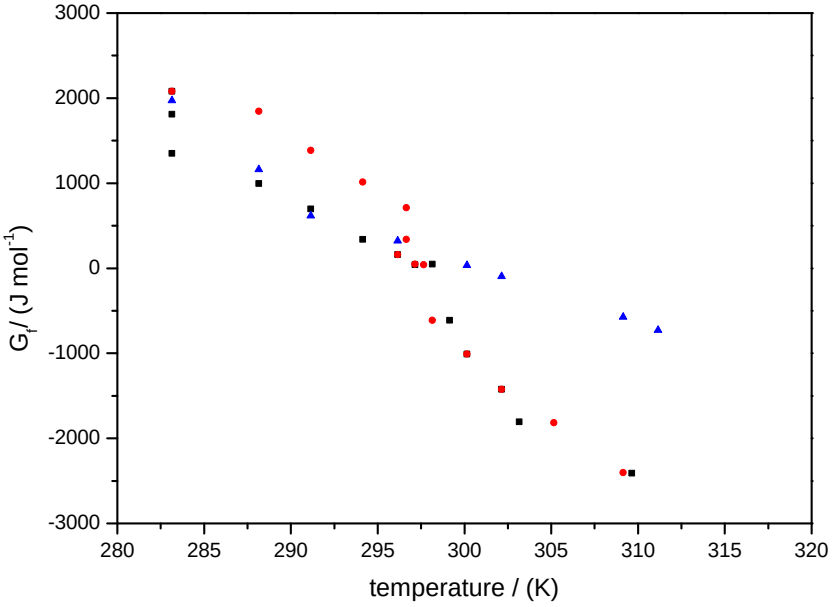

Figure 4.21: A figure showing the variation of G_f the free energy of a non-interfacial fluid phase lipid molecule, relative to the free energy of a solid state molecule, as a function of temperature for a POPE SLBs on silica in: 20 mM tris buffer pH7.4 (black squares), 20 mM tris buffer pH 7.4 + 100 mM NaCl (red circles), 20 mM tris buffer pH 7.4 + 2 mM $CaCl_2$ (blue triangles).

Solution	T_m (°C)	ΔH_{vH} (kJ mol^{-1})	$[\Delta H_t]$ (kJ mol^{-1})	$1/\sqrt{\sigma}$	G_i (kJ mol^{-1})
20 mM tris pH 7.4 + 2 mM $CaCl_2$	27.2	-134	-18.4	4 ($1.88\text{x}10^{-2}$)	9.93
20 mM tris pH 7.4 + 100 mM NaCl	24.6	-2778	-18.4	91 ($4\text{x}10^{-5}$)	24.9
20 mM tris pH 7.4	25.3	-1128	-20.5	33 ($3.3\text{x}10^{-4}$)	19.9

Table 4.2: A table showing the transition temperatures, van't Hoff enthalpies, cooperative unit sizes, and interfacial free energies calculated for POPE SLBs in tris buffer with added $CaCl_2$ or NaCl. The cooperative unit sizes are given as the nearest whole integer values and the extracted σ values used in their calculation are given below in brackets. The literature calorimetric transition enthalpies were taken from reference;[75] the value used for the pure tris buffer was measured in pure water, the value used for the salt containing solutions were measured in 0.1 mM NaCl. No calorimetric data was found for $CaCl_2$ containing solutions in the literature.

only and NaCl containing systems poorly, however as I am primarily interested in acquiring the gradient at $\theta = 0.5$ this issue was not a restriction. Another important point was for the pure tris data the rapid step did not occur until the degree of transition was greater 0.5, for this reason I used the gradient at ≈ 0.52 for this system. In fact it is hard to justify the use of the Zimm and Bragg model for this system owing to these issues in its behaviour. Figure 4.20 shows the s values required to accurately fit the experimental θ values for this system, we notice the gradual almost linear variation in s for the NaCl and $CaCl_2$ containing systems; although the gradient is significantly higher for the $CaCl_2$ data. Generally, as $\theta \to 0$ and $\theta \to 1$ s becomes increasingly small and large respectively, owing to the form of equation 4.25. However, unlike the other two systems, the pure tris dataset shows a significant change in gradient at $\theta \approx 0.52$. The fluid phase free energy shown in figure 4.21 is perhaps more instructive, unlike the DMPC data, the NaCl containing and pure tris systems show rapid fall offs in free energy at the mid point of the transition. This rapid change in free energy suggests a fundamental change in the structure of these SLBs at $\theta \approx 0.5$. The $CaCl_2$ system does not exhibit this behaviour; the binding of Ca^{2+} not only reduces the cooperativity of the transition, but also prevents whatever structural change is taking place in the NaCl and pure tris systems. Table 4.2 shows the thermodynamic data acquired using the Zimm and Bragg analysis. The van't Hoff enthalpies vary broadly for POPE, from very large when NaCl is added (-2778 kJ mol^{-1}), to very low when $CaCl_2$ was used (-134 kJ mol^{-1}). As expected owing to the small differences in the calorimetric enthalpies, these variations can only be brought about by large differences in the size of the cooperative unit. Indeed, when we calculate the interfacial free energy we see that Ca^{2+} binding reduces this free energy relative to the pure tris system, whereas the inclusion of Na^+ increases it. These data highlight the large effect of the added salts can have upon the cooperativity of SLB phase transitions.

Owing to the large difference between the $CaCl_2$ system and any of the others discussed so far, I thought it prudent to examine the main phase transition of POPE in the $CaCl_2$ containing tris buffer with fluid tapping-mode AFM. Some of the AFM images acquired are shown in figure 4.22, I have chosen to primarily present phase images as it is far easier to see the structure of the interface in these images than in their topographic equivalents. These data clearly show the nature of the POPE phase transition in 20 mM tris buffer pH 7.4 with added 2 mM $CaCl_2$. In (a) at 35°C there is a homogenous surface, as indicated by the same characteristic energy dissipation on the surface. Subfigure (b) shows the sample after it was cooled to 27°C, notice the many domain like structures; at this temperature we were approximately halfway through the transition as indicated by figure 4.19. Closeup phase and topographic images of these domains are shown in subfigures (c) and (d) respectively. The darker domains in the phase image are approximately 0.5 nm taller than the surrounding areas and are L_β regions. Notice the irregular shape of the interfacial regions between L_α and L_β phases; this is highly suggestive of low interfacial energy; interfaces with a high energetic penalty would lead to the formation of spherical domains. In addition I also observe L_β domains of many different sizes; the domains in the image are clearly far larger than the cooperative unit of nine POPE molecules for this system. The fact that regions of L_β phase larger than the cooperative unit exist means that there is some larger scale cooperativity, stemming from a minimisation of interface. Subfigure (e) shows another closeup image of the same surface as (c) and (d), rotated by 90° and shifted slightly (see for instance the scratch in the silica surface) after a number of heating and cooling cycles. For this image, during acquisition, the sample was cooled from 35°C to 27°C, observe the increase in dark areas as one moves from the upper section (higher temperature) to the lower section (lower temperature) in the image. Subfigure (f) shows the same surface at 24°C, the lowest temperature recorded, in this image just over half of the surface has changed to the L_β phase. It is worth noting that none of the AFM images acquired show any evi-

dence of tubule formation as observed by Tamm and McConnell, but this is expected as they were prepared above the main phase transition temperature from suspension. What is more interesting is the absence of any defects during cooling; even for a complete SLB cooling from the L_α phase to the L_β is expected to coincide with a reduction in the area per molecule.

Bonn and coworkers observed a disordering of POPE monolayers at high surface pressures at the air-water interface with bound Ca^{2+}. The analogous scenario in my work is the value of the primary order parameter at low temperature. For both sodium and calcium containing systems I observed a decrease of ≈0.05 in the low temperature order compared to the tris only system – this is in agreement with Bonn and coworkers. AFM measurements of my clean SiO_2 substrates showed an RMS roughness of 0.20 nm the same as the values Seeger *et al.* obtained for their substrates. My TIR-Raman data provide no evidence for a strong interaction with the support as we observe no decoupled transition; if this were the case one would expect to observe double sigmoidal behaviour in the primary order parameter and peak position data. In addition, close inspection of my AFM data shows that with repeated heating and cooling of the same interfacial region I did not observe the same domains forming at the same temperature for different cycles; this means that the surface was not acting as a template for the main phase transition. Templating would be expected if there were regions of the support that had a higher interaction potential with the SLB. Overall these observations imply a limited interaction with the silica support. The changes observed in the data with respect to the presence of the chlorides are most likely specific to the interaction of their ions with the SLB itself, largely independent of the support.

4.4.4 Egg-SM

Figure 4.23 (a) shows S-polarised TIR-Raman spectra of an egg-SM SLB in 20 mM tris pH 7.4 with 2 mM $CaCl_2$ as a function of temperature and (b) a close-up of the symmetric and antisymmetric stretches. As for the the other two lipid species investigated we observe a decrease in the S-polarised data and a small increase in the P-polarised data (shown in Appendix A). Broadly we see the same increase in the peak positions with temperature and a decrease in the $I(d^-)/I(d^+)$ ratio in both S and P-polarised TIR-Raman spectra. Figure 4.24 shows the change in the primary order parameter as a function of temperature for the three buffer conditions. The data here show large changes in the primary order parameter that are comparable to those seen for DMPC. In my review section I discussed a paper in which Law and coworkers examined the phase behaviour of sphingomyelins from three natural sources.[105] They observed that no L_β phase was present at low temperature for egg-SM at atmospheric pressure concluding that the low temperature phase was a ripple phase. In my work the phase transition measured is so similar to the main phase transition of DMPC and POPE that I cannot discern whether or not a P_β phase is present. In this study egg-SM was obtained from Fluka, whereas Law and coworkers obtained egg-SM from Avanti Polar Lipids Inc. so the actual source of the natural product could be the cause of potential differences. The data for the NaCl containing buffer clearly show the highest phase transition temperature for this lipid system. For the other lipid species investigated this was not the case and the $CaCl_2$ containing system was the most shifted. Interestingly, in the fluid phase for all three buffers, the degree of ordering was the same. However, at low temperatures, there are clear differences in order – the $CaCl_2$ containing system was the most ordered having the fewest number of gauche defects. Figure 4.25 shows the variation in the peak positions of the symmetric and antisymmetric CH stretches for egg-SM in the three buffer solutions as a function of temperature. The NaCl containing system shows significantly different packing compared with

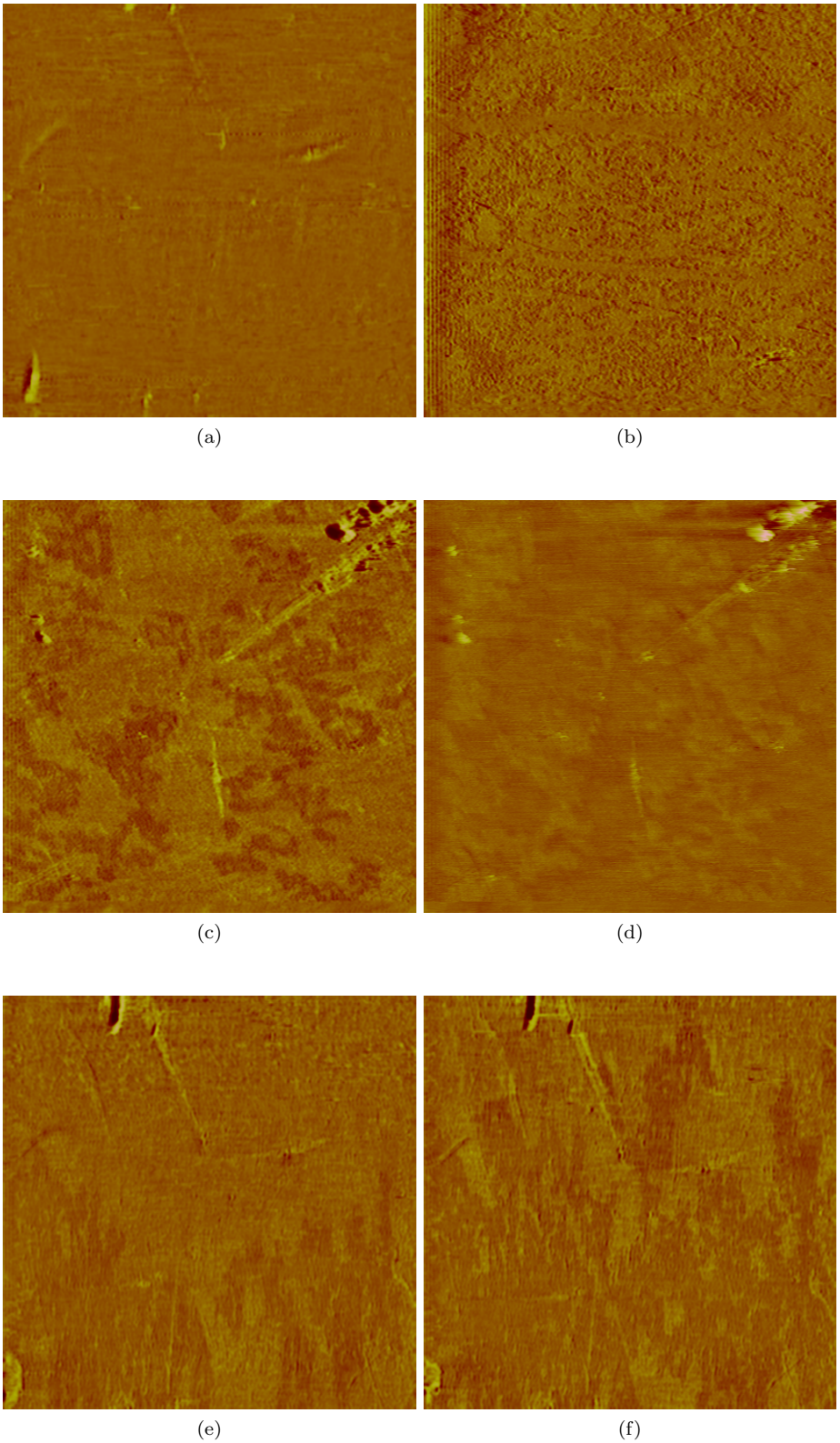

Figure 4.22: AFM tapping mode phase images of a POPE SLB on SiO_2 in 20 mM tris pH 7.4, with added 2 mM $CaCl_2$ acquired at different temperatures and different scales.(a) 35°C 15μm, (b) 27°C 80 μm, (c) 27°C 15 μm, (d) topographic image of (c), (e) 35 $\rightarrow$ 27°C 'cooling' scan 15 μm, (f) 24°C 15 μm.

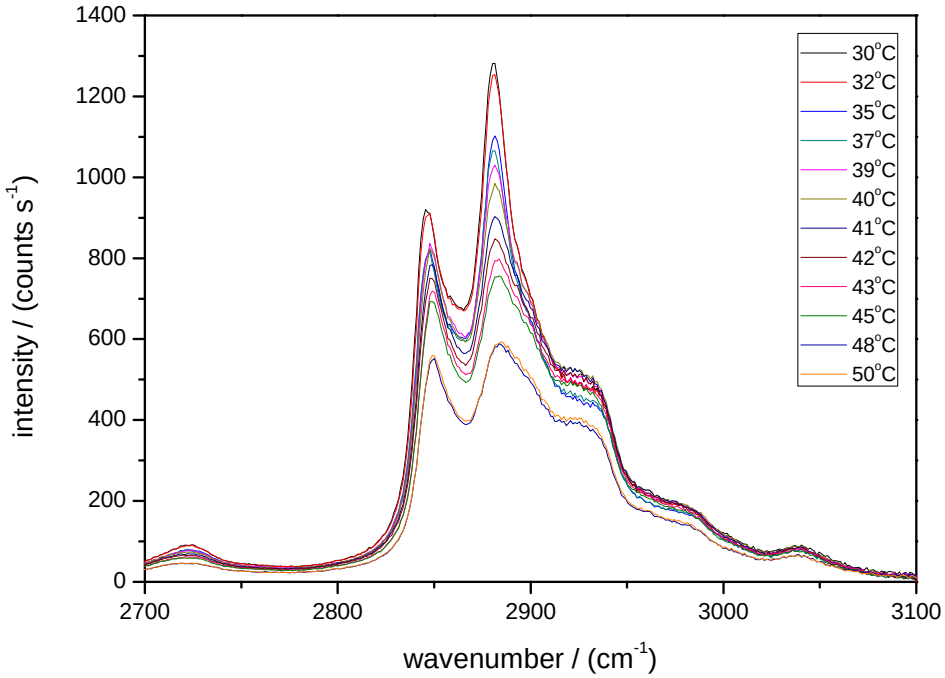

(a)

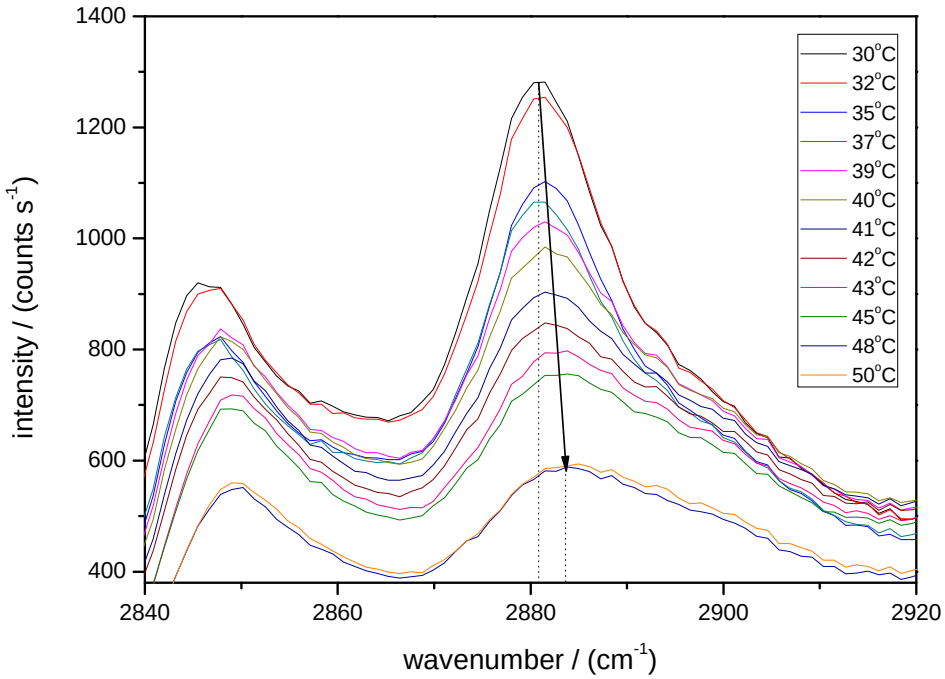

(b)

Figure 4.23: Temperature dependent S-polarised TIR-Raman spectra of an egg-SM SLB on SiO_2 in 20 mM tris pH 7.4 + 2 mM $CaCl_2$. 800 mW laser output power, 73° incidence, unpolarised detection. Arrow indicates the direction of increasing temperature.

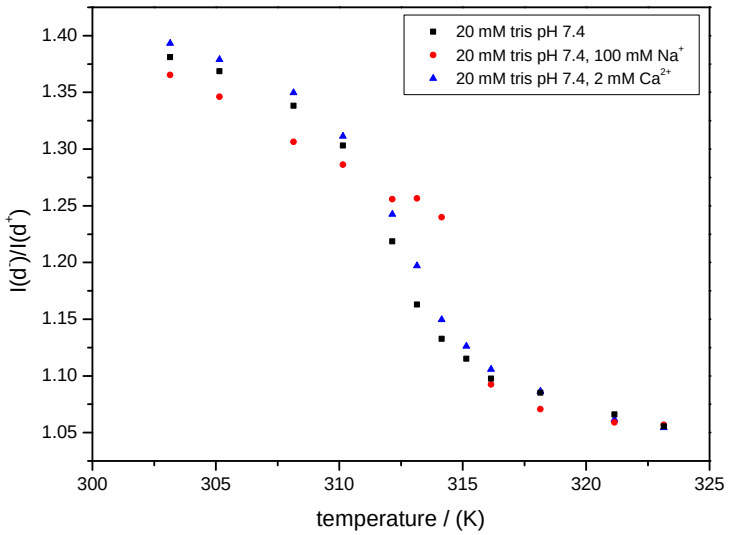

Figure 4.24: Graph showing the variation in the peak $I(d^-)/I(d^+)$ ratio as a function of temperature for three egg-SM SLBs in three different buffers. 20 mM tris pH 7.4 (black squares), 20 mM tris pH 7.4 + 100 mM NaCl (red circles), 20 mM tris pH 7.4 + 2 mM $CaCl_2$ (blue triangles).

the calcium and tris only buffers. The data also show a higher transition temperature for sodium containing system in comparison to the calcium or tris only buffers. These data combined with the primary order parameter data discussed above show that sodium has a stronger interaction with egg-SM (irrespective of concentration), whereas the for DMPC and POPE the Ca^{2+} containing data showed the higher transition temperature or greatest change in transition behaviour highlighting a stronger interaction in those systems. Figure 4.26 shows the change in average lipid chain tilt for egg-SM in the three buffer conditions. All three systems show qualitatively similar behaviour, with an increase in the integrated intensity ratio with temperature, although we see no changes at low temperatures. This point is noteworthy because we observe a decrease in the primary order parameter at low temperatures with increasing temperature – chain tilt is not necessarily coupled to internal chain order. The main difference between egg-SM in the three different buffers here is the degree of chain tilt at the highest temperature. For the sodium containing buffer, which I have already shown to have the greatest effect on the phase transition for egg-SM, shows the lowest degree of chain tilt at the highest temperature; perhaps suggesting the resistance to chain tilting owing to sodium binding. The next highest is the calcium containing system, which is understandable in terms of a certain degree of cation binding. The tris only buffer shows the highest intensity ratio and thus the greatest degree of chain tilting at the highest temperatures. These data highlight the effect of the cations on the egg-SM system at higher temperatures, the binding of these cations prevents the egg-SM from tilting as much as it would in their absence.

Figure 4.27 shows the rescaled primary order parameter as a function of $1/T$ for egg-SM SLBs in the three different buffer solutions. These data show very similar transitions for the pure tris and $CaCl_2$ containing systems. However, egg-SM in the NaCl containing buffer shows quite different behaviour, whereas the the former systems show smooth sigmoidal transitions, the sodium containing system shows a sharp jump at $\theta \approx 0.4$. Table 4.3 shows the thermodynamic data extracted from figure 4.27. When we define the transition temperatures, we find that the sodium containing system has a higher transition temperature than the other two, 41.7°C. For

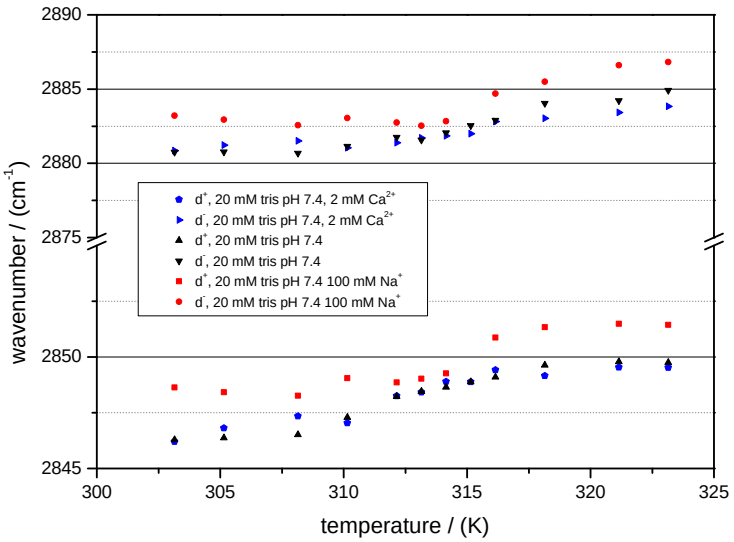

Figure 4.25: Graph showing the variation in the peak positions of the symmetric and antisymmetric CH stretches as a function of temperature for egg-SM SLBs in three different buffers. 20 mM tris pH 7.4 (black up pointing and down pointing triangles), 20 mM tris pH 7.4 + 100 mM NaCl (red circles and squares) and 20 mM tris pH 7.4 + 2 mM $CaCl_2$ (blue pentagons and side pointing triangles).

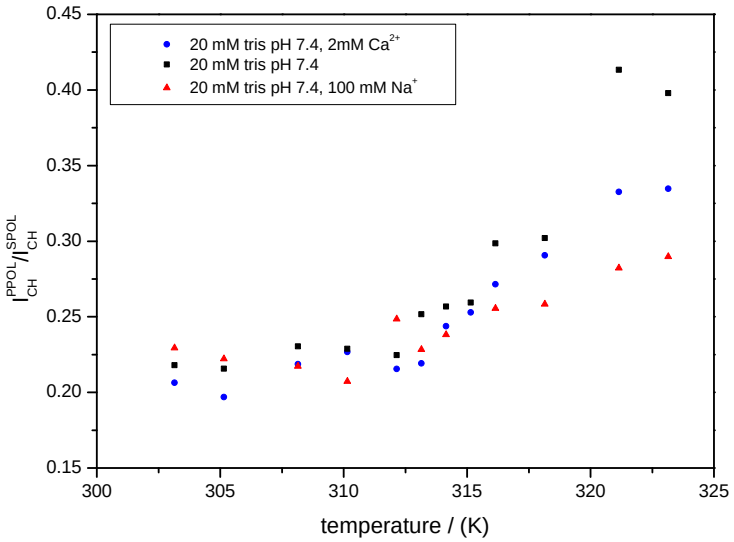

Figure 4.26: Graph showing the variation in the ratio of P-polarised to S-polarised CH region integrated intensity as a function of temperature for three egg-SM SLBs: 20 mM tris pH 7.4, 20 mM tris pH 7.4 + 100 mM NaCl, 20 mM tris pH 7.4 + 2 mM $CaCl_2$.

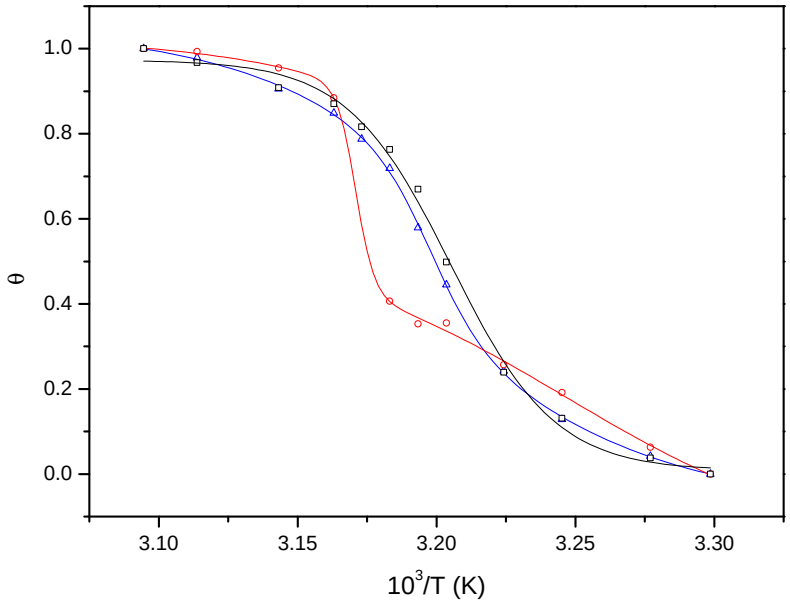

Figure 4.27: A graph showing θ, the rescaled primary order parameter, as a function of temperature for three egg-SM SLBs in 20 mM tris buffer pH 7.4 (black squares), with added NaCl (red circles) or $CaCl_2$ (blue triangles).

POPE we found that $CaCl_2$ had the greatest effect on the transition, broadening it significantly; for egg-SM clearly NaCl has the greater effect. Taken together the data for these two lipids show how ions have specific effects for different lipid systems, which is probably a result of their different ionic radii and the structure of the different lipid bilayers. The van't Hoff enthalpies and $1/\sqrt{\sigma}$ values shown in table 4.3 suggest very similar cooperative unit sizes for the calcium containing and tris only systems, but a much larger unit size for the NaCl containing system, at least at the mid point of the transition. These in turn mean that the NaCl containing system has a higher interfacial tension between regions of L_β and L_α phase, the values for the interfacial free energy are given in table 4.3.

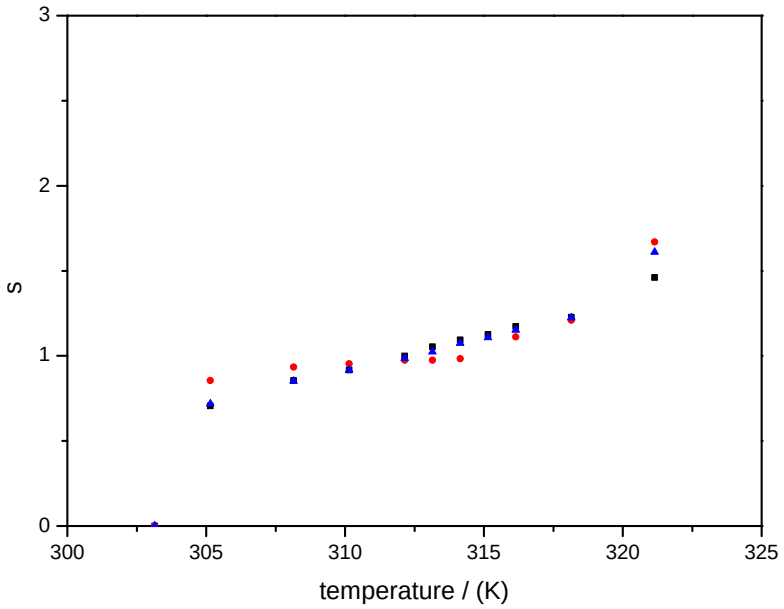

Figure 4.28: A graph showing the scaling of s the statistical weight of a fluid state molecules as a function of temperature for egg-SM SLBs in: 20 mM tris pH 7.4 (black squares), 20 mM tris pH 7.4 + 100 mM NaCl (red circles), 20 mM tris pH 7.4 + 2 mM $CaCl_2$. The values were obtained numerically by a least squares procedure following the determination of σ at $\theta = 0.5$.

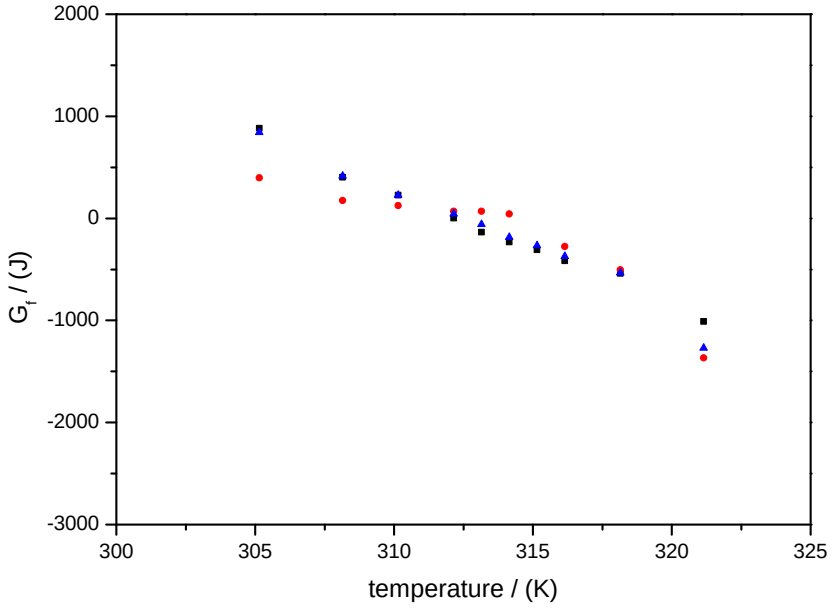

Figure 4.29: A figure showing the variation of G_f the free energy of a non-interfacial fluid phase lipid molecule, relative to the free energy of a solid state molecule, as a function of temperature for a egg-SM SLBs on silica in: 20 mM tris buffer pH 7.4 (black squares), 20 mM tris buffer pH 7.4 + 100 mM NaCl (red circles), 20 mM tris buffer pH 7.4 + 2 mM $CaCl_2$ (blue triangles).

Solution	T_m (°C)	ΔH_{vH} (kJ mol^{-1})	$[\Delta H_t]$ (kJ mol^{-1})	$1/\sqrt{\sigma}$	G_i (kJ mol^{-1})
20 mM tris pH 7.4 + 2 mM $CaCl_2$	39.4	-477	-34.7	14 ($5.3x10^{-3}$)	14.4
20 mM tris pH 7.4 + 100 mM NaCl	41.7	-797	-34.7	23 ($1.9x10^{-3}$)	17.2
20 mM tris pH 7.4	38.9	-430	-31	14 ($5.2x10^{-3}$)	13.8

Table 4.3: A table showing the transition temperatures, van't Hoff enthalpies, cooperative unit sizes, and interfacial free energies calculated for egg-SM SLBs in tris buffer with added $CaCl_2$ or NaCl. The cooperative unit sizes are given as the nearest whole integer values and the extracted σ values used in their calculation are given underneath in brackets. The literature calorimetric transition enthalpies are taken from reference.[75] No specific calorimetric values for egg-SM were available so the transition enthalpy of the predominate species was used throughout. The enthalpy for the pure tris buffer was measured in pure water, the value used for the salt containing solutions was measured in 0.1 mM tris-acetate pH 7.0.

4.5 Conclusions

It is well known that the addition of salts at low and moderate concentrations has a limited effect on the calorimetric transition enthalpy (ΔH_t) of hydrated lipid bilayers, and only a limited effect on the transition temperature. However, I have been able to show by the application of the Zimm and Bragg model to my TIR-Raman data that low concentrations of NaCl and $CaCl_2$ can lead to changes in the cooperativity of the phase transitions of supported lipid bilayers. These changes are brought about by alterations in the interfacial energy between regions of L_α and L_β phase within the temperature range of phase coexistence; often only by a few kJ mol^{-1}. I have observed these effects to be specific and unrelated to concentration, for instance POPE shows a massive collapse in transition cooperativity in $CaCl_2$-containing tris buffer at neutral pH owing to a decrease in the interfacial energy, whereas the opposite effect was observed for egg-SM in NaCl containing tris buffer where the cooperativity increased; the binding of Na^+ to the lipid headgroup region in this system increased the inter-phase interfacial energy. On the other hand DMPC seems to show the smallest changes in cooperativity upon the inclusion of NaCl or $CaCl_2$, but of the salts added the $CaCl_2$ had the greatest effect – reducing the cooperativity.

The use of specific group I and II salts often had effects on the structural nature of the transition in terms of chain tilt, chain packing and internal chain order. In my review section I summarised some older work by various authors. My measurements of SLB phase transitions show no or very limited evidence of a ripple phase – the order parameter changes observed for egg-SM and DMPC in all three buffer solutions are commensurate with the values obtained for POPE which does not have a P_β phase. Therefore either TIR-Raman is insensitive to the ripple phase relative to the L_β, or the ripple phase is being suppressed at the silica-water interface. In all my measurements I never once observed double sigmoidal behaviour in the order parameters used. This implies that in all of the systems I observed completely coupled phase transitions; this when considering the absence of 'templating' in my AFM measurements indicated a weak interaction between the silica supports and the respective SLBs.

Perhaps further measurements with techniques such as AFM would permit a direct determination of the cooperative unit size at different temperatures. These measurements would provide an avenue to explore the parity between my spectroscopic measurements and other workers calorimetric data as well a potential justification of the Zimm and Bragg model being used to understand these transitions. This further work is particularly important owing to the size of the domains ob-

served in my POPE AFM studies; in those images the domains, whilst appearing significantly smaller than the typical laser spot size used for my Raman measurements, were significantly larger than the cooperative unit size suggested by the Zimm and Bragg model. The gel phase domains were forming in sites adjacent to one another; thus a larger scale cooperativity was at work that enhanced the likelihood of neighbouring units changing phase at similar temperatures – this could potentially explain the strange form of my θ vs 1/T data for POPE. One problem in this field is the wide range of solution conditions used by different workers (see for instance Marsh[75]) this means that specific calorimetric data are rare. This becomes a significant problem when studying bilayers at interfaces, where the bilayer/support interaction can have a strong effect on the nature of any phase transitions particularly on mica. Calorimetric measurements in the vein of Bayerl and coworkers are required to resolve this issue for supported lipid systems. An idea for future work could be the replacement of the silica supports used in this study for ones comprised of glasses which do not occlude the lipid phosphate bands. Changes in this spectral region could indicate the strength of binding of cations such as Na^+ and Ca^{2+} thus potentially providing further insight into how these cations affect the interfacial energies I have calculated.

Chapter 5

The Interaction of Surfactants with SLBs

5.1 Introduction

In this chapter I will examine the interaction of SDS with a selection of SLB systems on silica. Surfactant lipid interactions play an important role in numerous situations: the regulation of cellular processes, the delivery of drugs, the extraction and purification of proteins, in the theory of lipid rafts, in the use of personal care products and cleaning detergents. Much of the work carried out to date has been conducted on vesicular systems, but very little fundamental work has be done on SLBs. TIR-Raman is a technique well suited to study these interfacial systems. The aim of this chapter is to follow the kinetics of SDS partitioning and rinsing from SLBs on silica, to investigate the structural changes that accompany these processes and to compare the equilibrium data acquired to established partitioning models.

5.2 Theory

In a key 1975 review, Helenius and Simons divided the interaction of surfactants and membranes into three stages. In stage I which they called "detergent binding" they describe a process where surfactant monomers partition into the bilayer phase. In stage II, there is a lamellar to micellar phase transition after the lamellar phase becomes saturated with surfactant; mixed micelles form at the expense of the mixed lamellar phase. In stage III only mixed micelles remain and as the concentration of surfactant increases, the size of the mixed micelles decreases. The 'three stage model' only includes three aggregate structures and says nothing of the dynamic processes that occur upon partitioning and solubilisation; it is these aspects which I have studied.

Heerklotz has reviewed several thermodynamic treatments of surfactant lipid bilayer partitioning, and several groups have used the models described below.[82]

At very low mole fractions, non-ionic surfactant partitioning can be given an ideal mixing treatment. At higher mole fractions, the case of non-ideal mixing must be considered. Lastly for charged surfactant species such as SDS, electrostatic effects must be considered and appropriate corrections to surface concentration made.

5.2.1 Ideal mixing

For ideal mixing, as in the thermodynamics of ideal dilute solutions, the chemical potential of a surfactant, μ_s^b, in a lipid bilayer can be written as

$$\mu_s^b = \mu_s^{0,b} + RT \ln X_s^b, \tag{5.1}$$

where X_s^b is the mole fraction of surfactant partitioned into the bilayer, given by

$$X_s^b = \frac{n_s^b}{n_s^b + n_L^b}, \tag{5.2}$$

where n_s^b and n_L^b are the number of moles of surfactant and lipid in the bilayer. R is the molar gas constant and T is the temperature. Equation 5.1 only holds where a bilayer is free to change its area, otherwise,

$$\frac{\partial \mu_s^b}{\partial n_s^b} \to \infty \text{ as } X_s \to 1 \tag{5.3}$$

since there is nowhere for the surfactant molecules to partition if the bilayer has no room to expand. The standard state $\mu_s^{0,aq}$ is defined as

$$\mu_s^{0,aq} = \lim_{X_s^{aq} \to 1} (\mu - RT \ln X_s^{aq}) \tag{5.4}$$

For ideal mixing where there is no enthalpic contribution to the molar Gibbs energy, the $RT \ln X_s^b$ term corresponds to the entropic contribution. When one considers the aqueous surfactant solution and the insoluble lipid bilayer as two distinct phases, equilibrium partitioning is attained when the chemical potential of surfactant monomers in solution is equal to that of those in the bilayer phase. Therefore

$$\mu_s^{0,b} + RT \ln X_s^b = \mu_s^{0,aq} + RT \ln X_s^{aq} \tag{5.5}$$

where X_s^{aq} is the mole fraction of surfactant in solution and $\mu_s^{0,aq}$ is the standard chemical potential of the surfactant in aqueous solution. We can thus write

$$\Delta\mu_s^{0,aq \to b} = \mu_s^{0,b} - \mu_s^{0,aq} = -RT \ln \frac{X_s^b}{X_s^{aq}}. \tag{5.6}$$

This expression shows that the difference between the entropies associated with the chemical potentials of the two standard states leads to an intrinsic surfactant preference for partitioning, defined by the mole fractions of surfactant within each phase at equilibrium. At equilibrium, as the standard states are constant so too must be the ratio of the mole fractions and we can refer to this constant ratio as the partition coefficient,

$$K_X = \frac{X_s^b}{X_s^{aq}} = \frac{n_s^b(n_s^{aq} + n_w)}{(n_s^b + n_L^b)n_s^{aq}} \approx \frac{X_s^b \cdot C_w}{C_s^{aq}}; \tag{5.7}$$

where n_L^b is the number of moles of lipid in the bilayer, C_s^{aq} is the bulk concentration of surfactant, C_w is the bulk concentration of water (≈ 55 M in dilute solution) n.b. the concentration of lipid in water is ignored as lipids have extremely low solubility. Whether partitioning is spontaneous depends on whether K_X has been reached for a given bulk surfactant concentration.

5.2.2 Non-ideal mixing

In general surfactant mixing with water and lipids exhibits non-ideal behaviour owing the the multifarious interactions that occur between the chemical species present in the bilayer and water phases. As a result expressions for the free energy of surfactant in bilayer and water must contain a factor pertaining to the activity of the medium in question. These modified expressions for the chemical potential have the form;

$$\mu = \mu^0 + RT \ln[X \cdot f(X)], \tag{5.8}$$

where $f(X)$ is the activity coefficient and μ^0 is the relevant standard chemical potential. In an ideal dilute solution, $f(X) \approx 1$ for surfactant concentrations below the CMC (provided that, for ionic surfactants, the ionic strength is constant). Thus the standard free energy change may be written as,

$$\Delta\mu_s^{0,aq\to b} = -RT \ln[K_X(X_s^b) \cdot f(X_s^b)] = -RT \ln[K_X(0)]. \tag{5.9}$$

The latter equality highlights that in the limit of $X_s^b \to 0$, $f(X_s^b) \to 1$. There are two ways in which expressions for $f(X_s^b)$ have been derived, one semi-empirical the other statistical; I will describe the former as it is the most relevant when describing the effects of surfactant charge on partitioning. This model is based on the empirical observation that in non-ideal situations the mole ratio of surfactant to lipid in the bilayer phase, R_b is proportional to the free surfactant concentration. i.e.

$$K_R = \frac{n_s^b C_w}{n_L^b C_s^{aq}} = \frac{R_b C_w}{C_s^{aq}} \tag{5.10}$$

is a constant. Therefore if

$$[K_X(X_s^b) \cdot f(X_s^b)] = K_R, \tag{5.11}$$

then $f(X_s^b)$ must equal $(X_L^b)^{-1}$, for $K_X \cdot (X_L^b)^{-1} \approx K_R$. As X_L^b approaches unity i.e. $\lim_{X_s^b \to 0}$ K_R approaches K_X. In order to keep K_R constant, the change in the variable $K_X(X_s^b)$ must be compensated by a change in $f(X_s^b)$. As X_L^b decreases with increasing X_S^b, $f(X_s^b)$ must increase, therefore for constant K_R the variable $K_X(X_s^b)$ must decrease by the same factor. This implies that as the bulk concentration of surfactant increases, X_s^b increases by a smaller and smaller amount, in direct proportion to the increase in $f(X_s^b)$ brought about by the decrease in X_L^b.

5.2.3 Influence of charge on partitioning

The semi-empirical model described above for non-ideal mixing is adequate for a description of non-ionic or uncharged surfactants partitioning into lipid bilayers at higher concentrations. However, when studying the interaction of charged surfactants with lipid membranes, the effect of surface charge upon incorporation of surfactant into the bilayer must be considered as K_R is no longer constant. When the bilayer contains charged surfactants, its surface charge density is given by:

$$\sigma_0 = \frac{q \sum_i X_i^b z_i}{\sum_i X_i^b A_i}, \tag{5.12}$$

where q is the elementary charge, X_i^b is the mole fraction of the $i$the charged component within the bilayer, z_i is the charge of the ith charged component and A_i is the lateral area of this component. This surface charge density gives rise to a surface potential, ψ_0, which results in an electrical

double layer as described in my introductory chapter and the concomitant depletion of surfactant molecules close to the bilayer surface. ψ_0 is retrieved from the Gouy-Chapman theory. Where an estimate of σ_0 is available, ψ_0 is most easily obtained numerically from the equality of equations 5.12 and 5.13.

$$\sigma_0 = sgn(\psi_0)\sqrt{2000\epsilon_0\epsilon_r RT\sum_i C_i^{bulk}\left(\exp\left\{-\frac{z_i q N_A \psi_0}{RT}\right\}-1\right)} \tag{5.13}$$

This depletion, in the immediate vicinity of the surface, can be described by Boltzmann's distribution,

$$C_s^{aq,surf} = C_S^{aq,bulk}\cdot\exp\left\{-\frac{Z_s q N_A \psi_0}{RT}\right\} \tag{5.14}$$

As described before $K_R = R_b C_w / C_s^{aq,bulk}$, however, in the case of charged surfactants the intrinsic $K_R^0 = R_b C_w / C_s^{aq,surf}$. We can therefore write:

$$K_R^0 = \left[\frac{R_b C_w}{C_s^{aq,bulk}}\right]\cdot\exp\left\{+\frac{Z_s q N_A \psi_0}{RT}\right\}. \tag{5.15}$$

When the surfactants are uncharged or the charge is neutralised by counterion binding, the exponential term becomes equal to unity and $C_s^{aq,surf}$ becomes $C_s^{aq,bulk}$.

This method for finding the intrinsic partition coefficient has one key limitation in that it does not account for counterion binding. In salty conditions, counterions will bind to the charged surface and neutralise some of the surface charge density, effectively lowering it. This neutralisation then acts to reduce the surfactant depletion/increase at the interface and so raise or lower the partitioned mole fraction of charged surfactant depending on the relative charges of the lipid and surfactant. The model also assumes that the area per molecule does not change for either the surfactant or lipid as a function of R_b, but the local environment has a strong effect on the volume of charged species.

The issue of counterion binding can be addressed by modifying equation 5.12 using the Langmuir isotherm.[119] As an illustration I will consider the case of SDS partitioning into a neutral bilayer immersed in a solution containing Na^+ cations. Here θ gives the fractional coverage of bilayer partitioned DS^- monomers with Na^+ counterions

$$\theta = \frac{K_{Na^+}^{DS^-} c_{Na^+}^i}{1 + K_{Na^+}^{DS^-} c_{Na^+}^i}, \tag{5.16}$$

where $K_{Na^+}^{DS^-}$ is the binding constant of Na^+ to the charged surfactant and $c_{Na^+}^i$ is the aqueous phase concentration of Na^+ ions. By multiplying 5.12 when written for a binary mixture of SDS and a single lipid species by $(1-\theta)$ we have,

$$\sigma_0 = \frac{X_{sds} q z_{sds}}{(X_{sds}A_{sds} + X_{lip}A_{lip})(1 + K_{Na}C_{Na})} \tag{5.17}$$

which is the surface charge density corrected for the Langmuir type adsorption of a single counterion. Unfortunately without explicit knowledge of $K_{Na^+}^{DS^-}$ it is not possible to use this extension without considering $K_{Na^+}^{DS^-}$ as another fitting parameter.

5.2.4 Membrane curvature

As described in my introductory chapter, amphiphiles have a preferred curvature or critical packing parameter, Z_p, and so form aggregates of a specific geometry. The preferred curvature can vary, for instance the optimal headgroup area of SDS can change depending on its ionic environment as this acts to moderate the electrostatic interactions which govern the geometry of charged species.

Membrane curvature is analogous to the bending of a two-dimensional sheet embedded in three-dimensional Euclidian space. To define the curvature of such an embedded surface one requires the principal curvatures of two curves running along two planes, normal to, and passing through the surface. The principal curvatures are found by considering the radii of curvature of the arcs within each plane; in essence we treat the arcs as sections of two circles and the radii of curvature are the radii of the these two *osculating circles*.

$$c_1 = \frac{1}{R_1} \tag{5.18}$$

$$c_2 = \frac{1}{R_2} \tag{5.19}$$

The first surface curvature, called the mean curvature, is an extrinsic property of the surface and is defined as the sum of the two principal curvatures.

$$\bar{c} = c_1 + c_2. \tag{5.20}$$

The second curvature is the Gaussian curvature, which is intrinsic. The Gaussian curvature is defined as the product of the two principal curvatures,

$$\bar{c}_G^2 = c_1 c_2. \tag{5.21}$$

curvature is considered positive for convex surfaces and negative for concave ones. Helfrich has given the total bending free energy as,[120]

$$\Delta G_c(\bar{c}, \bar{c}_G) = \frac{1}{2} k_c A(\bar{c} - c_0)^2 + \bar{k}_c A \bar{c}_G^2. \tag{5.22}$$

where k_c is the mean curvature modulus, $\bar{k}_c$ is the Gaussian modulus, A is the area of bilayer under consideration and c_0 is the spontaneous curvature. For a flat non curved reference surface the elastic free energy is,

$$\Delta G(0,0) = \frac{1}{2} k_c A c_0^2, \tag{5.23}$$

which is the curvature frustration of the lipids as they are forced into a planar configuration. Symmetrical bilayers have zero spontaneous curvature, but the individual monolayer leaflets still experience spontaneous curvature stress where $Z_p \neq 1$.

When surfactant molecules with $Z_p \approx 1/3$ partition into a lipid lamellar phase, where the lipid has $Z_p = 1$, they create curvature strain within the bilayer. If the bilayer is not free to alter its geometry, this strain will build leading to a disordering of the lipid molecules, their cross-sectional area must adapt to fit the geometry being imposed upon them. If the surfactant only partitions into one leaflet, the disordering will be more pronounced on the opposite bilayer leaflet, the result being a thinner and more flexible mixed bilayer. However, if the bilayer is free to move, spontaneous curvature will be created, blebs and protrusions will form at the interface, the caps

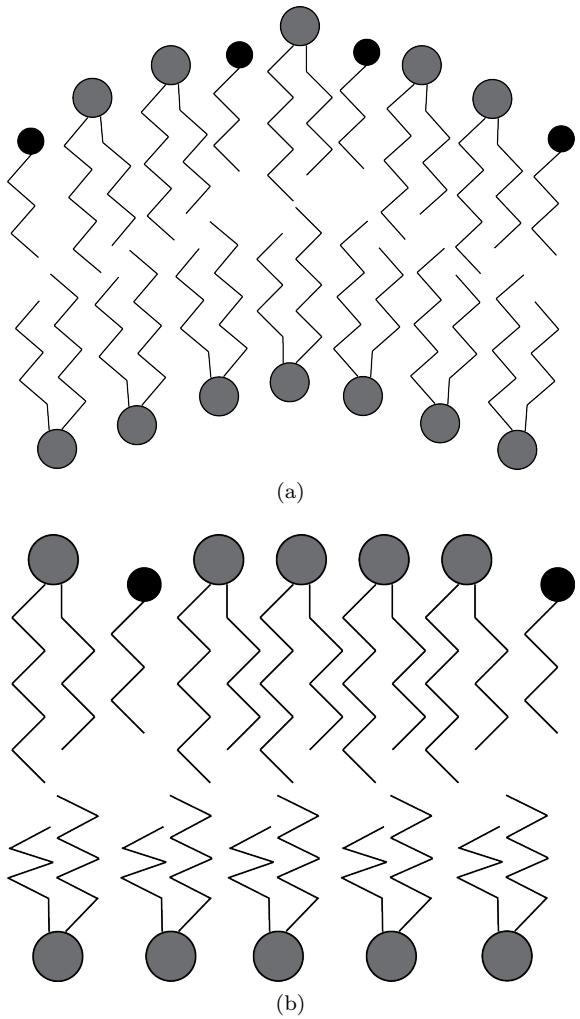

Figure 5.1: Two sketches depicting (a) spontaneous bilayer curvature and (b) bilayer curvature strain.

of which will be enriched in surfactant; this reduces the stress and lowers the bending free energy. These alternative situations are depicted in figure 5.1.

5.2.5 Unbinding transitions

Another hypothetical outcome of surfactant SLB interactions is an unbinding transition.[50,121] In general the interactions between two lipid bilayers or an SLB and a support are: i) The van der Waals interaction, ii) the hydration repulsion and iii) electrostatic double layer (electrostatic) repulsion. Here these are called the "direct interactions". These direct interactions are renormalised by bilayer fluctuation repulsion. The effect of this renormalisation is that upon reaching certain critical temperatures, or if there is a change in a bilayer's elastic properties, the bilayer can move from a bound state to an unbound state. By unbound state I mean a greater mean separation or complete separation of two bilayers or a bilayer and support. I will give an overview of the direct interactions now. I will then move on to describe the effect of renormalisation using a superposition based approach.

5.2.5.1 Hydration repulsion

It has been observed that a strong repulsion exists between lipid bilayers that approach to within 1 nm of each other. It was originally suggested that this force stemmed from ordered water layers existing close to bilayer surfaces. More recently it has been posited that the force could originate from the jostling and associated thermally induced protrusions of lipid molecules within bilayers. It is most likely that these two contributions are operating in concert. For example, if ordered water layers were to exist at bilayer interfaces, one would expect that these would lead to an oscillating interaction potential with regard to the density profile of water molecules in these ordered layers. Experimentally an exponential potential is observed suggesting that the protrusions and the intrinsic headgroup surface profile act to normalise the oscillatory behaviour "smearing it out". The hydration repulsion is modelled by the following empirical relation,

$$G_{hy}(d) = V_{hy} \exp[-d/l_{hy}], \tag{5.24}$$

where the hydration length l_{hy} is a phenomenological parameter.

5.2.5.2 Van der Waals interactions

Many molecules have permanent and induced dipole moments. The interactions between these are collectively known as van der Waals interactions. The expressions used for the van der Waals interaction in solution vary depending on the exact circumstances. For instance, two thin layers of thickness a separated by a distance d $\ll a$ can be treated as two half-spaces,

$$G_{vdw}(d) = \frac{H}{12\pi}\frac{1}{d^2} \tag{5.25}$$

where H is the Hamaker constant for the media in question. In fact, the Hamaker constant possesses two contributions, one static, from the static (zero frequency) polarisabilities of molecules, and the other from their frequency-dependent polarisabilities:

$$H = H_0(T, \kappa^{-1}) + H_f. \tag{5.26}$$

In "salty" solution conditions where the Debye length, κ^{-1} is short and electrostatic interactions screened, the static contribution to the Hamaker constant is reduced. Experimentally it been found that the above approximation for the VdW potential is accurate up to ≈ 5 nm for pure water and ≈ 4 nm in a solution of 200 mM NaCl ($\kappa^{-1} = 0.7$ nm).

For layers separated by distances large compared to the layer thickness a in salty conditions the half space approximation is a poor model and the interaction is better described by:

$$G_{vdw}(d) \approx \frac{H_f}{12\pi}\left[\frac{1}{d^2} - \frac{2}{(d+a)^2} + \frac{1}{(d+2a)^2}\right] \tag{5.27}$$

5.2.5.3 Electrostatic interactions

Earlier, in my introductory chapter, I derived expressions for the electrostatic potential near a flat surface and the distribution of charges in the proximity of that surface. In this section, I will extend these concepts to account for the interaction between two charged flat surfaces.[6] When the double layers of two charged flat surfaces begin to overlap, the ions around each surface are

displaced from their equilibrium positions leading to an increase in their potential energy. The increase in energy leads to a pressure between the two surfaces, which acts to push the surfaces apart. Figure 5.2 shows the situation before and after the overlap of the surfaces' double layers. In (a), the electrostatic potential is zero, i.e. the bulk value, but as shown in (b) when the double layers begin to overlap the potential is increased to ψ_m. Despite the increase in potential, there is no net electric field or force acting per unit charge at d/2 as $\mathrm{d}\psi/\mathrm{d}x = 0$. However, as the potential is greater than zero there must be a surfeit of ions and co-ions between the surfaces relative to the bulk despite the deficit in co-ions, and this local increase creates an osmotic pressure at the mid-plane between the two surfaces. This osmotic pressure can be calculated with knowledge of the ionic concentration at the mid-plane.

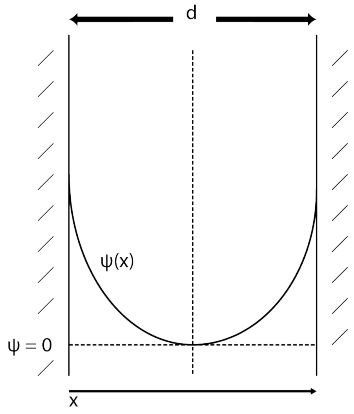

(a)

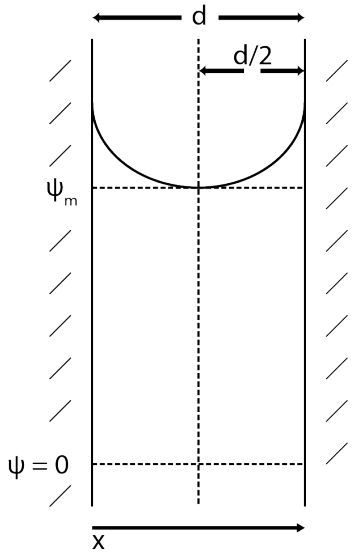

(b)

Figure 5.2: Schema showing the interaction of two charge flat surfaces and associated diffuse electrical double layers, (a) shows the situation before the overlap, $d >> \kappa^{-1}$. (b) shows the situation after overlap $d < \kappa^{-1}$.

The concentration of an ion at the mid-plane is given by,

$$C_m^T = \sum_i C_i(B) \exp\left[-\frac{Z_i q \psi_m}{kT}\right], \tag{5.28}$$

and for symmetrical electrolytes,

$$C_m^T = C(B)\left\{\exp\left[-\frac{Zq\psi_m}{kT}\right] + \exp\left[\frac{Zq\psi_m}{kT}\right]\right\} \tag{5.29}$$

$$C_m^T = 2C(B)\cosh\left[\frac{Zq\psi_m}{kT}\right]. \tag{5.30}$$

The osmotic pressure is,

$$P = CkT. \tag{5.31}$$

The difference between the osmotic pressure in the bulk and that between the two planes is given by

$$\Delta P = kT[C_m^T - 2C(B)], \tag{5.32}$$

which is equal to the repulsive pressure between the two surfaces, and

$$P_R = 2C(B)kT\left[\cosh\left(\frac{Zq\psi_m}{kT}\right) - 1\right]. \tag{5.33}$$

To calculate this we need to determine ψ_m as a function of x between the two interacting surfaces. Whilst it is possible to do this analytically for a single double layer, this is not the case for two interacting surfaces and must necessarily be determined by numerical integration of the Poisson-Boltzman equation. Despite this limitation, several approximate equations do exist. One such equation is obtained by using the Debye-Huckel approximation and the superposition principle. The Debye-Huckel approximation is essentially an expansion of the exponentials and a truncation after the first term. For low potentials ($\psi_0 < 25$ mV),

$$\psi(x) \cong \psi_0 \exp(-\kappa x), \tag{5.34}$$

where ψ_0 is the electrostatic potential at the surface and κ is the reciprocal Debye length. For the case of two overlapping double layers,

$$\psi_m \approx 2\psi_{d/2} \approx 2\psi_0 \exp(-\kappa d/2). \tag{5.35}$$

When we expand and truncate equation 5.33 we have

$$P_R \approx C(B)kT\left(\frac{Zq\psi_m}{kT}\right)^2, \tag{5.36}$$

which in combination with equation 5.35 yields,

$$P_R \approx \frac{C(B)Z^2q^2}{kT}4\psi_0^2\exp(-\kappa d) \tag{5.37}$$

$$P_R \approx 2\epsilon_0\epsilon\kappa^2\psi_0^2\exp(-\kappa d) \tag{5.38}$$

Finally the interaction potential at a separation d can be found by integrating equation 5.38 from d to infinity,

$$G_e = -\int_d^\infty p_R \mathrm{d}d. \tag{5.39}$$

Therefore,

$$G_e \approx 2\epsilon_0\epsilon\kappa\psi_0^2\exp(-\kappa d) \tag{5.40}$$

5.2.5.4 Fluctuation interactions

Supported and unsupported lipid bilayers are dynamic structures, particularly in the fluid phase. Bilayer structures undergo several types of fluctuations that include molecular protrusions, stretches and undulations. Both protrusions and undulations have a marked effect on the overall interaction of lipid bilayers with each other and supports. The effects of protrusion are included within a treatment of hydration repulsion (see above). Undulations however, are not included in any of the other interaction treatments and act to renormalise the direct interactions.[122] It is this renormalisation that leads to unbinding transitions. Fluctuations of a membrane confined by two hard-walls and with no lateral tension give rise to a roughness described by,

$$\xi_{\perp} \sim (k_B T/k_c)^{1/2} \xi_{\parallel}. \tag{5.41}$$

Where T is the temperature, k_c is the bending rigidity and $\xi_{\parallel}$ is the limiting wavelength above which the undulations are suppressed due to the confinement. Each limiting segment of the membrane has an associated volume given by

$$V \simeq \xi_{\parallel}^2 \xi_{\perp}, \tag{5.42}$$

and when using the ideal gas law ($pV = k_B T$) we have,

$$p \sim k_B^2 T^2 / k_c \xi_{\perp}^3. \tag{5.43}$$

The unsuppressed undulations of a confined membrane create a disjoining pressure, which decays with the roughness $\xi_{\perp}$. It is worth noting that $\xi_{\parallel}$ is proportional to the separation d between membranes or membrane and support. Therefore the disjoining pressure, $p \propto d^{-3}$, which is the same decay as van der Waals interactions (see for instance equation 5.25). The expressions derived thus far are for a membrane with no lateral tension. The roughness of a membrane under lateral tension will be reduced. The membranes roughness becomes the same as that of an interface governed by surface tension. The roughness of a membrane under tension is given by,

$$\xi_{\perp} \approx (k_B T/2\pi\gamma)^{1/2} \sqrt{\ln(\xi_{\parallel}/a_{\parallel})}, \tag{5.44}$$

where γ is the lateral tension and $a_{\parallel}$ is a small-scale cutoff given by the headgroup area. It is clear the roughness dependence on $\xi_{\parallel}$ becomes very weak for membranes under lateral tension and is thus primarily determined by the tension itself. The fluctuation induced interaction potential is then given by

$$G_{fl}(\xi_{\perp}) \sim \exp[-2(\xi_{\perp}/l_{\gamma})^2], \tag{5.45}$$

where

$$l_{\gamma} \equiv (k_B T/2\pi\gamma)^{1/2} \tag{5.46}$$

5.2.6 Renormalised interactions

In this sub-section I will describe the the interplay of bilayer fluctuations with the direct interaction arising between two bilayer segments or the limiting case of a bilayer and a solid support. The fluctuation interaction is not strictly additive to the other direct interactions, and for a thorough treatment the superposition principle does not apply. Lipowsky states that the separation of

two bilayers or a bilayer and its solid support is governed by the effective Hamiltonian,[122]

$$\mathcal{H}\{l\} = \int d^2x \left\{ Pl - G(l) + \frac{1}{2}k_c(\nabla^2 l)^2 \right\} \tag{5.47}$$

where k_c is the effective bending rigidity

$$k_c = \frac{k_{c,1}k_{c,2}}{(k_{c,1} + k_{c,2})} \tag{5.48}$$

and $k_{c,1}$ and $k_{c,2}$ are the bending ridgities of the two membranes. In the limiting case of a supported lipid bilayer, where $k_{c,2} = \infty$, k_c reduces to $k_c = k_{c,1}$. The probability of a given configuration of d is given by its Boltzmann weight,

$$\exp\left\{ \frac{\mathcal{H}\{d\}}{k_B T} \right\}. \tag{5.49}$$

In principle, to obtain the partition coefficient and other statistical quantities, one should sum over all possible configurations, but in practice one of several approximate methods must be used. The most systematic being that of functional renormalisation (RG), and the most "realistic" being simulations – I shall not enter into a description of these in this thesis. However, the simplest method is that of superposition of all the interactions. In this method the free energy per unit area is estimated by

$$G(d) = G_{hy}(d) + G_e(d) + G_{vdw}(d) + G_{fl}(d) \tag{5.50}$$

where

$$G_{fl}(d) \approx c_{fl}T^2/k_c d^2 \tag{5.51}$$

and c_{fl} is a dimensionless constant. The equilibrium mean separation can then be acquired from,

$$\frac{\partial G}{\partial d} = 0 \tag{5.52}$$

The superposition method fails if any of the non-fluctuation interactions have an attractive component that decays faster than $1/d^2$, for instance in the presence of attractive short ranged forces. For "bound states" equation 5.52 will show a global attractive minimum at some distance d. However, if the physical parameters are changed such as the temperature, the bending rigidity or the charge on the membrane for an SLB, the total potential may pass a critical point where there is no longer an attractive minimum and the membranes or membrane on support separate or "unbind" from the surface. One failure of the superposition approach is the nature of the transition itself. By the superposition approach, upon reaching the critical temperature, i.e. the temperature at which the bound and unbound states exist together, and then passing it, the transition is expected to be first order and discontinuous. However, more sophisticated methods for understanding the unbinding transition, such as the RG, result in a continuous transition where the attractive minimum moves to greater d until the bilayer unbinds. This difference in behaviour is shown in figure 5.3, the upper row of graphs illustrate the unbinding transition using the superposition approach. The lower graphs depict the unbinding transition calculated by renormalisation group. Despite this distinction, the critical points at which the transition takes place are accurate provided the supposition method is applied within the limits described above.

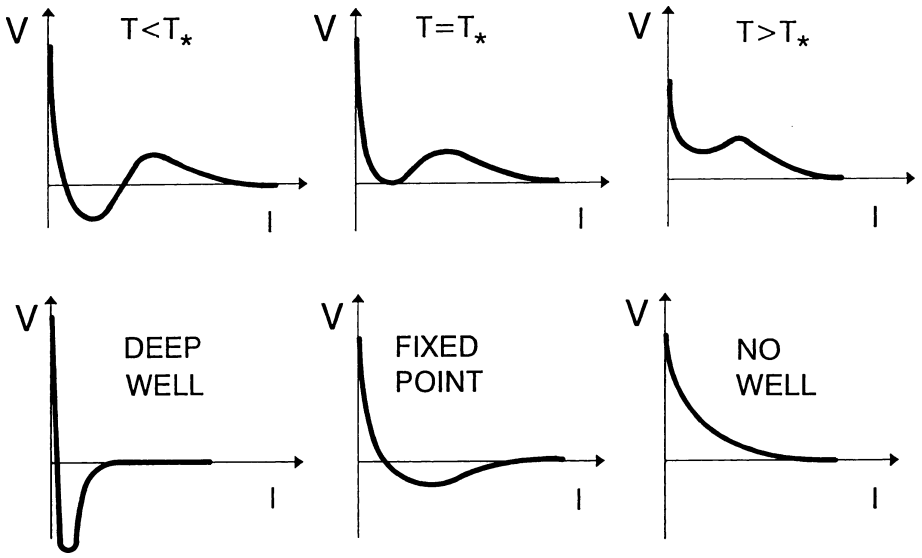

Figure 5.3: A figure showing the change in the total interaction potential with temperature calculated by (top) superposition (bottom) renormalisation group. Reprinted from Lipowsky,[122] with permission from Elsevier.

5.3 Experimental review

The experimental work done on the interaction of multifarious surfactants with vesicular systems is vast, and for this reason only a selection of that work will be discussed here. One motivation for my research is the limited work carried out on SLB systems, despite the large quantity of work carried out on bilayer vesicles. Schurtenberger and coworkers investigated the interaction of bile salts with lecithin systems using quasi-elastic light scattering and equilibrium dialysis.[123] They found that upon dilution changes in the polydispersity showed the formation of mixed bile salt/lecithin vesicles below a bulk bile salt concentration, thereby confirming the overall features of the three stage model. They were able to apply their own phenomenological model to the data acquired which allowed the authors to relate the mole fraction ratio of the two species to a given vesicle size. Indeed they found that the size of the mixed vesicles formed varied from 130-500 Å.

Lichtenberg published a paper in which he reviewed the data of others. He was able to relate the onset of vesicle saturation and solubilisation to a critical ratio R_b.[124] He found that R_b was related to the CMC of the surfactant being used and thus linked the bulk CMC to the onset of mixed micelle formation. His contributions implied that so long as the aqueous surfactant concentration was below the CMC of the pure surfactant solution bilayer solubilisation would not take place. Lichtenburg also related the ratio R_b to the the size of the mixed vesicles or micelles after the onset of solubilisation in a similar way to Schurtenberger. Lichtenberg continued in this vein and carried out experiments on systems containing the non-ionic surfactant octyl glucoside (OG) and egg-PC.[125] They showed in accordance with Lichtenberg's earlier analysis that the structural result of mixing depended on the value of R_b; below the critical value of R_b, where mixed micelles begin to form, as the concentration of OG increased so to did the diameter of the vesicles in suspension.

The group of de la Maza have conducted a large number of studies on the interaction of surfactants/mixed surfactant systems with lipid vesicles. In an early study they investigated the interaction of SDS with PC vesicles using photocorrelation spectroscopy and fluorescence tech-

niques,[126] the former quantifying vesicle size distributions and polydispersity index (PI) the latter showing how the permeability of the PC vesicles changed upon surfactant addition. They observed a linear relationship between dye release, R_b and vesicle growth. This relationship implied that lipid membrane permeability to surfactant increased with surfactant incorporation. In the same study it was shown that above the critical effective lipid surfactant ratio (i.e. at bulk surfactant concentrations above the solubilisation threshold), a linear dependence was established between the decrease in mixed vesicle size (from the static light scattering) and the effective surfactant/lipid ratio. The last trend stopped at very high surfactant concentration indicating that the great majority of aggregates were of the mixed micellar variety.

A few years later, another study published by the same authors investigated a more complex system that included both SDS and nonylphenol ethoxylate ($NP(EO)_{30}$) with phosphatidylcholine vesicles.[127] Similar trends were observed as in the prior SDS-only study, for example the onset of solubilisation did not occur until the free surfactant concentrations were equal to the mixed surfactant CMC. However, what was interesting for this mixed system was the synergy between the non-ionic and ionic components. At low overall surfactant concentrations, the maximum total surfactant partitioning took place at high dSDS mole fraction. As a result the influence of SDS at lower surfactant concentrations was greater whereas the influence of $NP(EO)_{30}$ was higher in the solubilisation regime and in the presence of mixed micelles.

More recently de la Maza investigated the role of ceramides (Cer) on the interaction of surfactant mixtures with complex stratum corneum (SC) lipid vesicles using the same techniques as his prior studies.[128] In this study it was shown that the activity of the SDS/C_{14}-BET mixture upon the SC liposomes was greater when there was less Cer present in the bilayer. Thus the ability of the surfactant mixture to alter the permeability of the lipid bilayer was lower when the bilayer approximated the real SC more closely.

de la Maza has also investigated some of the dynamic properties of the SDS interaction with PC lipid vesicles, specifically the trans-bilayer movement of the SDS monomers.[129] The authors carried out this investigation with fluorescence spectroscopy using the anionic fluorescent probe 2-(p-toluidinyl)napthalene-6-sodium sulphonate (TNS). The authors state that it was only possible to measure probe molecules in the outer bilayer leaflet as they assumed the probe did not cross into the inner leaflet; this was justified by control experiments on the pure fluorescently labelled vesicles showing no intensity changes over six hours and some prior work by other authors in a related field. However, the authors did not prove that transfer was not occurring once SDS was partitioned. TNS is sensitive to the presence of SDS because it interacts with the sulphate headgroup leading to changes in the TNS fluorescence intensity. The authors studied the change in fluorescent intensity with incubation time in the presence of SDS. These fluorescence data were then quantified as the variation in surface potential (ψ_0) of the liposomes. When the concentration of SDS was increased an initial increase in ψ_0 was seen, as SDS was incorporated into the bilayer. However, after a period of incubation a decrease was observed in ψ_0, which was associated with the movement of SDS into the inner vesicle leaflet by the "flip-flop" mechanism. The maximum decrease was observed from very low surfactant concentrations. Whilst the initial uptake of SDS into the outer bilayer leaflet was rapid, the flip-flop process of SDS within the bilayer was seen to be slow, on the order of 10-90 minutes after SDS addition. If one compares this figure to the rate of lipid only flip-flop in vesicles (0.7-3.0 hrs),[130] one sees that it is faster; one would suspect this is due to the increased size and hydrophobicity of lipids compared to the SDS. N.B it is worth repeating that the large variation in the reported lipid flip-flop rates depends on the geometry of the aggregate, the lipid species and headgroup, whether or not the bilayer is surface supported and if the SLB is tethered to the support.

Jørgensen and coworkers have investigated the partitioning of lysolipids and fatty acids in PC liposomes using isothermal titration calorimetry (ITC), again using the standard partitioning model.[131] They discovered that the partitioning of lyso-PC within the lipid membrane was strongly dependent on the phase of the vesicle bilayer. In the L_α phase where the lipid molecules are more disordered K was large and lyso-PC was heavily incorporated in the vesicle bilayer. However, in the L_β phase lyso-PC incorporation was much lower and the partitioning coefficient was relatively small. For fatty acid incorporation, partitioning was independent of bilayer phase. Lastly the authors observed a order-of-magnitude increase in partitioning upon increasing surfactant tail length by two carbons for both lyso-PC and FA between 10 to 16 carbon atom chain length.

Somasunduran and Deo have studied the complete interaction mechanism of pure and mixed liposomes with SDS using optical density measurements and composition analysis.[132] They show that phosphatidic acid (PA) vesicles are solubilised much more easily in the presence of SDS than are PC vesicles. They relate these results to the simpler structure of PA and the more complicated structure of the zwitterionic PC. They also show that the solubilisation of vesicles comprising a 1:1 mixture of PA/PC occurred at lower concentration than similar pure lipid vesicles, they relate this to the resulting instability in the liposome generated when the PA is removed preferentially at lower SDS concentrations where PC is not. These results show that the ideal partitioning model is not adequate to describe common surfactant partitioning into lipid bilayers and subsequent solubilisation. The three stage model does not take the specifics of the surfactant and lipid into account or their interactions with each other.

Menger and coworkers have investigated some dynamic properties of a variety of both conventional and gemini surfactants embedded within vesicle bilayers.[133] They used laser microelectrophoresis coupled with conductance, fluorescence and dynamic light scattering (DLS) to show that cationic conventional surfactants would only flip-flop from the outer leaflet to the inner leaflet of anionic lipid vesicles if the bilayer was in the fluid state. Lastly they showed that surfactants can only hop from one vesicle to another when the initial vesicle was in the fluid state. Despite these seemingly conclusive results one must always be aware that the fluorescent tag may have a large effect on dynamic behaviour such as flip-flop.

In a more recent study, Somasundaran and Deo have investigated the structural changes induced by SDS on mixed PA/PC liposomes by way of the lipid probe molecule 5-hydroxy stearic acid (5-DSA).[134] Their results show that upon the initial uptake of SDS the liposome is not disrupted but SDS adsorbs to the surface of the liposome. During their experiment, after a concentration of 2 mM SDS was reached a sharp change in the mobility of 5-DSA takes place, indicating the rapid onset of bilayer disruption and the onset of solubilisation. These data conflict with almost all of the other studies which suggest surfactant partitioning *into* the bilayer at all concentration regimes.

Surface plasmon resonance (SPR) has been used by Stroeve and coworkers to study the "corrosive" effects of various substances on hybrid supported POPC bilayers, amongst these substances were CTAB and SDS.[135] The bilayers were fused on top of a layer of alkyl thiols previously adsorbed to gold coated silica. The article was written from the point of view of preserving biosensors which include systems comprised of lipid bilayers. The results from this hybrid layer are fairly consistent with bulk vesicular studies, complete bilayer solubilisation required surfactant concentrations nearing the CMC, however, the onset of solubilisation began to take place at concentrations an order of magnitude lower than the CMC of the bulk surfactant. This was not observed in the other vesicle based studies hitherto described, and is in contradiction to the analysis of Lichetenberg, who related the start of mixed micelle formation to the CMC of the bulk surfactant. Again this discrepancy is likely to be related to the simplicity of the three stage model, however in this case

it could be a result of the fact that the authors are now working with surface supported layers and particularly a hybrid lipid system.

Somasundaran and Deo have produced another work investigating the solubilisation of PC/PA bilayers by SDS.[136] In this study they used turbidity, surface tension and monomer concentration techniques. Their results have nothing to show that has not already been shown before with regard to the three-stage interaction model, but their results do corroborate with those of Stroeve and coworkers, at least over a long period of incubation.

Small angle X-Ray scattering (SAXS) has been used to investigate the effects of the non ionic N-alkyl-N,N-dimethylamin-N-oxides on egg-PC bilayers in the L_α phase.[137] Balgavý and coworkers show an increase in surface area per lipid at the water/lamellar interface across the entire homologous series of surfactants by $\approx$0.3 nm^2 which varied slightly with the exact surfactant chosen. They attributed this expansion to surfactant incorporation and the concomitant lateral expansion of the vesicle bilayer. They also report a decrease of up to 0.85 nm in bilayer thickness with surfactant incorporation, this depending on the surfactant/lipid ratio and the specific member of the homologous series; some members did not decrease bilayer thickness at all.

Keller *et al.* have used isothermal titration calorimetry to monitor the translocation of dSDS across the bilayer of large unilamellar POPC vesicles.[138] By using a series of uptake and release titrations they have been able to discriminate between the two extreme cases of half side binding and a balanced transbilayer distribution of SDS. They applied a selection of the thermodynamic models described above including the one used to correct for charged species partitioning. Specifically they found that utilising the electrostatic corrections, they could evaluate the partitioning of dSDS with an ideal partitioning model. They note that SDS does not equilibrate across the POPC bilayer at 25°C, but that this translocation rate is markedly increased when the temperature was increased to 65°C. However, this temperature rise also decreased the partition coefficient by a factor of three. It is also worth noting that this work did not go so far as to following the kinetics in real time, they were simply able to discern whether of not flip-flop was occurring and what time was required for complete equilibration; in this was the authors found that at 65°C the required equilibration time was 20 minutes which establishes an approximate limit for the time required for flip-flop.

Cheng and coworkers have used SPR and FRAP to investigate Triton X-100 and SDS interacting with SLBs prepared on calcinated silicate layers on gold. The most relevant SLBs were comprised of PC and a 50:50 mixture of PC and PE but other species including some synthetic lipids were used.[139] Their study was mainly aimed at establishing which of the lipid systems studied were the most stable with respect to SDS and Triton X-100 treatment. They correlated a change in SPR angle with a percentage loss of the SLB under study. Their work provides some useful empirical information about the resistance of a selection of different SLB systems to air exposure and surfactant exposure.

Moreno *et al.* have investigated the interaction of dSDS with phospholipid vesicles comprised of POPC using isothermal titration calorimetry. They also used the electrostatic corrections described earlier in my theoretical review. They found that even when using these corrections the "intrinsic" non-ideal partition coefficient obtained varied with surface surfactant concentration; thus indicating that further interactions or structural changes must be mediating SDS partitioning into the POPC bilayer.

Riske and coworkers have studied the interaction of POPC giant unilamellar vesicles (GUVs) with SDS and Triton X-100 using phase contrast and fluorescence microscopy.[140] They note several distinctions between the behaviour of the vesicles interacting with the two surfactants. Firstly, in the presence of Triton X-100, the vesicles showed an increase in surface area indicating the parti-

tioning of the surfactant into the POPC bilayer; above the saturation concentration holes began to appear in the vesicles and they took on a perforated appearance, eventually they disappeared completely. In the presence of SDS the GUVs behaved differently, whereas the Triton X-100 was able to partition into both bilayer leaflets, SDS was only able to partition into the outer leaflet; this lead to spontaneous curvature and the authors observed large shape fluctuations and budding transitions, seen as excrescenses in the microscope images; the authors justified their comments about flip-flop in terms of presence of spontaneous curvature – if flip-flop was taking place, spontaneous curvature would not have been evident. Above the bulk CMC of SDS in the media used, all the vesicles eventually burst, the small fragments of which were below the resolution of the microscope used.

Heerklotz and coworkers have used the time-resolved fluorescence anisotropy of 1,6-diphenylhexatriene (DPH) to understand the disordering effect of a selection of surfactants on POPC lipid vesicles and how this correlates with solubilisation.[141] They found that the disordering effect correlates well with the point of bilayer solubilisation for many of the common surfactants such as SDS, $C_{12}EO_8$ or lauryl maltoside, but for many fungicidal lipopeptides, CHAPS and digitonin this was not the case and solubilisation seemed to take place without substantial measured disordering.

5.4 Results

5.4.1 Overview

In this section I will explore the kinetic, thermodynamic and structural changes that take place when dSDS partitions into SLBs composed of i) POPC, ii) POPE iii) egg-SM and iv) a 1:1:1 mixture of POPE, egg-SM and Cholesterol. In preliminary work I studied the interaction of both dSDS and dCTAB with an SLB comprised of POPE. I found that whilst the dSDS could be removed from the SLB phase completely in was unclear if dCTAB had done the same. dCTAB may adsorb to clean silica surfaces irreversibly whereas dSDS does not; if defects were present in the SLB it was unclear whether or not the dCTAB was simply adsorbing to the bare silica, remaining as part of the SLB, or a combination of the two. For this reason I chose to focus purely on SDS.

5.4.2 POPC

5.4.2.1 Equilibrium measurements

Initially the POPC SLBs were prepared by vesicle fusion under the constant flow regime utilised throughout Chapter 3. Once this procedure had been completed any remaining loosely adhered vesicles were removed by copious and lengthy rinsing with 20 mM tris buffer at pH 7.4. Subsequently, dSDS solution was flowed into the cell at a rate of 0.300 ml min^{-1}. During this time, kinetic measurements of the partitioning process were acquired by monitoring changes in the CD stretching region of the Raman spectrum. Longer extended spectra were then acquired at equilibrium for both S- and P-polarised incident light; these were required to obtain a partitioning isotherm. In general this method (kinetic followed by equilibrium measurements under constant flow) was utilised multiple times for the same SLB with increasing dSDS concentration. It was expected that the partitioning kinetics for each successive dSDS addition would change as the SLB coverage was altered; as a result the first addition(s) offer the best insight into the partitioning

kinetics of a complete SLB. For a number of dSDS additions, particularly the first and last, the cell was rinsed with copious buffer. Concurrently, the CD region was monitored to observe the removal of dSDS from the SLB and also extended scans were acquired to gather equilibrium information after rinsing. Occasionally kinetic behaviour was monitored in the CH stretching region to observe real time changes of the lipid component as the dSDS partitioned and was subsequently rinsed. It was not possible to monitor both regions simultaneously during kinetic measurements – the diffraction grating did not cover the required frequency range.

Deuterated SDS was used to remove spectral overlap arising from both lipid and surfactant contributions to the CH stretching region. By using dSDS I was able to analyse the Raman signals from both species separately. Figure 5.4 shows the equilibrium S- and P-polarised spectra for 0.2 mM dSDS addition and subsequent rinsing. In figure 5.4 (a), the S-polarised data, I show a repeat measurement of the pure SLB to highlight the stability of the system, the two spectra are virtually identical.

Looking at the CD region in figure 5.4, between 2050 and 2250 cm^{-1}. The bands that reside within this region have been assigned previously for crystalline nonadecane-d_{40} by Pemberton and coworkers:[142] symmetric $\nu_s(CD_3)$ mode at 2073 cm^{-1}, symmetric $\nu_s(CD_2)$ mode at 2104 cm^{-1}, Fermi resonance of the symmetric $\nu_s(CD_3)$ stretching mode at 2137 cm^{-1} (not usually present in liquid samples), two antisymmetric $\nu_a(CD_2)$ modes at 2173 and 2196 cm^{-1} (these modes contain both Raman and IR active components), antisymmetric $\nu_a(CD_3)$ stretching mode at 2216 cm^{-1}. In my spectra the whole CD region is shifted to higher frequency by approximately 10 cm^{-1} as a consequence of the liquid like nature of the dSDS within the POPC SLB.

The behaviour shown in figure 5.4 is typical of many of the SLB systems investigated. We observe a decrease in the CH region upon dSDS partitioning and a concomitant increase in the CD region indicating the presence of dSDS within the SLB. However, the most interesting feature of the data, and what originally captured my interest, was the recovery in the CH region upon rinsing. In this system when the surfactant was removed, the lipid signal recovered to slightly lower levels that were observed before dSDS addition. Further, rinsing appears incomplete, a small dSDS remnant remained within the lipid bilayer and this explains the difference in the original and after rinsing CH intensities. The key question is why the lipid signal returns? In a flow-cell environment one expects any loss of signal from the exit of material from probed volume to be permanent; on the other hand several other mechanisms exist for the loss of signal that do not depend on the permanent removal of material. For instance, one possibility is that the existing SLB expands into free surface volume (located outside the laser spot) to accommodate the partitioning dSDS, this would result in a reduction in the surface density of lipid and hence a reduction in signal. However, this mechanism acting alone would suggest a heterogeneous surface coverage with a length scale greater that the size of the laser spot. Provided there was no bias towards lipid vesicles rupturing at the laser spot's location, if there was an optical trapping effect, we would expect a certain degree of irreproducibility in the lipid signal between experiments; for instance, if there was a large block of free volume within the laser spot one would expect the lipid signal to increase upon dSDS partitioning – I have almost always observed a decrease. Another option is some form of restructuring, such as an unbinding transition or the onset of spontaneous bilayer curvature; the latter including such structures as tubules and blebs, see for instance Staykova and Stone.[143] The final possibility is that a number of these mechanisms could be operating in concert to produce an overall change. The original premise for the following section was to apply all the qualities of TIR-Raman to find out which signal loss mechanisms are occurring and to what extent and to explain why.

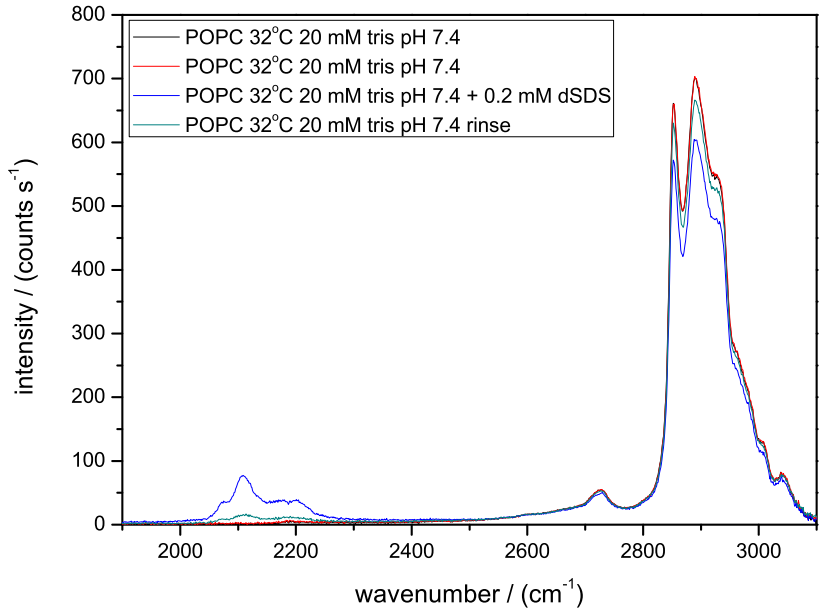

(a)

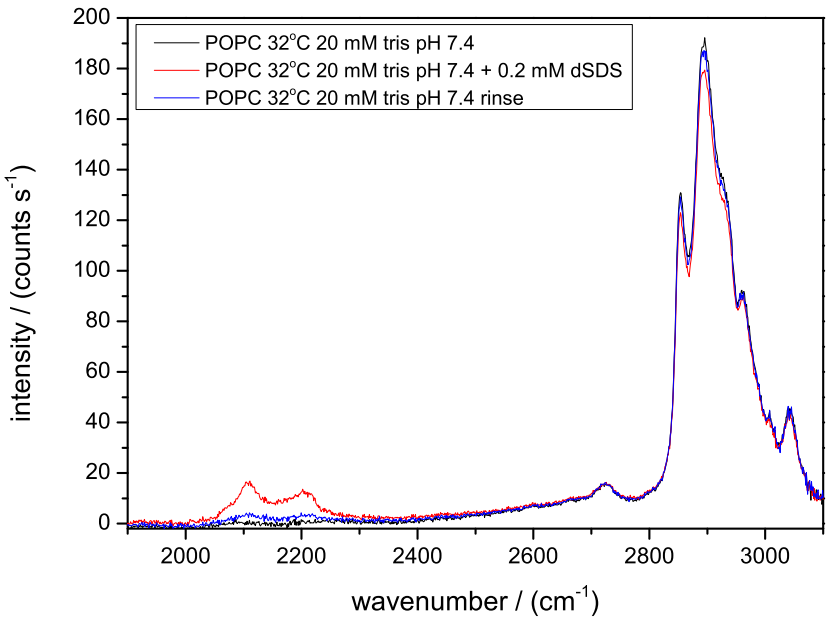

(b)

Figure 5.4: TIR-Raman spectra showing the interaction of 0.2 mM dSDS with an SLB comprised of POPC in 20 mM tris pH 7.4. 73° incidence, 800 mW, with equilibration at 32°C. 10 second spectra with 20 accumulations. Both S-polarised (a) and P-polarised (b).

Figure 5.5 shows partitioning data for dSDS incorporation into two POPC SLBs. These data characterise the changing mole fraction of dSDS within each SLB as a function of bulk dSDS concentration. Figure 5.5 also shows the effect of dSDS partitioning on the total adjusted normalised

signal level, which is an empirical measure of the overall coverage at the interface. As the bulk dSDS concentration is increased we observe an increase in the mole fraction of partitioned dSDS. However, this increase decreases as the bulk concentration is raised highlighting a lack of ideality. Moreover, as the mole fraction of partitioned dSDS reaches a value of approximately 0.5, both POPC SLBs become saturated and further increases in bulk surfactant concentration no longer increase the dSDS mole fraction. In the saturation concentration regime, we observe the solubilsation of the SLB as indicated by the sudden drop in normalised signal.

The effect of the partitioning on the normalised signal levels are interesting, these levels are calculated by summing the integral CH region intensity with the adjusted CD region intensity; the CD region intensity normalised by the appropriate Raman cross-section ratio. The normalised signal is a measure of the total number of CH and CD bonds within the bilayer (N.B. See for instance my introductory section on composition analysis). In experiment (1) the cell was flushed after each new surfactant addition, whereas in experiment (2), the flow cell was flushed only after the first two measurements, this difference in protocol could explain the divergence in overall signal after 0.5 mM dSDS. But there is a second possibility; it is expected that not every SLB formation for a given lipid/lipid mixture will lead to the same surface coverage, another plausible explanation is that in experiment (2), the surface has a lower coverage to start with and so more space is available at the interface to incorporate dSDS. It is instructive to look at the raw spectra of the two pure SLB's in order to determine which of these alternatives is the cause of the difference in behaviour. Figure 5.6 shows these raw spectra, the intensity ratio of the lipid bands in the CH region to the water band gives an indication of coverage, the data shown indicate a difference in surface coverage of $\approx$7 % with SLB POPC (2) having greater coverage. As the data in figure 5.5 show a difference in the maximum normalised signal of 40 %, it is far more probable that the difference in coverage is a result of the extra rinses conducted during the POPC (1) experiment and not the initial surface coverage. These data also imply that material exists some distance from the interface after the addition of surfactant. Owing to the no-shear condition at the stagnation point, no shear should be acting on a "flat" SLB at the centre of the hemisphere where the probe beam is incident. If blebs or tubules are forming as a result of spontaneous curvature, shear could be acting on them as they would protrude into the bulk solution; it is expected that some material would be irrevocably removed from the interface. For both SLBs the normalised signal levels increased at the lowest bulk dSDS concentrations, implying that additional material was adsorbing to the interface and there was no loss in normalised signal even with copious rinsing; perhaps the tubules/blebs are more stable if subjected to shear forces when they are shorter.

I have analysed my partitioning data using both the non-ideal and charged surfactant extended models described earlier in the introduction to this chapter. Figure 5.7 shows the change in the mole ratio of surfactant to lipid (R_b) in POPC SLB (1), the fact that these data are linear in [dSDS] concentration implies that the surface charge developed by dSDS partitioning is being neutralised by either or both of Na^+ and $tris^+$ binding to the DS^- within the SLB. Without additional measurements – streaming potentials – it is not possible to acquire the counterion binding constant although estimates could be acquired by Na^+ binding to SDS micelles or from simulation studies. The slope of a plot of R_b vs. $[dSDS]_{bulk}$ yields K_R, which was acquired by linear fitting. I calculated this value to be $K_R = 990\ M^{-1} \pm 50\ M^{-1}$ which gives standard partitioning free energy of $\Delta\mu_{dSDS}^{0aq\rightarrow B} = -27.7\ kJ\ mol^{-1} \pm 0.1\ kJ\ mol^{-1}$; a very similar value was obtained for POPC SLB (2). These values are in good agreement with Bloom and coworkers who obtained a value of –29 kJ mol^{-1} with ITC. However, whereas I have found that the non-ideal model provides an adequate description for the POPC SLBs, Bloom and coworkers required a model that took into account surface DS^- depletion and associated counterion binding for vesicle systems. For this reason I used

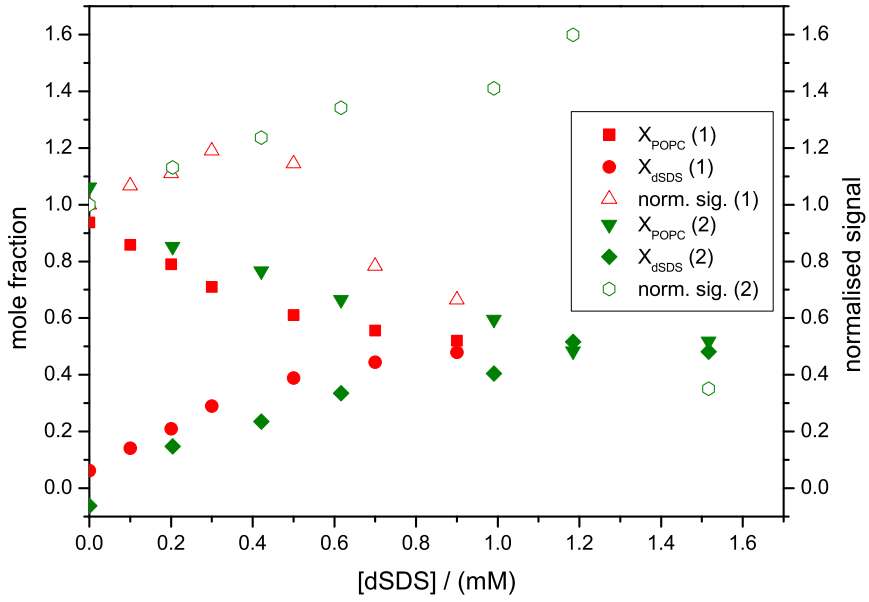

Figure 5.5: Figure showing two partitioning isotherms for dSDS incorporating into POPC SLBs (1) and (2), 32°C, 73° incidence, 20 mM tris pH 7.4. Calculated from combined S- and P-polarised spectra.

the model that accounts for surface charge for means of comparison. Figures 5.8 (a) and (b) show the theoretical build-up of surface potential – calculated from knowledge of areas per lipid and surfactant molecule and the measured mole-fractions of surfactant and lipid mole fraction respectively – and a plot of R_b as a function of depleted surface DS^- concentration as calculated from the Gouy-Chapman theory. It is immediately apparent from (b) that there is no linear relationship between these quantities – the negative slope is not physically meaningful. This indicates that K_R^0 the intrinsic mole ratio partition coefficient is not constant when taking into account expected surface anionic surfactant depletion assuming no counterion binding is taking place. The fact that the value for K_R is constant implies that the surface charge is being effectively neutralised by counterion binding as soon as it is acquired on the SLB. It is not obvious as to why this behaviour should be so different from that observed by Bloom and coworkers. Their studies were conducted in 10 mM phosphate buffer with 154 mM NaCl at pH 7.4 with a similar SDS concentration regime. In theory surface charge should be further neutralised in their conditions owing to the far higher ionic strength. Given that they were working with LUVs geometric considerations should be of limited importance; the disparity could result from the fact that we are investigating SDS binding thermodynamics at the silica-water interface whereas they are examining the same behaviour in bulk vesicular systems. Lastly it is worth noting that my standard states differ from theirs by definition – the buffer conditions were quite different, caution must be taken when comparing the calculated standard free energy differences.

The two thermodynamic models represent extremes between a non-ideal mixing with no electrostatic effects and one in which the electrostatic surfactant depletion is at its maximum, allowing for counterion binding in a quantitative way permits the merging of the extremes to account for something in between the two behaviours, although I have found this to be unnecessary here.

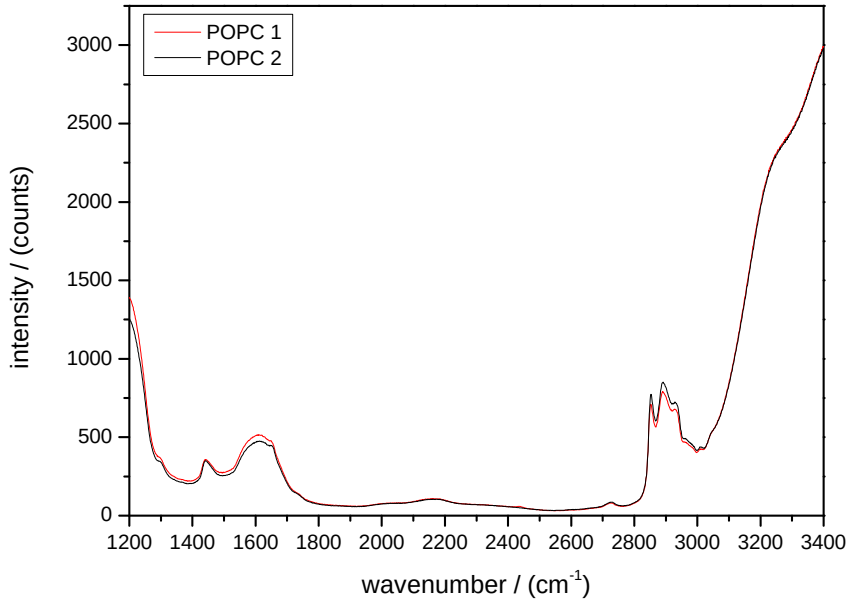

Figure 5.6: A figure showing raw S-polarised TIR-Raman spectra of SLBs POPC (1) and POPC (2) in order to demonstrate the difference in surface coverage. Acquired at 32°C, 73° incidence, 800mW, 20 acquisitions, 10 second spectra, 20 mM tris pH 7.4.

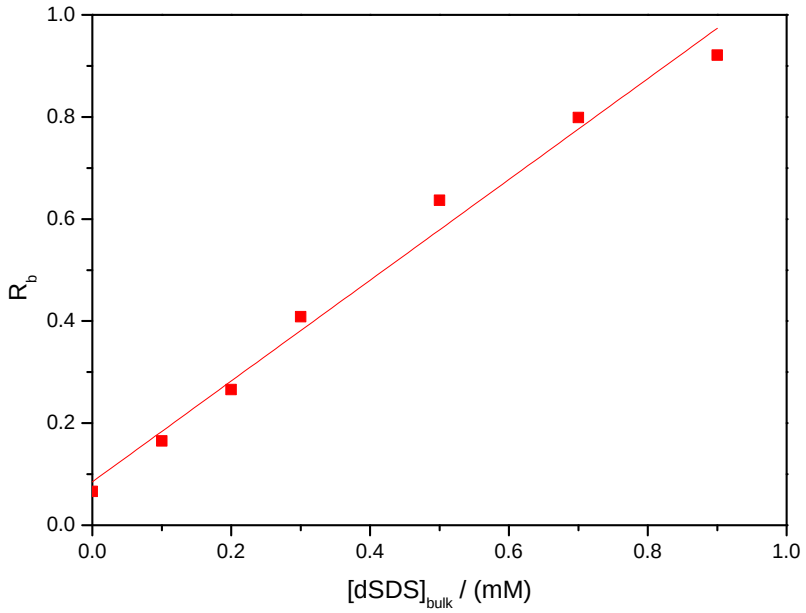

Figure 5.7: A figure showing the change in the mole ratio of dSDS to POPC within SLB (1) as a function of dSDS concentration, 32°C, 73° incidence, 20 mM tris, pH 7.4

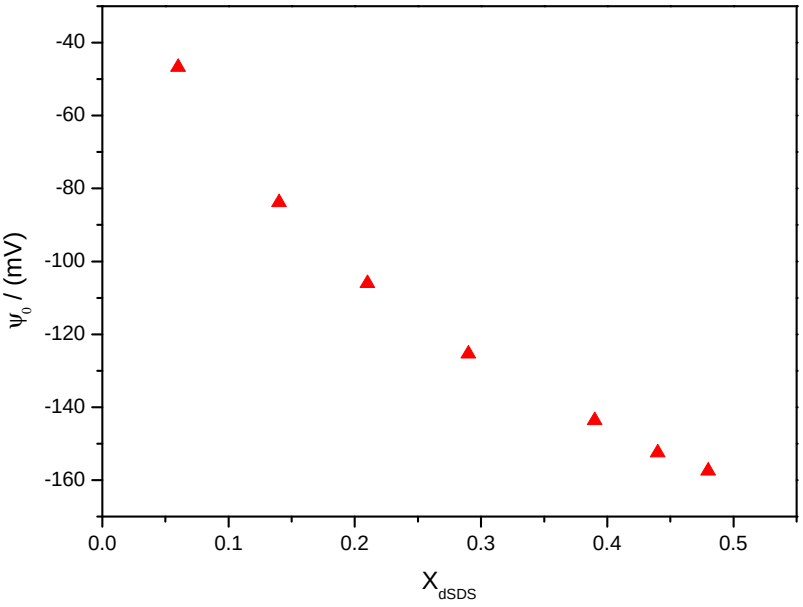

(a)

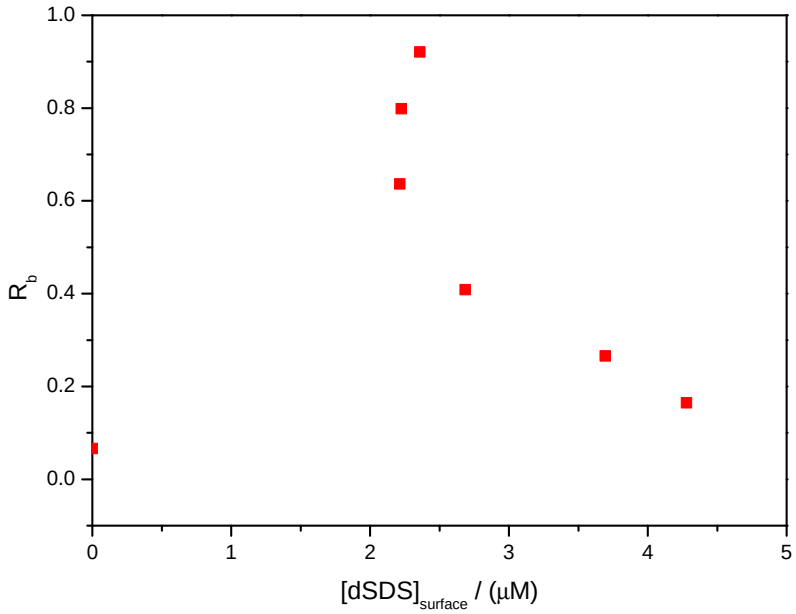

(b)

Figure 5.8: (a) A figure showing the theoretical development of SLB surface potential as a function of dSDS mole fraction within a POPC SLB. (b) A graph showing the variation in the surfactant to POPC mole ratio as a function of theoretical dSDS surface concentration for POPC SLB (1), 73° incidence, 32°C, 20 mM tris pH 7.4.

5.4.2.2 Structure

Figure 5.9 demonstrates the effect of dSDS partitioning on the overall order within the POPC SLB; as the dSDS mole fraction increases, there is a moderate increase in the degree of order in the lipid chains. If the mixed POPC/dSDS system is more ordered than the pure POPC SLB system at the same temperature it is likely that no thermal unbinding transition is taking place; enhanced order implies an increased bending modulus relative to kT or an enhanced lateral tension, either implying that thermal membrane fluctuations will be further suppressed. In addition the success of the non-ideal mixing model in fitting the isotherm data informs us that any negative surface charge is being neutralised, it is unlikely for there to be an increase in the electrostatic repulsion between the dSDS/POPC SLB and the silica substrate. It is not clear why there is a disparity in the primary order parameter values between the two systems. A slight difference in the alignment of the spectrometer could be considered a reason for the difference, but the similarity in the raw spectra shown in figure 5.6 eliminate this as a possibility. Regardless, a difference of ≈ 0.01 at similar dSDS concentration is very small.

Figure 5.10 shows the change in the symmetric and antisymmetric stretch peak positions as a function of dSDS mole fraction. I have found this order parameter to be generally less sensitive than the peak intensity ratio described above and we observe very small changes. However, it is interesting that the peak positions increase; one expects to see a decrease when the primary order parameter increases – generally the peak positions increase with disorder as the vibrational modes can oscillate more freely in these situations.

Figure 5.11 shows the variation in the ratio of the integrated intensities in the CH region for the P-polarised and S-polarised TIR-Raman spectra of POPC SLBs (1) and (2) as a function of dSDS mole fraction – this parameter correlates with average lipid chain tilt. As the dSDS mole fraction increases so does the average chain tilt. Combining these data with the those shown in figure 5.9 a picture emerges in which the partitioning of dSDS results in a structure which is more ordered, but also more tilted.

5.4.2.3 Kinetics

Figure 5.12 and 5.14 show sequential kinetic data for 0.1 mM and 0.2 mM dSDS partitioning (a) and rinsing (b) from POPC SLB (1). These data were extracted from time series of S-Polarised spectra using target factor analysis. The data were fitted using the same refined spectra so the component weights are directly comparable. For both additions we see a rise in the component weight of dSDS indicating the partitioning of the surfactant into the SLB. The component weight reaches a greater value in the 0.2 mM addition as the ratio R_b is higher at this concentration. Looking carefully at figure 5.14 (a) we note the slight positive gradient during the addition step after the first rapid uptake of dSDS. One possible interpretation of this slow secondary increase is that it is evidence of lipid flip-flop taking place. Further, when we examine figure 5.12 (a) we see that the same is not true and after the initial uptake the values are stationary; flip-flop was not taking place if the interpretation is correct – or only to a very limited extent. For both runs, the time taken for the initial rapid uptake was approximately 100 seconds and upon rinsing the component weights drop by 0.2 cw. Whereas in the 0.1 mM run, the final value was approaching 0 cw, in the 0.2 mM addition it was 0.3 cw. Taken with the flip-flop interpretation, these observations imply that during the 0.1 mM measurement the dSDS had only partitioned into the outer leaflet, but during the 0.2 mM run it had also partitioned into the inner SLB leaflet and

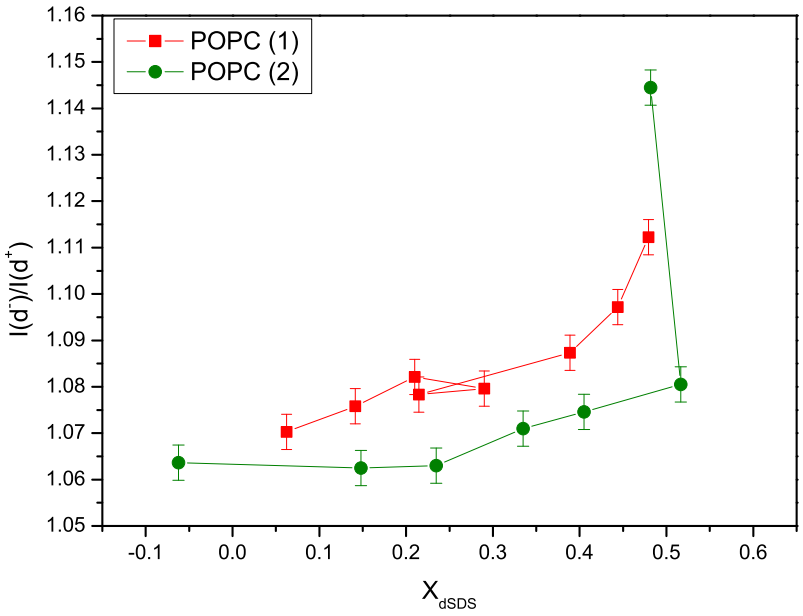

Figure 5.9: A figure showing the variation in the primary order parameter for a POPC SLBs (1) and (2) with increasing dSDS mole fraction. Based on two seperate experiments. 73° incidence, 32°C, 20 mM tris pH 7.4. Error bars indicate the standard deviation.

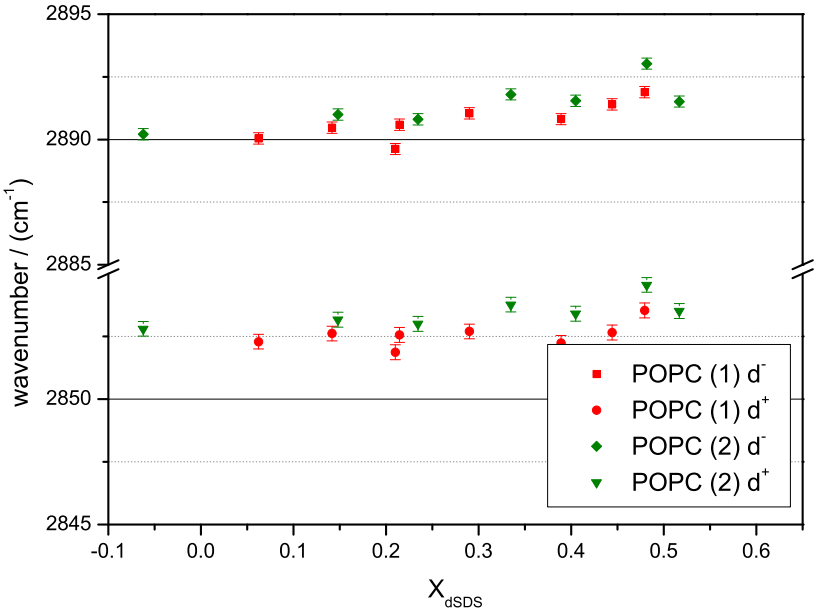

Figure 5.10: Figure showing the variation in both the POPC symmetric and antisymmetric CH stretches with increasing dSDS mole fraction for POPC SLBs (1) and (2). 32°, 73° incidence, 20 mM tris pH 7.4. Error bars indicate the standard deviation.

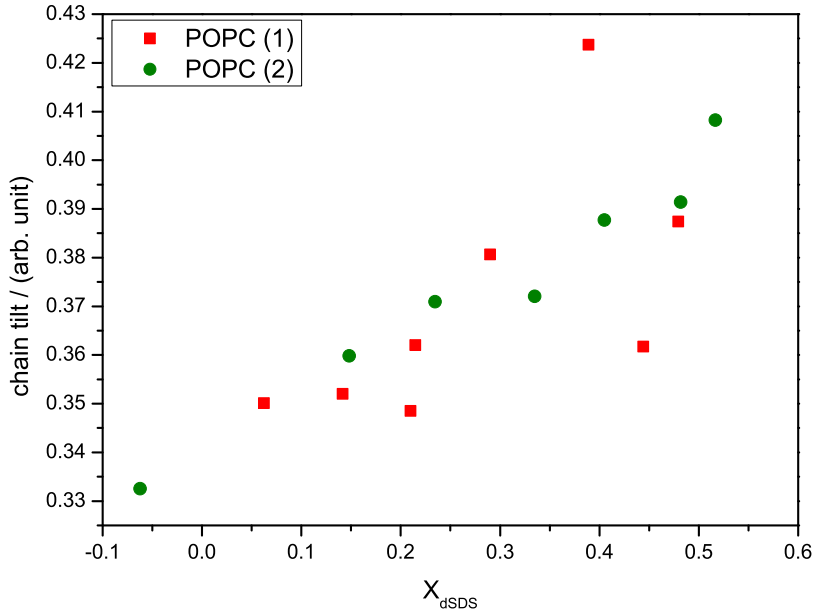

Figure 5.11: Figure showing the variation in average lipid chain tilt with increasing dSDS mole fraction for POPC SLBs (1) and (2). 32°C, 73° incidence, 20 mM tris pH 7.4.

this component was not removed upon rinsing. In the work of other groups on vesicular systems, SDS does not partition into the inner bilayer leaflet unless the temperature is raised significantly (25→65°C).[138,144] In the 0.1 mM addition I believe we are seeing a similar effect. However, other workers have shown that at a higher fixed concentration typical surfactants lead to an increase in the rate of flip-flop within vesicle bilayers above which further increases exponentially enhance flip-flop;[145] this enables surfactant penetration into the inner leaflet as when the dSDS mole fraction in the outer leaflet is raised, transfer to the inner monolayer is enhanced. Upon rinsing the sudden loss of surfactant from the outer monolayer could possibly explain the reduced rate of flip-flop from the inner leaflet to the outer that I have observed but we would also expect to see evidence of spontaneous bilayer curvature and the formation of blebs and tubules (or an extension of) due to the resulting asymmetry. This onset of sudden membrane curvature should be confirmed by some transient variation in the lipid signal. For this reason I monitored the CH region at 0.3 mM dSDS as a function of time. Figure 5.16 (a) and (b) show these data, we see an initial decrease in the POPC component weight in (a) as further dSDS partitions into the SLB, upon rinsing in (b) after the last surfactant has passed through the flow cells internal tubing, we observe a remarkable fluctuation which I believe corresponds to the onset of transient membrane curvature, and subsequent rupture and annealing; it is probable that membrane rupture is taking place as the final POPC component weight values are the lowest for the run – during rupture some POPC is irretrievably lost into solution. By following the CH region kinetics I was able to follow the change in $I(d^+)/I(d^-)$ with time in the same way as for my formation kinetics work (Chapter 3). Recall that spherical vesicles had a lower order parameter value than the planar SLB. I interpreted the changing value of the order parameter as an average over different structures present at the interface. Figure 5.17 shows the relevant order parameter data for the addition and rinsing of 0.3 mM dSDS to and from POPC SLB (1). I have combined the partitioning and rinsing data from 5.16 (a) and (b) onto one time base to visually aid direct comparison. There is no measurable

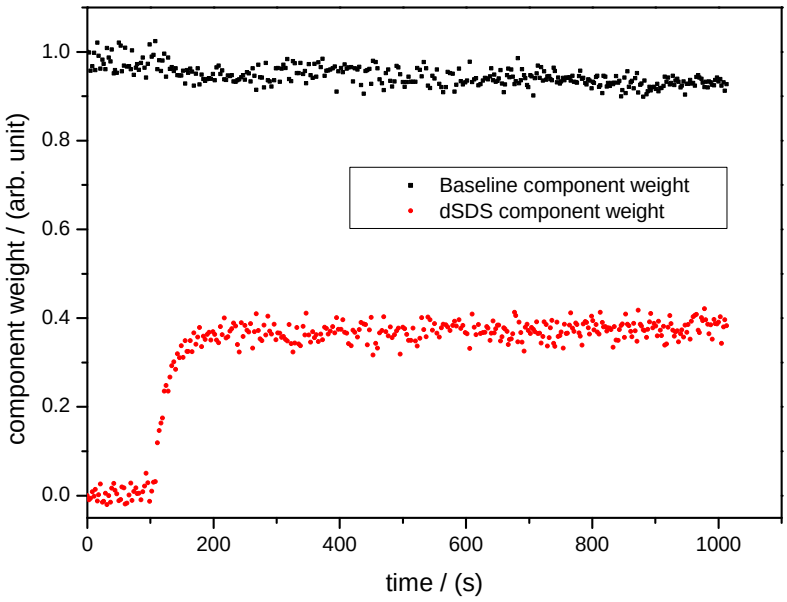

(a)

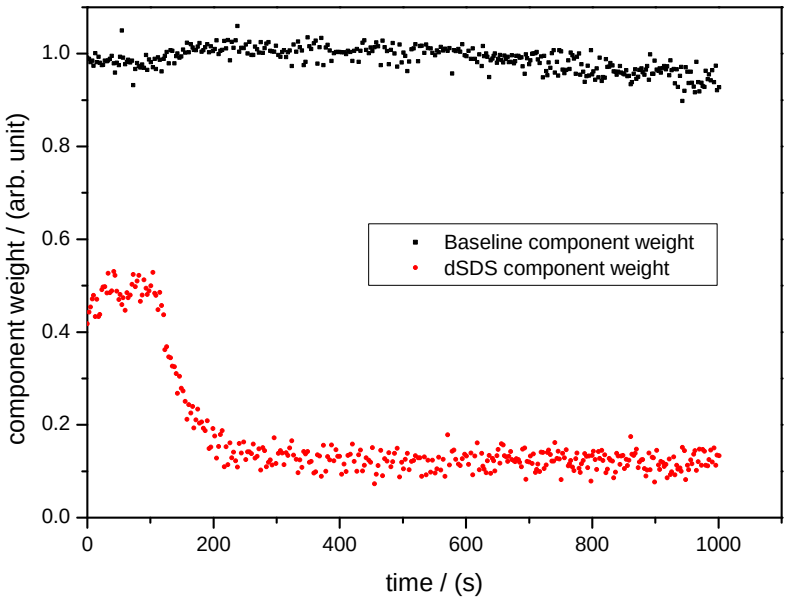

(b)

Figure 5.12: Figures showing the (a) addition and (b) rinsing of 0.1 mM dSDS to and from POPC SLB (1). 73° incidence, 32°C, 20 mM tris pH 7.4.

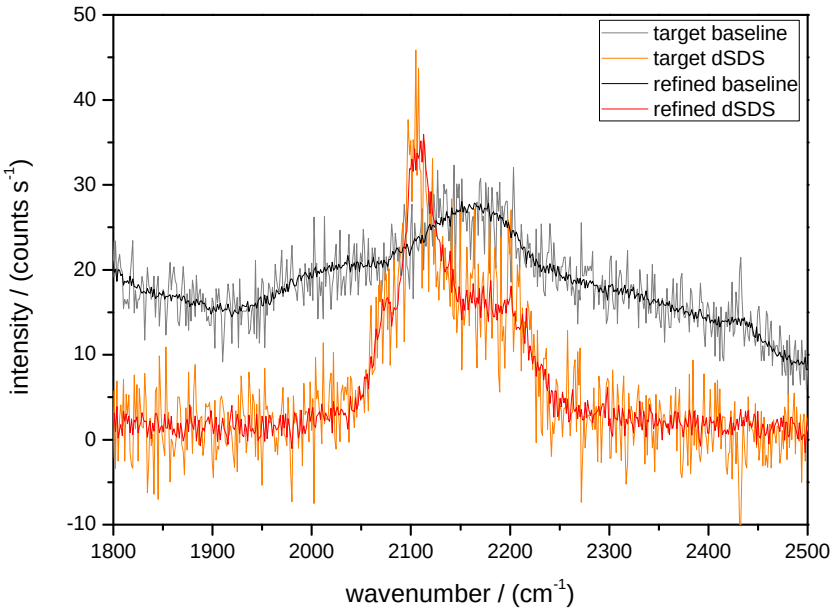

Figure 5.13: Figure showing example target spectra and the refined spectra calculated from them by target factor analysis. Note the large reduction in noise in the refined spectra. The refined spectra shown are those used in linear combinations to generate the component weights for the POPC kinetic partitioning data sets presented.

change in the order parameter, any structural changes that are taking place cannot lead to a state that is significantly distinct from an SLB.

In both the 0.1 mM and 0.2 mM additions there are slight drops in the baseline component weight as dSDS partitions into the SLB, this occurs at the same time as the increase in the component weight of dSDS. Upon rinsing these slight decreases in the baseline component weight recover. It is tempting to attribute these changes to some physical change, such as the expansion of the SLB into uncovered areas of substrate. However, examination of the refined spectra in figure 5.13 and comparison of the results obtained with refined spectra calculated from alternate runs explain the true origin of the changes. When looking at the refined spectra we see that their actual shapes are fairly similar in form, as a result there is a slight mixing of the components that varies according to the targets chosen. For instance if I chose target spectra from the 0.4 mM addition and calculated the refined spectra, and then did the same for the 0.2 mM addition, at the linear combinations stage the baseline component weight decrease would vary, in fact in some instances it actually increases. The behaviour can only result from a mixing of the components at the linear combination stage of the analysis. As my analysis of these data is essentially qualitative, these artefacts do not present a problem. However, if one was planning on modelling surfactant partitioning into SLBs these artefacts would present a real problem. In this situation a strong Raman scattering internal marker that is inert to the rest of the system should be used, this would afford the ability to normalise the data without relying on the baseline component weight.

Despite the above interpretation of the baseline component weight changes, it is not fundamentally clear what should happen to the water component weight in the CH region upon surfactant partitioning or rinsing in terms of surface coverage changes. In general the refractive index of SLB is comparable to that of silica; exactly where the evanescent field begins decaying

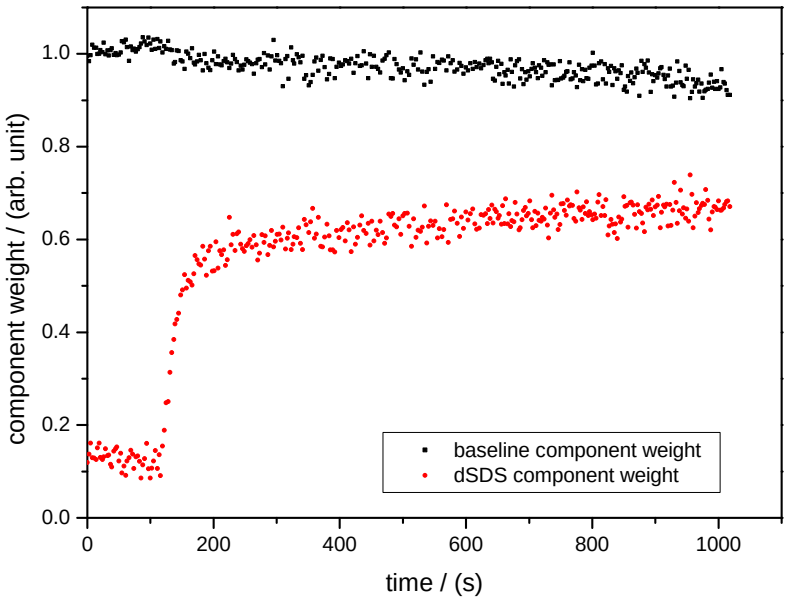

(a)

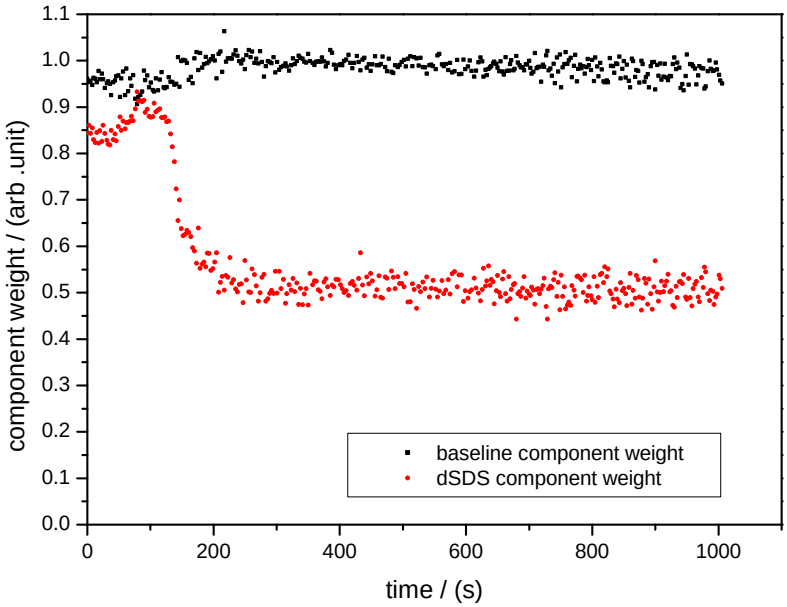

(b)

Figure 5.14: Figures showing the (a) addition and (b) rinsing of 0.2 mM dSDS to and from POPC SLB (1). 73° incidence, 32°C 20 mM tris pH 7.4.

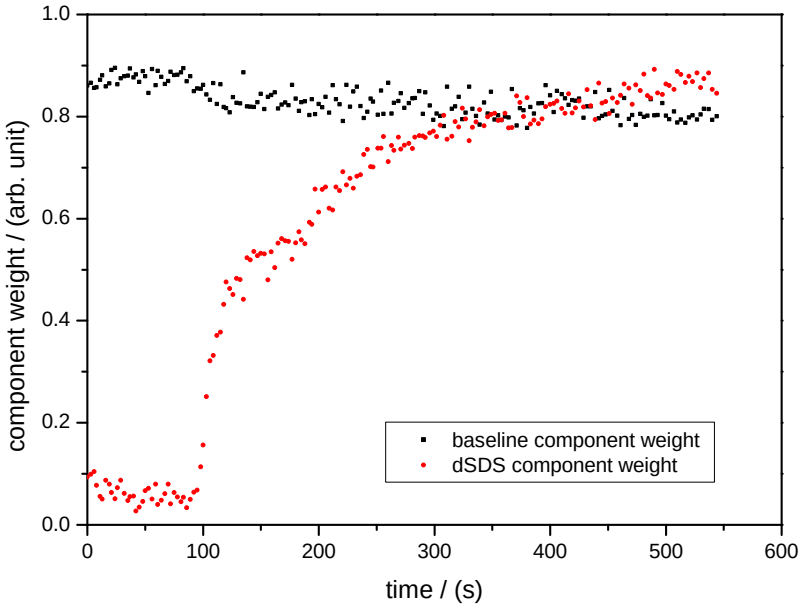

(a)

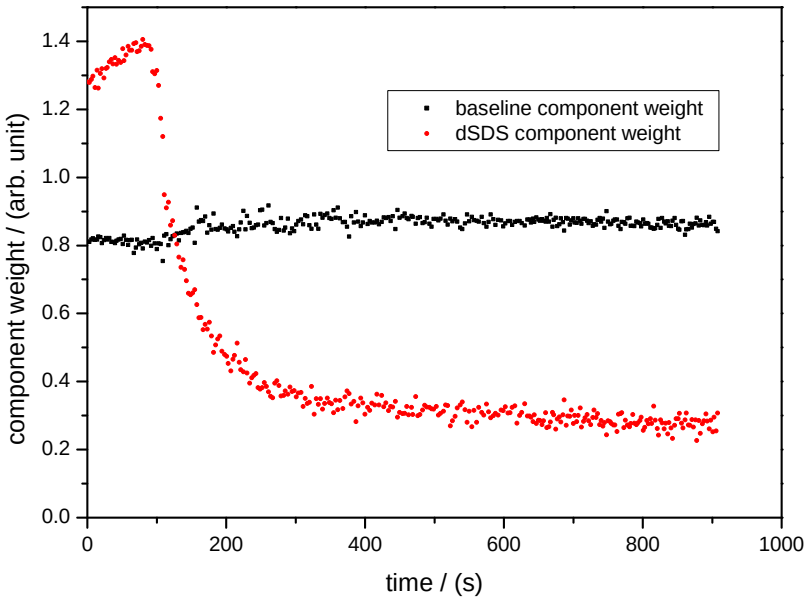

(b)

Figure 5.15: Figures showing the (a) addition and (b) rinsing of 0.4 mM dSDS to and from POPC SLB (2). 73° incidence, 32°C, 20 mM tris pH 7.4.

is therefore ambiguous in the presence of the SLB – it could be that it begins from the SLB water-interface. In this case incomplete coverage leads to a weighted average of signals from the interfacial regions with SLB and those without. If the evanescent field after SLB formation begins to decay after the SLB, one would expect to see limited change in the component weight of water as the SLB expands provided the electric field at the SLB-water interface is similar to that at the silica-water interface. However, if the field begins decaying at the silica-SLB interface, an increase in coverage would lead to a decrease in water component weight of water. One must also consider what is happening to the electric field within the SLB in the former case, if it is higher than for a bare silica-water interface one could expect the component weight of water to actually increase with increasing surface coverage. For rigour, this problem would require detailed quantitative modelling of the electric fields for the different scenarios with very accurate refractive indices for the media concerned – this is beyond the scope of this thesis.

Figure 5.15 (a) and (b) show CD region kinetic data for POPC SLB (2) at 0.4 mM dSDS; I am discussing this dataset separately from the data acquired for POPC SLB (1) as the rinsing behaviour is quite different. In figure 5.15 we observe that the dSDS can largely be removed upon rinsing, whereas the relevant data in 5.14 (b) show limited flip-flop upon rinsing. It is not clear from the TIR-Raman data why two almost identical SLBs should show such different rinsing behaviour. Perhaps the history of the system in terms of the number of surfactant additions and subsequent rinses plays a role. Another possibility is that the initial SLB coverage could lead to differences in the rate of flip-flop, particularly if there were a large number of defects as these would create a diffusion pathway for surfactant molecules to move into the distal monolayer. In my measurements, SLB (2) has greater initial coverage, it also displays SDS removal in the second stage of rinsing. It is therefore unlikely that coverage is a contributing factor to the measured differences between the two SLBs. Unfortunately it is not possible to explain this disparity with TIR-Raman alone.

Step changes in water signal have significant consequences for normalising. As described in my methods, there was always some drift in the focus of the microscope during the course of a measurement. Whilst it was possible to reduce this drift by trying to limit the lash in the micro-motion stage motors and ensuring thermal equilibrium it was not possible to remove it completely and for this reason each successive Raman measurement where TFA was not being used was normalised to a reference water or buffer background spectrum; this served two purposes, to remove spectral contributions from the buffer solution, but also to make the data from each successive spectrum quantitatively comparable. For the TFA data most recently described, when comparing dSDS normalised component weights before and after a step in the baseline component weight, there would be an exaggeration of the dSDS component weight. For this reason I have not normalised any of my CD region TFA kinetic data to the baseline where this issue occurs, and, as stated before, this does not affect my interpretations as they are essentially qualitative in terms of the component weight – I have not estimated surface excess. However, if the surface excess was required, as stated before an inert maker would be required for absolute normalisation.

In summary, the time taken for dSDS to partition into POPC SLBs is essentially constant for the concentration regime considered here. The rate of flip-flop from the outer leaflet to the inner leaflet depends on the bulk concentration of the dSDS. During rinsing the rate of flip-flop from the inner leaflet appears to depend on the prior history of the SLB under investigation. The ability of dSDS to irretrievably remove POPC before the onset of the solubilisation regime depends on whether or not the system is rinsed after addition. Lastly the rapid loss of dSDS from the outer leaflet during rinsing leads to fluctuation in the component weight of lipid, this was interpreted as a transient change in structure as the original average component weight value was recovered.

As the transient signal was fast, it was not possible to acquire AFM images and so no further information of the actual transient structure formed was available.

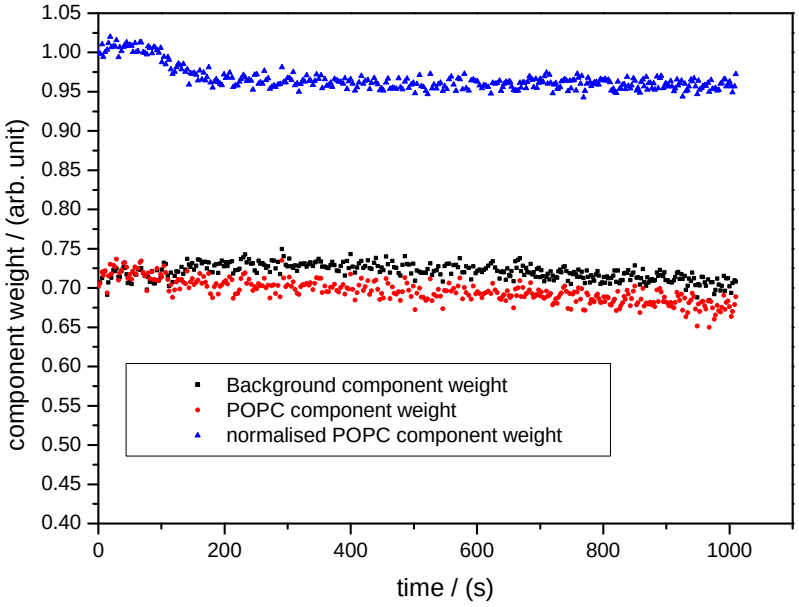

(a)

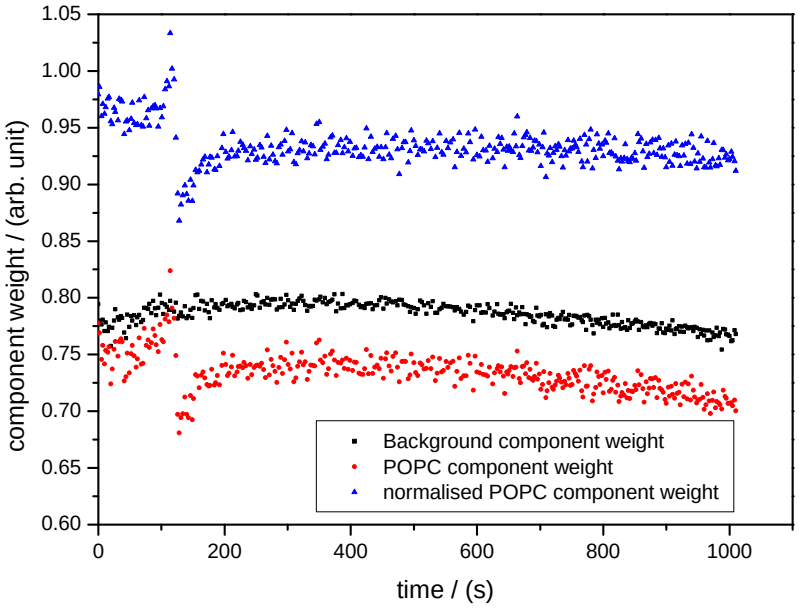

(b)

Figure 5.16: Figures showing the effect of 0.3 mM dSDS partitioning on POPC component weight during (a) addition and (b) rinsing. 73° incidence, 32°C, 20 mM tris pH 7.4.

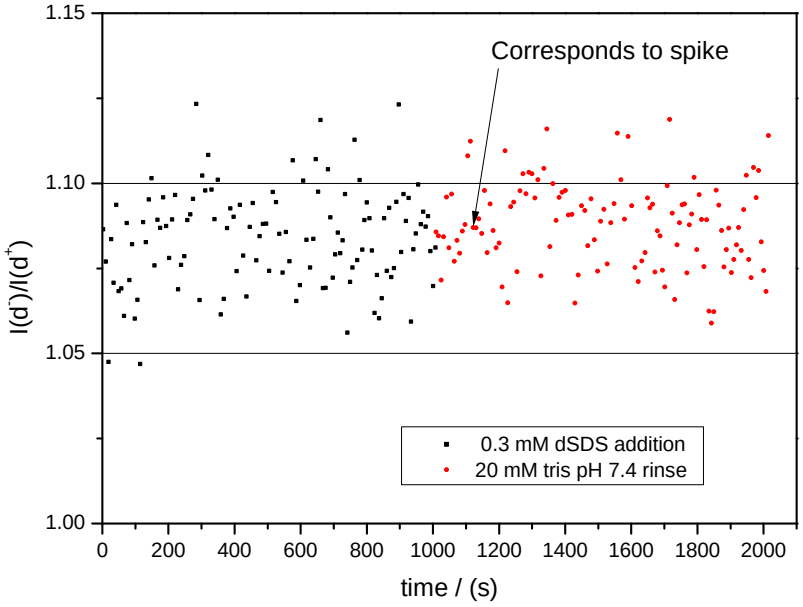

Figure 5.17: A graph showing the intensity ratio $I(d^-)/I(d^+)$ as a function of time for the 0.3 mM dSDS addition and subsequent rinse.

5.4.3 POPE

POPE is a homologue of the lipid POPC; the difference in structure being the replacement of the methyl headgroup substituents with hydrogens. This makes studying the interaction of POPE with dSDS potentially very rewarding; any changes in the behaviour can only be the result of that one difference in structure. All my measurements were conducted at pH 7.4, as the PE headgroup has a pKa of 11.25 and the phosphate group has a pKa of 1.7, throughout my measurements POPE was zwitterionic. As seen in Chapter 3, one problem with POPE is the difficulty in reproducibly forming SLBs, as a result the quantity of data that I was able to acquire was limited in comparison to POPC.

5.4.3.1 Equilibrium measurements

Figure 5.18 show subtracted TIR-Raman data for the addition of 0.1 and 0.4 mM dSDS to a POPE SLB in the L_α phase. The assignments for these spectra are identical as those for POPC except for the absence of the choline methyl CH stretch at 3041 cm^{-1}. dSDS addition to a POPE SLB is very similar to POPC SLBs in terms of the raw spectra; we note the increase in CD signal and decreases in the CH signal. Upon rinsing, the CH signal recovers following exposure to 0.1 mM dSDS but not after exposure to 0.4 mM SDS. The extent of the recovery seen after 0.1 mM dSDS is rinsed out is less than was observed with POPC. At both concentrations, rinsing completely removed the dSDS. For other surfactant concentrations (omitted for graphical clarity) the degree of loss of CH signal upon dSDS addition and rinsing increases as a function of total dSDS concentration. Figure 5.19 shows raw spectra of POPC SLBs (1) and (2) prior to any surfactant

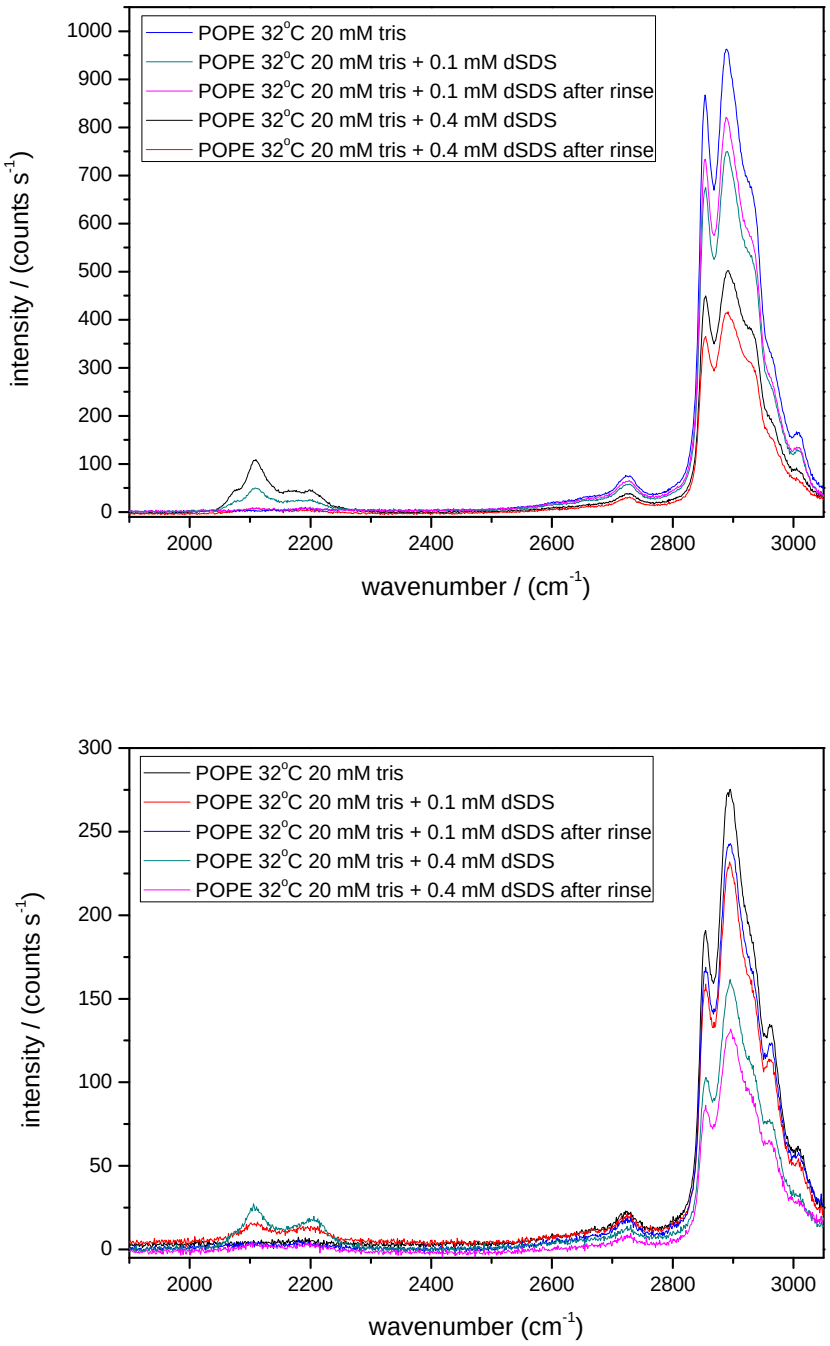

Figure 5.18: TIR-Raman spectra showing the interaction of 0.1 and 0.4 mM dSDS with an SLB comprised of POPE in 20 mM tris pH 7.4. 73° incidence with equilibration at 32°C. 10 second spectra with 18 accumulations. Both S-polarised (a) and P-polarised (b).

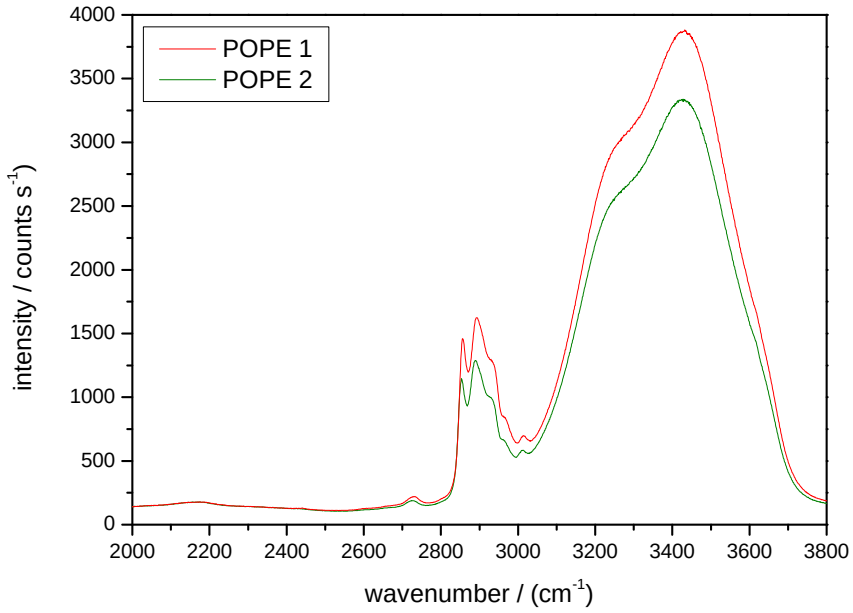

Figure 5.19: A figure showing raw S-polarised TIR-Raman spectra of SLBs POPE (1) and POPE (2). 20 mM tris pH 7.4, 32°C, 73° incidence, 800 mW, 10 s spectra, 18 acquisitions.

addition. As done with POPC, I have estimated the difference in coverage by calculating the ratio of the CH region to water band peak intensities. For these systems the difference was found to ≈ 8% with SLB POPE (1) having greater coverage.

Figure 5.20 shows the partitioning data for dSDS and two different POPE SLBs. In comparison to the data acquired for POPC I have noted two key differences. Firstly, unlike POPC there does not appear to be a saturation limit; the mole fraction of dSDS continues to rise at all concentrations investigated. Secondly, the normalised total signal levels drop almost continuously for both SLBs; this is in marked contrast to the POPC data which show a clear increase in normalised total signal as a function of dSDS concentration; at least at low dSDS concentrations. For POPE (2) the system was rinsed after each addition up until 1.0 mM; this explains the greater loss of total signal for this system when compared with POPE (1) at lower concentrations. Overall, these data highlight a stronger interaction between POPE and dSDS than POPC and dSDS; without the bulky choline headgroup, the dSDS can interact more strongly with the cationic ammonium sub-group. In addition, as the headgroup of POPE has such a small cross-sectional area, it is likely that there is some monolayer curvature strain in both bilayer leaflets to begin with. Additional dSDS would negate this preference for a spontaneously curved monolayer geometry. It is therefore strange to observe the continual loss of lipid from the interface. However, if the charge on dSDS were being neutralised by Na^+ and $tris^+$ counterions, any monolayer curvature strain would be reduced and the whole SLB structure would still prefer a more curved geometry.

As for the POPC system, I have analysed the partitioning behaviour with both the non-ideal and charged surfactant models described in the introduction to this chapter. Figure 5.21 (a) shows the variation in R_b for the POPE dSDS system as a function of dSDS bulk concentration. The relationship is linear, again indicating that the majority of surface charge was being neutralised by counterion binding. The value of K_R obtained was 1400 ± 130 M^{-1} which yields a standard free energy change $\Delta\mu_{dSDS}^{0,aq\rightarrow B}$ = -28.6 kJ mol^{-1} ± 0.2 kJ mol^{-1}. This value is significantly higher than

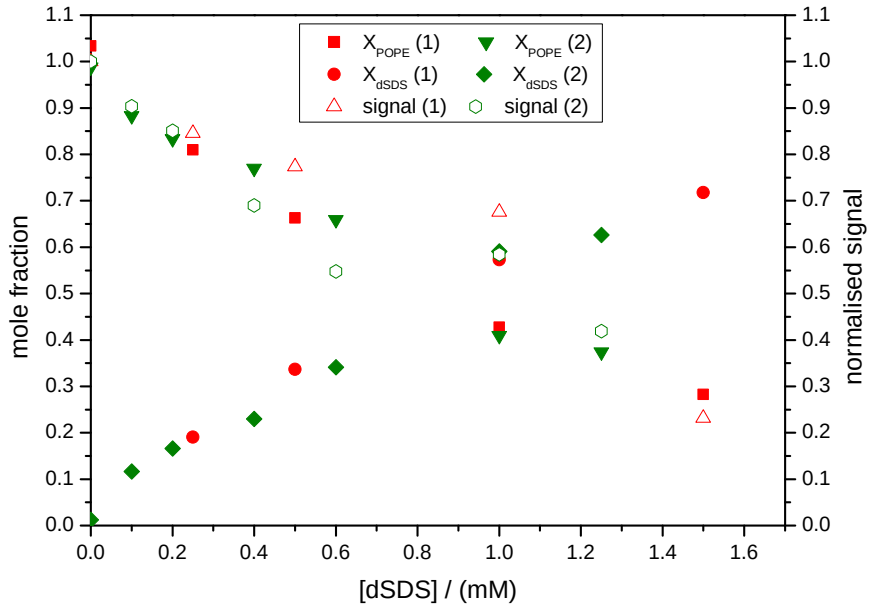

Figure 5.20: A graph showing two partitioning isotherms for dSDS incorporating into POPE SLBs (1) and (2), 32°C, 73° incidence. Calculated from combined S- and P-polarised spectra.

that obtained for POPC and can be attributed to the closer proximity of the charged SDS and POPE headgroups. When attempting to use the charged surfactant model, similar to the POPC system we find that there is a non-linear relationship between surface dSDS concentration and R_b, this model is therefore inapplicable; counterion binding precludes its use without knowledge of the relevant binding constants.

5.4.3.2 Structure

Figure 5.22 shows the change in the primary order parameter as a function of dSDS mole fraction. Overall there isn't a large variation across the full range of dSDS concentrations used and the pure POPE SLBs but we do see a slight increase. For both SLBs the difference between the first at last data points is ≈0.03 this corresponds reasonably well with the POPC data where we observed a similar but larger increase of ≈0.07. Again, note the slight difference between the absolute values obtained for the two SLBs.

Figure 5.23 shows the change in the wavenumber of the symmetric and antisymmetric CH stretches as a function of dSDS mole fraction. Both SLBs have slightly different absolute peak position values as the calibration of the spectrometer was slightly out for POPC SLB (2). The changes in the peak positions are broadly similar with the antisymmetric stretch showing a clear increase with mole fraction. This is counter intuitive as one would expect an increase in peak position to be accompanied by a decrease in the more sensitive primary order parameter, I observed similar behaviour with both POPC SLBs.

Figure 5.24 shows the change in the average lipid chain tilt as a function of dSDS mole fraction. The data follow the trends in the primary order parameter closely, for both there appears

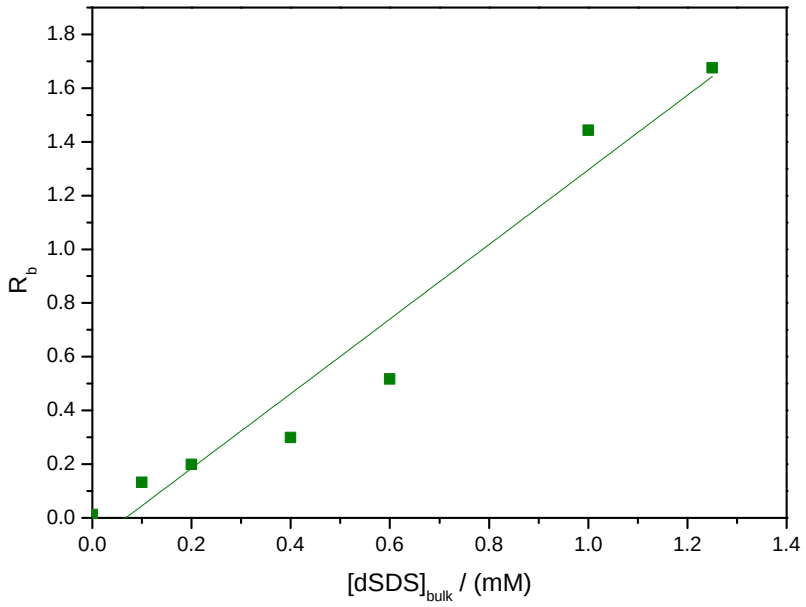

(a)

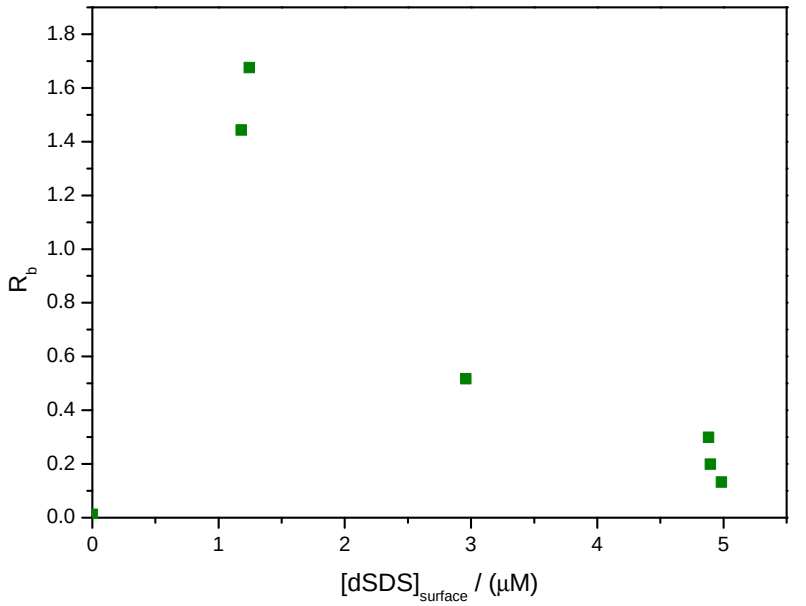

(b)

Figure 5.21: Graphs showing the variation in dSDS to POPE mole ratio within POPE SLB (2) as a function of (a) bulk dSDS concentration and (b) surface concentration considering accumulated surface charge. 73° incidence, 32°C, 20 mM tris pH 7.4.

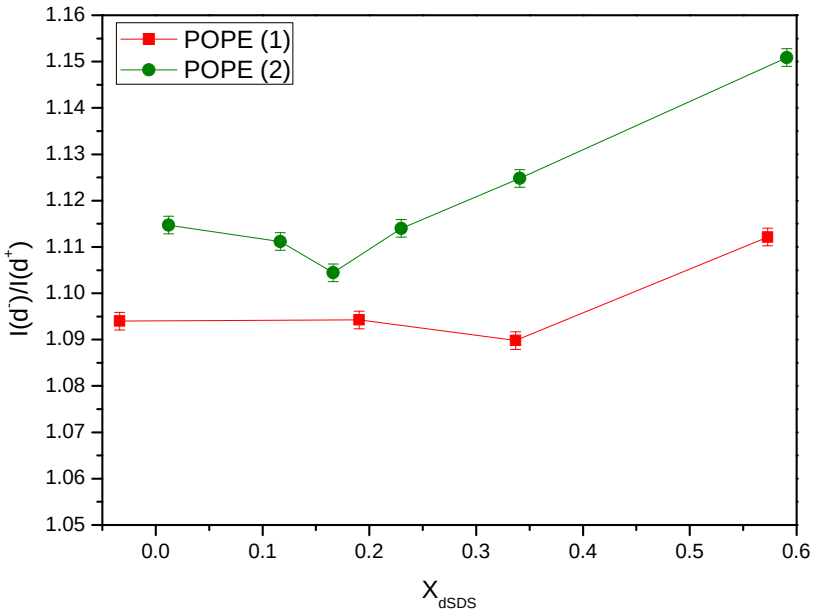

Figure 5.22: A graph showing the variation in both the POPE symmetric and antisymmetric CH stretches with increasing dSDS mole fraction for POPE SLBs (1) and (2). 32°C, 73° incidence, 20 mM tris pH 7.4.

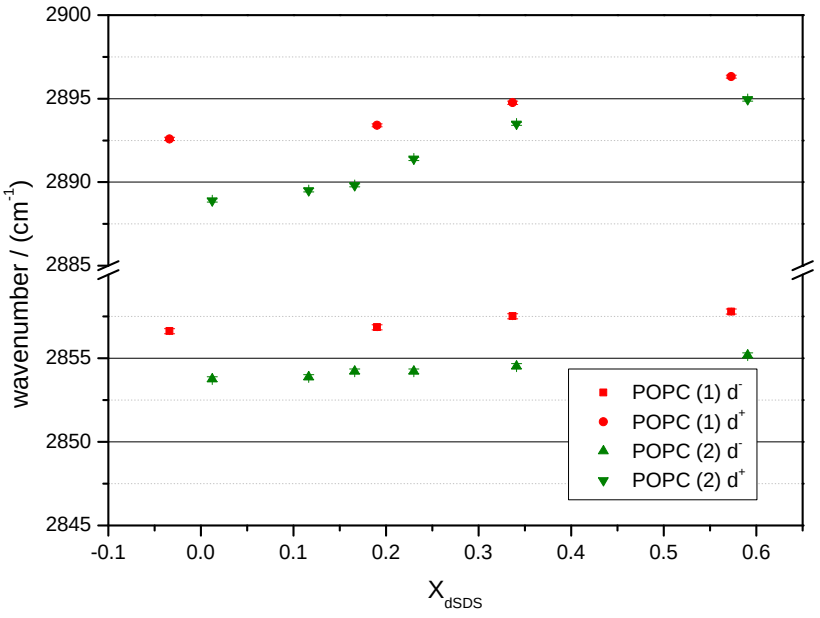

Figure 5.23: Figure showing the variation in both the POPE symmetric and antisymmetric CH stretches with increasing dSDS mole fraction for POPE SLBs (1) and (2). 32°C, 73° incidence, 20 mM tris pH 7.4.

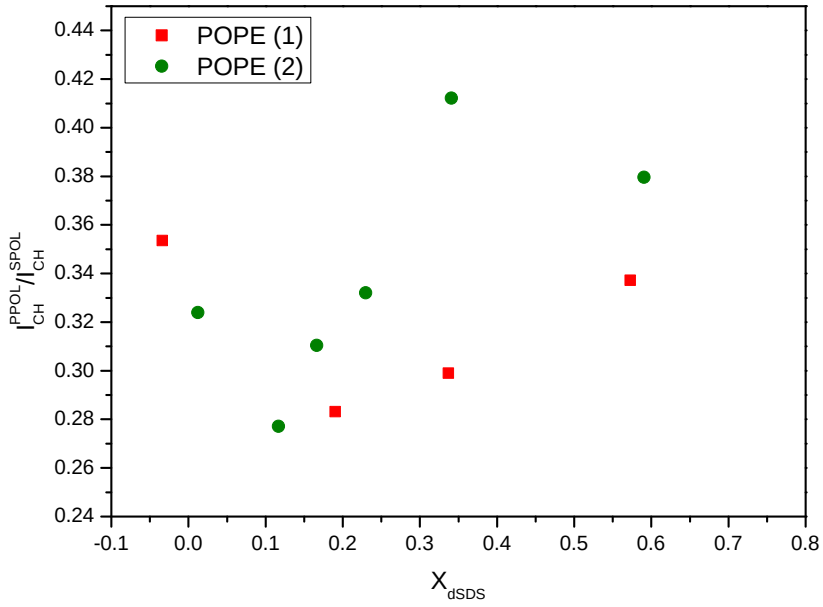

Figure 5.24: Figure showing the variation in average lipid chain tilt with increasing dSDS mole fraction for a POPE SLB system. 32°C, 73° incidence, 20 mM tris pH 7.4.

to be an initial decrease and then subsequent increase in the average lipid chain tilt.

5.4.3.3 Kinetic measurements

Figure 5.25 and 5.26 show (a) the partitioning and (b), the rinsing kinetics of 0.4 mM dSDS for two POPE SLBs. In subfigure (a) there was an initial rapid uptake of surfactant, followed by a slower region of uptake. Similar to the POPC system, one plausible explanation of these data is that the first fast stage could indicate the partitioning dSDS into the outer bilayer leaflet, which takes approximately 100 seconds, the second slow stage may indicate the penetration of dSDS into the inner SLB leaflet by flip-flop. In the second stage a plateau was reached after approximately 10 minutes. During rinsing the component weights drop suddenly and this is followed by a slower protracted decrease in dSDS component weight. Based on the same ideas invoked for the addition, the two decrease stages could indicate a first rapid loss of dSDS from the outer SLB leaflet followed by a slower stage involving the transfer of dSDS from the inner leaflet. In figure 5.26 (b) I spent longer rinsing the system than in figure 5.25 (b) to establish if any other changes were taking place during dSDS removal. During this measurement I observed a continuation of the same slow loss of dSDS signal. In comparison with my measurements of the POPC dSDS interaction, I have not observed any step changes in the background component weight. I have recorded only more subtle changes characteristic of signal loss due to degrading alignment. This implies that the TFA analysis is not having the same problems with this system as in the POPC case. As such I have normalised the POPE component weight by the baseline component weight. As POPE was removed from the interface at all concentrations of dSDS for both SLBs regardless of initial surface coverage, the rate of removal has nothing to do with the degree of surface coverage, but is instead dependent purely on the interaction of dSDS with the POPE monomers and their mutual preferred geometry

as well as rinsing history. The variation that does exist in the baseline component weight for the measurements in figure 5.26 is the result of the alignment drifting.

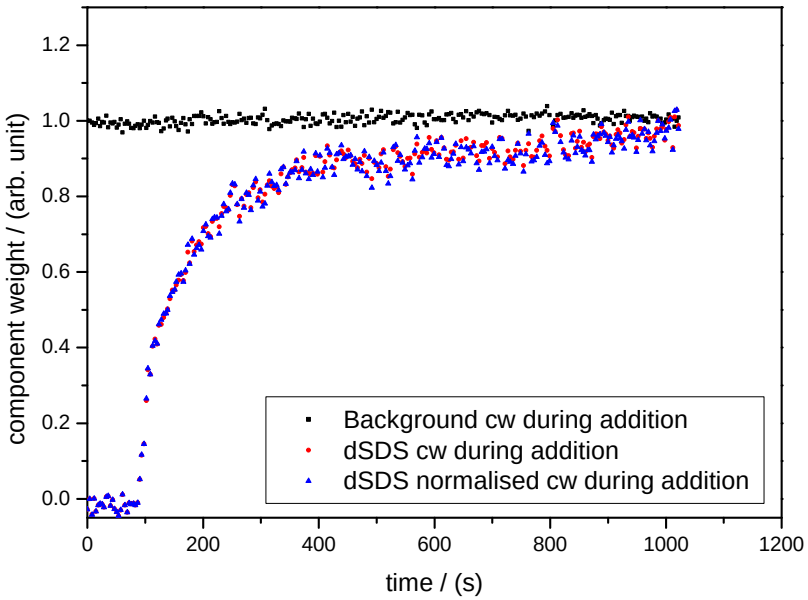

(a)

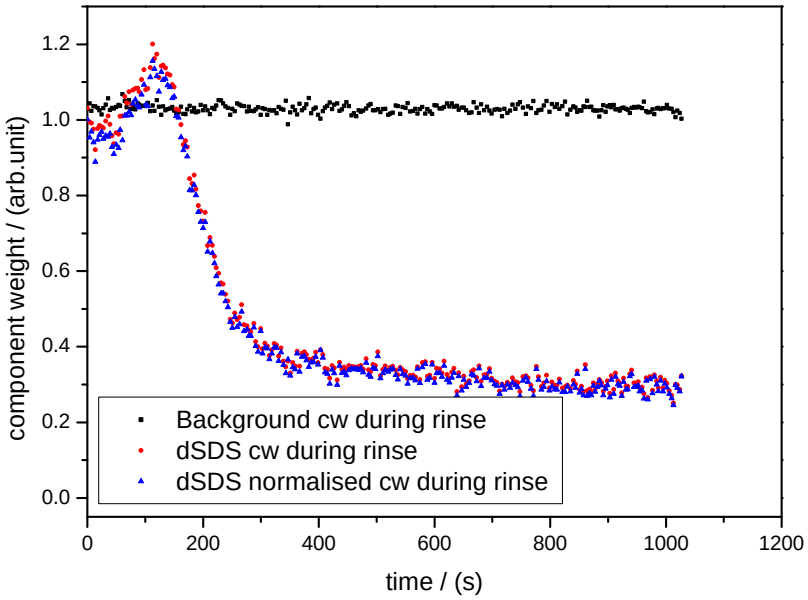

(b)

Figure 5.25: Figures showing the (a) addition and (b) rinsing of 0.4 mM dSDS to and from a POPE SLB. 32°C 20 mM tris pH 7.4.

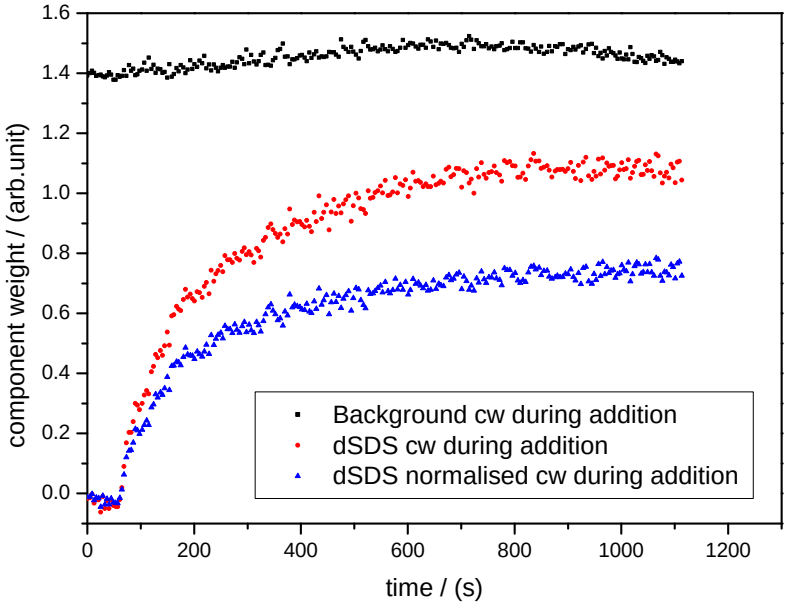

(a)

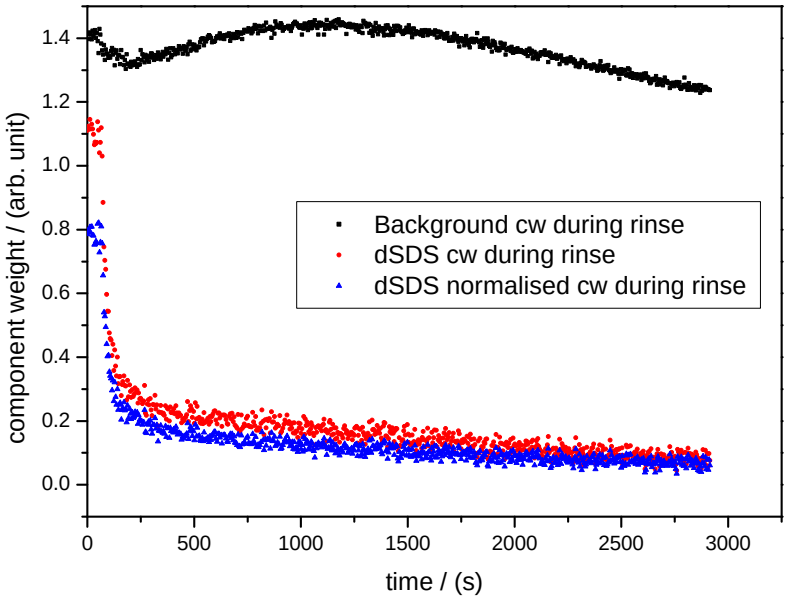

(b)

Figure 5.26: Figures showing the (a) addition and (b) rinsing of 0.4 mM dSDS to and from a POPE SLB. 32°C 20 mM tris pH 7.4.

5.4.4 Egg-SM

5.4.4.1 Equilibrium measurements

Sphingolipids differ from glycero-phospholipids in that they have a sphingosine rather than glycerol backbone, although they have the choline headgroup as in POPC. They generally form more ordered bilayers than glycero-phospholipids, and as shown earlier in Chapter 4 generally have a higher melting transition temperature than glycero-phospholipids. Sphingolipids also form hydrogen bond networks between their phosphate oxygens and hydroxyl hydrogens.[146] I chose to study the interaction of egg-SM with dSDS partly for its own sake, but also because sphingomyelin purportedly makes up 30% of so called lipid raft/DRM mixtures;[74] it is therefore necessary to evaluate the interaction of dSDS with egg-SM as a pure species before trying to understand the role of egg-SM in a DRM mixture. Sphingomyelins make up 20-35% of all plasma membrane lipids,[81] and are found to be most prevalent in nerve axon sheaths and red blood cells.[147]

Figure 5.27 (a) and (b) show S- and P-polarised subtracted TIR-Raman spectra of 0.29 mM dSDS interacting with an SLB. The assignments for egg-SM in the CH stretching region are the same as those for POPC. The peak at approximately 2440 cm^{-1} has the same intensity in both the S- and P-polarised spectra, is the result of a small light leak during the measurements. It is unfortunate that this error occurred but it had no adverse effect on the experiment and the results obtained. The addition data follow the same trend as that observed for other species, as the surfactant partitions into the original SLB, the bands corresponding to dSDS appear and the CH region intensity decreases. However, the rinsing behaviour is different; as the surfactant signal is lost there is no recovery in the CH region indicating the permanent removal of egg-SM from the interface.

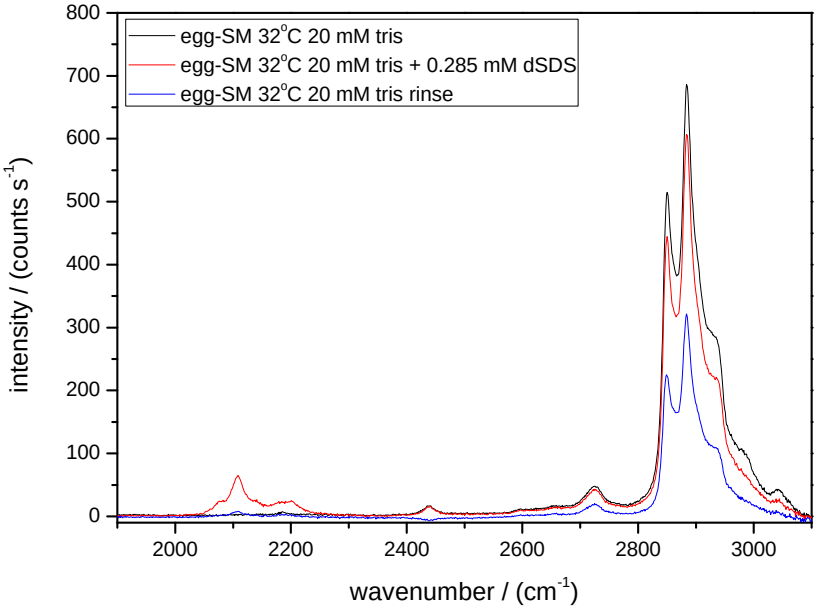

(a)

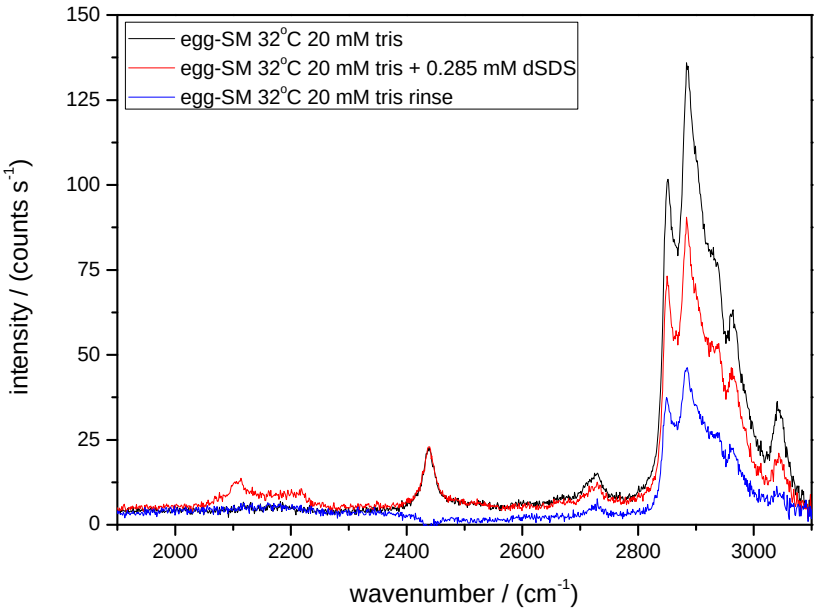

(b)

Figure 5.27: A figure showing subtracted TIR-Raman spectra of an egg-SM SLB and its interaction with dSDS, both (a) S-polarised and (b) P-polarised data are shown. Angle of incidence 73°, 800 mW, 32°C, 10 s spectra, 5 acquisitions, 20 mM tris pH 7.4.

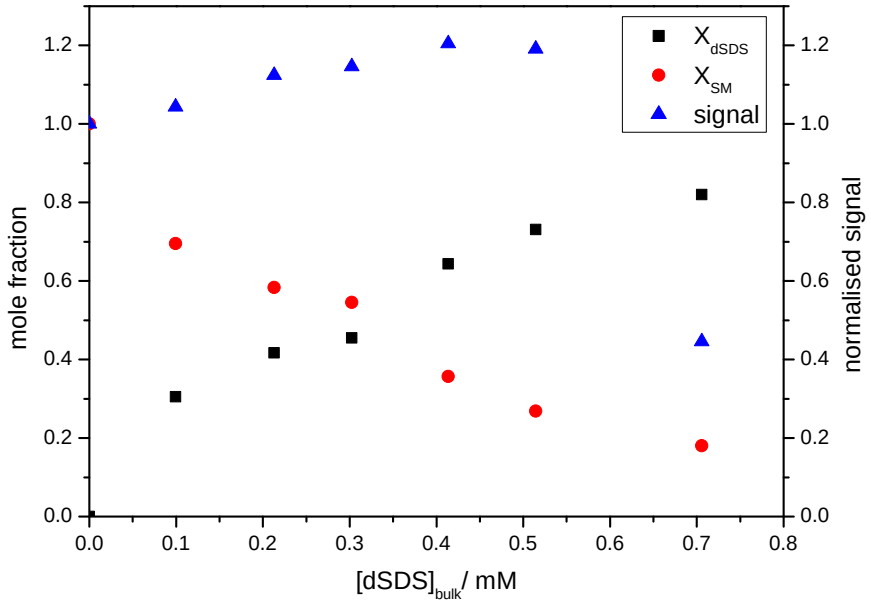

Figure 5.28: Figure showing a partitioning isotherm for dSDS incorporating into an egg-SM SLB, 32°C, 73° incidence, calculated from combined S- and P-polarised spectra.

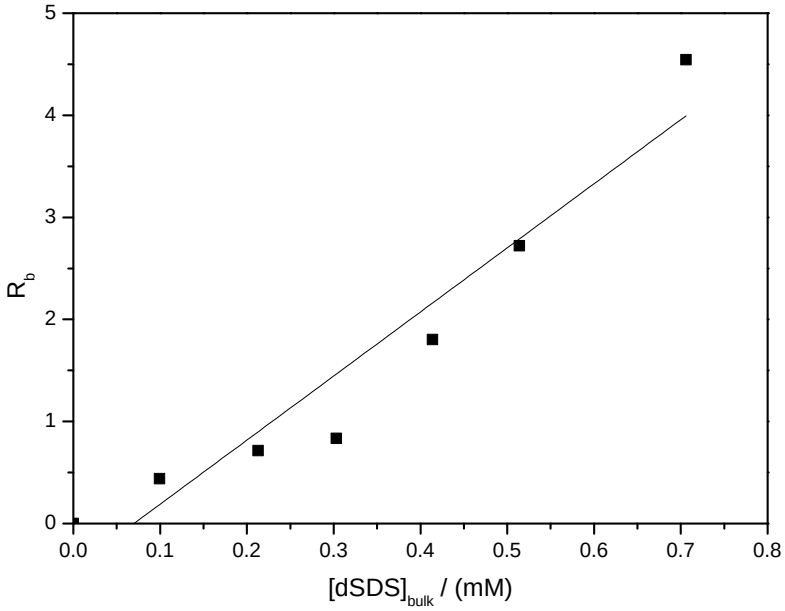

(a)

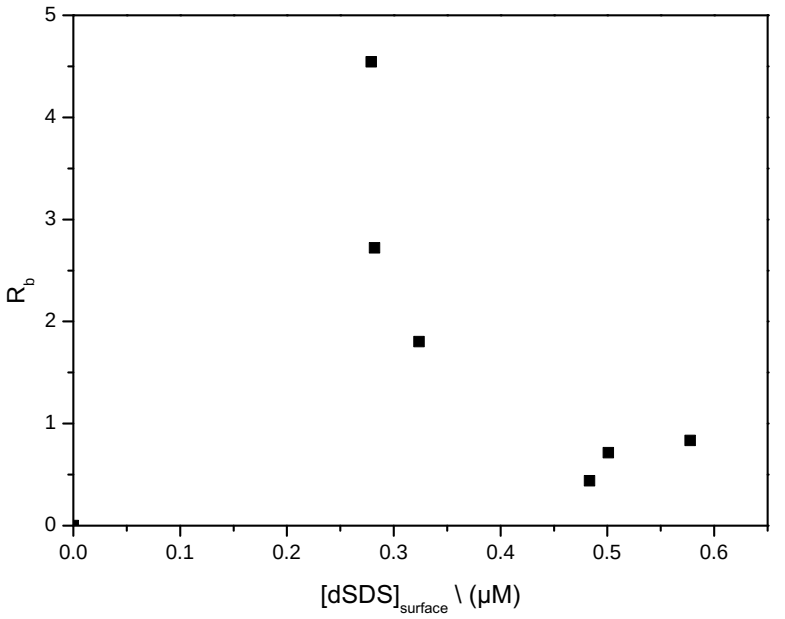

(b)

Figure 5.29: Graphs showing the variation in the mole ratio of dSDS to egg-SM, R_b, as a function of (a) bulk dSDS concentration and (b) theoretical dSDS surface concentration. 73° incidence, 32°C, 20 mM tris pH 7.4.

Figure 5.28 shows the partitioning isotherm for the dSDS interaction with an SLB comprised of egg-SM. The egg-SM SLB appears to have a more favourable interaction with dSDS than does POPC. The mole fraction continues to rise with dSDS concentration until the SLB reaches a sat-

urating dSDS mole fraction of ≈ 0.8. This is substantially higher than POPC which saturated at approximately ≈0.5. In essence the sphingomyelin stabilises a layer primarily comprised of dSDS. Interestingly, despite the stronger interaction, the coverage does not drop linearly as with POPE. In fact we see a situation analogous with POPC where the surface coverage increases as dSDS partitions into the SLB – the total normalised signal increases with bulk dSDS concentration and thus dSDS mole fraction. However, we notice the sudden drop of signal at 0.7 mM dSDS indicating the onset of SLB solubilisation. This is an interesting system because at neutral pH in the absence of background electrolyte one would expect the double layer repulsion between the anionic silica and an SLB with negative charge to dominate and force the SLB from the surface, or at least renormalise the interactions leading to a total potential with a minimum far further from the surface. The fact that we see few structural changes is indirect evidence of counterion binding. The total signal reaches a plateau at ≈1.2 times the value for pure egg-SM, which corresponds to a bulk dSDS concentration of 0.4 mM, this implies that the surface is essentially covered at this concentration.

Figure 5.29 (a) and (b) show the variation in the mole ratio of dSDS to egg-SM as a function of bulk and hypothetical surface dSDS concentration respectively. As for the other systems previously analysed with the non-ideal and charged surfactant models, I have found that the non-ideal model exhibits the most linear relationship with concentration, and thus fits the data best. A linear fit shown in figure 5.29 yields a K_R of 6300 ± 790 M^{-1} which corresponds to a $\Delta\mu_{dSDS}^{0,aq\rightarrow B}$ = -32 kJ mol^{-1} ± 0.3 kJ mol^{-1}. This is higher than the values obtained from my experiments on POPC and POPE. However, inspection of figure 5.29 reveals that R_b is not linear in $[dSDS]_{bulk}$ suggesting that the non-ideal model does not provide a realistic description of this system's behaviour – the larger error in the standard free energy change indicating this. Again, I was unable to fit my experimental data with the charged surfactant model – this model also provides a poor description. It is not clear what is causing both of these models to fail but it is likely that surface charge is not the source of non-ideality and other factors must be contributing.

5.4.4.2 Structure

Figure 5.30 shows the change in the primary order parameter as a function of dSDS mole fraction. Previously we have seen a slight increase in ordering within POPC and POPE SLBs as dSDS partitions into the L_α phase. For egg-SM however, we observe an initial increase in order up to a dSDS mole fraction of 0.3. Subsequently the order parameter decreases until SLB saturation, indicating increasing disorder. Intriguingly, the increase in order seems to occur as the surface coverage is still increasing whilst the decrease in order appears to correspond to the dSDS concentrations where the surface is already completely covered and is likely a result of the disruption of the hydrogen bond network at moderate and high dSDS concentrations. The final data point corresponds to an interface in which ≈55 % of the original SLB was removed and of the remaining material 18% was egg-sm.

Figure 5.31 shows the change in the antisymmetric and symmetric CH stretches for the egg-SM SLB. These data show changes that correspond well with the variation of the primary order parameter and indicate that changes in chain packing must be occurring along with changes in intramolecular order. The fact that the changes in the order match up so well, and that they happened throughout the partitioning isotherm is evidence of a much more intricate partitioning behaviour – several changes in structure are occurring as the mole fraction of dSDS within the

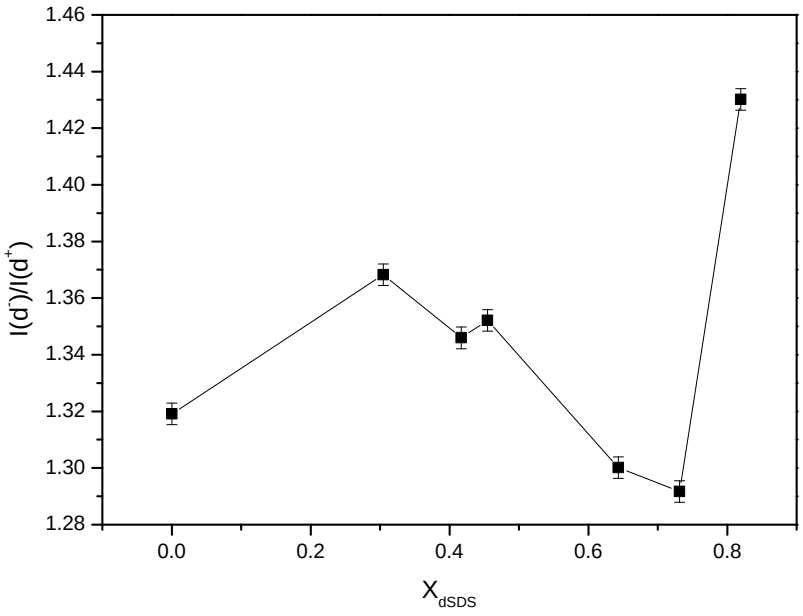

Figure 5.30: Figure showing the change in the primary order parameter as a function of dSDS molefraction, 73° incidence, 32°C, 20 mM tris, pH 7.4.

SLB increases. It is not unexpected that egg-SM would display different behaviour to POPC and POPE as it is far more ordered as a pure SLB system.

Figure 5.32 shows the change in average lipid chain tilt as a function of dSDS mole fraction. The data show that initially as dSDS partitions into the SLB, the chains de-tilt, however, as the mole fraction of dSDS increases, the chain tilt increases proportionately. As this subsequent increase is small and coincides with the decrease in order shown in figure 5.30 the increase probably indicates the onset of average tilting brought about by an increase in gauche defects in the hydrocarbon chains of the egg-SM.

5.4.4.3 Kinetic measurements

Figures 5.33 (a) and (b) show the kinetics of partitioning and rinsing for a solution of 0.4 mM dSDS with an egg-SM SLB. In most ways the data are qualitatively similar to those obtained for POPC; there is a period of rapid initial dSDS uptake followed by a more gradual partitioning, upon rinsing this is followed by a rapid initial loss and then a more gradual loss. The time required for the initial uptake is, like the other systems studied approximately, 100 seconds. The dSDS component weight after the rapid initial uptake is the same as that after rinsing, but the time required for the slower step, where flip-flop may be occurring, is longer during rinsing. This could be a result of structural changes taking place in the outer leaflet of the SLB during rinsing, for instance if it was more ordered, flip-flop would be slower. In subfigure (a) when looking at the component weight of water one observes a stepwise change. This is similar to the stepwise changes in the component weight of water for the POPC SLBs and is likely an artefact of the TFA linear combination step, where the program is getting confused between the baseline and dSDS refined spectra.

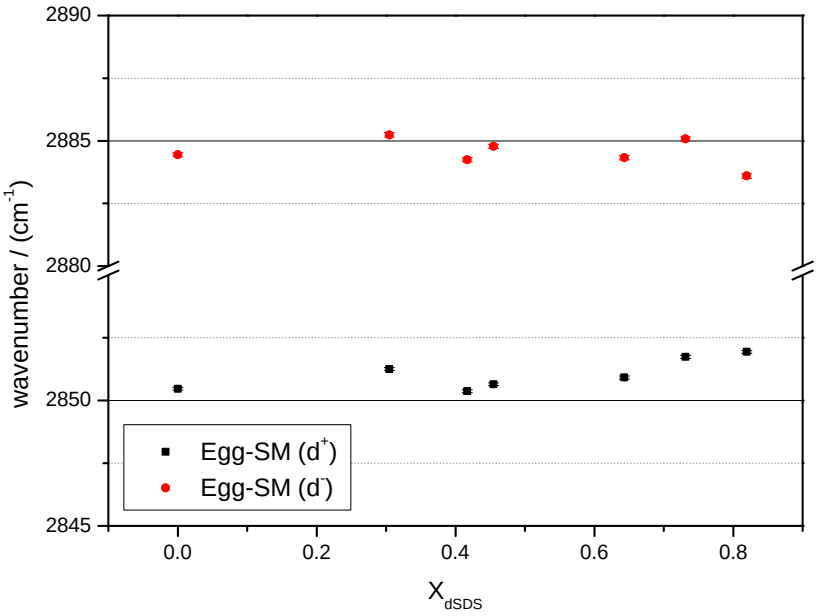

Figure 5.31: A figure showing the change in the anti-symmetric and symmetric CH stretches as a function of dSDS mole fraction, 73° incidence, 32°C 20 mM tris pH 7.4.

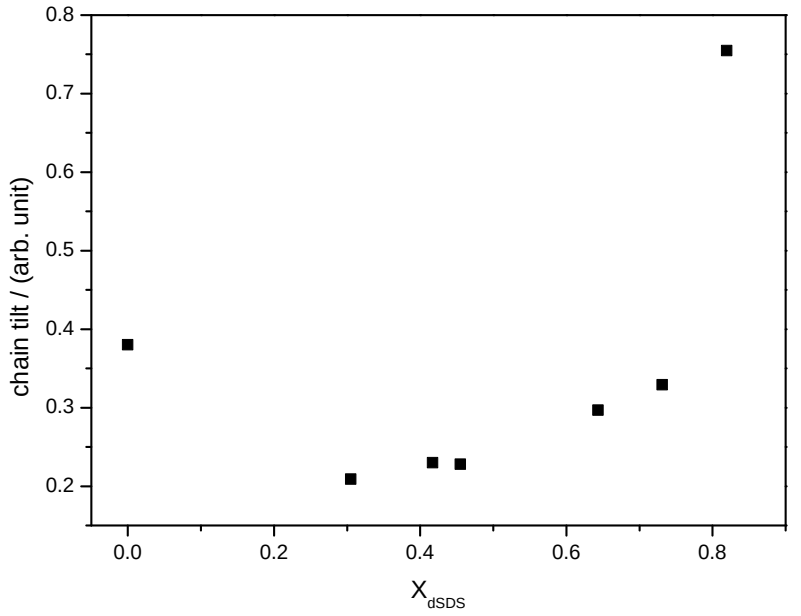

Figure 5.32: A figure showing the change in average lipid chain tilt as a function of dSDS molefraction, 73° incidence, 32°C, 20 mM tris pH 7.4.

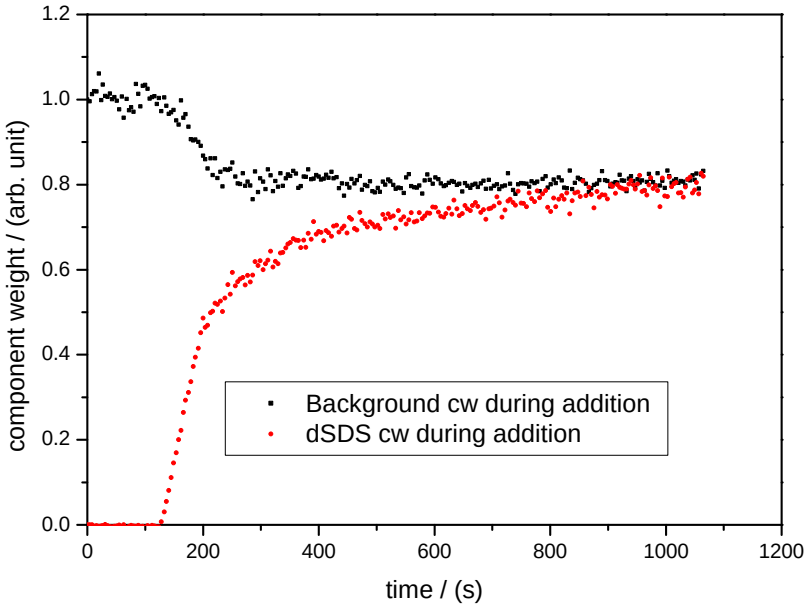

(a)

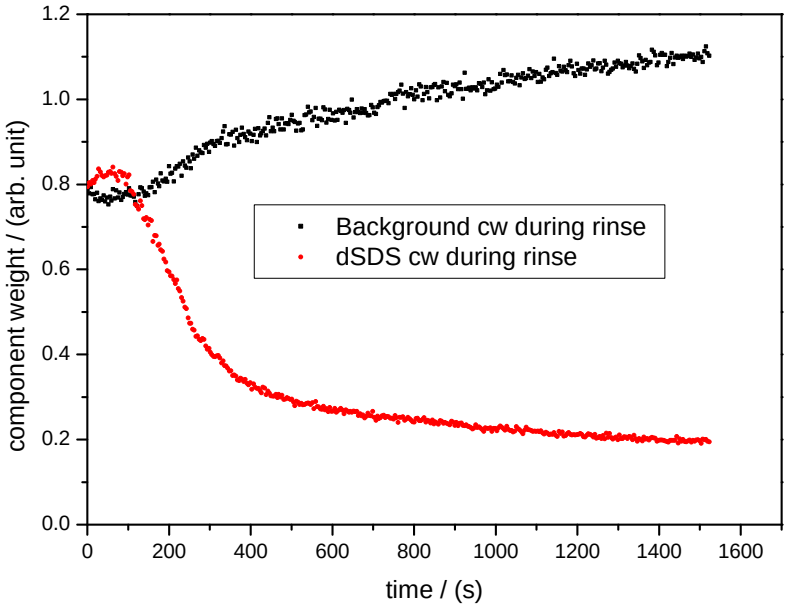

(b)

Figure 5.33: Figures showing the kinetics of (a) partitioning and (b) rinsing of 0.4 mM dSDS with an egg-SM SLB, calculated using TFA from S-polarised spectra. 73° incidence, 32°C, 20 mM tris, pH 7.4.

5.4.5 1:1:1 POPE:egg-SM:chol

There has been much interest in the role and origin of the hypothetical lipid rafts – functionalised lateral heterogeneities in real biological membranes. Part of the suggested evidence for these functional domains stems from the observation that certain fractions of real membranes appear to be insoluble in a selection of cold surfactant solutions. One problem with this concept is the assumption that these fractions correspond to specific laterally ordered domains within the cell membranes of the cell lines being investigated; it is equally plausible that the insoluble phase is generated as a result of the surfactants intrinsic preferences and the binding preferences of different species present in the plasma membrane under study. For this reason investigating the partitioning behaviour of dSDS into an SLB comprising multiple species and cholesterol should be rewarding. I have already followed the interaction of dSDS with POPE and egg-SM; also, it has been shown that monounsaturatedturated PE does not phase separate from detergent resistance fractions.[148] In this section I will follow the partitioning behaviour of dSDS with a 1:1:1 mixture of POPE, egg-SM and cholesterol, whilst examining any structural changes indicated by TIR-Raman and the interaction kinetics. It is important to use egg-SM rather than bovine SM as egg-SM contains long chain fatty acids which are present in DRM fractions extracted from biological membranes.[149]

5.4.5.1 Equilibrium measurements

Figure 5.34 (a) and (b) show subtracted S- and P-polarised spectra for dSDS interacting with the mixed SLB at a number of dSDS concentrations and with rinsing after the 0.1 mM addition. As before, we note the general increase in the dSDS region and decrease in the CH region. Upon rinsing during the 0.1 mM addition we observe the removal of dSDS whilst the amount of lipid at the interface decreases slightly; whereas the S-polarised intensity remains effectively constant, the P-Polarised intensity decreases somewhat – there is slightly less lipid but there is also a decrease in average chain tilt.

Figure 5.35 shows the partitioning data and normalised signal for the dSDS mixed SLB interaction. The degree of binding for a given bulk dSDS concentration was far lower for the mixture than any other SLB system investigated in my study. The saturating mole fraction of dSDS was 0.3, the nearest other system was pure POPC where the value was 0.5. As a result far more lipid remained in the sampled region for any given dSDS concentration used. Having studied both the egg-SM and POPE systems in isolation already, where the dSDS binds strongly in both cases, one possible explanation for the mixed systems behaviour is the strong interaction between the cholesterol and the two lipid species; indeed the interaction of the lipids would have to be stronger for us to observe the reduced dSDS partitioning behaviour. From figure 5.35 it is clear that the surface coverage was effectively constant, this implies that the original mixture, or possibly some ratio of the original species were removed from the interface. Any hypothetical and significant change in the composition of the mixed SLB would be evidenced by changes in the CH region. Examining the spectra in figure 5.34 we see that this is unequivocally not the case; the shape of the spectra are identical – no compositional changes were taking place. The material being removed was of the original composition. This result in many ways could be more interesting than the opposite where one or two of the original components were removed preferentially – the three components have a stronger affinity for each other, than any one component has for dSDS.

Figure 5.36 shows the variation in R_b as a function of total bulk dSDS concentration. For the mixed system we find a linear relationship between R_b and the bulk dSDS concentration. The

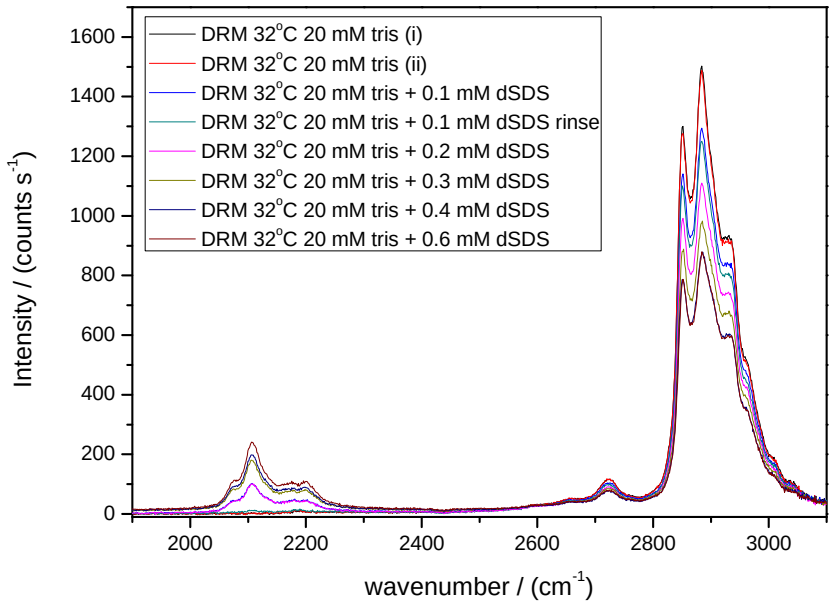

(a)

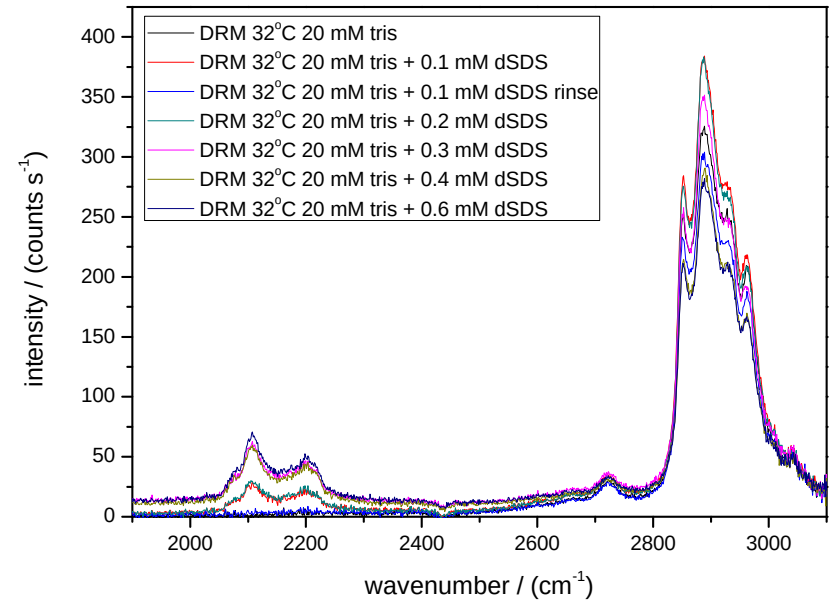

(b)

Figure 5.34: S- and P-polarised TIR-Raman spectra of dSDS interacting with an SLB comprised of 1:1:1 POPE:egg-SM:chol, 73° incidence, 32°C, 20 mM tris pH 7.4.

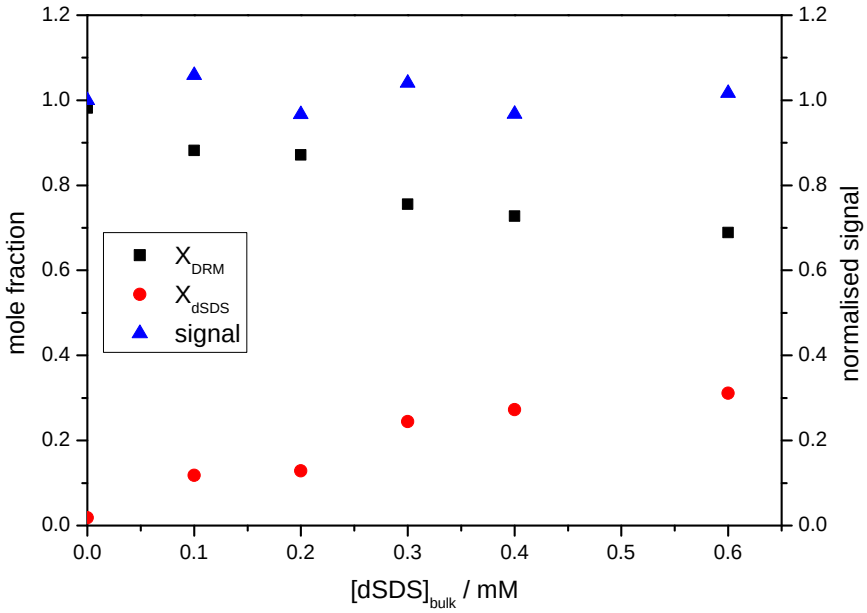

Figure 5.35: A figure showing the partitioning isotherm and total signal variation for dSDS interacting with an SLB comprised of 1:1:1 POPE:egg-SM:chol, 73° incidence, 32°C, 20 mM tris pH 7.4.

value of K_R obtained is 750 M^{-1} ± 100 M^{-1}. Corresponding to a free energy of $\Delta\mu_{dSDS}^{0,aq\rightarrow B}$ = -27.0 kJ mol^{-1} ± 0.3 kJ mol^{-1}. I have not attempted to calculate a theoretical surface charge density for this system as the area per molecule is ambiguous. As a result it is not possible to investigate using the charged surfactant model without more accurate information on the spatial distribution of molecules within the SLB. However, as the relationship between R_b and the bulk dSDS concentration is linear we can determine that as with the other systems investigated, the surface charge is being neutralised.

5.4.5.2 Structure

Figure 5.37 shows the variation in the primary order parameter as a function of dSDS mole fraction. At first, the ratio of the anti-symmetric to symmetric CH stretches decreases as the mole fraction increases. However, at high mole fractions the order parameter increases slightly. This trend is the one I would expect to occur upon partitioning and is in fact the opposite of the trend observed for POPC where the lipid molecules within the SLB become more ordered or the egg-SM system where the trends change depending on the exact point in the partitioning isotherm. The error bars indicate the standard deviation and were calculated from the time series of spectra acquired during the formation of this SLB. The fact that the errors are so small indicate that these changes are significant.

Figure 5.38 shows the change in the symmetric and antisymmetric CH stretch positions as a function of dSDS mole fraction, the values increase as the primary order parameter increases. Here the errors are also very small, the strong correlation between the changes in the order parameter values and the precise peak positions leads me to believe the changes are real.

Figure 5.39 shows the change in average lipid chain tilt as a function of dSDS mole fraction,

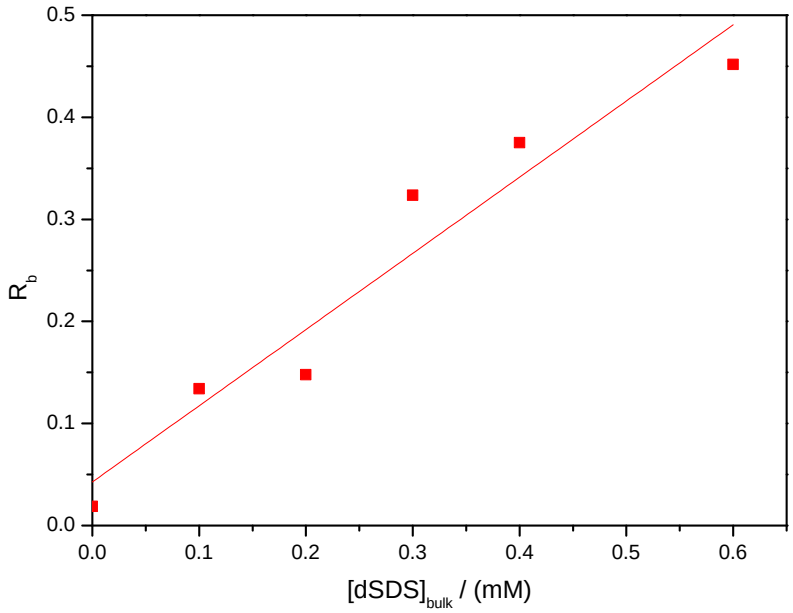

Figure 5.36: A figure showing the mole ratio of dSDS to the SLB mixture as a function of total dSDS concentration.

the data indicate that chain tilt increases with mole fraction. This tilting behaviour was also observed with POPC, however, in that system, the increase went alongside an increase in order. Here it happens with a decrease in order; this implies that the tilting for the mixture is a result of twists and kinks in the tails of the two lipid species.

5.4.5.3 Kinetic measurements

Figure 5.40 (a) and (b) show kinetic partitioning and rinsing data for 0.4 mM dSDS interacting with the mixed SLB. As with the other systems used we observe an initial rapid uptake followed by slower partitioning behaviour that results in saturation. However, the initial rapid uptake for this system appears to end at 0.3 cw which, as a relative proportion of the total, is significantly lower than the other systems – the second slower stage seems to make up the majority of the dSDS component weight increase. Assuming my previous interpretation of the two stage kinetics representing an initial partitioning/rinsing followed by a flip-flop mechanism. The data here indicate that less dSDS was initially partitioning into the outer leaflet for this system in comparison to the other systems investigated. When examining the rinsing behaviour in (b) this system shows a very sharp drop followed by a limited protracted rinsing stage. This indicates that the majority of the dSDS that partitioned was located in the outer leaflet, or was in some way immediately accessible to the water sub-phase. As in the POPC and egg-SM systems we observe another step change in the baseline component weight in this system, except in this system the baseline component weight increases as dSDS partitions. This step increase is again most likely an artefact of the TFA linear combination step owing to the similarities of the baseline and dSDS refined spectra – as we are mostly interested in the qualitative aspects of the data, particularly in terms of the component weight, this does not amount to a problem. As stated previously this

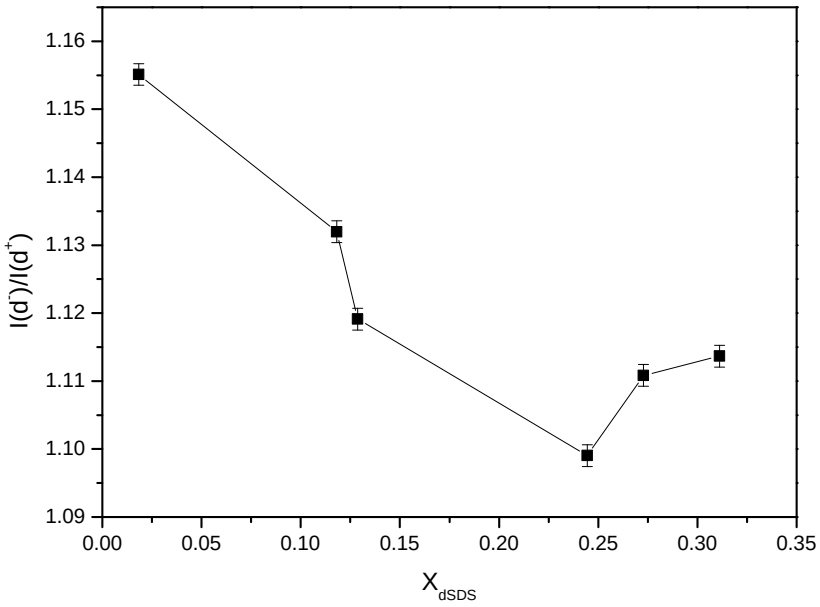

Figure 5.37: A graph showing the primary order parameter as a function of dSDS mole fraction for a 1:1:1 ratio of POPE:egg-SM:chol. 73° incidence, 32°C, 20 mM tris, pH 7.4.

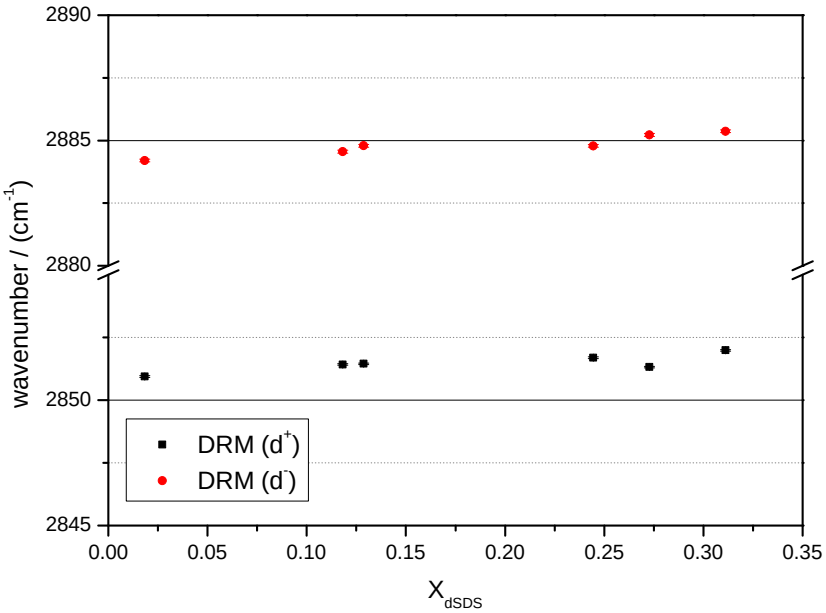

Figure 5.38: A graph showing the positions of the symmetric and antisymmetric CH stretches for an SLB comprised of 1:1:1 POPE:egg-SM:chol, as a function of dSDS mole fraction, 73° incidence, 20 mM tris, pH 7.4.

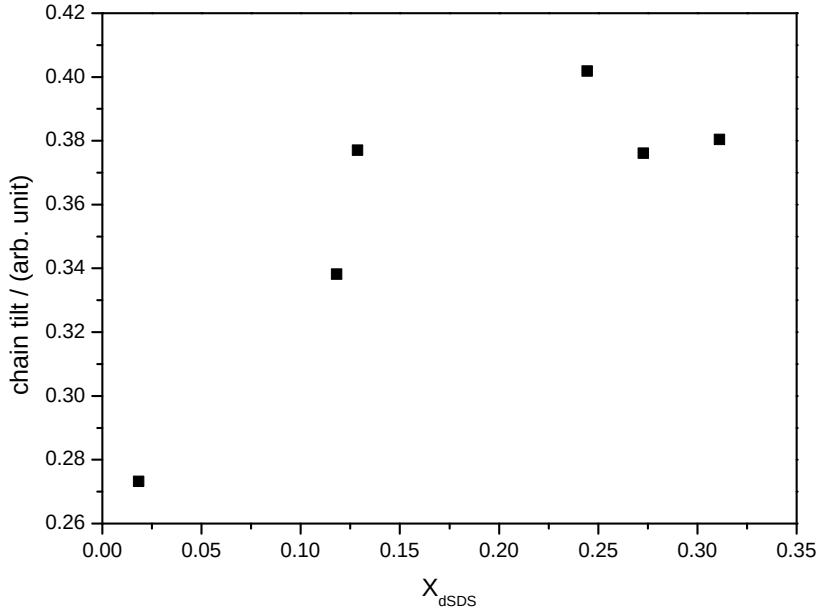

Figure 5.39: A figure showing the variation in average lipid chain tilt as a function of dSDS mole fraction within an SLB comprised of 1:1:1 POPE:egg-SM:chol, 73° incidence, 32°C, 20 mM tris pH 7.4.

problem could be dealt with by including an inert strong Raman marker such as acetonitrile.

5.4.5.4 AFM images

Figures 5.41, 5.42 and 5.43 show three topographic AFM images of the lipid mixture at different experimental stages. In the first, 5.41 (a) we see the SLB prior to dSDS addition, we notice a large number of small bright blobs. Figure 5.41 (b) shows a cross-section of one such blob. My interpretation of these features is that they are trapped, flattened vesicles held within an otherwise complete SLB. Other workers have observed this vesicle trapping behaviour previously.[64] It occurs when the vesicles are unable to rupture owing to limited free volume as an SLB approaches full surface coverage. Figure 5.42 shows the same SLB after the addition of 0.8 mM dSDS. The SLB surface appears to be very similar to that of the pure DRM, there are fewer trapped vesicles, however, we notice the presence of several small pore like defects. This result is in agreement with the isotherm data shown in figure 5.35, which shows very little change in total normalised signal even at the highest measured dSDS concentrations. Figure 5.42 (b) shows two cross-sections of different defects. The defects appear to be on the order of 5 nm deep, this is expected for a single bilayer thickness. Why such defects appear after the addition of the dSDS solution is unclear. Figure 5.43 shows the same system after rinsing, we notice the formation of gaps within the SLB that account for around 30 % of the surface. Other images show regions where there is less coverage and others more; this implies that any recovery behaviour in the Raman data depends on the exact location on the surface. Experiments where we observe high recovery will either be those where the dSDS concentration is low and thus mole fraction is low, or those were we happen to sample a region of high coverage after rinsing. The AFM images presented are at equilibrium and they show no evidence of spontaneous curvature or an unbinding transition. However, as these measurements

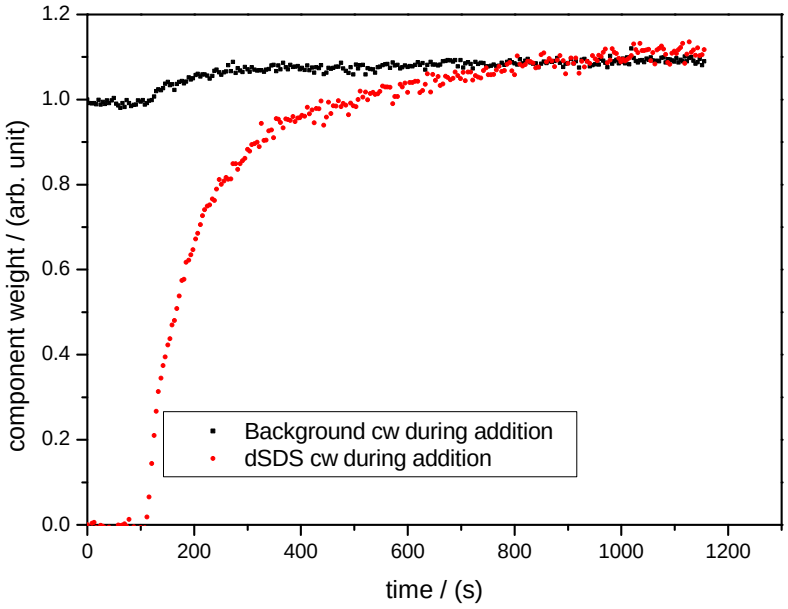

(a)

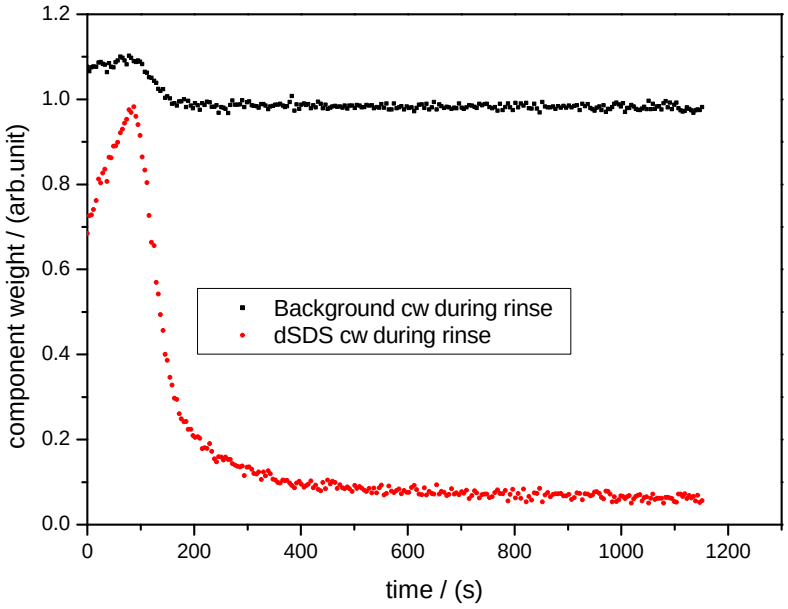

(b)

Figure 5.40: Figures showing the kinetics of (a) partitioning and (b) rinsing of 0.4 mM dSDS with an SLB comprised of a 1:1:1 mixture of POPE:egg-SM:chol, calculated using TFA from S-polarised spectra.

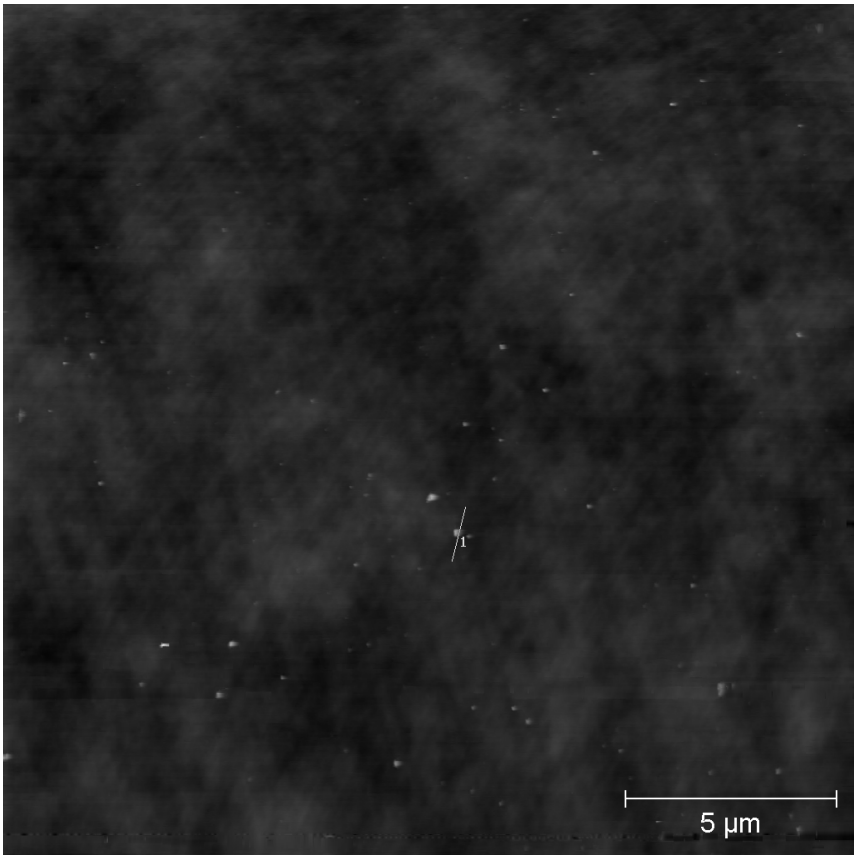

(a)

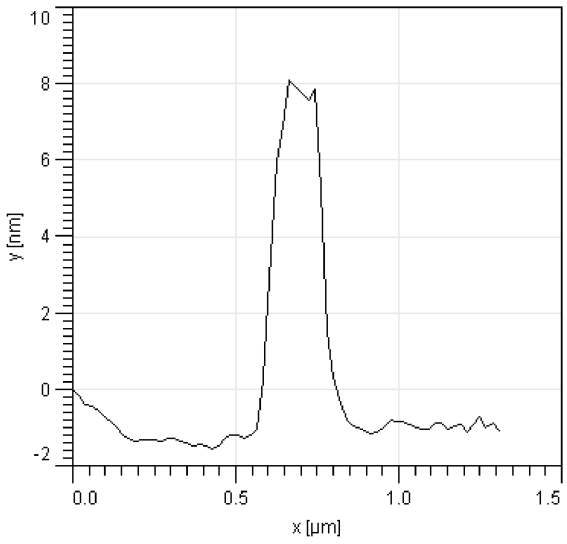

(b)

Figure 5.41: Two sub-figures showing (a) A topographic AFM image showing the 1:1:1 POPE:egg-SM:cholesterol SLB after formation, 32° C, 20 mM tris, pH 7.4. (b) A cross-section of a trapped vesicle.

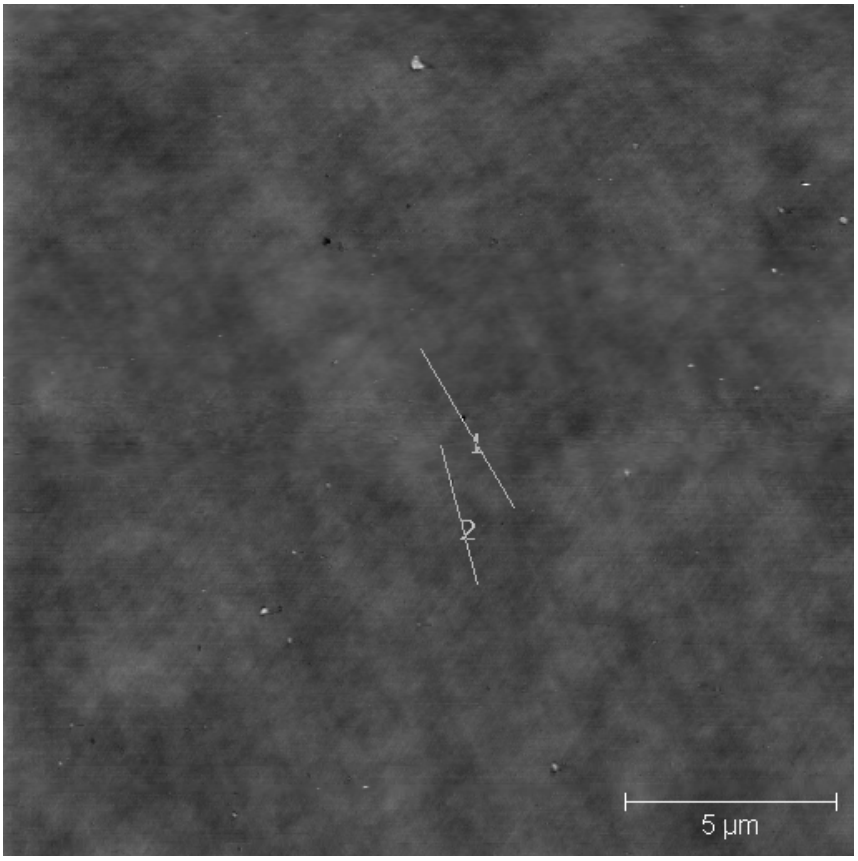

(a)

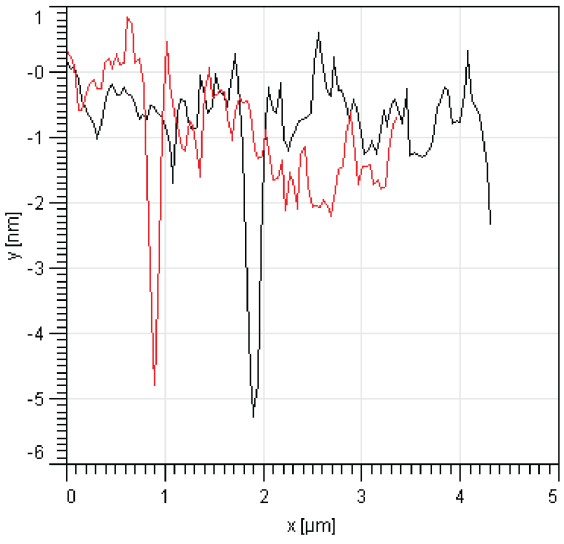

(b)

Figure 5.42: Two sub-figures showing (a) A topographic AFM image showing the 1:1:1 POPE:egg-SM:cholesterol SLB after the addition of 0.8 mM dSDS, 32° C, 20 mM tris, pH 7.4. (b) Two cross-sections of pore-like defects.

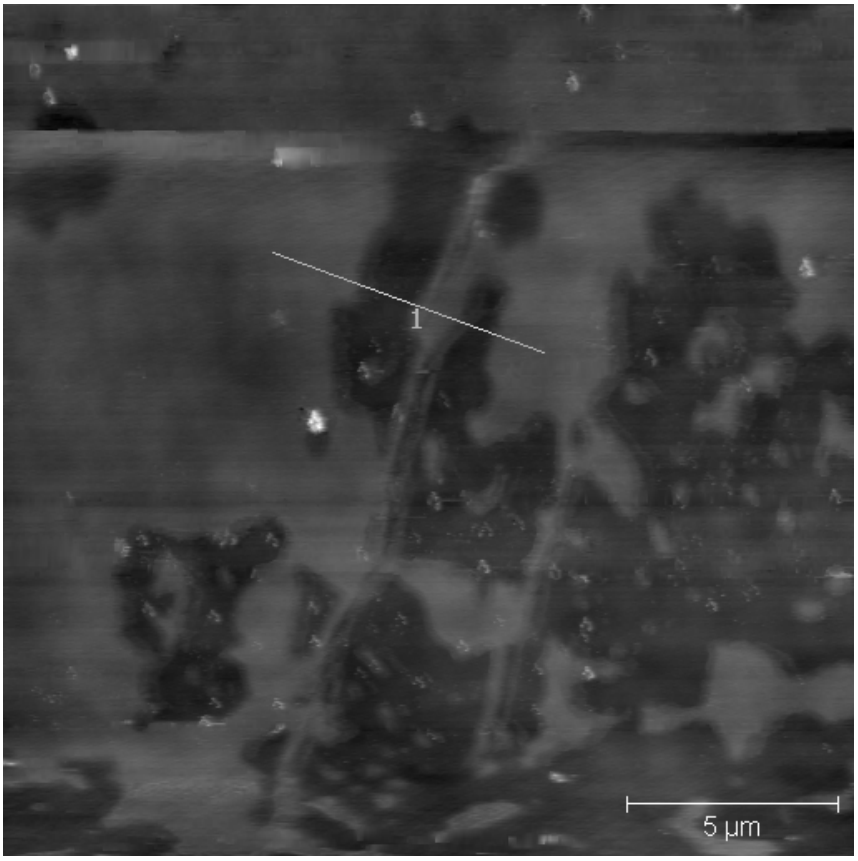

(a)

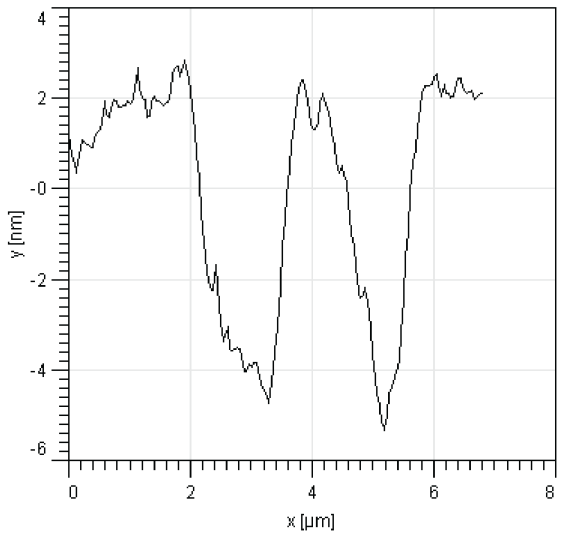

(b)

Figure 5.43: Two sub-figures showing (a) A topographic AFM image showing the 1:1:1 POPE:egg-SM:cholesterol SLB after rinsing following treatment with 0.8 mM dSDS, 32° C, 20 mM tris, pH 7.4. (b) A cross-section of residual patches.

were acquired at equilibrium any spontaneous curvature induced by changes in the distribution of dSDS about the bilayer normal would have been missed. It is worth stating that I observed no lateral phase separation within the SLB in any of the images obtained which compares favourably with the fact that only the intensity in the relevant TIR-Raman spectra fell and the shape of the CH region remained constant after dSDS addition.

5.5 Conclusions

For POPC, the system which I studied most extensively, the greater the number of dSDS additions and subsequent rinses the more dSDS was removed from the substrate. Structural data showed that as the mole fraction of dSDS within the SLB increased, so did the overall lipid order within the bilayer, and the POPC monomers were forced to adopt a tilted configuration. Thermodynamically I found that the best model to fit the data obtained was the simpler non-ideal model that ignores electrostatic effects. This implied that any charge associated with the partitioned dSDS was being effectively neutralised by counterion binding. I found the standard free energy of transfer to be -27.7 kJ mol^{-1} $\pm$ 0.3 kJ mol^{-1} which is similar to that measured by other workers who used ITC. However, some confusion remained as to how the similar value was acquired by using the simpler partitioning model (they took account of surface charge and counterion binding), and why I found it unnecessary for SLB systems to consider surface charge. Also, they were using a different buffer with far greater sodium chloride content, and so there was a difference in standard states. It is likely that the origin of these differences lies in the choice of system (their study was on bulk vesicles). Kinetically, I was able to determine that the the time taken for dSDS to initially partition into the outer SLB leaflet was constant across the concentration regime used. This implied that the rate of partitioning increased with concentration. The second slow-step was interpreted in terms of flip-flop. Using this interpretation, the rate of initial flip-flop depended on the bulk concentration of dSDS and thus the mole fraction of dSDS within the outer leaflet during the process of partitioning; at the lowest concentrations flip-flop seemed not to be occurring. The rinsing behaviour depended on the previous rinsing history, translocation from the proximal monolayer was far slower if the SLB had been rinsed after a previous addition.

In my investigation of the POPE SLB's interaction with dSDS I measured several differences in comparison with POPC. These were interesting owing to the subtle difference in their headgroups. Whereas for POPC removal was based largely on the number of intermediate rinses and whether or not the SLB was saturated, for POPE I observed consistent removal at all surface coverages with added removal with intermediate rinses. I also observed that there was no saturation limit for POPE SLBs within the concentration regime explored – the dSDS mole fraction continued to increase irrespective of the dSDS mole fraction prior to an increase in dSDS concentration. Thermodynamically, the standard free energy of transfer was calculated to be -28.6 kJ mol^{-1} $\pm$ 0.2 kJ mol^{-1} which characterises the difference in dSDS's interaction with PE and PC headgroups. Although less kinetic data is available for the POPE system, I observed very similar behaviour to POPC, a period of rapid dSDS uptake followed by a possible slower flip-flop regime. During rinsing we also see almost identical behaviour to POPC – a fast initial decrease in dSDS component weight, followed by a more gradual decrease, which again was interpreted in terms of a translocation mechanism.

Egg-SM showed equilibrium behaviour more akin to POPC than POPE, although the SLB saturates at a higher dSDS mole fraction. Also, I calculated the standard free energy of partition-

ing to be -32.4 kJ mol^{-1} ± 0.3 kJ mol^{-1} significantly higher than POPC and POPE. Kinetically, again I observed behaviour very similar to that of POPC, two step partitioning and removal, with the slower steps very likely corresponding to flip-flop to and from the inner SLB leaflet.

For the POPE:egg-SM:Cholesterol mixture, I have found that despite the previously measured preferences of both egg-SM and POPE for dSDS the mixed SLB shows are very weak affinity for dSDS. This SLB reaches saturation at a dSDS mole fraction of approximately 0.3. This can only come about as a result of the stronger interactions of these components with each other than with dSDS. I found that the standard free energy of transfer of this system to be -27.0 kJ mol^{-1} ± 0.3 kJ mol^{-1} which is the smallest of the systems investigated. Kinetically this system showed similar behaviour to the other systems, but the extent of initial partitioning was lower. AFM images allowed me to confirm that there were very limited mesocopic structural changes taking place after dSDS had been incorporated, but on rinsing large areas of bare silica were opened up. Overall the data for this system clarifies the idea that certain mixtures of lipids and cholesterol show a reduced saturation R_b value where the individual components show much higher values. These data support the idea that membrane regions comprised of these mixtures could be separated independently from the bulk lipid matrix. Lastly the fact that the mole ratio of the original mixture's components remained constant despite the partitioning of dSDS supports the idea that dSDS does not dynamically alter the mixed SLBs composition during the interaction.

Throughout this chapter some problems were described. I will briefly summarise the most important here in the context of future work. Probably the most important problem is that concerning the normalisation of the kinetic data acquired from the CD stretching region of the spectrum. Here the baseline component was found to mix with that of dSDS during the linear combination step of the TFA analysis. It was stated in the text that some inert marker would need to be included in future measurements to enable normalisation and allow quantitative analysis of the kinetic data where this mixing occurs. Another possible extension of this project could be a detailed look at the binary mixture of egg-SM and cholesterol in order to gain a greater understanding of the interesting PE:egg-SM:chol system investigated here. In some of my last experiments I found it impossible to prepare quality SLBs of POPE and cholesterol in a 2:1 mixture by the vesicle fusion method. The interface was found to support large aggregates that clearly did not resemble an SLB. However, perhaps an alternative method to prepare and SLB of this mixture could be found.

Appendices

Appendix A

TIR-Raman spectra of phase transitions

This appendix includes the subtracted temperature dependant TIR-Raman spectra of SLB phase transitions not included in Chapter 4 but necessary for completeness. The data are ordered systematically according to lipid system and buffer solution composition.

A.1 DMPC

A.1.1 20 mM tris pH 7.4

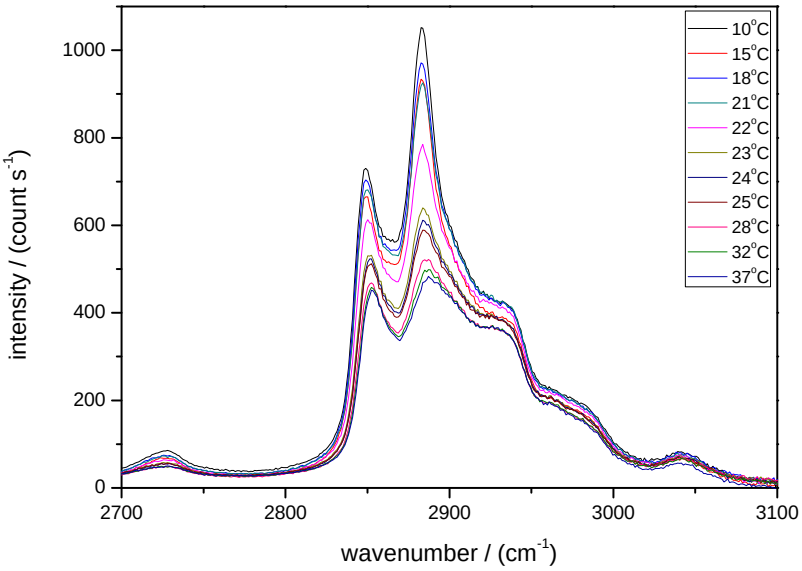

(a)

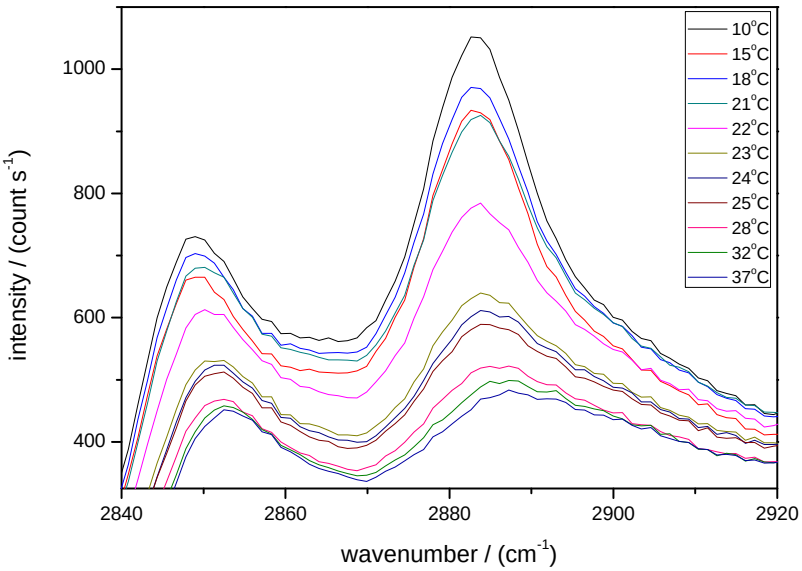

(b)

Figure A.1: Temperature dependent S-polarised TIR-Raman spectra of a DMPC SLB on SiO_2 in 20 mM tris pH 7.4. 800 mW laser output power, 73° incidence, unpolarised detection (a) full CH stretching region (b) closeup of symmetric and anti-symmetric stretches.

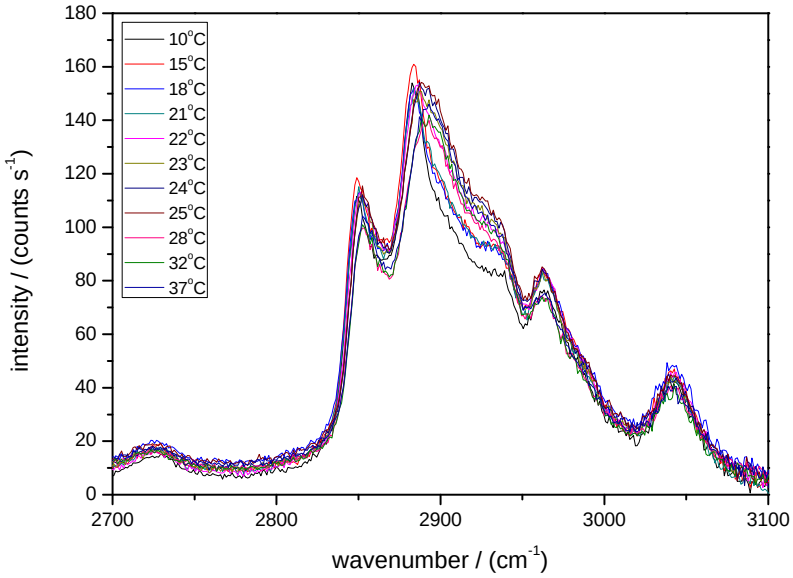

(a)

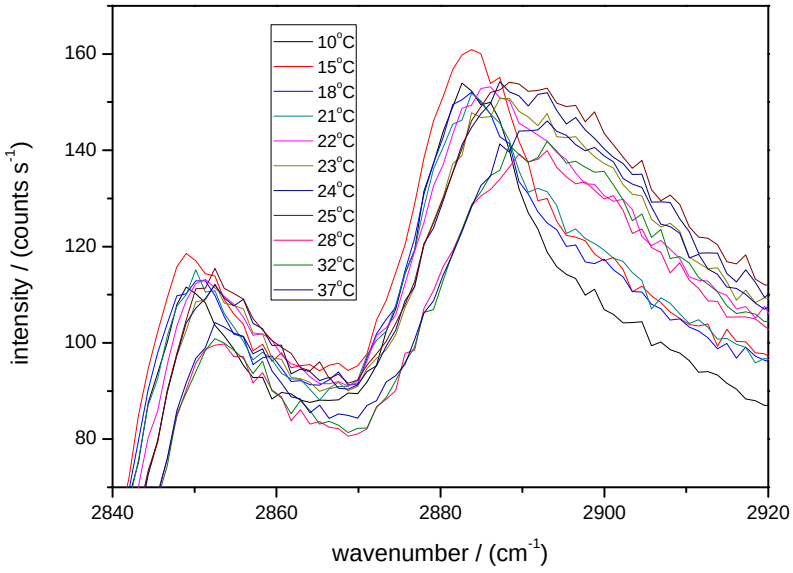

(b)

Figure A.2: Temperature dependent P-polarised TIR-Raman spectra of a DMPC SLB on SiO_2 in 20 mM tris pH 7.4. 800 mW laser output power, 73° incidence, unpolarised detection (a) full CH stretching region (b) closeup of symmetric and anti-symmetric stretches.

A.1.2 20 mM tris pH 7.4 + 100 mM NaCl

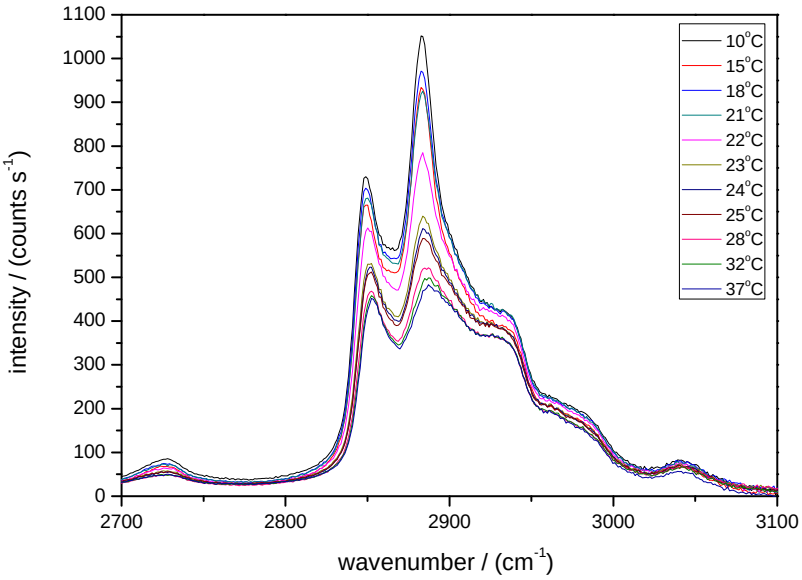

(a)

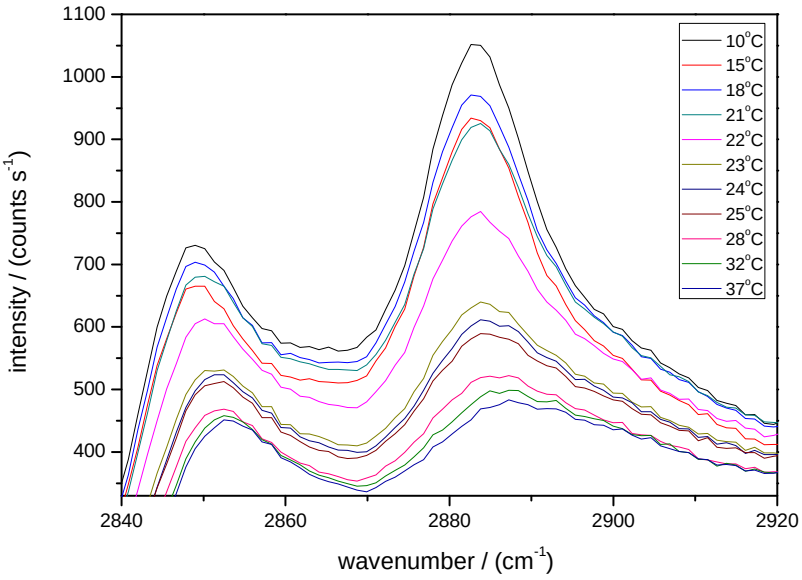

(b)

Figure A.3: Temperature dependent S-polarised TIR-Raman spectra of a DMPC SLB on SiO_2 in 20 mM tris pH 7.4 + 100 mM NaCl. 800 mW laser output power, 73° incidence, unpolarised detection (a) full CH stretching region (b) closeup of symmetric and anti-symmetric stretches.

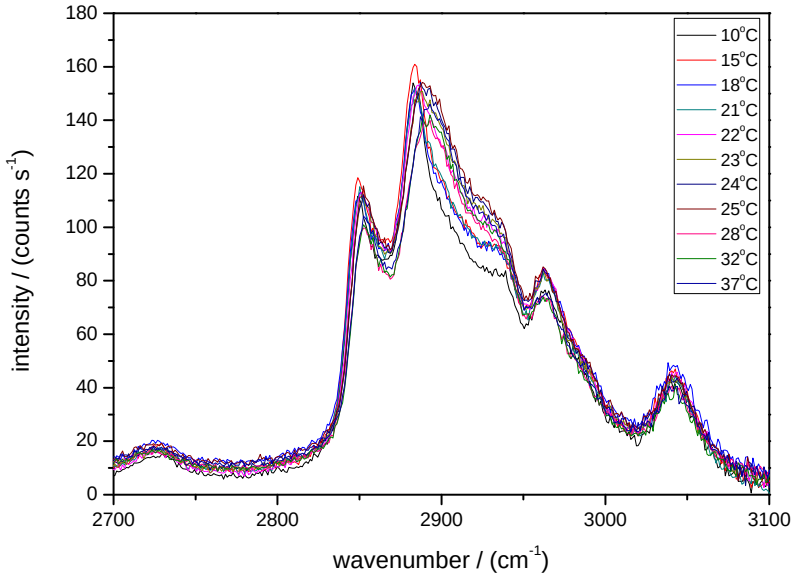

(a)

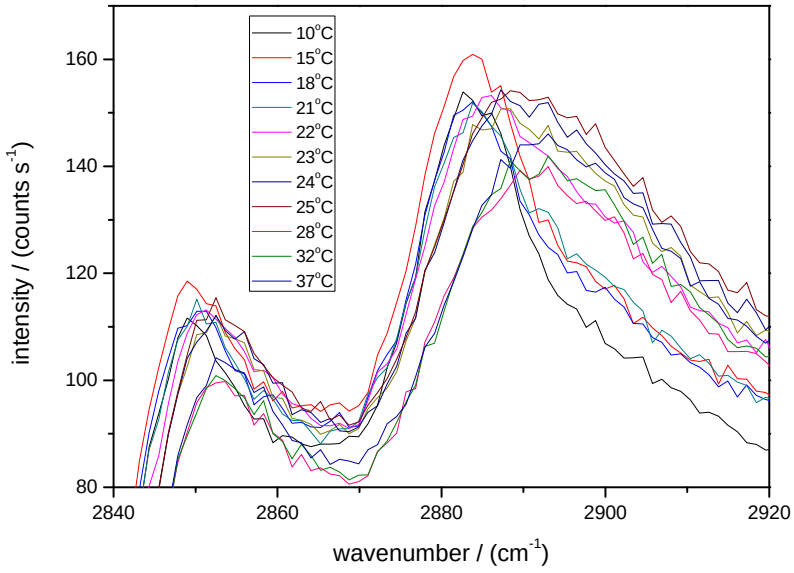

(b)

Figure A.4: Temperature dependent P-polarised TIR-Raman spectra of a DMPC SLB on SiO_2 in 20 mM tris pH 7.4 + 100 mM NaCl. 800 mW laser output power, 73° incidence, unpolarised detection (a) full CH stretching region (b) closeup of symmetric and anti-symmetric stretches.

A.2 POPE

A.2.1 20 mM tris pH 7.4

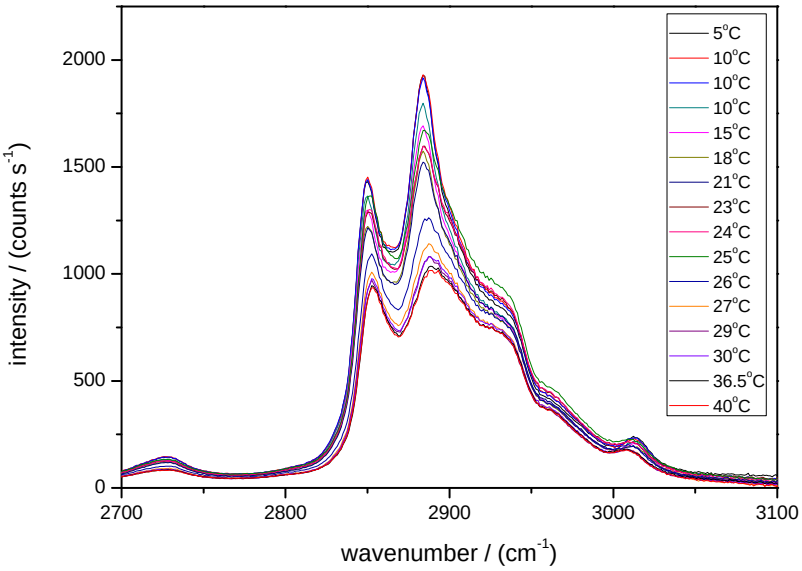

(a)

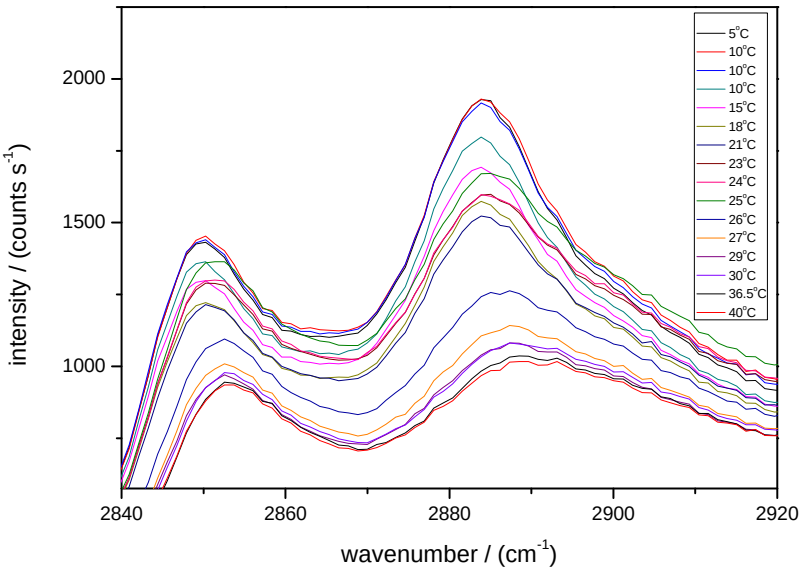

(b)

Figure A.5: Temperature dependent S-polarised TIR-Raman spectra of a POPE SLB on SiO_2 in 20 mM tris pH 7.4. 800 mW laser output power, 73° incidence, unpolarised detection (a) full CH stretching region (b) closeup of symmetric and anti-symmetric stretches.

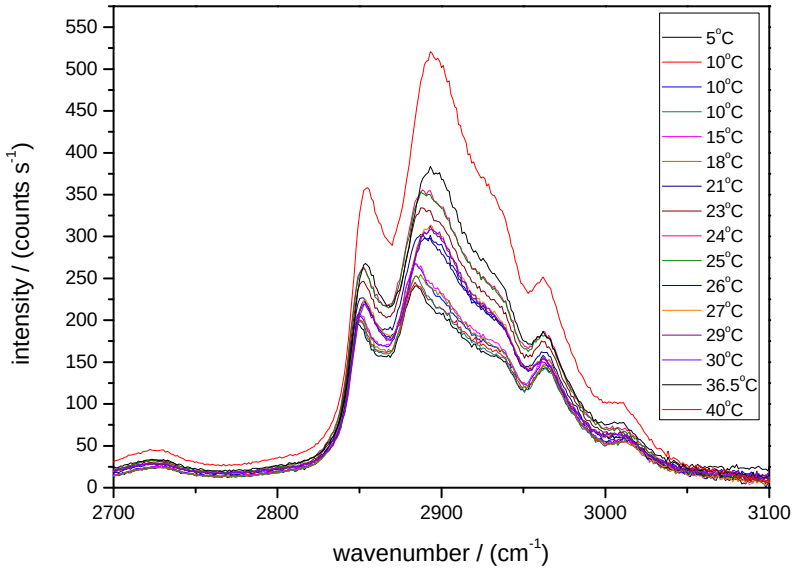

(a)

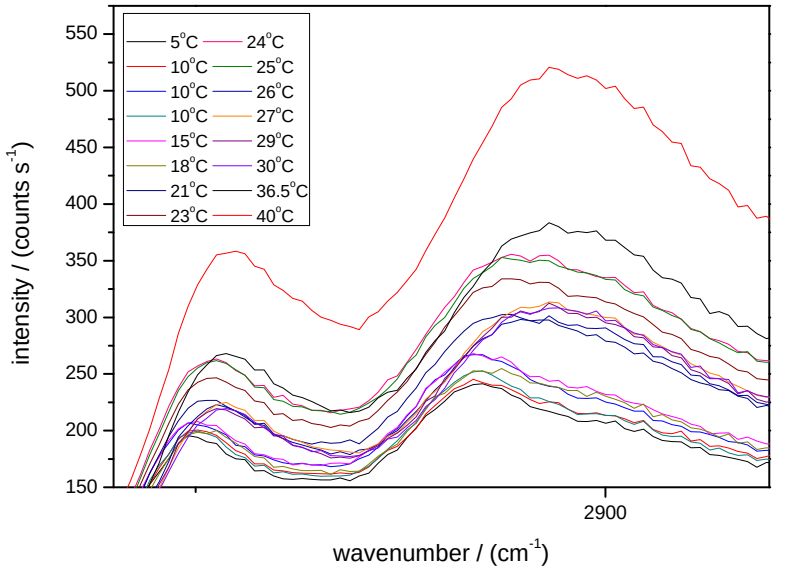

(b)

Figure A.6: Temperature dependent P-polarised TIR-Raman spectra of a POPE SLB on SiO_2 in 20 mM tris pH 7.4. 800 mW laser output power, 73° incidence, unpolarised detection (a) full CH stretching region (b) closeup of symmetric and anti-symmetric stretches.

A.2.2 20 mM tris pH 7.4 + 100 mM NaCl

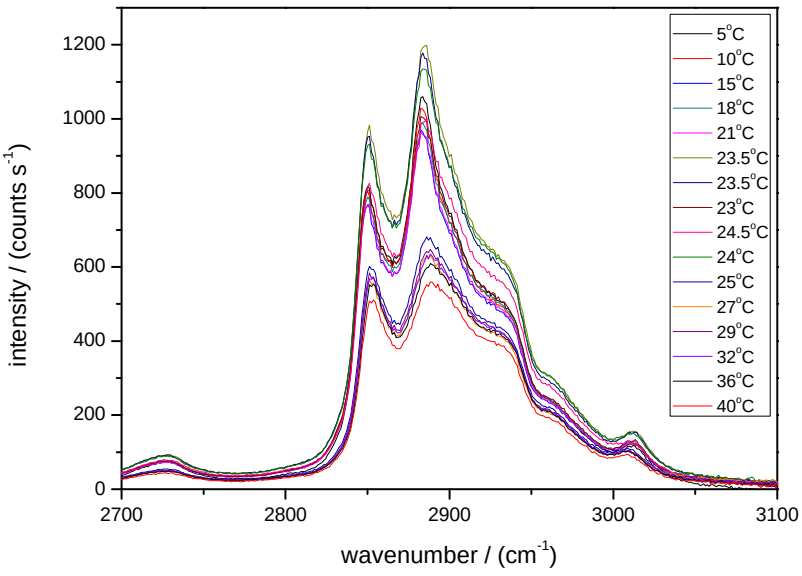

(a)

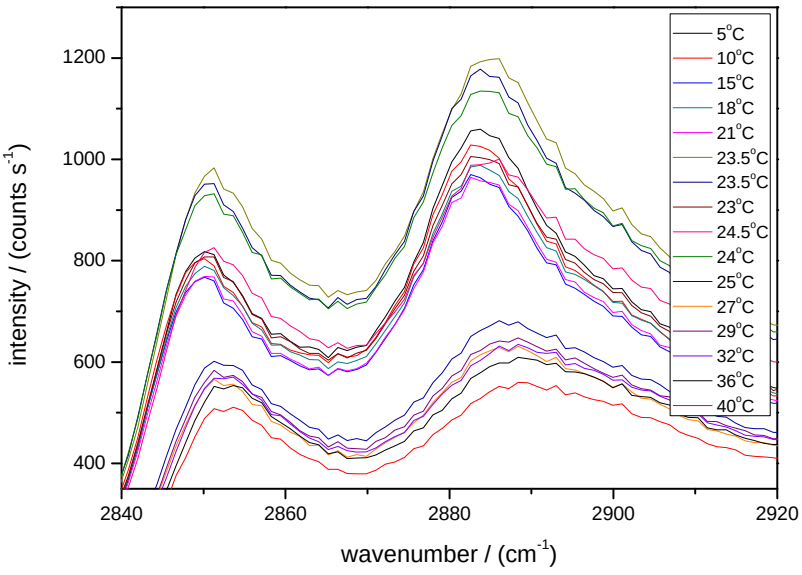

(b)

Figure A.7: Temperature dependent S-polarised TIR-Raman spectra of a POPE SLB on SiO_2 in 20 mM tris pH 7.4 + 100 mM NaCl. 800 mW laser output power, 73° incidence, unpolarised detection (a) full CH stretching region (b) closeup of symmetric and anti-symmetric stretches.

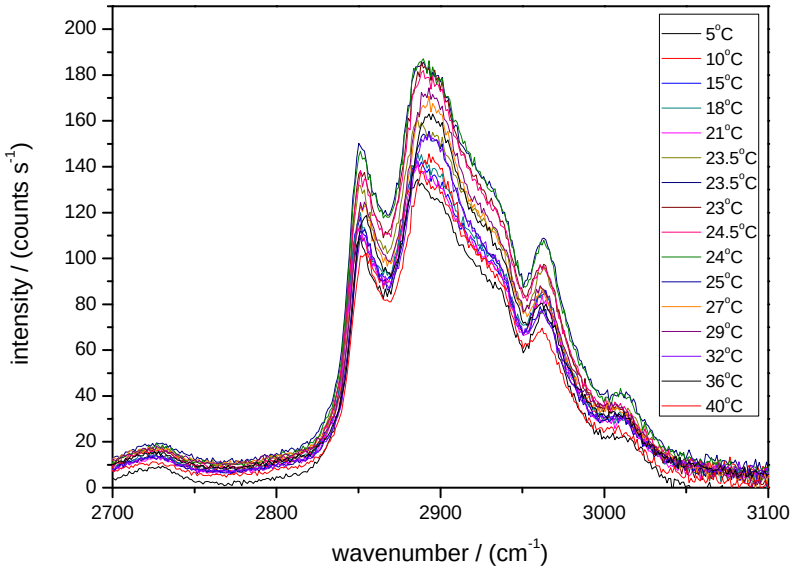

(a)

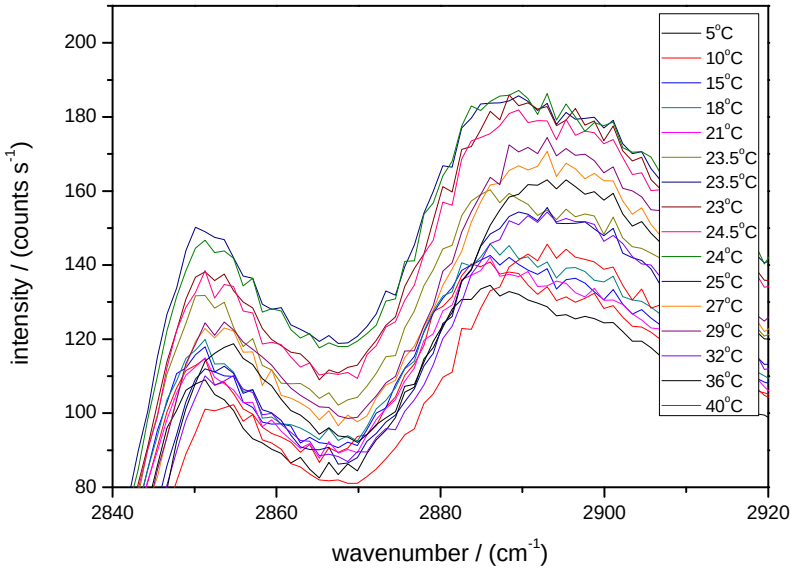

(b)

Figure A.8: Temperature dependent P-polarised TIR-Raman spectra of a POPE SLB on SiO_2 in 20 mM tris pH 7.4 + 100 mM NaCl. 800 mW laser output power, 73° incidence, unpolarised detection (a) full CH stretching region (b) closeup of symmetric and anti-symmetric stretches.

A.3 Egg-SM

A.3.1 20 mM tris pH 7.4

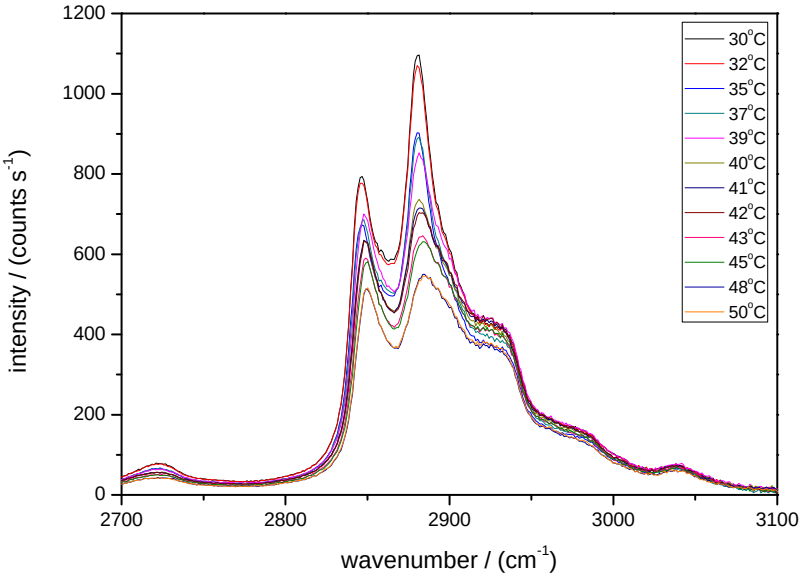

(a)

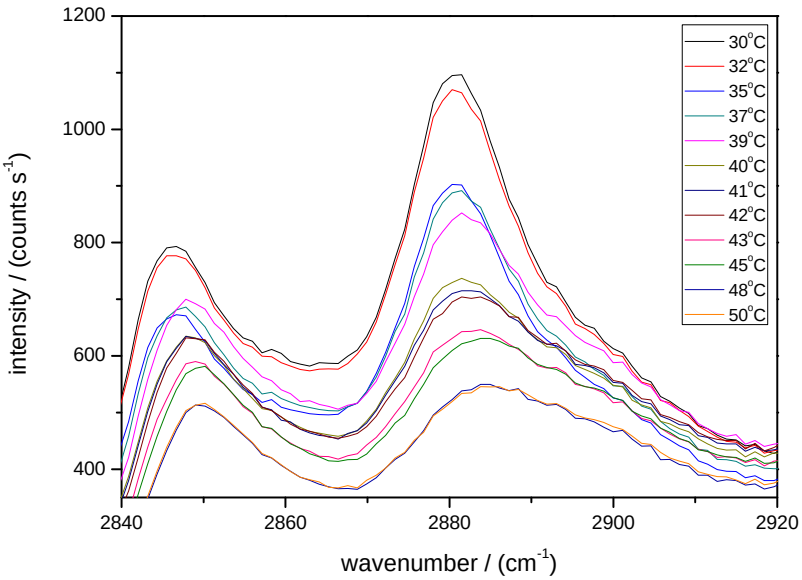

(b)

Figure A.9: Temperature dependent S-polarised TIR-Raman spectra of an egg-SM SLB on SiO_2 in 20 mM tris pH 7.4. 800 mW laser output power, 73° incidence, unpolarised detection (a) full CH stretching region (b) closeup of symmetric and anti-symmetric stretches.

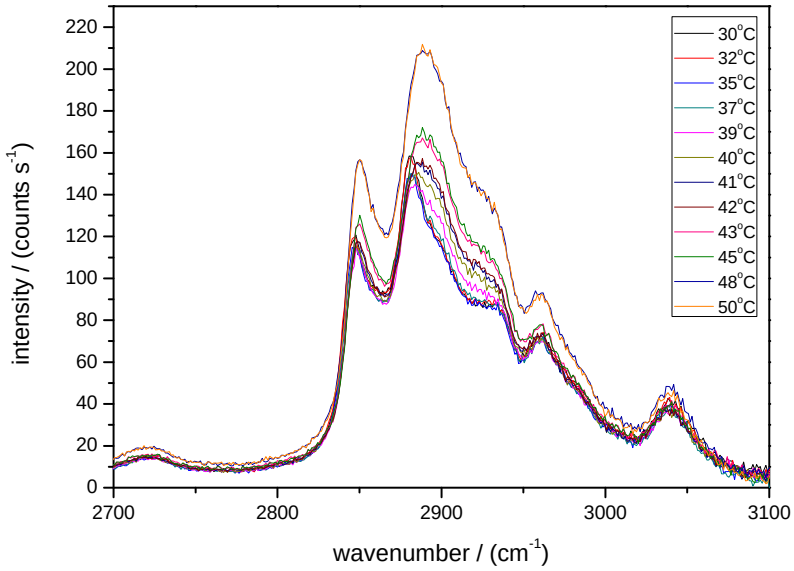

(a)

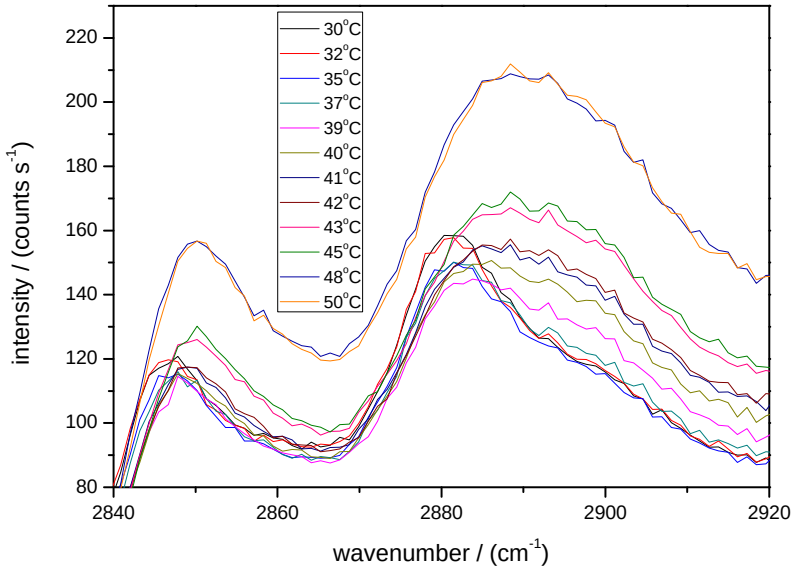

(b)

Figure A.10: Temperature dependent P-polarised TIR-Raman spectra of a POPE SLB on SiO_2 in 20 mM tris pH 7.4. 800 mW laser output power, 73° incidence, unpolarised detection (a) full CH stretching region (b) closeup of symmetric and anti-symmetric stretches.

A.3.2 20 mM tris pH 7.4 + 100 mM NaCl

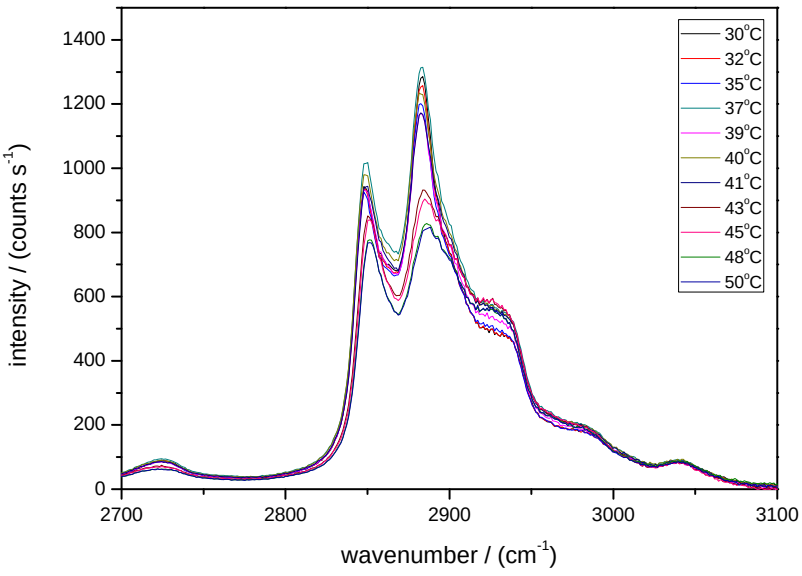

(a)

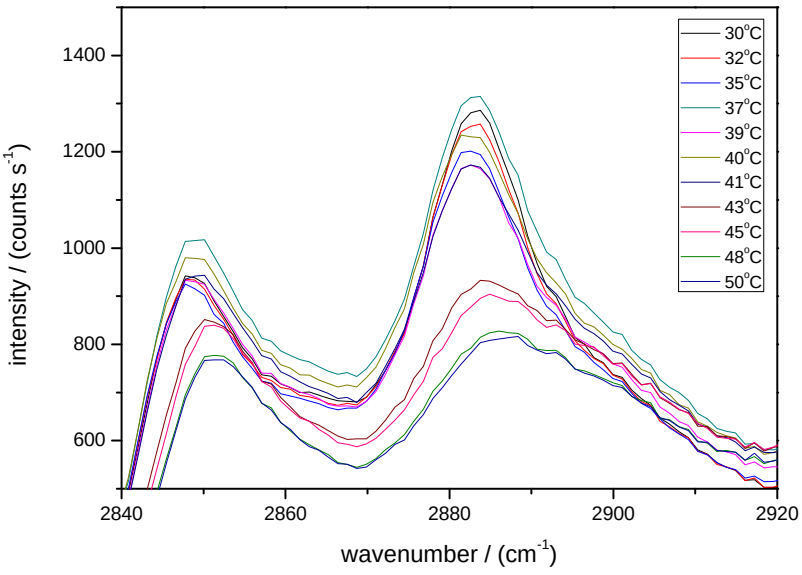

(b)

Figure A.11: Temperature dependent S-polarised TIR-Raman spectra of a POPE SLB on SiO_2 in 20 mM tris pH 7.4 + 100 mM NaCl. 800 mW laser output power, 73° incidence, unpolarised detection (a) full CH stretching region (b) closeup of symmetric and anti-symmetric stretches.

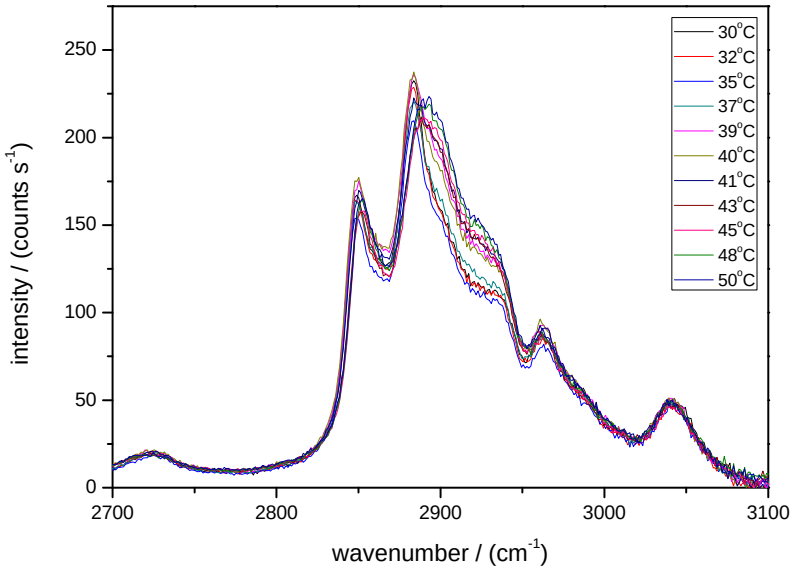

(a)

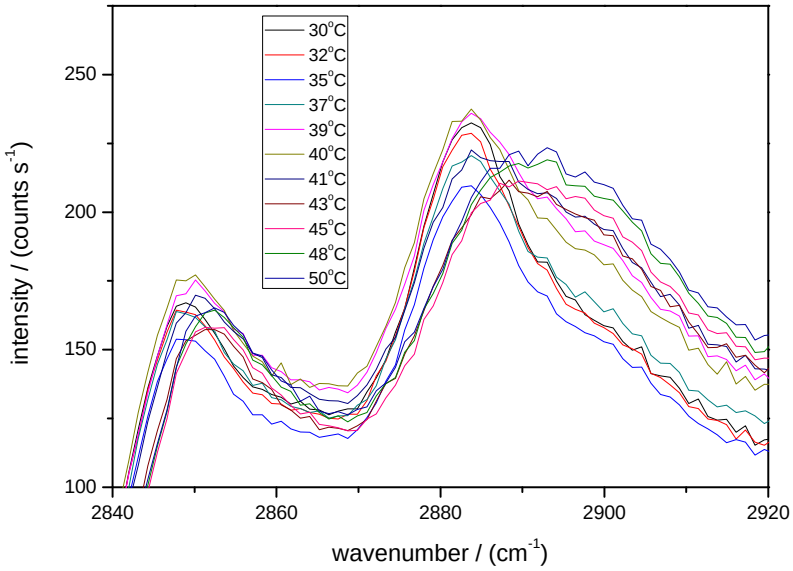

(b)

Figure A.12: Temperature dependent P-polarised TIR-Raman spectra of a POPE SLB on SiO_2 in 20 mM tris pH 7.4 + 100 mM NaCl. 800 mW laser output power, 73° incidence, unpolarised detection (a) full CH stretching region (b) closeup of symmetric and anti-symmetric stretches.

Appendix B

Matlab Code

B.1 SLB formation - vesicle fusion

B.1.1 Target factor analysis

The TFA programs used throughout my studies were modifications of programs originally developed by Malinowski.[42] These modifications were carried out by Woods to enhance speed.[150]

B.1.2 Background subtraction

```
%Function bcksub removes a weighted background from an array of n spectra
%Due to the slow degradation of sample alignment signal levels are lost
%Background subtraction has to take this into account.

function [dsub] = bcksub(data)
d=data(2:end,2:end).';
bck=d(:,1);
f=bck(1,1)./d(1,:);
fy=f./f;
bcks=bck*fy;
dg=diag(f);
ds=d*dg;
dsub=ds-bcks;
end
```

B.1.3 Order parameter extraction

```
%MULTIPOLY : A Program to analyse time series  TIR-Raman data; it returns
%the primary order parameter, the ratio of the antisymmetric CH stretch to the
%symmetric stretch and the positions of both these peaks. Also integrates each
%spectrum, provided they are of the CH region only; this contains the raw and
%averaged data if used. Averaging can be avoided by entering 1 at the relevant
%prompt.
```

```
%First prompt asks for the number of spectra to average over (useful for
%noisy short time step data).

%Second prompt is a graph and crosshair to select the spectral ranges to
%fit the two peaks with polynomials, click from right to left, higher index
%to lower (smaller wave number to higher) otherwise program won't function
%correctly.

%Was built in... and with the following toolpacks.
%--------------------------------------------------------------------------
%MATLAB Version: 7.14.0.739 (R2012a) MATLAB License Number: STUDENT
%Operating System: Mac OS X  Version: 10.8.1 Build: 12B19 Java Version:
%Java 1.6.0_35-b10-428-11M3811 with Apple Inc. Java HotSpot(TM) 64-Bit
%Server VM mixed mode
%--------------------------------------------------------------------------
%(R2012a) MATLAB                                        Version 7.14
%(R2012a) Simulink                                      Version 7.9
%(R2012a) Control System Toolbox                        Version 9.3
%(R2012a) Curve Fitting Toolbox                         Version 3.2.1
%(R2012a) DSP System Toolbox                            Version 8.2
%(R2012a) Image Processing Toolbox                      Version 8.0
%(R2012a) Optimization Toolbox                          Version 6.2
%(R2012a) Signal Processing Toolbox                     Version 6.17
%(R2012a) Simulink Control Design                       Version 3.5
%(R2012a) Statistics Toolbox                            Version 8.0
%(R2012a) Symbolic Math Toolbox                         Version 5.8


function [idmidp,posa,posb,intb,trav,trar]=multipoly(data,dsub)
sizedsubinit=size(dsub,2);
inta=trapz(dsub);
figure(2)
plot(inta);
[xdt,ydt]=ginput(1);
xdtr=round(xdt);

dsub=dsub(:,xdtr:end);
dsub=sgolayfilt(dsub,3,11);

xdtro=xdtr-1;
%xdtrt=xdtr+1;
display(xdtro)

diff=sizedsubinit-xdtro;
display(diff)

%figure(3)
%plot(inta)
%[x3]=ginput(1);
%x3r=round(x3);
%dsub=dsub(:,x3r:end);

spcremar=inputdlg('Number of spectra to remove');
spcrem=str2double(spcremar);
szdsub=size(dsub,2);
display(szdsub)
dsubred=szdsub-spcrem;
display(dsubred)
dsubredpo=(dsubred+1+xdtro);
```

```
display(dsubredpo)

dsub=dsub(:,1:dsubred);
szdsub2=size(dsub,2);
display(szdsub2)

avnar=inputdlg('Number of spectra to average?');
avn=str2double(avnar);


dsubar=mat2cell(dsub,size(dsub,1),avn*ones(1,(size(dsub,2)./avn)));
om=2*ones(1,(size(dsub,2)./avn));
omar=mat2cell(om,size(om,1),ones(1,size(om,2)));
dsubavar=cellfun(@mean,dsubar,omar,'UniformOutput',false);
d=cell2mat(dsubavar);
figure(3)
plot(d);

xdtrpo=xdtr+1;
display(xdtrpo);

tr=data(xdtrpo:dsubredpo,1).';
sztr=size(tr,2);
display(sztr)
trar=mat2cell(tr,size(tr,1),avn*ones(1,size(tr,2)./avn));
trarav=cellfun(@mean,trar,omar,'UniformOutput',false);
trav=cell2mat(trarav);


intb=trapz(d);
figure(4);
hold on
scatter(trav,intb,35,'filled');

%dsubar=mat2cell(dsub,size(dsub,1),5*ones(1,(size(dsub,2)./5)));
%dsubavar=cellfun(@mean,dsubavar);
%dsubav=cell2mat(dsubavar);

%multipoly is a MATLAB function designed to facilitate the analysis
%of CH stretching region vibrational spectra. It calcualtes the various
%order parameters over large datasets.

WN=data(1,2:end).';
o=ones(1,size(d,2));
WNex=WN*o;

%Prepares a suitably sized array of integers representing the polynomial
%order for polyfit.

ord=4*ones(1,size(d,2));
orda=mat2cell(ord,size(ord,1),ones(1,size(ord,2)));

%generates a figure showing a sample spectrum from the series, change the
%column index in the line plot... to change the sample spectrum to the
%"right" one for a given data set.

figure(5)
plot(d(:,50));
[x1]=ginput(2);
```

```
x1r=round(x1);

%assigns index references to variables.

f=x1r(2,1);
g=x1r(1,1);
n=f:g;

%generates the data cellarray for fitting of peak 1, i.e. a cell array,
%each cell containing a column representing a section of a spectrum in the
%data series.

da=d(n,:);
DA1=mat2cell(da,size(da,1),ones(1,size(da,2)));
WNA1=WNex(n,:);

%some more index reference variable assinments.

a=WNA1(end,1);
b=WNA1(1,1);

%generation of interpolated wavenumber data for the function polyval, and
%conversion into a cell array, for use with cellfun.

WNINTA1=(a:0.001:b).';
WNINTA1ex=WNINTA1*o;
WNINTA1exa=mat2cell(WNINTA1ex,size(WNINTA1ex,1),ones(1,size(WNINTA1ex,2)));

%generates the cell array of actual wavenumbers for polyfit.

WNA1a=mat2cell(WNA1,size(WNA1,1),ones(1,size(WNA1,2)));

%polynomial fitting of peak 1 for each spectrum in series.
[A1,S1,mu1]=cellfun(@polyfit,WNA1a,DA1,orda,'UniformOutput',false);

%generation of interpolated value pairs for each polynomial fit, plus the
%associated delta error values.
[A1Va]=cellfun(@polyval,A1,WNINTA1exa,S1,mu1,'UniformOutput',false);

%conversion of polynomial value data from cell array to matrix.
A1Vm=cell2mat(A1Va);

%plot of fit data for peak 1.
figure(6)
plot(WNINTA1,A1Vm)


%finding the peak position and intensities from fits.
[pksdp,locs1]=cellfun(@findpeaks,A1Va,'UniformOutput',false);
pksdpm=cellfun(@mean,pksdp);
locs1m=cellfun(@nanmean,locs1);
locs1m(isnan(locs1m))=1;
locs1mr=round(locs1m);
%display(locs1mr)

%locs1mr=abs(locs1mr);

posa=WNINTA1(locs1mr,1);
```

```
%idp=cell2mat(pksdpm);

%-------------------------------------------------------------------
% following section is a repeat of section 1 for peak 2.
%-------------------------------------------------------------------

figure(5)
plot(d(:,50));
[x2]=ginput(2);
x2r=round(x2);

u=x2r(2,1);
k=x2r(1,1);
m=u:k;

db=d(m,:);
DA2=mat2cell(db,size(db,1),ones(1,size(db,2)));
WNA2=WNex(m,:);

c=WNA2(end,1);
u=WNA2(1,1);

WNINTA2=(c:0.001:u).';
WNINTA2ex=WNINTA2*o;
WNINTA2exa=mat2cell(WNINTA2ex,size(WNINTA2ex,1),ones(1,size(WNINTA2ex,2)));

WNA2a=mat2cell(WNA2,size(WNA2,1),ones(1,size(WNA2,2)));
[A2,S2,mu2]=cellfun(@polyfit,WNA2a,DA2,orda,'UniformOutput',false);

[A2Va]=cellfun(@polyval,A2,WNINTA2exa,S2,mu2,'UniformOutput',false);

A2Vm=cell2mat(A2Va);

figure(7)
plot(WNINTA2,A2Vm);

[pksdm,locs2]=cellfun(@findpeaks,A2Va,'UniformOutput',false);
pksdmm=cellfun(@mean,pksdm);
locs2m=cellfun(@nanmean,locs2);
locs2m(isnan(locs2m))=1;
locs2mr=round(locs2m);
%locs2mr=abs(locs2mr);

posb=WNINTA2(locs2mr,1);

%idm=cell2mat(pksdmm);
%-------------------------------------------------------------------
%-------------------------------------------------------------------

%calculation of I(dm)/I(dp) for the two peaks of interest!

idmidp=pksdmm./pksdpm;

%idmidpsm=smooth(idmidp,5,'moving');

%locs1msm=smooth(locs1m,5,'moving');
%locs2msm=smooth(locs2m,5,'moving');
```

```
%scatter plot of I(dm)/I(dp) data.
figure(8)
scatter(trav,idmidp);

figure(9)
scatter(trav,posa);
hold on
scatter(trav,posb);
end
```

B.2 Phase transitions

B.2.1 Background subtraction

```
%A simple function to subtract backgrounds from TIR—Raman spectra arranged
%as column vectors. Requires no input of wavenumber data, assumes the
%wavenumber range is identical for all spectra; such as that
%obtained from a single experiment after calibration. Uses the first data
%point in each spectrum and relavant background to determine the subtraction factor.

function [dsub1,dsub2]=bcksubpt(data1,bcks1,data2,bcks2)
f1=bcks1(1,:)./data1(1,:);
f1=diag(f1);
d1=data1*f1;
dsub1=d1—bcks1;

f2=bcks2(1,:)./data2(1,:);
f2=diag(f2);
d2=data2*f2;
dsub2=d2—bcks2;

figure(11)
plot(dsub1)

figure(12)
plot(dsub2);

end
```

B.2.2 Order parameter extraction

```
%A program to take subtracted spectra (SPOL and PPOL) of a
%phase transition and acquire order parameter data for this.

function [idmidp,posa,posb,ct]=ptorder(dsubS,dsubP,WN)
intspol=trapz(dsubS);
intppol=trapz(dsubP);
ct=intppol./intspol

figure(1)
plot(ct);
```

```
ord=4*ones(1,size(dsubS,2));
orda=mat2cell(ord,size(ord,1),ones(1,size(ord,2)));

figure(2)
plot(dsubS(:,1));
[x1]=ginput(2);
x1r=round(x1);

f=x1r(2,1);
g=x1r(1,1);
n=f:g;

o=ones(1,size(dsubS,2));

WN=WN*o;

dred1=dsubS(n,:);
DRED1A=mat2cell(dred1,size(dred1,1),ones(1,size(dred1,2)));
WNA1=WN(n,:);

a=WNA1(end,1);
b=WNA1(1,1);

WNINTA1=(a:0.001:b).';
WNINTAex=WNINTA1*o;
WNINTA1exa=mat2cell(WNINTAex,size(WNINTAex,1),ones(1,size(WNINTAex,2)));

WNA1a=mat2cell(WNA1,size(WNA1,1),ones(1,size(WNA1,2)));

[A1,S1,mu1]=cellfun(@polyfit,WNA1a,DRED1A,orda,'UniformOutput',false);

[A1Va]=cellfun(@polyval,A1,WNINTA1exa,S1,mu1,'UniformOutput',false);

A1Vm=cell2mat(A1Va);

figure(3)
plot(WNINTA1,A1Vm)

[pksdp,locs1]=cellfun(@findpeaks,A1Va,'UniformOutput',false);
pksdpm=cellfun(@mean,pksdp);
locs1m=cellfun(@nanmean,locs1);
locs1m(isnan(locs1m))=1;
locs1mr=round(locs1m);

posa=WNINTA1(locs1mr,1);


%second half for second peak


figure(4)
plot(dsubS(:,1));
[x2]=ginput(2);
x2r=round(x2);

x2r=round(x2);

u=x2r(2,1);
k=x2r(1,1);
```

```
m=u:k;

dred2=dsubS(m,:);
DRED2A=mat2cell(dred2,size(dred2,1),ones(1,size(dred2,2)));
WNA2=WN(m,:);

c=WNA2(end,1);
d=WNA2(1,1);

WNINTA2=(c:0.001:d).';
WNINTA2ex=WNINTA2*o;
WNINTA2exa=mat2cell(WNINTA2ex,size(WNINTA2ex,1),ones(1,size(WNINTA2ex,2)));

WNA2a=mat2cell(WNA2,size(WNA2,1),ones(1,size(WNA2,2)));
[A2,S2,mu2]=cellfun(@polyfit,WNA2a,DRED2A,orda,'UniformOutput',false);
[A2Va]=cellfun(@polyval,A2,WNINTA2exa,S2,mu2,'UniformOutput',false);

A2Vm=cell2mat(A2Va);

figure(5)
plot(WNINTA2,A2Vm);

[pksdm,locs2]=cellfun(@findpeaks,A2Va,'UniformOutput',false);
pksdmm=cellfun(@mean,pksdm);
locs2m=cellfun(@nanmean,locs2);
locs2m(isnan(locs2m))=1;
locs2mr=round(locs2m);

posb=WNINTA2(locs2mr,1);

idmidp=pksdmm./pksdpm;
end
```

Bibliography

[1] Tamm, L. K.; McConnell, H. M. *Biophysical Journal* **1985**, *47*, 105–113.

[2] Rosen, M. J. *Surfactants and Interfacial Phenomena*, 2nd ed.; Wiley, 1989.

[3] Somasundaran, P.; Shrotri, S.; Huang, L. *Pure and Applied Chemistry* **1998**, *70*, 621–626.

[4] Langmuir, I. *Journal of the American Chemical Society* **1918**, *40*, 1361–1403.

[5] Frumkin, A. *Zeitschrift für Physik A Hadrons and Nuclei* **1926**, *35*, 792–802.

[6] Pashley, R. M.; Karaman, M. E. *Applied Colloid and Surface Chemistry*; Wiley, 2004.

[7] Verwey, E. J. W.; Overbeek, J. T. G. *Theory of the Stability of Lyophobic Colloids*; Elsevier, 1948.

[8] Israelachvili, J. *Intermolecular and Surface Forces*, 3rd ed.; Elsevier, 2011.

[9] Saffman, P. G.; Delbruck, M. *Proceedings of the National Academy of Sciences of the United States of America* **1975**, *72*, 3111–3113.

[10] Saffman, P. G. *Journal of Fluid Mechanics* **1976**, *73*, 593–602.

[11] Evans, E.; Sackmann, E. *Journal of Fluid Mechanics* **1988**, *194*, 553–561.

[12] Cohen, M. H.; Turnbull, D. *Journal of Chemical Physics* **1959**, *31*, 1164–1169.

[13] Turnbull, D.; Cohen, M. H. *Journal of Chemical Physics* **1961**, *34*, 120–125.

[14] Turnbull, D.; Cohen, M. H. *Journal of Chemical Physics* **1970**, *52*, 3038–3041.

[15] Grest, G. S.; Cohen, M. H. *Advances in Chemical Physics*; Wiley, 2007; pp 455–525.

[16] Macedo, P. B.; Litovitz, T. A. *The Journal of Chemical Physics* **1965**, *42*, 245–256.

[17] Galla, H. J.; Hartmann, W.; Theilen, U.; Sackmann, E. *Journal of Membrane Biology* **1979**, *48*, 215–236.

[18] McCarthy, J. E.; Kozak, J. J. *Journal of Chemical Physics* **1982**, *77*, 2214–2216.

[19] Vaz, W. L. C.; Clegg, R. M.; Hallmann, D. *Biochemistry* **1985**, *24*, 781–786.

[20] Almeida, P. F. F.; Vaz, W. L. C.; Thompson, T. E. *Biochemistry* **1992**, *31*, 6739–6747.

[21] Ariola, F. S.; Li, Z.; Cornejo, C.; Bittman, R.; Heikal, A. A. *Biophysical Journal* **2009**, *96*, 2696–2708.

[22] Kahya, N.; Schwille, P. *Journal of Fluorescence* **2006**, *16*, 671–678.

[23] Przybylo, M.; Sýkora, J.; Humpolícková, J.; Benda, A.; Zan, A.; Hof, M. *Langmuir* **2006**, *22*, 9096–9099.

[24] Filippov, A.; Orädd, G.; Lindblom, G. *Biophysical Journal* **2003**, *84*, 3079–3086.

[25] Mathews, C.; van Holde, K. *Biochemistry*, 2nd ed.; The Benjamin/Cummings Publishing Company, 1996.

[26] Langmuir, I. *Science* **1938**, *87*, 493–500.

[27] McConnell, H. M.; Kornberg, R. D. *Biochemistry* **1971**, *10*, 1111–1120.

[28] Liu, J.; Conboy, J. C. *Langmuir* **2005**, *21*, 9091–9097.

[29] Liu, J.; Conboy, J. C. *Biophysical Journal* **2005**, *89*, 2522–2532.

[30] Liu, J.; Conboy, J. C. *Journal of Physical Chemistry C* **2007**, *111*, 8988.

[31] Anglin, T. C.; Conboy, J. C. *Biophysical Journal* **2008**, *95*, 186–193.

[32] Anglin, T. C.; Conboy, J. C. *Biochemistry* **2009**, *48*, 10220–10234.

[33] Malmsten, M. *Journal of Colloid and Interface Science* **1994**, *168*, 247–254.

[34] Tiberg, F.; Harwigsson, I.; Malmsten, M. *European Biophysics Journal* **2000**, *29*, 196–203.

[35] Lee, C.; Wacklin, H.; Bain, C. D. *Soft Matter* **2009**, *5*, 568–575.

[36] Hecht, E. *Optics*, 2nd ed.; Addison-Wesley Publishing Company, Inc., 1987.

[37] Born, M.; Wolf, E. *Principles of Optics*, 7th ed.; Cambridge University Press, 2010.

[38] Beattie, D. A.; Haydock, S.; Bain, C. D. *Vibrational Spectroscopy* **2000**, *24*, 109–123.

[39] Long, D. A. *The Raman Effect*; Wiley, 2002.

[40] Baraska, H.; Labudzinska, A.; Terpiski, J. *Laser Raman Spectrometry*; Ellis Horwood, 1987.

[41] Orendorff, C. J.; Ducey, M. W.; Pemberton, J. E. *The Journal of Physical Chemistry A* **2002**, *106*, 6991–6998.

[42] Malinowski, E. R. *Factor Analysis in Chemistry*, 3rd ed.; Wiley, 2002.

[43] Woods, D. A.; Petkov, J.; Bain, C. D. *Journal of Physical Chemistry B* **2011**, *115*, 7341–7352.

[44] Nollert, P.; Kiefer, H.; Jähnig, F. *Biophysical Journal* **1995**, *69*, 1447–1455.

[45] Kiefer, H.; Klee, B.; John, E.; Stierhof, Y.-D.; Jähnig, F. *Biosensors and Bioelectronics* **1991**, *6*, 233–237.

[46] Keller, C. A.; Kasemo, B. *Biophysical Journal* **1998**, *75*, 1397–1402.

[47] Cremer, P. S.; Boxer, S. G. *Journal of Physical Chemistry B* **1999**, *103*, 2554–2559.

[48] Egawa, H.; Furusawa, K. *Langmuir* **1999**, *15*, 1660–1666.

[49] Reviakine, I.; Brisson, A. *Langmuir* **2000**, *16*, 1806–1815.

[50] Seifert, U. *Advances in Physics* **1997**, *46*, 13–137.

[51] Lipowsky, R.; Seifert, U. *Langmuir* **1991**, *7*, 1867–1873.

[52] Leonenko, Z. V.; Carnini, A.; Cramb, D. T. *Biochimica et Biophysica Acta* **2000**, *1509*, 131–147.

[53] Pabst, G.; Hodzic, A.; Strancar, J.; Danner, S.; Rappolt, M.; Laggner, P. *Biophysical Journal* **2007**, *93*, 2688–2696.

[54] Cunningham, B. A.; Shimotake, J. E.; Taumralis, W.; Mastran, T.; Kwok, W. M.; Kuaffmann, J. W.; Lis, L. J. *Chemistry and Physics of Lipids* **1986**, *39*, 135–143.

[55] Bockmann, R. A.; Hac, A.; Heimburg, T.; Grubmuller, H. *Biophysical Journal* **2003**, *85*, 1647–1655.

[56] Garcia-Manyes, S.; Oncins, G.; Sanz, F. *Biophysical Journal* **2005**, *89*, 1812–1826.

[57] Cordomi, A.; Edholm, O.; Perez, J. J. *Journal of Physical Chemistry B* **2008**, *112*, 1397–1408.

[58] Gurtovenko, A. A.; Vattulainen, I. *Journal of Physical Chemistry B* **2008**, *112*, 1953–1962.

[59] Klasczyk, B.; Knecht, V.; Lipowsky, R.; Dimova, R. *Langmuir* **2010**, *26*, 18951–18958.

[60] Zhdanov, V. P.; Keller, C. A.; Glasmastar, K.; Kasemo, B. *The Journal of Chemical Physics* **2000**, *112*, 900–909.

[61] Zhdanov, V. P.; Kasemo, B. *Langmuir* **2001**, *17*, 3518–3521.

[62] Reimhult, E.; Höök, F.; Kasemo, B. *Langmuir* **2002**, *19*, 1681–1691.

[63] Johnson, J. M.; Ha, T.; Chu, S.; Boxer, S. G. *Biophysical Journal* **2002**, *83*, 3371–3379.

[64] Richter, R.; Mukhopadhyay, A.; Brisson, A. *Biophysical Journal* **2003**, *85*, 3035–3047.

[65] Reimhult, E.; Larsson, C.; Kasemo, B.; Höök, F. *Analytical Chemistry* **2004**, *76*, 7211–7220.

[66] Richter, R. P.; Brisson, A. R. *Biophysical Journal* **2005**, *88*, 3422–3433.

[67] Tawa, K.; Morigaki, K. *Biophysical Journal* **2005**, *89*, 2750–2758.

[68] Seantier, B.; Breffa, C.; Felix, O.; Decher, G. *Journal of Physical Chemistry B* **2005**, *109*, 21755–21765.

[69] Weirich, K. L.; Israelachvili, J. N.; Fygenson, D. K. *Biophysical Journal* **2010**, *98*, 85–92.

[70] Weirich, K. L.; Israelachvili, J. N.; Fygenson, D. K. *Biophysical Journal* **2010**, *98*, 85–92.

[71] Ahmed, S.; Madathingal, R. R.; Wunder, S. L.; Chen, Y. J.; Bothun, G. *Soft Matter* **2011**, *7*, 1936–1947.

[72] Powell, H. V.; OConnell, M. A.; Zhang, M.; Mackenzie, S. R.; Unwin, P. R. *Analytical Chemistry* **2012**, *84*, 2585–2591.

[73] Hernandez, M. R.; Towns, E. N.; Ng, T. C.; Walsh, B. C.; Osibanjo, R.; Parikh, A. N.; Land, D. P. *Applied Optics* **2012**, *51*, 2842–2846.

[74] McMullen, T. P. W.; Lewis, R.; McElhaney, R. N. *Current Opinion in Colloid & Interface Science* **2004**, *8*, 459–468.

[75] Marsh, D. *Handbook of Lipid Bilayers*, 2nd ed.; CRC Press, 2013; p 1174.

[76] Hamai, C.; Yang, T.; Kataoka, S.; Cremer, P. S.; Musser, S. M. *Biophysical Journal* **2006**, *90*, 1241–1248.

[77] Picas, L.; Montero, M. T.; Morros, A.; Oncins, G.; Hernandez-Borrell, J. *Journal of Physical Chemistry B* **2008**, *112*, 10181–10187.

[78] Seeger, H. M.; Marino, G.; Alessandrini, A.; Facci, P. *Biophysical Journal* **2009**, *97*, 1067–1076.

[79] Papahadjopolous, D.; Miller, N. *Biochimica et Biophysica Acta* **1967**, *135*, 624–638.

[80] Lingwood, D.; Simons, K. *Science* **2010**, *327*, 46–50.

[81] van Meer, G.; Lisman, Q. *Journal of Biological Chemistry* **2002**, *277*, 25855–25858.

[82] Heerklotz, H. *Quarterly Reviews of Biophysics* **2008**, *41*, 205–264.

[83] Woods, D. A.; Bain, C. D. *Analyst* **2012**, *137*, 35–48.

[84] Wacklin, H. P. *Langmuir* **2011**, *27*, 7698–7707.

[85] Williamson, I. M.; Alvis, S. J.; East, J. M.; Lee, A. G. *Cellular and Molecular Life Sciences* **2003**, *60*, 1581–1590.

[86] Irvine, D. J. *Nature Materials* **2011**, *10*, 342–343.

[87] Nagarajan, S.; Schuler, E. E.; Ma, K.; Kindt, J. T.; Dyer, R. B. *Journal of Physical Chemistry B* **2012**, *116*, 13749–13756.

[88] Rappolt, M.; Hickel, A.; Bringezu, F.; Lohner, K. *Biophysical Journal* **2003**, *84*, 3111–3122.

[89] Koynova, R.; Caffrey, M. *Chemistry and Physics of Lipids* **1994**, *69*, 1–34.

[90] Koynova, R.; Caffrey, M. *Biochimica et Biophysica Acta* **1998**, *1376*, 91–145.

[91] Marsh, D. *Biochimica et Biophysica Acta* **2010**, *1798*, 40–51.

[92] Zimm, B. H.; Bragg, J. K. *The Journal of Chemical Physics* **1959**, *31*, 526–535.

[93] Marsh, D.; Watts, A.; Knowles, P. F. *Biochimica et Biophysica Acta* **1977**, *465*, 500–514.

[94] Cevc, G.; Marsh, D. *Phospholipid Bilayers*; Wiley, 1987.

[95] Yeagle, P. L.; Hutton, W. C.; Martin, R. B. *Biochemistry* **1978**, *17*, 5745–5750.

[96] Epand, R. M.; Bottega, R. *Biochimica et Biophysica Acta* **1988**, *944*, 144–154.

[97] Kwon, K. O.; Kim, M. J.; Abe, M.; Ishinomori, T.; Ogino, K. *Langmuir* **1994**, *10*, 1415–1420.

[98] Mattai, J.; Hauser, H.; Demel, R. A.; Shipley, G. G. *Biochemistry* **1989**, *28*, 2322–2330.

[99] Hauser, H.; Shipley, G. G. *Journal of Biological Chemistry* **1981**, *256*, 1377–1380.

[100] Hauser, H.; Shipley, G. G. *Biochemistry* **1983**, *22*, 2171–2178.

[101] Hauser, H.; Shipley, G. G. *Biochemistry* **1984**, *23*, 34–41.

[102] Hauser, H.; Shipley, G. G. *Biochimica et Biophysica Acta* **1985**, *813*, 343–346.

[103] Garidel, P.; Blume, A.; Hubner, W. *Biochimica et Biophysica Acta* **2000**, *1466*, 245–259.

[104] Fox, C. B.; Uibel, R. H.; Harris, J. M. *Journal of Physical Chemistry B* **2007**, *111*, 11428–11436.

[105] Shaw, K. P.; Brooks, N. J.; Clarke, J. A.; Ces, O.; Seddon, J. M.; Law, R. V. *Soft Matter* **2012**, *8*, 1070–1078.

[106] Naumann, C.; Brumm, T.; Bayerl, T. M. *Biophysical Journal* **1992**, *63*, 1314–1319.

[107] Lee, C. S.; Bain, C. D. *Biochimica et Biophysica Acta* **2005**, *1711*, 59–71.

[108] Sovago, M.; Wurpel, G. W. H.; Smits, M.; Muller, M.; Bonn, M. *Journal of the American Chemical Society* **2007**, *129*, 11079–11084.

[109] Enders, O.; Ngezahayo, A.; Wiechmann, M.; Leisten, F.; Kolb, H. A. *Biophysical Journal* **2004**, *87*, 2522–2531.

[110] Seeger, H. M.; Di Cerbo, A.; Alessandrini, A.; Facci, P. *Journal of Physical Chemistry B* **2010**, *114*, 8926–8933.

[111] Yarrow, F.; Kuipers, B. W. M. *Chemistry and Physics of Lipids* **2011**, *164*, 9–15.

[112] Szmodis, A. W.; Blanchette, C. D.; Levchenko, A. A.; Navrotsky, A.; Longo, M. L.; Orme, C. A.; Parikh, A. N. *Soft Matter* **2008**, *4*, 1161–1164.

[113] Ohlsson, G.; Tigerstrom, A.; Hook, F.; Kasemo, B. *Soft Matter* **2011**, *7*, 10749–10755.

[114] Oleson, T. A.; Sahai, N.; Pedersen, J. A. *Journal of Colloid and Interface Science* **2010**, *352*, 327–336.

[115] Bockmann, R. A.; Grubmuller, H. *Angwandte Chemie-International Edition* **2004**, *43*, 1021–1024.

[116] Huster, D.; Arnold, K.; Gawrisch, K. *Biophysical Journal* **2000**, *78*, 3011–3018.

[117] Hauser, H.; Dawson, R. M. C. *European Journal of Biochemistry* **1967**, *1*, 61–69.

[118] Lee, C. S.; Bain, C. D. *Biochimica et Biophysica Acta* **2005**, *1711*, 59.

[119] Keller, S.; Heerklotz, H.; Jahnke, N.; Blume, A. *Biophysical Journal* **2006**, *90*, 4509–4521.

[120] Marsh, D. *Chemistry and Physics of Lipids* **2006**, *144*, 146–159.

[121] Lipowsky, R.; Leibler, S. *Physical Review Letters* **1986**, *56*, 2541–2544.

[122] Lipowsky, R. *Handbook of Biological Physics*; Elsevier, 1995; Chapter 11, pp 521–602.

[123] Schurtenberger, P.; Mazer, N.; Kanzig, W. *Journal of Physical Chemistry* **1985**, *89*, 1042–1049.

[124] Lichtenberg, D. *Biochimica et Biophysica Acta* **1985**, *821*, 470–478.

[125] Almog, S.; Litman, B. J.; Wimley, W.; Cohen, J.; Wachtel, E. J.; Barenholz, Y.; Benshaul, A.; Lichtenberg, D. *Biochemistry* **1990**, *29*, 4582–4592.

[126] de la Maza, A.; Parra, J. L. *Colloids and Surfaces A: Physiochemical and Engineering Aspects* **1996**, *112*, 63–71.

[127] de la Maza, A.; Parra, J. L. *Journal of the American Oil Chemists Society* **1997**, *74*, 9–17.

[128] Lopez, O.; Cocera, M.; de la Maza, A. *Colloids and Surfaces A: Physicochemical and Engineering Aspects* **1999**, *157*, 167–176.

[129] Cocera, M.; Lopez, O.; Estelrich, J.; Parra, J. L.; de la Maza, A. *Langmuir* **1999**, *15*, 6609–6612.

[130] Sanderson, J. M. *Molecular Membrane Biology* **2012**, *29*, 118–143.

[131] Hoyrup, P.; Davidsen, J.; Jorgensen, K. *Journal of Physical Chemistry B* **2001**, *105*, 2649–2657.

[132] Deo, N.; Somasundaran, P. *Colloids and Surfaces A: Physicochemical and Engineering Aspects* **2001**, *186*, 33–41.

[133] Yaroslavov, A. A.; Udalykh, O. Y.; Melik-Nubarov, N. S.; Kabanov, V. A.; Ermakov, Y. A.; Azov, V. A.; Menger, F. M. *Chemistry-A European Journal* **2001**, *7*, 4835–4843.

[134] Deo, N.; Somasundaran, P.; Subramanyan, K.; Ananthapadmanabhan, K. P. *Journal of Colloid and Interface Science* **2002**, *256*, 100–105.

[135] Artyukhin, A. B.; Stroeve, P. *Industrial & Engineering Chemistry Research* **2003**, *42*, 2156–2162.

[136] Deo, N.; Somasundaran, P. *Langmuir* **2003**, *19*, 7271–7275.

[137] Karlovska, J.; Lohner, K.; Degovics, G.; Lacko, I.; Devinsky, F.; Balgavy, P. *Chemistry and Physics of Lipids* **2004**, *129*, 31–41.

[138] Keller, S.; Heerklotz, H.; Blume, A. *Journal of the American Chemical Society* **2006**, *128*, 1279–1286.

[139] Han, J. H.; Taylor, J. D.; Phillips, K. S.; Wang, X.; Feng, P.; Cheng, Q. *Langmuir* **2008**, *24*, 8127–8133.

[140] Sudbrack, T. P.; Archilha, N. L.; Itri, R.; Riske, K. A. *Journal of Physical Chemistry B* **2011**, *115*, 269–277.

[141] Nazari, M.; Kurdi, M.; Heerklotz, H. *Biophysical Journal* **2012**, *102*, 498–506.

[142] Liao, Z.; Pemberton, J. E. *Journal of Physical Chemistry A* **2006**, *110*, 13744–13753.

[143] Staykova, M.; Arroyo, M.; Rahimi, M.; Stone, H. A. *Physical Review Letters* **2013**, *110*, 28101–28106.

[144] Tan, A. M.; Ziegler, A.; Steinbauer, B.; Seelig, J. *Biophysical Journal* **2002**, *83*, 1547–1556.

[145] Pantaler, E.; Kamp, D.; Haest, C. W. M. *Biochimica et Biophysica Acta* **2000**, *1509*, 397–408.

[146] Chiu, S. W.; Vasudevan, S.; Jakobsson, E.; Mashl, R. J.; Scott, H. L. *Biophysical Journal* **2003**, *85*, 3624–3635.

[147] Voet, D.; Voet, J.; Pratt, C. *Principles of Biochemistry*, 3rd ed.; Wiley, 2008.

[148] Shaikh, S. R.; Brzustowicz, M. R.; Gustafson, N.; Stillwell, W.; Wassall, S. R. *Biochemistry* **2002**, *41*, 10593–10602.

[149] Chachaty, C.; Rainteau, D.; Tessier, C.; Quinn, P. J.; Wolf, C. *Biophysical Journal* **2005**, *88*, 4032–4044.

[150] Woods, D. A. Dynamics of Surfactant Adsorption at Solid-Liquid Interfaces. Ph.D. thesis, University of Durham, 2011.